Silicon Nanocrystals Embedded in Silicon Carbide for Tandem Solar Cell Applications

Manuel Schnabel
St. Anne's College

Thesis submitted for the Degree of Doctor of Philosophy
Michaelmas Term 2014
Supervisors: Prof. P. R. Wilshaw, Dr. S. Janz

Abstract

Silicon Nanocrystals Embedded in Silicon Carbide for Tandem Solar Cell Applications

Manuel Schnabel
St. Anne's College
Department of Materials, University of Oxford

Thesis submitted for the degree of Doctor of Philosophy
Michaelmas Term 2014

Tandem solar cells are potentially much more efficient than the silicon solar cells that currently dominate the market but require materials with different bandgaps. This thesis presents work on silicon nanocrystals (Si-NC) embedded in silicon carbide (SiC), which are expected to have a higher bandgap than bulk Si due to quantum confinement, with a view to using them in the top cell of a tandem cell.

The strong photoluminescence (PL) of precursor films used to prepare Si-NC in SiC (Si-NC/SiC) was markedly reduced upon Si-NC formation due to simultaneous out-diffusion of hydrogen that passivated dangling bonds. This cannot be reversed by hydrogenation and leads to weak PL that is due to, and limited by, non-paramagnetic defects, with an estimated quantum yield of $\leq 5\times10^{-7}$. Optical interference was identified as a substantial artefact and a method proposed to account for this.

Majority carrier transport was found to be Ohmic at all temperatures for a wide range of samples. Hydrogenation decreases dangling bond density and increases conductivity up to 1000 times. The temperature-dependence of conductivity is best described by a combination of extended-state and variable-range hopping transport where the former takes place in the Si nanoclusters. Furthermore, n-type background doping by nitrogen and/or oxygen was identified.

In the course of developing processing steps for Si-NC-based tandem cells, a capping layer was developed to prevent oxidation of Si-NC/SiC, and diffusion of boron and phosphorus in nanocrystalline SiC was found to occur via grain boundaries with an activation energy of 5.3±0.4 eV and 4.4±0.7 eV, respectively. Tandem cells with a Si-NC/SiC top cell and bulk Si bottom cell were prepared that exhibited open-circuit voltages V_{oc} of 900 mV and short-circuit current densities of 0.85 $mAcm^{-2}$. Performance was limited by photocurrent collection in the top cell; however, the V_{oc} obtained demonstrates tandem cell functionality.

Preface

This thesis is an account of the work carried out by the author at the Fraunhofer-Institute for Solar Energy Systems (ISE) in Freiburg, Germany, under the supervision of Dr. Stefan Janz from ISE and Prof. Peter R. Wilshaw from the Department of Materials, University of Oxford, from Hilary Term 2011 to Michaelmas Term 2014. No part of this thesis has previously been submitted for a degree at the University of Oxford or elsewhere. The work of other authors has been freely drawn upon and is duly acknowledged in the text. A list of references is given at the end of the thesis.

Work presented in this thesis has been published as follows:

Peer-reviewed Journal Articles

1. **M. Schnabel**, C. Weiss, P. Löper, M. Canino, C. Summonte, P.R. Wilshaw, and S. Janz. *Nanocrystalline SiC formed by annealing of a-SiC:H on Si substrates: A study of dopant interdiffusion.* Journal of Applied Physics **116** (2), 024315 (2014).
2. **M. Schnabel**, C. Weiss, M. Canino, T. Rachow, P. Löper, C. Summonte, S. Mirabella, S. Janz, and P.R. Wilshaw. *Boron diffusion in nanocrystalline 3C-SiC.* Applied Physics Letters **104** (21), 213108 (2014).
3. **M. Schnabel**, P. Löper, M. Canino, S.A. Dyakov, M. Allegrezza, M. Bellettato, J. López-Vidrier, S. Hernández, C. Summonte, B. Garrido, P.R. Wilshaw, and S. Janz. *Electrical and optical characterisation of silicon nanocrystals embedded in SiC.* Solid State Phenomena **205-6**, 480-5 (2014).
4. **M. Schnabel**, P. Löper, S. Gutsch, P.R. Wilshaw, and S. Janz. *Thermal oxidation and encapsulation of silicon–carbon nanolayers.* Thin Solid Films **527**, 193-9 (2013).

5. S. Janz, P. Löper, and **M. Schnabel**. *Silicon nanocrystals produced by solid phase crystallisation of superlattices for photovoltaic applications.* Materials Science and Engineering B **178** (9), 542-50 (2013).
6. **M. Schnabel**, C. Weiss, P. Löper, P.R. Wilshaw, and S. Janz. *Self-assembled silicon nanocrystal arrays for photovoltaics.* physica status solidi (a) (accepted).
7. **M. Schnabel**, C. Summonte, S.A. Dyakov, M. Canino, L. López-Conesa, P. Löper, S. Janz, and P.R. Wilshaw. *Absorption and Emission of Silicon Nanocrystals Embedded in SiC: Eliminating Fabry-Pérot Interference.* Journal of Applied Physics (in press).
8. **M. Schnabel**, A.B. Siddique, S. Janz, and P.R. Wilshaw. *Phosphorus Diffusion in Nanocrystalline 3C-SiC.* submitted to Applied Physics Letters.
9. **M. Schnabel**, M. Canino, S. Kühnhold, J. López-Vidrier, T. Klugermann, C. Weiss, L. López-Conesa, M. Zschintzsch, C. Summonte, P. Löper, P.R. Wilshaw, and S. Janz. *Charge Transport in Nanocrystalline SiC with and without embedded Si Nanocrystals*. submitted to Physical Review B.

Conference Contributions:

1. **M. Schnabel**, P. Löper, M. Canino, M. Allegrezza, M. Bellettato, J. López-Vidrier, S. Hernández, S. Janz, C. Summonte, B. Garrido, and P. Wilshaw. *Conduction and Luminescence of Silicon Nanocrystals Embedded in an SiC Matrix*, in *EMRS Spring Meeting* (Strasbourg, France, 2013).
2. **M. Schnabel**, P. Löper, M. Canino, M. Allegrezza, M. Bellettato, J. López-Vidrier, S. Hernández, S. Janz, C. Summonte, B. Garrido, and P. Wilshaw. *Optoelectronic Characterisation of Silicon Nanocrystals Embedded in Silicon Carbide*, in *EMRS Spring Meeting* (Strasbourg, France, 2012).

3. **M. Schnabel**, T. Klugermann, M. Canino, J. López-Vidrier, S. Hernández, C. Summonte, B. Garrido, P. Löper, P. Wilshaw, and S. Janz. *Charge Transport in Poly-SiC with Embedded Si Nanocrystals for all-Si Tandem Solar Cells*, in *MRS Spring Meeting* (San Francisco, CA, USA, 2014).
4. **M. Schnabel**, A. Witzky, P. Löper, R. Gradmann, M. Künle, and S. Janz. *Electrical properties of recrystallised SiC films from PECVD precursors for silicon quantum dot solar cell applications*, in *Proceedings of the 26th EU PVSEC* (Hamburg, Germany, 2011).
5. S. Janz, **M. Schnabel**, P. Löper, C. Summonte, M. Canino, J. López-Vidrier, S. Hernández, B. Garrido, and S.W. Glunz. *Processing and characterisation of tandem solar cells from crystalline silicon materials*, in *Proceedings of the 28th EU PVSEC* (Paris, France, 2013).

In addition, the author of this thesis has, in the course of his research on the topic of this thesis, co-authored the following publications:

Peer-reviewed Journal Articles:

1. P. Löper, D. Stüwe, M. Künle, M. Bivour, C. Reichel, R. Neubauer, **M. Schnabel**, M. Hermle, O. Eibl, S. Janz, M. Zacharias, and S.W. Glunz. *A membrane device for substrate-free photovoltaic characterization of quantum dot based p-i-n solar cells.* Advanced Materials **24**, 3124-9 (2012).
2. P. Löper, M. Canino, D. Qazzazie, **M. Schnabel**, M. Allegrezza, C. Summonte, S.W. Glunz, S. Janz, and M. Zacharias. *Silicon nanocrystals embedded in silicon carbide: investigation of charge carrier transport and recombination.* Applied Physics Letters **102** (3), 033507 (2013).

3. D. Hiller, A. Zelenina, S. Gutsch, S.A. Dyakov, L. López-Conesa, J. López-Vidrier, S. Estradé, F. Peiró, B. Garrido, J. Valenta, M. Kořínek, F. Trojánek, P. Malý, **M. Schnabel**, C. Weiss, S. Janz, and M. Zacharias. *Absence of quantum confinement effects in the photoluminescence of Si_3N_4–embedded Si nanocrystals.* Journal of Applied Physics **115** (20), 204301 (2014).
4. M. Kořínek, **M. Schnabel**, M. Canino, M. Kozák, F. Trojánek, J. Salava, P. Löper, S. Janz, C. Summonte, and P. Malý. *Influence of boron doping and hydrogen passivation on recombination of photoexcited charge carriers in silicon nanocrystal/SiC multilayers.* Journal of Applied Physics **114** (7), 073101 (2013).
5. J. López-Vidrier, Y. Berencén, S. Hernández, O. Blázquez, S. Gutsch, J. Laube, D. Hiller, P. Löper, **M. Schnabel**, S. Janz, M. Zacharias, and B. Garrido. *Charge transport and electroluminescence of silicon nanocrystals/SiO_2 superlattices.* Journal of Applied Physics **114** (16), 163701 (2013).
6. M. Canino, C. Summonte, M. Allegrezza, R. Shukla, I.P. Jain, M. Bellettato, A. Desalvo, F. Mancarella, M. Sanmartin, A. Terrasi, P. Löper, **M. Schnabel**, and S. Janz. *Identification and tackling of a parasitic surface compound in SiC and Si-rich carbide films.* Materials Science and Engineering B **178** (9), 623– 629 (2013).
7. J. López-Vidrier, S. Hernández, J. Samà, M. Canino, M. Allegrezza, M. Bellettato, R. Shukla, **M. Schnabel**, P. Löper, L. López-Conesa, S. Estradé, F. Peiró, S. Janz, and B. Garrido. *Structural, optical and electrical properties of silicon nanocrystals embedded in Si_xC_{1-x}/SiC multilayer systems for photovoltaic applications.* Materials Science and Engineering B **178** (9), 639-44 (2013).
8. P. Löper, M. Canino, J. López-Vidrier, **M. Schnabel**, F. Schindler, F. Heinz, A. Witzky, M. Bellettato, M. Allegrezza, D. Hiller, A. Hartel, S. Gutsch, S. Hernández, R. Guerra, S. Ossicini, B. Garrido, S. Janz, and M. Zacharias. *Silicon*

nanocrystals from high-temperature annealing: Characterization on device level. physica status solidi (a) **210** (4), 669-75 (2013).

9. C. Summonte, M. Allegrezza, M. Bellettato, F. Liscio, M. Canino, A. Desalvo, J. López-Vidrier, S. Hernández, L. López-Conesa, S. Estradé, F. Peiró, B. Garrido, P. Löper, **M. Schnabel**, S. Janz, R. Guerra, and S. Ossicini. *Silicon nanocrystals in carbide matrix.* Solar Energy Materials and Solar Cells **128**, 138-149 (2014).

Conference Contributions:

1. J. López-Vidrier, D. Hiller, S. Gutsch, A. Hartel, **M. Schnabel**, P. Löper, M. Foti, L. López-Conesa, S. Estradé, F. Peiró, M. Zacharias, S. Janz, and B. Garrido. *Silicon quantum dots embedded in SiO_2 for tandem solar cells*, in *17th Workshop on Dielectrics in Microelectronics* (Dresden, Germany, 2012).
2. M. Korínek, F. Trojánek, J. Salava, P. Malý, **M. Schnabel**, S. Janz, M. Canino, and C. Summonte. *Photoexcited charge carrer dynamics in silicon nanocrystal/SiC multilayers*, in *EMRS Spring Meeting* (Strasbourg, France, 2013).
3. P. Löper, **M. Schnabel**, C. Summonte, S. Janz, and M. Zacharias. *Silicon Nanocrystal p-i-n Solar Cells*, in *EMRS Spring Meeting* (Strasbourg, France, 2013).
4. J. López-Vidrier, D. Hiller, A. Hartel, S. Gutsch, **M. Schnabel**, P. Löper, L. López-Conesa, S. Estradé, F. Peiró, S. Janz, M. Zacharias, and B. Garrido. *Assessment of the Degree of Crystallinity of Si-NC/SiO_2 by Means of Cross-Section Raman Scattering*, in *EMRS Spring Meeting* (Strasbourg, France, 2012).
5. C. Summonte, M. Allegrezza, M. Bellettato, R. Shukla, A. Desalvo, A. Terrasi, S. Mirabella, I. Crupi, S. Janz, P. Löper, **M. Schnabel**, J. López-Vidrier, L. López-Conesa, S. Hernández, S. Estradé, F. Peiró, B. Garrido, and J. Valenta. *Optical Absorption of Silicon Nanocrystals in Silicon Carbide Matrix*, in *EMRS Spring Meeting* (Strasbourg, France, 2012).

6. C. Summonte, S. Hernández, J. López-Vidrier, L. López-Conesa, M. Allegrezza, F. Liscio, **M. Schnabel**, P. Löper, S. Janz, S. Estradé, F. Peiró, and B. Garrido. *Space of formation of silicon nanocrystals in silicon carbide*, in *EMRS Spring Meeting* (Strasbourg, France, 2013).
7. S. Janz, P. Löper, **M. Schnabel**, M. Zacharias, D. Hiller, S. Gutsch, A. Hartel, C. Summonte, A. Canino, M. Allegrezza, S. Ossicini, R. Guerra, I. Marri, B. Garrido, S. Hernández, J. López-Vidrier, J. Valenta, T. Kubera, M. Foti, and C. Gerardi. *The NASCEnT project*, in *Proceedings of the 26th EU PVSEC* (Hamburg, Germany, 2011).
8. P. Löper, M. Canino, J. López-Vidrier, **M. Schnabel**, A. Witzky, M. Belletato, M. Allegrezza, D. Hiller, A. Hartel, S. Gutsch, S. Hernández, R. Guerra, S. Ossicini, B. Garrido, S. Janz, and M. Zacharias. *Silicon quantum dots in photovoltaic devices: device fabrication, characterization and comparison of materials*, in *Proceedings of the 27th EU PVSEC* (Frankfurt, Germany, 2012).
9. C. Weiss, M. Rumpel, **M. Schnabel**, P. Löper, and S. Janz. *Novel silicon nanocrystal materials for photovoltaic applications*, in *Proceedings of the 28th EU PVSEC* (Paris, France, 2013).
10. J. López-Vidrier, Y. Berencén, B. Mundet, S. Hernández, S. Gutsch, D. Hiller, P. Löper, **M. Schnabel**, S. Janz, M. Zacharias, and B. Garrido. *Electrical and electroluminescence properties of silicon nanocystals/SiO_2 superlattices*, in *Proceedings of SPIE Vol. 9133* (Brussels, Belgium, 2014).

Book chapters

1. S. Janz, P. Löper, and **M. Schnabel**. *Prototype PV cells with Si nanoclusters*, in *Nanotechnology and Photovoltaic Devices: Light Energy Harvesting with Group IV Nanostructures*, ed. J. Valenta and S. Mirabella. 2014: Pan Stanford Publishing. p. 381-415.
2. P. Löper, M. Canino, **M. Schnabel**, C. Summonte, S. Janz, and M. Zacharias. *High-Bandgap Silicon Nanocrystal Solar Cells: Device Fabrication, Characterization, and Modeling*, in *High-Efficiency Solar Cells*, ed. X. Wang and Z.M. Wang. 2014: Springer International Publishing. p. 165-194.

Manuel Schnabel, Oxford

20th January 2015

Acknowledgements

I would like to thank both of my supervisors, Dr. Stefan Janz at Fraunhofer ISE and Prof. Peter R. Wilshaw at the University of Oxford, for going along with a DPhil split over two institutions and for making this rather unusual arrangement work. I thank Dr. Stefan Janz for his guidance and for providing me with the resources and the freedom to explore my field of research, and Prof. Peter R. Wilshaw for intense discussions, encouragement, and for his enthusiasm even when there were more questions than answers. I also acknowledge Dr. Martin Hermle for fruitful discussions.

I am grateful to Dr. Philipp Löper and Dr. Matthias Künle for carrying out the initial work on Si NCs in SiC at ISE that I was able to build upon, and in particular thank Dr. Philipp Löper for helping me with my first experiments and essentially supervising me during the first year of my DPhil. I also thank Charlotte Weiss, whom the Si NC torch now goes to, for her support and the enthusiasm she has brought to the group.

I would further like to thank the European Commission for funding the project NASCEnT that funded my research under grant number 245977, and the project partners for making the project, and thence my thesis, run so smoothly. I thank Dr. Caterina Summonte and Dr. Marica Canino from CNR-IMM for providing me with samples and for putting up with my endless questions regarding these samples. I thank Prof. Margit Zacharias, Dr. Daniel Hiller, Dr. Sebastian Gutsch, and Dr. Andreas Hartel from IMTEK for letting me process some samples in their lab, and for in-depth discussions on Si NCs, and Julià López-Vidrier from UB for educating me on all things Raman.

I am indebted to the technicians and interns at ISE without whom the work presented in this thesis would not have been possible. I gratefully acknowledge the support of Antonio

Leimenstoll, Felix Schätzle, Sonja Seitz, Nadine Weber, Nicholas König, Harald Lautenschlager, Mira Kwiatkowska, Philipp Barth, Michaela Winterhalder, Rainer Neubauer, Karin Zimmermann, Andreas Lösel, Nicole Hoffmann, and Manuel Moser for sample processing; Andreas Reichert and Janina Löffler for routine measurements; Jutta Zielonka for SEM; Annika Raugewitz for ECV; Elisabeth Schäffer for solar cell characterisation and general guidance on how to get things done at ISE; and Christian Schetter, Björn Debowski, and Harald Steidl for being quick to help in fixing broken equipment.

I am also grateful to fellow Ph.D. students Thomas Rachow and Kai Schillinger for fulfilling a range of APCVD requests, Saskia Kühnhold for ESR measurements, Dr. Jonas Schön for diffusion simulations, and Martin Bivour and Dr. Christian Reichel for fruitful discussions about tandem cells. I am also indebted to Sergey Dyakov from Trinity College Dublin (now at KTH in Stockholm) for performing photoluminescence simulations.

I thank Hanna-Sophie Maier, Till Klugermann, Matthias Rumpel, and Jared Lolli for taking it upon themselves to do their Bachelor's thesis or internship under my supervision and for their invaluable contributions to the work presented in this thesis. I also thank Gina Kraft, Andreas Reichert, Till Klugermann, and Anke Witzky for babysitting the rather erratic IV setup, and thank Anke specifically for helping me get through the fairly fruitless first year and a half of my DPhil with her wry sense of humour.

I am grateful to Milan Padilla, Stephen Haag, Elisabeth Schäffer, and Dr. Philipp Löper for making our office a pleasure to work in and for generally being awesome.

I wish to thank everyone in the ISE departments SEC, MST, and PTQ with whom I have worked in the past four years.

I acknowledge my local kebab shop and the high-throughput coffee machine at ISE for helping me work the long hours without which this thesis would still be far from finished.

Finally, I want to thank my parents, family and friends for their love and support, and EunJu Oh for being there for me.

Contents

1. Introduction

1.1 Photovoltaics

An exponentially growing global population and increasing standards of living across the world create the need for a fuel-free energy supply that eases the demand on the world's limited natural resources and mitigates global warming. This need is increasingly met by photovoltaics (PV) which offer a range of advantages over other power sources. They do not need any fuel, have no moving parts (unless tracking is used) which cuts down on maintenance, can be installed in a wide range of capacities, from kW to GW, and do not affect the landscape in the way hydroelectric and wind power do. As can be seen in Figure 1.1(a), the globally installed capacity has increased exponentially since 2000, to 139 GW_p (GW peak capacity) in 2013 [1]. During that time, the average price of PV modules has dropped from 5 to 0.6 $€_{2013}/W_p$ (corrected for inflation) [2], and in countries with large installed PV capacities such as Germany, PV is in summer months able to meet a substantial part of the peaks in power demand that occur during the day (see Figure 1.1(b)) [3].

The PV market is dominated by crystalline Si (c-Si) modules that have a market share of over 90% [2]. Their price has fallen due to technology transfer from the laboratory to industry and cost savings by manufacturers but as can be seen in Figure 1.1(c) the laboratory efficiencies for Si cells have stagnated in the past ten years [2, 4]. This has not been for lack of trying, but because the current record efficiency of 25.6% [4] is already very close to the theoretical limit of 29.4% [5]. This limit arises from the fact that Si cells have a single bandgap (1.12 eV [6]) that prevents them from absorbing lower-energy photons (transmission losses), and from converting more than 1.12 eV of the energy of higher-energy photons to electricity because

carriers excited by higher-energy photons rapidly thermalise to the band edges (thermalisation losses). This is illustrated in Figure 1.2(a).

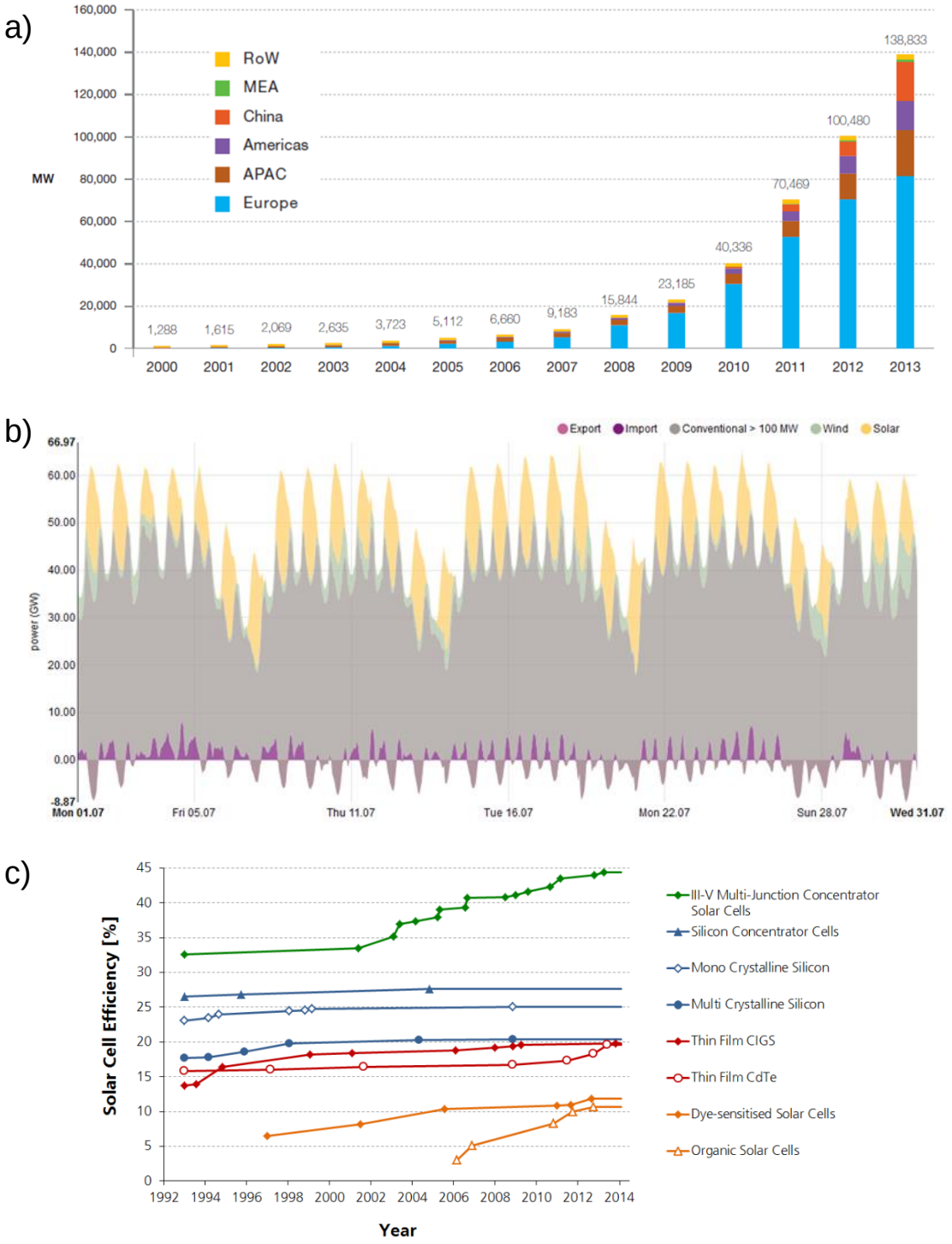

Figure 1.1. (a) Development of globally installed PV capacity (reproduced from Ref. [1], MEA: Middle East and Africa, APAC: Asia Pacific, RoW: rest of world). (b) Electricity supply of Germany in July 2013 by source (reproduced from Ref. [3], © Fraunhofer-Gesellschaft). (c) Development of record laboratory efficiencies for different PV cell types (reproduced from Ref. [2], © Fraunhofer ISE).

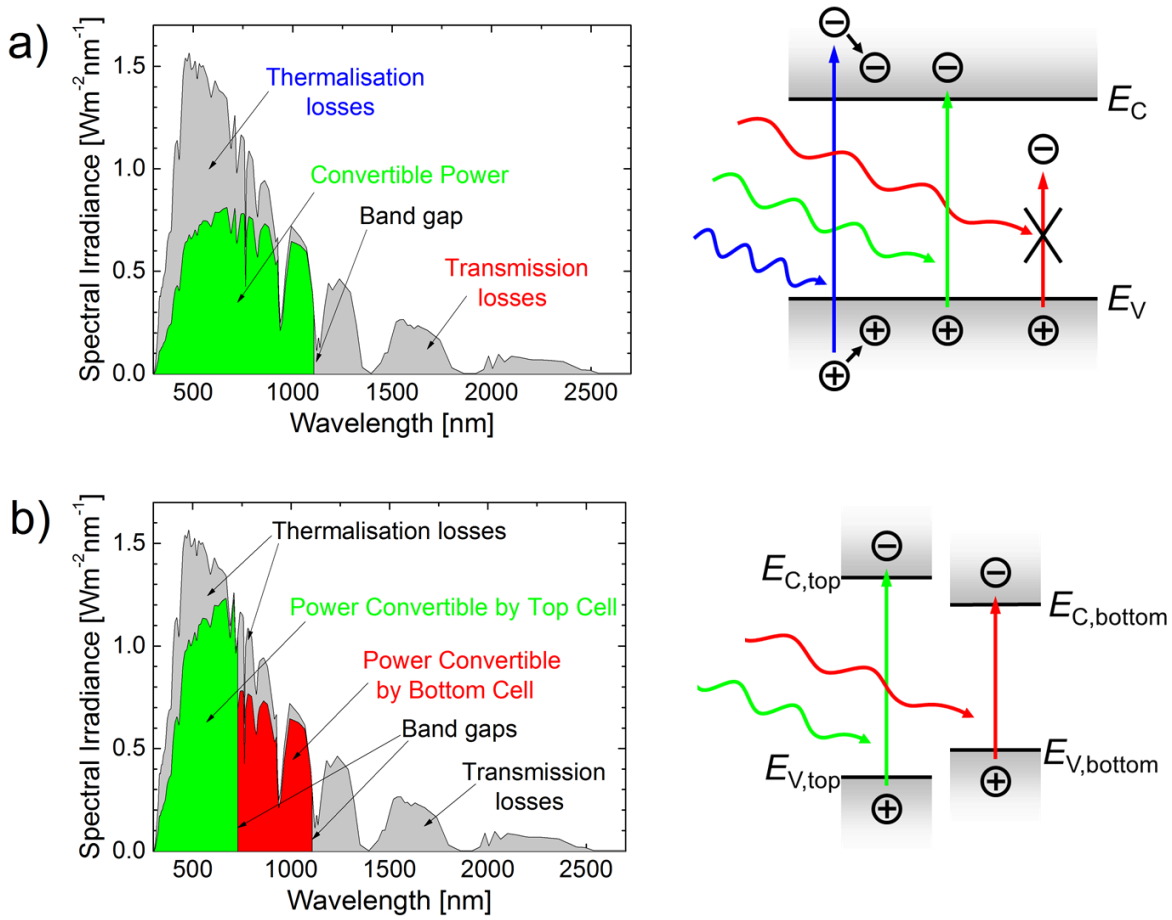

Figure 1.2. Convertible part of the solar spectrum, and band diagram showing transitions for incident photons of different energy, for (a) a Si solar cell (b) a two-junction tandem cell. In (b) the colours represent the convertible energy for the two different subcells.

The efficiency limit is mainly the result of the trade-off between thermalisation and transmission losses in the case of a single p-n junction. Several technologies to circumvent this single-junction efficiency limit have been proposed [7], but only multi-junction cells (also called tandem cells), have succeeded (see Figure 1.1(c)). In tandem cells, multiple cells with different bandgaps are stacked in order of increasing bandgap with the highest bandgap towards the incident light. The top cell can now have a high bandgap to reduce thermalisation losses because the high transmission losses of this cell are converted by the cell(s) with lower bandgap below it. Figure 1.2(b) shows this process schematically and highlights the larger convertible proportion of the solar spectrum. Using this approach, the theoretical efficiency limit under diffuse illumination increases from 31.0% for a single-junction cell to 42.5% for

two junctions, 48.6% for three junctions, and 68.2% for an infinite stack of cells where each cell absorbs photons with energy equal to its bandgap only [7].

Tandem cells based on III-V semiconductors have achieved efficiencies of up to 37.9% under one sun illumination [4], but remain restricted to space and concentrated PV applications due to high raw material and processing costs. It is therefore desirable to develop a tandem cell that is more efficient than a conventional Si cell but based on inexpensive materials. Ideally, it would use a conventional Si cell as the bottom-most cell and be compatible with standard Si solar cell manufacturing to enable a rapid transfer to industry.

1.2 Silicon Nanocrystals

Si dominates the PV market because it is abundant, non-toxic, inert, and because a lot of processes and know-how were adopted from the microelectronics industry. It would therefore be desirable to construct a tandem cell entirely from Si. “Micromorph” tandem cells made of a-Si:H and μc-Si:H have been produced with efficiencies of up to 13.4% [4] but are limited by the poor carrier mobility and light-induced degradation of a-Si:H [8]. In crystalline silicon, which does not suffer from these shortcomings, different bandgaps can be achieved by exploiting the quantum confinement effect in silicon nanocrystals (Si NCs, see Figure 1.3(a)). Bright, size-dependent Si NC luminescence peaking between 1.3 and 2.0 eV has been reported in solution [9], but integration into solar cells requires Si NCs embedded in a solid film, a host matrix. The Si NCs should have uniform size and separation such that wavefunction overlap is optimised and minibands are formed (see Figure 1.3(b)).

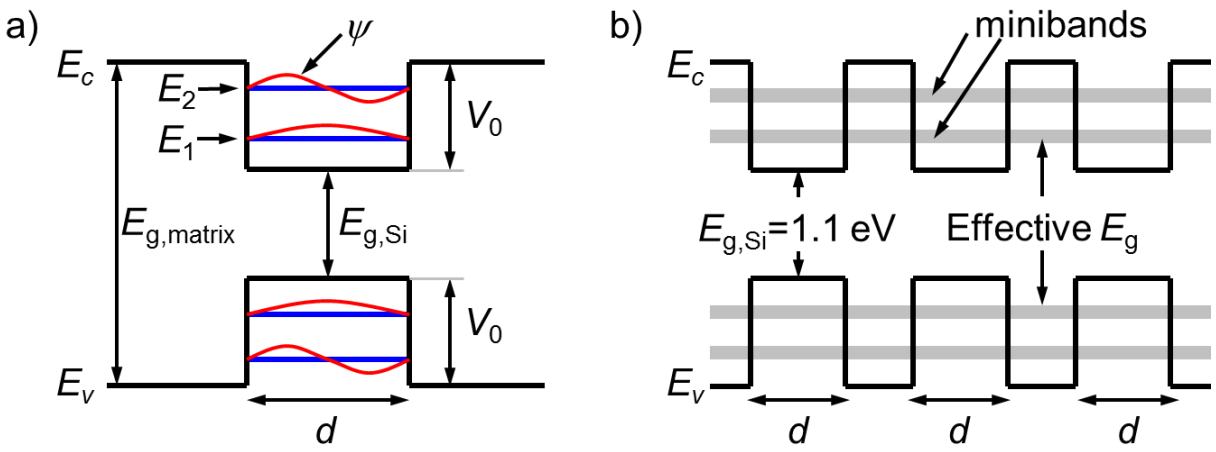

Figure 1.3. Band diagram illustrating quantum confinement due to a confinement potential V_0 in a Si NC of diameter d showing the first and second energy levels (E_1, E_2) and wavefunctions ψ in the valence and conduction band (a). In an array of monodisperse and closely spaced Si NCs, wavefunction overlap through the confinement potential leads to the formation of minibands (b). Figure adapted from Ref. [10].

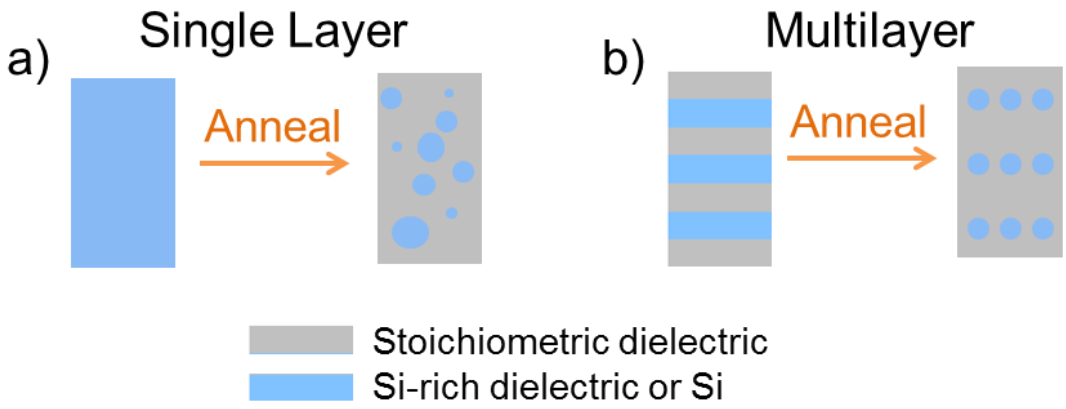

Figure 1.4. Si NC formation by thermally induced phase separation in (a) a bulk Si-rich dielectric film, (b) a multilayer of Si-rich and stoichiometric films.

The most viable approach involves the deposition of a Si-rich layer of a Si-based dielectric such as SiO_2, Si_3N_4 or SiC followed by annealing. Upon annealing, the Si-rich layer de-mixes to form Si nanoclusters in the Si-based dielectric and the nanoclusters crystallise to form Si NCs (see Figure 1.4(a)) provided a suitable annealing temperature is chosen. By depositing a multilayer consisting of alternating nm-thick layers of Si-rich and stoichiometric dielectric, such as SiO_x/SiO_2 [11-14] and Si_xC_{1-x}/SiC [15-17], the size of the Si NCs can in principle be restricted to the thickness of the Si-rich layers (see Figure 1.4(b)) while the areal density can

be controlled by the stoichiometry of the Si-rich layers. Since layer deposition is via sputtering or plasma-enhanced chemical vapour deposition (PECVD) [16-22] this approach is compatible with current PV manufacturing.

1.3 Host Matrix

Si NCs embedded in SiO_2 (Si NC/SiO_2) have been studied in detail and quantum confinement has been shown optically [23] and optoelectronically [24]. However, the conduction and valence band offsets between Si NCs and SiO_2 are large, creating large tunnelling barriers (V_0 in Figure 1.3(a)) which makes transport between Si NCs difficult even when their density is relatively high [25, 26]. For solar cells, Si NCs embedded in SiC (Si NC/SiC) are expected to be more suitable as the conduction and valence band offsets are much smaller, which leads to better carrier transport, even across wider gaps between NCs, as the wavefunctions penetrate further into the SiC matrix (see Figure 1.5 (a)) [27].

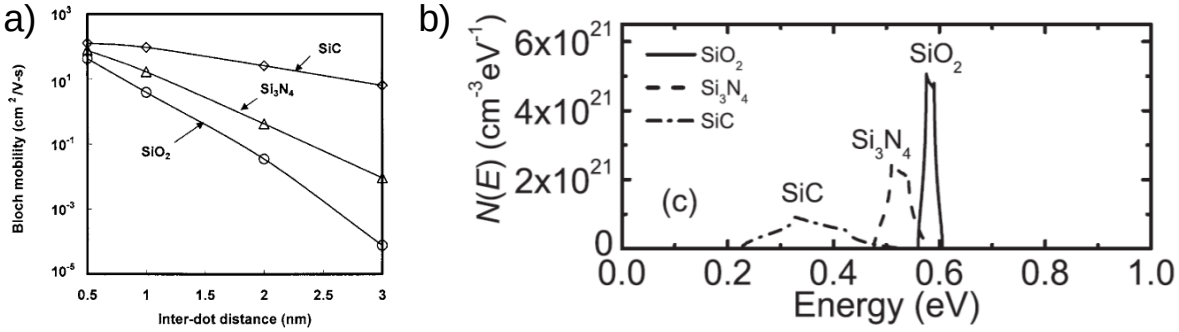

Figure 1.5. (a) Bloch mobilities in the minibands of Si NC superlattices embedded in different dielectrics as a function of NC separation (reprinted with permission from Ref. [27], ©2006 AIP Publishing LLC). (b) Density of states in the first miniband of a Si NC superlattice (0.5 nm NC separation, reprinted with permission from Ref. [28], ©2011 American Physical Society). Both calculations assume cubic NCs with 2 nm edge length arranged on a simple cubic lattice and apply the Kronig-Penney model.

The weaker confinement also leads to a broader density of states per unit energy *N(E)* in the Si NCs [27-29] (see Figure 1.5(b)), which improves band alignment and hence transport in

Si NC populations with a non-uniform size distribution and increases absorption. Absorption is further increased by the SiC matrix itself which with a bandgap of only 2.4 eV [30] also absorbs sunlight [31]. There is an inherent trade-off between absorption and transport on the one hand and effective quantum confinement on the other hand, but band structure calculations show that confinement by SiC is still sufficiently effective to obtain a Si NC bandgap of 1.7 eV [28] that would be optimal for a two-junction tandem cell with a bulk Si bottom cell [32].

1.4 Objectives of This Work

The objective of this work is to develop Si NC/SiC for use in all-crystalline silicon tandem solar cells. It follows the theses of Künle [33], who developed the PECVD and annealing processes required to synthesise Si NC/SiC and characterised the film structure, and of Löper [34], who carried out initial optical and electrical measurements on Si NC/SiC and built a Si NC/SiC solar cell [35]. The specific goals of this work were:

1. To determine the bandgap of Si NC/SiC materials and develop an understanding of carrier recombination mechanisms using photoluminescence spectroscopy.
2. To develop an in-depth understanding of carrier transport using current-voltage measurements.
3. To investigate processing steps needed for the preparation of a Si NC/SiC solar cell, and a tandem cell.
4. To prepare and study a [Si NC/SiC] / bulk c-Si tandem solar cell.

This work was carried out at the Fraunhofer-Institute for Solar Energy Systems (ISE) in Freiburg, Germany. It formed part of the EU-funded project NASCEnT (http://cordis.europa.eu/project/rcn/96716_en.html) which was aimed at developing Si NCs embedded in different host matrices (SiO_2, Si_3N_4, SiC) for photovoltaic applications and

included four universities, two research institutes, and two companies from across Europe. As one of the purposes of NASCEnT was to apply the particular strengths of each institution to each experiment, many samples studied in this thesis were produced wholly or in part at another institution, and studied at different institutions. It is often necessary to refer to the findings of other institutions on the same samples to put the results into context. Where this is done, the contribution of the partner institution is clearly identified with the acronym in Table 1.1, and/or with an adequate reference in cases where their data has already been published. The approval of the partner institutions for use of their data was obtained. Similarly, work performed in collaboration with other Ph.D. candidates at ISE is clearly identified as such.

Table 1.1. Partner institutions involved in the EU-funded project NASCEnT who contributed to work presented in this thesis.

Acronym	***Institution***	***Location***	***Head of Research Group***	***Tasks in NASCEnT***
ISE	Fraunhofer-Institute for Solar Energy Systems	Freiburg, Germany	Dr. S. Janz	Electro-Optical Characterisation, Devices
CNR	Consiglio Nazionale delle Ricerche - Istituto per la Microelettronica e i Microsistemi	Bologna, Italy	Dr. C. Summonte	Synthesis of Si NC/SiC
UB	Universitat de Barcelona	Barcelona, Spain	Prof. B. Garrido	Electro-Optical Characterisation
IMTEK	Institute of Microsystems Technology	Freiburg, Germany	Prof. M. Zacharias	Synthesis of Si NC/SiO_2

1.5 Outline

This thesis is structured as follows:

In **Chapter 2**, the literature on the synthesis and nanostructure, optical properties, and electrical properties of Si NC/SiC is reviewed. Since Si NC/SiC is a relatively new material that is not yet well-understood, an overview of findings on Si NC/SiO_2 and a-Si_xC_{1-x} films is also given. These materials exhibit strong confinement and no confinement, respectively, and are therefore suitable reference systems that Si NC/SiC should lie between. The chapter concludes with a review of existing Si NC solar cells.

Chapter 3 covers the experimental techniques used to synthesise and characterise Si NC/SiC in this thesis. Photoluminescence spectroscopy and current-voltage measurements were optimised for studying Si NC/SiC and are treated in detail.

In **Chapter 4**, photoluminescence (PL) results on Si NC/SiC are presented. The effect of annealing, nominal Si NC size, and substrate on PL are studied and correlated with the sample nanostructure.

Chapter 5 examines charge carrier transport in Si NC/SiC films as a function of annealing ambient, hydrogen passivation, background doping, and nominal Si NC size. The data is discussed and the majority carrier conduction mechanisms are extracted.

Section 5.5 offers a combined discussion and outlook on the results of Chapters 4 and 5.

The development of processing steps for tandem solar cells is described in **Chapter 6**. Oxidation of Si NC/SiC during annealing, diffusion of boron and phosphorus in Si NC/SiC during and after annealing, and the preparation of tunnel junctions to connect the top and bottom cell in a tandem cell are studied.

In **Chapter 7**, the development of a process chain for the preparation of [Si NC/SiC] / bulk c-Si tandem cells is described, and results on tandem cells thus produced are presented.

Chapter 8 concludes the thesis and provides an outlook on future research on Si NC/SiC for tandem solar cell applications.

2. Literature Review

This chapter reviews the literature pertinent to Si NC/SiC and the development of all-crystalline silicon tandem solar cells. In each subtopic the extensive literature on the Si NC/SiO_2 system which inspired the development of Si NC/SiC is reviewed first, and then compared to the existing literature on Si NC/SiC. The properties of a-Si_xC_{1-x} films are also reviewed, for two reasons: first, Si NC/SiC films are usually produced from a-Si_xC_{1-x} precursors, and second, this unconfined system may provide a better reference for Si NC/SiC than Si NC/SiO_2 which exhibits strong confinement. Finally, the literature on existing Si NC cells is discussed. Some parts of this literature review were published in Refs. [36-38].

2.1 Synthesis and Nanostructure

Shortly after Furukawa and Miyasato [39] and Canham [40] observed quantum confinement in Si NCs and porous Si, respectively, it was found that both materials luminesce more strongly and stably when the surfaces are oxidised [41, 42]. This, together with the need for bulk films rather than porous structures in optoelectronic devices, prompted work on nanosized Si embedded in SiO_2. It had been found as early as 1985 that annealing Si-rich SiO_2 (SiO_x) bulk films (where "bulk" signifies that it is a homogeneous film, rather than a particularly thick film, and is used in this sense throughout the thesis) above 800°C could lead to the precipitation of Si NCs, growth being diffusion-controlled and the temperature needed for crystallisation decreasing with increasing Si excess (lower *x*) [43]. A minimum Si NC diameter of 2.5 nm was found. Kanzawa *et al*. then found that such films exhibit NC size-dependent photoluminescence (PL, albeit in a limited range of 1.42-1.54 eV) [44], while

Dovrat *et al*. found that the PL peak position decreased from 1.9 to 1.5 eV with increasing Si excess [45]. However, the NC size distributions were quite broad, and the one tuneable parameter, the composition, modifies both NC size and density [46], whereas a large density of monodisperse NCs, ideally with uniform separation, are required to maximise wavefunction overlap and produce a bulk material with a tuneable bandgap.

After it was found that a stack of alternating layers of a-Si and SiO_2 exhibited an increase in PL peak energy from 1.7 to 2.1 eV as the a-Si sublayer thickness $t_{a\text{-}Si}$ was decreased from 3 to 1 nm [47], annealing of such multilayers at 1050-1250°C was performed to obtain quantum confined crystalline silicon [14, 48, 49]. Multilayers prepared using magnetron sputtering and in-situ plasma oxidation, as well as ones prepared by plasma-enhanced chemical vapour deposition (PECVD), survived the anneal, but for $t_{a\text{-}Si}$>4 nm the resulting Si NCs were brick-shaped and touching each other, which meant most of the samples produced did not exhibit quantum confinement. To obtain confinement, $t_{a\text{-}Si}$<1.5 nm was required [14]. This produced isolated, luminescent Si NCs and limited their mean size to $\sim t_{a\text{-}Si}$. Zacharias *et al*. [11] applied a combination of the multilayer and the SiO_x approach and prepared multilayers consisting of SiO_x and SiO_2 layers (SiO_x / SiO_2 multilayers) by evaporation of SiO powder, followed by 1100°C annealing. This allowed them to control the Si NC size at larger mean diameters, from 2.0 to 3.8 nm, with PL peak positions ranging from 1.3 to 1.6 eV, inversely correlated with NC size. Transmission electron microscopy (TEM) images of similar samples are shown in Figure 2.1.

This result has also been obtained using PECVD-deposited SiO_xN_y / SiO_2 multilayers [19] and magnetron sputtered (MS) SiO_x / SiO_2 multilayers [50, 51]. The nitrogen incorporation in the former work was by no means intended – it actually increases the thermal budget required for Si NC formation [19, 52, 53] – but was a result of using N_2O as the oxygen precursor in PECVD [54]. This is likely also to have been the case in Refs. [14, 49, 52] where this effect was neglected. A direct comparison of MS and PECVD films showed that the former phase-

separate into Si and SiO_2 at lower temperatures and yield a higher proportion of Si nanoclusters for a given film composition [54]. PECVD is usually preferred because lower growth rates are possible that permit the preparation of multilayers with thinner sublayers; however, this does lead to the requirement of higher temperatures for Si NC formation which, as will be seen in Sec. 2.4 as well as in Chapters 6 and 7, constrains processing routes for Si NC solar cells. Efforts have been made to reduce the annealing time at these high temperatures [55, 56], but while the crystallisation process as observed by TEM seems to be unaffected even if the annealing time is reduced to 10 s, the PL yield suffers, indicating a higher defect density [55, 56].

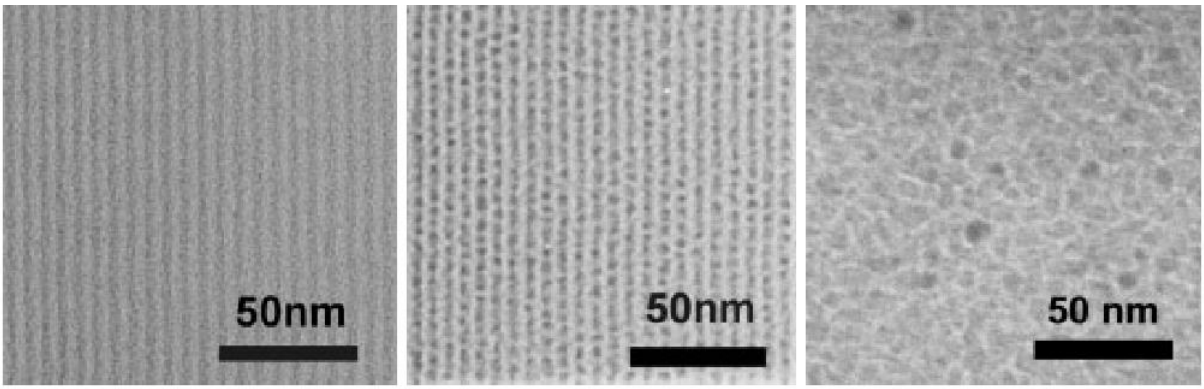

Figure 2.1. TEM images of as-deposited (left) and 1100°C-annealed (middle) SiO_x / SiO_2 multilayers as well as a 1100°C-annealed SiO_x bulk film (right). The multilayer structure survives the anneal and yields size-controlled Si NCs that are not achieved in the bulk film. Reprinted from Ref. [46], ©2005 John Wiley & Sons, and from Ref. [57], ©2002 with permission from Elsevier.

Most papers discussed so far provide evidence for the crystallisation of Si nanoclusters [14, 41, 43-45, 50, 51] but do not rule out the presence of a-Si nanoclusters or provide reliable information on the proportion of nanoclusters that had crystallised. Iacona *et al*. compared dark-field TEM (DFTEM) and energy-filtered TEM (EFTEM) images and found that in PECVD SiO_x films, Si NCs appear at ~1100°C, but only dominate over a-Si nanoclusters above ~1200°C [52]. This indicates that a-Si nanoclusters form first and subsequently crystallise at higher temperature.

Raman spectroscopy studies have shown that Si NCs rarely crystallise fully, but that an a-Si shell remains at the Si NC/SiO_2 interface to accommodate interfacial stress. Raman spectroscopy therefore underestimates the true proportion of Si NCs since an a-Si signal also arises from every NC. Ehrhardt *et al.* [58] and Hernández *et al.* [59] both found that high x (low excess Si content) decreases the crystallinity of the excess Si, which the latter attributes to a greater hydrostatic stress that acts on a-Si nanoclusters when they are fewer and smaller. This would explain Nesbit's minimum Si NC diameter of 2.5 nm [43]. It appears that the crystallinity and size of Si nanoclusters are not independent, and that complete crystallisation of a-Si nanoclusters is not necessarily possible in every sample. Nevertheless, it is remarkably straightforward to prepare monodisperse Si NC superlattices in SiO_2 from evaporated [11], sputtered [50, 51], or PECVD precursors [19].

A transfer of Si NC processing to the Si NC/SiC system typically involves depositing an a-Si_xC_{1-x}:H bulk film or a-Si_xC_{1-x}:H / a-SiC:H multilayer by PECVD that is then annealed. Controlled deposition of nm-thick a-Si_xC_{1-x}:H layers typically involves deposition with precursor gases SiH_4 and CH_4 in the silane-starving plasma regime [33, 60, 61] where the plasma power is chosen so that only SiH_4, but not CH_4, is directly dissociated. As CH_4 is poorly dissociated, an increased CH_4/SiH_4 gas flux ratio leads to an increased incorporation of C *and* H. As much as 50% H is present in films with x=0.6 [62], which effuses on annealing before any other phase transformations occur [63], and leads to film shrinkage [20] which severely modifies the films.

Somewhat counterintuitively, adding H_2 to the gas mixture decreases the H content of the films [64-66]. This is attributed either to etching of Si-H and C-H bonds by H_2 [65], or a promotion of surface diffusion by H_2 [66], and improves the electronic quality of the as-deposited films by decreasing defect and tail state density, increasing the mobility-lifetime ($\mu\tau$) product [64], and reducing light-induced degradation [67]. Very strong hydrogen dilution permits the direct deposition of microcrystalline films [65, 68-70], albeit at deposition rates

that are most likely too low for commercial applications. An increase in C content, provided $x \geq 0.5$, leads to an increase in the bandgap [71, 72], band tail width [62, 72], and defect density [62].

Upon annealing, the PECVD precursor films first lose hydrogen and shrink [60, 63]. This process is essentially complete at 800°C [15, 73]. Above 800°C, the formation of Si NCs begins in both MS and PECVD precursor films, but there are two key differences to the Si NC/SiO_2 system: the SiC matrix can crystallise too (usually in the cubic 3C polytype [15, 74]), and the crystallisation temperatures of both Si and SiC are dependent on the precursor, most importantly its composition. A summary of the temperatures at which Si and SiC NCs begin to form in different precursor films is given in Table 2.1.

Generally, Si crystallisation begins between 800 and 1000°C, while SiC crystallisation begins between 900 and 1000°C. However, Si only crystallises before SiC in films or a-Si_xC_{1-x}:H sublayers with an extremely high Si content, in which it is likely that a percolating Si network, or Si planes (as observed in annealed a-Si / SiO_2 multilayers [49]) will form. These are unlikely to exhibit quantum confinement. From the literature it therefore seems rather improbable that it is possible to produce highly crystalline and clearly separated Si NCs in an a-SiC matrix. The literature does not paint a clear picture as to whether this is a problem, or whether a 3C-SiC matrix is perfectly acceptable from an electronic standpoint. Only one group comments on this, noting that annealed multilayers in which they had suppressed a-SiC crystallisation by adding nitrogen [75] or oxygen [76] yielded superior solar cells. One issue that has been noted in Si NC/SiC, but to the author's knowledge not in Si NC/SiO_2, is that both Si and SiC NCs can exhibit stacking faults or dislocations [15, 77]. A study on Si NCs produced in an entirely different manner found dislocations and grain boundaries in Si NCs with a mean size of 4-10 nm, and correlated this with electrical measurements from which they extracted a value of ~100 defects per NC [78].

Table 2.1. Summary of the temperatures at which Si and SiC begin to crystallise upon annealing in different precursor films studied in the literature.

Precursor	***Deposition Method***	***Si crystallisation temperature [°C]***	***SiC crystallisation temperature [°C]***	***Ref.***
a-$Si_{0.9}C_{0.1}$:H	PECVD	900	1000	[73]
a-$Si_{0.8}C_{0.2}$:H	PECVD	700 (900)[a]	1000	[79] ([80])
a-$Si_{0.79}C_{0.21}$:H	PECVD	1200	900	[81]
a-$Si_{0.7}C_{0.3}$:H	PECVD	1000	1000	[73]
a-$Si_{0.65}C_{0.35}$:H	PECVD	900	900	[80]
20x [5.5 nm a-$Si_{0.96}C_{0.04}$ / 2.5 nm a-SiC]	MS	800	900	[17]
20x [5.5 nm a-$Si_{0.9}C_{0.1}$ / 2.5 nm a-SiC]	MS	900	900	[17]
20x [5 nm a-$Si_{0.9}C_{0.1}$:H / 4 nm a-SiC:H]	PECVD	900	900	[15]
30x [5 nm a-Si_xC_{1-x}:H / 3 nm a-SiC:H]	PECVD	900	>900	[16][b]

[a]in the case of this film, two publications that discuss the same data set disagree on the crystallisation temperature. Ref. [80] claims that the XRD reflections observed at 700 and 800°C merely indicate de-mixing of the precursor, not crystallisation.
[b]composition unknown.

The trends in crystallisation temperatures occur in both bulk films and multilayers; however, the latter ought to control Si NC size, as well as Si NC separation in the out-of-plane direction. Künle *et al*. compared an a-$Si_{0.8}C_{0.2}$:H bulk film to a 5 nm a-$Si_{0.95}C_{0.05}$:H / 3 nm a-SiC:H multilayer and found that after annealing at 900°C, the sizes of Si and SiC NCs as determined by DFTEM were as high as 13 and 11 nm, respectively, in the case of the bulk film, but remained limited to 4 nm and 3 nm, respectively, in the case of the multilayer. In the case of the 5.5 nm a-$Si_{0.96}C_{0.04}$ / 2.5 nm a-SiC and the 5.5 nm a-$Si_{0.9}C_{0.1}$ / 2.5 nm a-SiC multilayers studied by Song *et al.* [17], the sizes of Si NCs stayed below 5.5 nm and those of

SiC NCs did not exceed 3.5 nm up to the maximum annealing temperature of 1100°C. The authors interpret this in terms of Si NC and SiC NC sizes being limited by the a-Si_xC_{1-x} and a-SiC sublayer thickness, respectively. However, x-ray reflectivity measurements indicated that the multilayer structure of the 5.5 nm a-$Si_{0.9}C_{0.1}$ / 2.5 nm a-SiC multilayer was no longer present in films annealed at 1000°C and above, which together with the observation by Song *et al.* that the Si NC size in a bulk a-$Si_{0.75}C_{0.25}$ film annealed at 1100°C is 3-7 nm [77] suggests that the multilayer structure may not be controlling nanocrystal sizes as effectively as anticipated. Künle *et al*. observed the same gradual dissolution of the multilayer structure at ~1000°C by EFTEM [15].

Overall it appears that the synthesis of well-ordered Si NCs in SiC is not as straightforward as in the Si NC/SiO_2 system because the criteria for the survival of the multilayer structure (high Si excess, low temperature) conflict with those for the synthesis of isolated, crystalline Si NCs (Si content below the percolation threshold, high temperature). However, this issue may not be critical because as noted in Sec. 1.3, tunnelling through SiC is much more efficient than through SiO_2, which means less ordered Si NCs may be tolerable in terms of carrier transport.

2.2 Optical Properties

The better-known and more readily controlled Si NC/SiO_2 system has permitted a comprehensive characterisation of the optical properties of Si NCs. It was already noted in Sec. 2.1 that most groups observed a dependence of the PL peak position on mean Si NC size that was in agreement with quantum confinement. Most groups continued their research on this basis but it was only in 2008 that Godefroo *et al*. proved that the PL originated from band-to-band recombination, rather than from defects whose levels move with the conduction or valence bands, by measuring PL under an applied magnetic field [23]. The magnetic field confines an exciton further, leading to a peak shift if the exciton was delocalised over the NC,

but not leading to a shift if the exciton was already confined to a localised defect state. A 1 meV peak shift was interpreted as evidence of the former [23], indicating the difficulty of distinguishing between the two cases experimentally.

Heisenberg's uncertainty principle states that the momentum of spatially confined carriers is increasingly undefined, which raised hopes that Si could, in sufficiently small NCs, become a direct bandgap material which would open up a wide range of additional applications. Using resonant excitation, Kovalev *et al*. found that the intensity of the phonon-related PL peaks (that are distinguishable from no-phonon luminescence at low sample temperatures) was strongly reduced at increased energy, and deduced a change from predominantly indirect to direct recombination at 1.8-1.9 eV [82]. Dao *et al*. ruled out a direct bandgap based on the deduced oscillator strength [83], while more recent temperature-dependent luminescence studies by Hartel *et al*. suggest a quasi-direct bandgap where the role of phonons is gradually reduced, but never eliminated, with decreasing Si NC size [84, 85]. Time-resolved PL decay measurements on Si NC/SiO_2 typically find exciton lifetimes in the µs range [14, 45, 83, 84], and luminescence quantum yields above 10% have been reported for samples that underwent a forming gas or H_2 anneal at 450°C [86, 87]. Both indicate that non-radiative recombination in Si NC/SiO_2 is efficiently suppressed, particularly when a hydrogen post-treatment is used to passivate dangling bonds.

PL is the most common method for determining bandgaps of Si NC/SiO_2 films, but for Si NC/SiC, where absorption is much stronger, bandgaps are often derived from spectrophotometry data using Tauc plots [88, 89]. The Tauc plot as a method for extracting the optical bandgap E_{Tauc} (Tauc gap) was developed for amorphous semiconductors [8, 88, 89] and as such, is not strictly suitable for describing multiphase materials and quantum dots but is nevertheless widely used due to its simplicity. Song *et al.* [77] studied sputtered a-Si_xC_{1-x} films and found that as-prepared films exhibited an increase in E_{Tauc} with carbon content, in line with what has been found for PECVD a-Si_xC_{1-x}:H films from absorption and

PL [62, 90-92]. They also report the same trend with carbon content after annealing the films at 800°C and 1100°C, and for each film, E_{Tauc} increases with temperature, reaching values of 1.9-2.2 eV at 1100°C. This is rather difficult to reconcile with the formation of a-Si nanoclusters at 800°C, and of Si NCs with a predicted bandgap below 1.5 eV at 1100°C [77], and the authors attempt an explanation in terms of masking of the Si nanocluster absorption by that of the SiC matrix. However, they do not show the actual Tauc plots, which can be extremely difficult to fit [81]. In another work, the same group studied 6 nm a-$Si_{0.9}C_{0.1}$ / 2.5 nm a-SiC multilayers and observed a blueshift of E_{Tauc} from 1.4 to 2.0 eV upon annealing at 1100°C (at which point Si NCs 3-4 nm in size and SiC NCs are formed [93]). This time the plots were provided, and indicate that the values are correct to within ~0.2 eV (see Figure 2.2(a)). Igarashi *et al*. find the same value for Si nanodisks with a diameter of 10 nm and a thickness of 4 nm embedded in SiC [94]; however, their fit is rather poor (see Figure 2.2(b)).

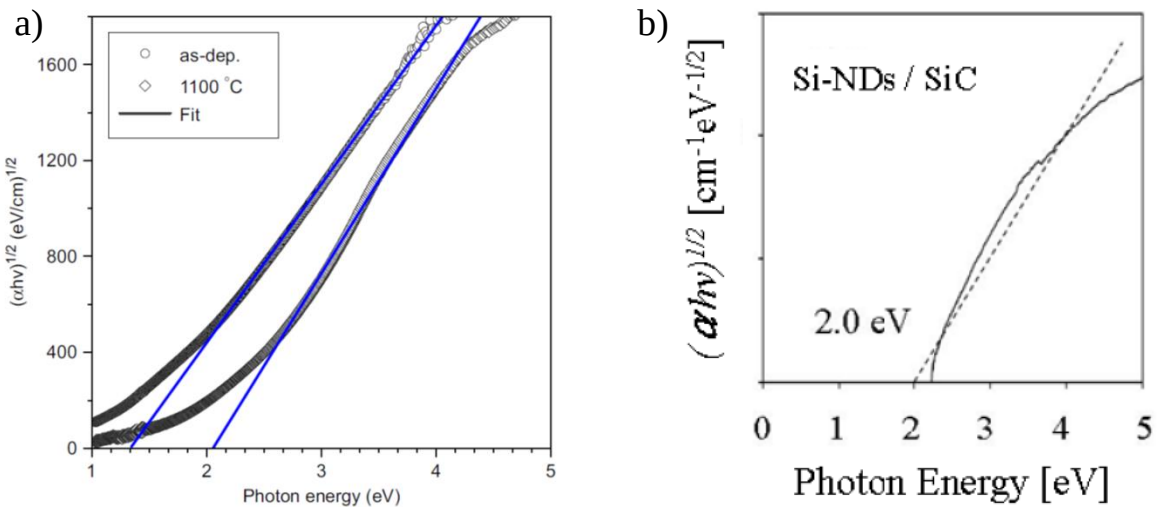

Figure 2.2. Tauc plots for Si nanoclusters embedded in SiC. (a) 3-4 nm Si NCs in largely crystalline SiC (1100°C curve), reprinted from Ref. [93] ©2008 with permission from Elsevier. (b) Si nanodisks 4 nm thick with a diameter of 10 nm in SiC. Reproduced by permission of IOP Publishing from Ref. [94]. © IOP Publishing. All rights reserved.

Summonte *et al*. took a different approach and fitted the raw reflection and transmission data using an effective medium of a-Si, µc-Si, and c-SiC [81, 95-97]. This approach has the advantage that both real and imaginary parts of the refractive index are considered (as opposed to fitting absorption, which only depends on the imaginary part) but is inherently unable to provide actual information on the effect of quantum confinement on the absorptivity of NCs because only bulk materials are used as inputs. This is not to say that successful fitting by this group indicates the absence of quantum confinement: both quantum-confined Si NCs and a-Si are characterised by quasi-direct transitions, and as such it is plausible that optically, Si NCs can be described as a mixture of µc-Si and a-Si. They found that after annealing at 900°C, a-$Si_{0.79}C_{0.21}$:H films have E_{Tauc}=1.6 eV and consist of 64% a-Si and 36% c-SiC, while a-$Si_{0.79}C_{0.21}$:H films annealed at 1200°C have a poorly fitted E_{Tauc}=2.05 eV and consist of 67% µc-Si and 33% c-SiC [81].

Similarly, a study of a-$Si_{0.95}C_{0.05}$ / a-SiC multilayer films annealed at 1100°C showed a blueshift of the absorption edge and an increase in Si crystallinity with increasing a-$Si_{0.95}C_{0.05}$ thickness [95]. This is the opposite of the trend expected in the case of size-controlled Si quantum dots in the a-$Si_{0.95}C_{0.05}$ layers. It is explained in terms of the greater crystallinity of Si nanoclusters in thicker a-$Si_{0.95}C_{0.05}$ films, which weakens their absorption as compared to a-Si nanoclusters below the direct c-Si bandgap of 3.6 eV [95]. It is the same as the argument made by Mirabella *et al*. [54] to explain the discrepancy between E_{Tauc} and PL peak position of Si NCs in SiO_2, and indicates that the interpretation of reflection and transmission data is difficult for Si NC films because the results are affected both by the proportions of the different phases present (a-Si, Si NCs, SiC), and the size-dependent absorptivity of the Si NCs themselves, and it is not always possible to cleanly separate the two effects.

Tidier results would be expected from luminescence measurements since these ought to give a distinct peak, rather than a rising edge, for each phase present. As mentioned in Sec. 2.1, the SiC matrix is mainly 3C-SiC, which contrary to a SiO_2 matrix exhibits its own absorption and

luminescence. Suzuki *et al*. found that 3C-SiC exhibits efficient donor-acceptor pair or conduction band-acceptor luminescence when doped with B, Ga, or Al acceptors (N donors are almost unavoidable in SiC growth), depending on whether *kT* exceeds the ionisation energy of N [98]. For B, Ga, and Al-doped 3C-SiC, donor-acceptor pair luminescence peaks at 1.64, 2.04, and 2.13 eV, respectively.

Unfortunately, the literature on the luminescence of nanocrystalline SiC (nc-SiC), with or without embedded Si NCs, paints a rather confusing picture. Nanocrystalline SiC consisting of a mixture of 3C and 6H polytypes exhibited PL bands at 400 and 450 nm, which due to their variation with annealing and high-power laser irradiation were assigned to band-to-band and defect luminescence [99], necessarily in the 6H phase, respectively. Given the grain size of 3-10 nm, it seems strange that no radiative recombination in the 3C phase that has a lower bandgap should occur. Another group deposited a mixture of a-SiC and nc-SiC with a mean grain size of 4 nm by PECVD and deconvolved the PL signal into bands at 1.91 and 2.56 eV [100]. These were assigned to band-to-band recombination in the a-SiC matrix and in quantum-confined 3C-SiC NCs, respectively, though the paper fails to explain how quantum confinement is supposed to occur in a crystal embedded in a matrix of lower bandgap. The same fallacy crops up in two recent studies of Si NCs embedded in SiC [101, 102], both of which observed a broad PL band from ~400-600 nm (~2-3 eV) which they fitted with up to six separate PL bands attributed to differently sized Si QDs, despite the fact that the matrix is in both cases 3C-SiC or a-SiC which are not reported to have bandgaps exceeding 2.5 eV in the literature.

A different group measured broadband PL in the wavelength range 600-800 nm but nevertheless reported ambiguous results [72, 79, 80]. One author reported that the PL of a-$Si_{0.8}C_{0.2}$:H, a-$Si_{0.65}C_{0.35}$:H, and a-$Si_{0.55}C_{0.45}$:H films is stronger after annealing at 1100°C than at 900°C, more so the greater the Si content [80], while a follow-up paper by the same author states that the PL of a-$Si_{0.8}C_{0.2}$:H films increases with annealing up to 950°C and then

decreases again for 1050°C and 1100°C anneals [72]. Another paper from the same group reported similar PL for a-$Si_{0.8}C_{0.2}$:H annealed at 700 and 900°C, but over an order of magnitude stronger PL after a 1100°C anneal [79]. This trend persisted upon hydrogen passivation but the absolute emission of all films decreased by an order of magnitude [79], indicating that the PL in all these works arose from luminescent defects. However, a new weak PL peak appeared at ~1.2 eV that the authors tentatively ascribe to Si quantum dots, which is consistent with the Si NC size of ~6 nm [79, 92]. In the Si NC/SiC system the only clear observation of PL that shifts in agreement with quantum confinement comes from Kurokawa *et al.* [103] and stems from a-Si_xC_{1-x}:H / a-SiC:H multilayers annealed at 900°C and exposed to a hydrogen plasma which reduced the defect density as detected by electron spin resonance (ESR). It is shown in Figure 2.3.

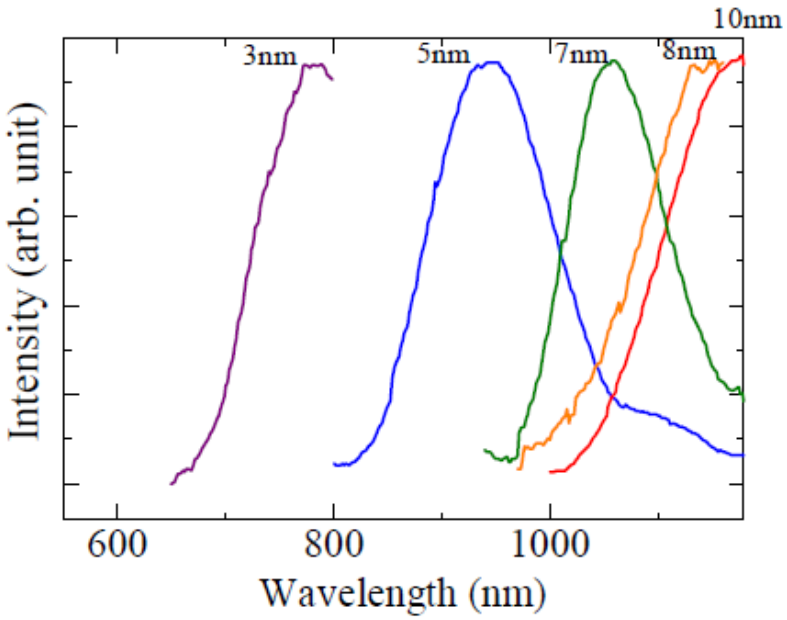

Figure 2.3. PL of Si NCs in SiC as a function of mean Si NC size as measured by TEM. Reproduced from Ref. [103] with permission from WIP.

Overall, it can be said that while the optical properties of Si NC/SiO_2 are well understood to the point where the data allows insight into radiative and non-radiative recombination rates, the same cannot be said for Si NC/SiC. This is mainly due to the fact that Si NC/SiC typically

contains 3-4 absorbing phases, as opposed to just one for Si NC/SiO_2, and that luminescence is less defined and weaker. However, by virtue of having an absorbing matrix Si NC/SiC simply absorbs more light, and it has been calculated that for typical materials parameters ~300 nm Si NC/SiC absorbs enough light to deliver a short-circuit current of 10 $mAcm^{-2}$ in a solar cell [95], whereas 3 µm Si NC/SiO_2 would be needed [97].

2.3 Electrical Properties

In order for the aforementioned current densities generated in a solar cell absorber to be extracted in an external circuit, efficient charge transport to the contacts is required. In a study of Si / 3 nm SiO_2 multilayers, the in-plane (lateral) conductivity exceeded the out-of-plane (vertical) conductivity 1000× even when the Si planes were only 3 nm thick [104], revealing the current-blocking nature of SiO_2. One group reported that annealed SiO_x layers only exhibit measurable lateral dark- and photoconductivity once *x* is sufficient for Si percolation [105, 106]. At this stage PL, which is sometimes interpreted as a measure for the electronic quality of the films [55], is strongly reduced [105, 106], and of course quantum confinement is weakened. A review article by Balberg notes that many conduction mechanisms fit the data for annealed SiO_x above the percolation threshold, and care must be taken to justify the mechanism physically [106]. For example, an explanation based on thermal activation over barriers arising from band bending at grain boundaries is nonsensical in materials where the Debye length greatly exceeds the grain size. His article proposes extended-state and hopping conduction as observed in amorphous semiconductors as a valid model, based on the fact that the defects at the many grain boundaries can result in a defect population similar to disordered semiconductors.

Out-of-plane (vertical) transport in annealed SiO_x / SiO_2 multilayers prepared from PECVD precursors (i.e. containing nitrogen) was studied by Puglisi *et al*. [25] and Gutsch *et al*. [26].

Both found that care had to be taken to avoid transient charging effects as these could occur on macroscopic timescales (50-60 s in Ref. [25]). Current depended exponentially on voltage [25, 26], but only weakly on temperature [25], which led both to deduce that tunnelling is the dominant transport mechanism in the Si NC superlattices (see current-voltage (IV) curves in Figure 2.4).

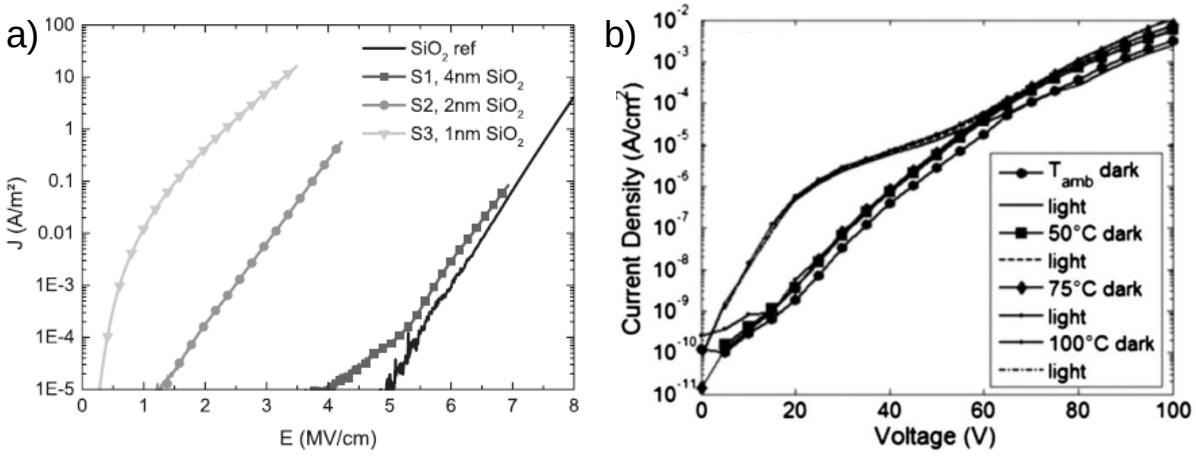

Figure 2.4. Current-voltage (IV) curves of Si NC/SiO_2 as a function of SiO_2 sublayer thickness (a), reprinted with permission from Ref. [26], ©2013 AIP Publishing LLC; and as a function of illumination and temperature (b), reprinted with permission from Ref. [25], ©2010 AIP Publishing LLC.

This is promising in principle since transport in an ideal quantum dot superlattice as shown in Figure 1.3(b) and modelled in Figure 1.5(a) ought to be by interdot tunnelling. However, Gutsch *et al*. found that when the SiO_2 sublayers in the multilayer are 4 nm thick, transport is similar to bulk SiO_2 (see Figure 2.4(a)), indicating that no interdot coupling occurs [26], and even when the SiO_2 sublayers are only 1-2 nm thick, fields >1 $MVcm^{-1}$ are required to conduct 10 $mAcm^{-2}$ [25, 26] which is a conservative estimate for the short-circuit current of an efficient tandem cell. This greatly exceeds the maximum built-in field that a p-i-n solar cell utilising Si NC/SiO_2 could have, assuming a built-in voltage of 1-2 V as achievable with p-a-Si:H and n-a-Si:H contacts and absorber thicknesses as proposed in Sec. 2.2 from an absorption viewpoint. TEM images indicate that both studies used superlattices with good

Si NC size control, and Gutsch *et al*. used SiO_2 barriers as thin as 1 nm, which corresponds to ~2 monolayers. It is therefore improbable that better transport will be achieved by optimising the size and separation of Si NCs in SiO_2 further.

Several groups have tackled the issue of low conductivity in the Si NC/SiO_2 system by doping with boron [107, 108] or phosphorus [109-112]. The lateral dark conductivity of B-doped annealed SiO_x layers increased $10^4\times$ [108], whereas that of B-doped SiO_x / SiO_2 multilayers increased up to $10^6\times$ [107] while the activation energy for conduction decreased from 0.5 to 0.1 eV. Similarly, P increased the lateral conductivity in annealed SiO_x / SiO_2 multilayers up to $10^7\times$ [111], and the vertical conductivity up to 10× (see Figure 2.5(a)) [112]. However, the studies that examined PL also found a strong reduction by doping with B [107] and P (see Figure 2.5(b)) [110], which one study attributed to efficient Auger recombination since an electron excited in a doped Si NC is necessarily extremely close to the doping electron [110]. It is therefore not entirely clear whether doping Si NC/SiO_2 systems makes them better solar cell absorbers or not.

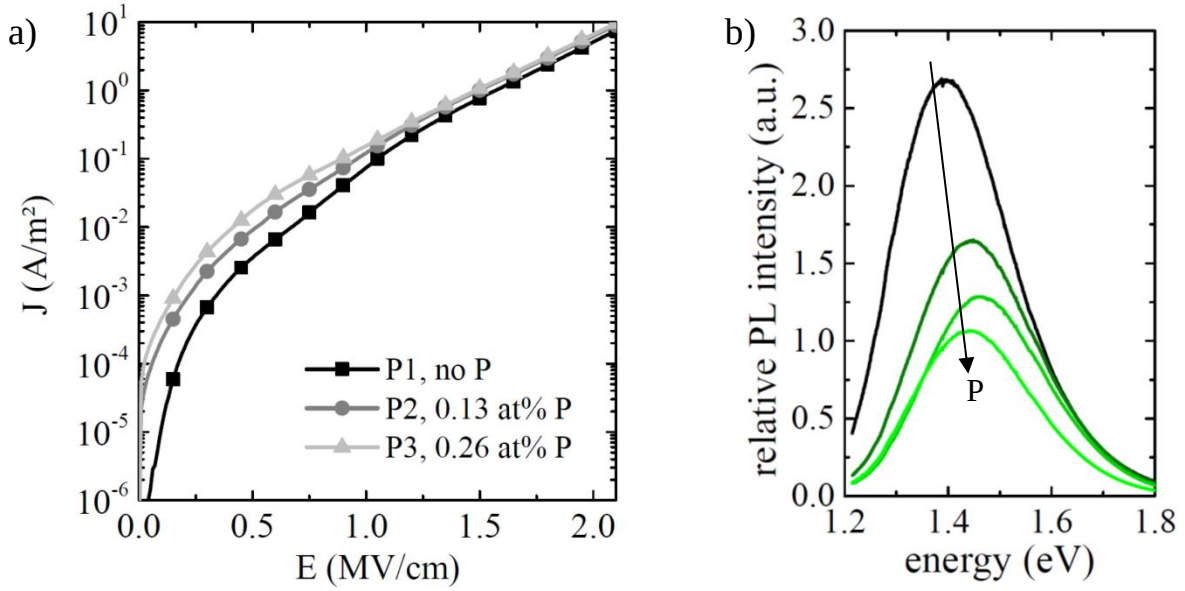

Figure 2.5. Improvement in electrical transport (a) and decrease in photoluminescence yield (b) upon phosphorus doping, both reproduced from Ref. [112].

A materials system based on Si and SiC promises better conductivity as both are semiconductors. The a-Si_xC_{1-x}:H precursor films exhibit the same conduction mechanisms as a-Si:H [64, 71, 91] which was intensely researched in the 1970s and 1980s [8, 88, 113]. As these conduction mechanisms have also been proposed for transport in percolating networks of Si NCs in SiO_2 [106], they are presented in detail in the following. In a-Si:H, a distribution of bond lengths and angles leads to a distribution of conduction and valence band states resulting in a smearing-out of the band edges [8]. The band edges E_C, E_V are then defined as the energies where the carrier wavefunctions are no longer localised, and the bandgap between these is termed the mobility gap [88]. Furthermore, dangling bonds exist that create a finite density of deep defect states near the middle of the bandgap. The overall density of states per unit energy *N(E)* as compared to that in a crystal is given in Figure 2.6(a).

As a finite *N(E)* exists in much of the bandgap, the mechanism of doping is also different. Assuming n-type material, in a crystal, electrons would be donated to the conduction band and the donor density and temperature would define the Fermi level E_F. In amorphous material, donated electrons fill up the deep levels and tail states; the energy up to which these states are filled is then E_F (see Figure 2.6(b)). Efficient doping therefore requires that the dopant density exceed the deep defect density [114]. In principle, transport is possible at any energy, leading to the following equation for conductivity as a function of temperature $\sigma(T)$:

$$\sigma(T) = q \int_{E_F}^{\infty} n(E,T)\,\mu(E,T)dE = q \int_{E_F}^{\infty} N(E)\,\mu(E,T)\exp(-(\frac{E-E_F}{kT}))dE, \quad (2.1)$$

where n is the carrier concentration and μ the mobility at a given energy E and temperature T, q is the elementary charge, and k is Boltzmann's constant.

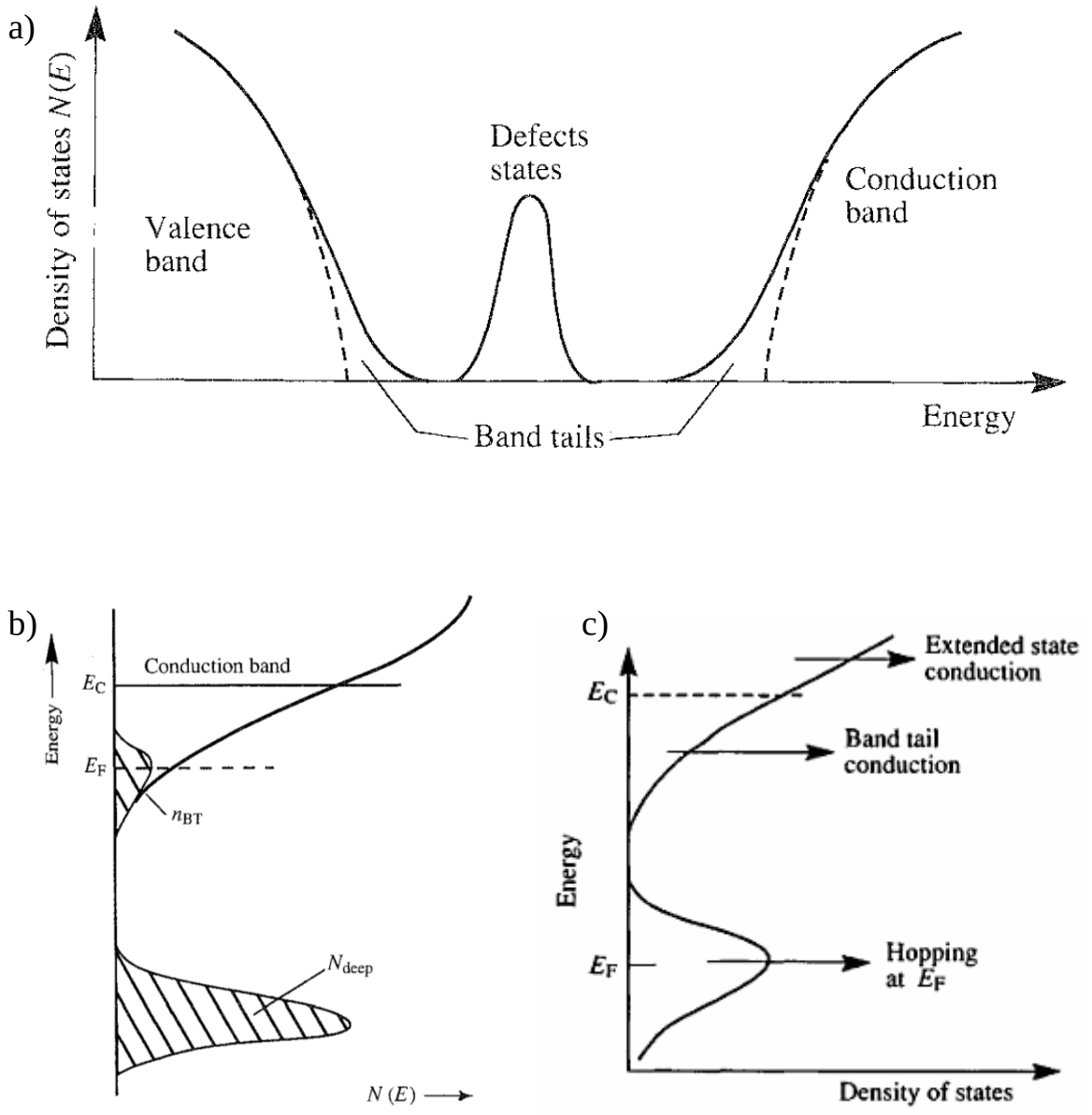

Figure 2.6. (a) Density of states *N(E)* in an amorphous semiconductor. A crystalline *N(E)* is given by dashed lines. (b) Occupancy of *N(E)* assuming n-type doping. A concentration of deep levels N_{deep} exists that are occupied by donated electrons. An additional electron concentration n_{BT} is present in the conduction band tail. (c) Possible conduction mechanisms in an amorphous *N(E)*. All reproduced from Ref. [8].

For n-type material, μ increases with energy while the Boltzmann factor decreases, which means there is typically a relatively narrow band in energy where most conduction takes place. Simpler expressions for $\sigma(T)$ exist for transport predominantly in extended states, tail states, or deep defects (see Figure 2.6(c)). In extended states, and assuming n-type doping,

$$\sigma_{ext}(T) = \sigma_{01} \exp\left(-\left(\frac{E_C - E_F}{kT}\right)\right), \tag{2.2}$$

where $\sigma_{01}=qN(E_C)\mu_{ext}kT$ because $N(E_C)$ and the extended-state mobility μ_{ext} are to a first approximation independent of energy and temperature. Spear and Le Comber showed that the conductivity of a-Si:H increased and the conductivity activation energy decreased with both boron and phosphorus doping level, in agreement with Eq. 2.2 [115]. However, they also found that E_C-E_F never decreased below ~0.2 eV, which they attributed to pinning of E_F by tail states.

Similarly, if E_F is in the defect band, but transport takes place at an energy band in the band tail that is centred at E_T and narrow compared to E_T-E_F, hopping transport with conductivity $\sigma_{tail}(T)$ given by

$$\sigma_{tail}(T) = \sigma_{02} \exp\left(-\left(\frac{E_T - E_F}{kT}\right)\right) \tag{2.3}$$

occurs. Both mechanisms have been observed in a-Si:H using a combination of time-of-flight and IV measurements [116]. The activation energy of μ_{ext} was interpreted as the width of the conduction band tail. A marked decrease in the mobility activation energy at low temperature was assigned to a transition to hopping transport. However, one source questions the concept of a hopping mobility because the associated scattering time would be so short that were it well-known, the energy at which the process occurs would be poorly defined due to

Heisenberg's uncertainty principle [117]. It has also been suggested that Hall effect measurements on samples in which hopping transport occurs would be erroneous, even yielding an incorrect carrier type [88].

If most conduction occurs near E_F, then the exact energy at which most conduction occurs becomes a function of temperature [88, 118]. The conductivity of the sample then becomes a question of the size of the percolating network of localised states to which carriers can be excited at a given temperature, for which it was found, given $N(E) \propto (E-E_F)^s$, that

$$\sigma_{VRH}(T) = \sigma_{00} \exp\left(-\left(\frac{T_0}{T}\right)^{\frac{s+1}{s+4}}\right), \tag{2.4}$$

where σ_{VRH} is the variable-range hopping conductivity and σ_{00} and T_0 are fitting parameters [113, 119]. Two particular cases are frequently found in the literature: s=0 and s=2. The former corresponds to a uniform $N(E)$ and is known as Mott variable-range hopping (VRH) [88], although it was recently shown by Godet [118, 120] that the same behaviour ($\ln(\sigma(T)) \propto T^{-1/4}$) is also expected for $N(E) \propto \exp((E-E_F)/E_s)$, where E_s is a fitting parameter, albeit with a different dependence of σ_{00} on T_0. The s=2 case corresponds to hopping in a parabolic $N(E)$ which arises when the Coulomb gap becomes relevant [121], is known as Efros-Shklovskii VRH, and has recently been suggested to describe hopping in an array of nanocrystals in which there is a distribution of conduction band levels due to randomly distributed ionised donors [122].

Two sources also note that an activation energy for transport can arise from long-range potential fluctuations that is given by the full width at half maximum of these fluctuations [8, 113]. However, this interpretation of activated transport is not widespread in the rest of the literature, perhaps because, as one of the sources notes, potential fluctuations are to some extent balanced by changes in charge states and carrier densities they induce [8].

Experimentally, it has been noted that IV measurements on thin films with coplanar contacts can be affected by conduction at surfaces and interfaces, either due to surface or interface states, or due to band bending at the surface or interface that can cause both depletion or accumulation [91, 123]. Both issues can be resolved by measuring sufficiently thick films.

The electronic properties of a-Si_xC_{1-x}:H are largely interpreted in the same framework: Anderson and Spear found transport following Eq. 2.2, with E_C-E_F=$E_g/2$ and hence a function of x, but constant σ_{01} [64, 71]. Minority carrier lifetime decreases with x [62] but increases with hydrogen dilution [64]. An increase in activation energy with x [124] and a decrease with hydrogen dilution [69] were reported for as-deposited boron-doped µc-Si_xC_{1-x}:H films, which are more similar to Si NC/SiC films. The authors of the latter study found tail-state hopping and VRH at high and low temperature, respectively, though their characterisation of high-temperature transport as hopping, rather than extended-state transport, is based solely on consistency with the empirical Meyer-Neldel rule [125]. Concari *et al*. observed Godet VRH in a wide range of nanocrystalline Si (nc-Si:H) films deposited by PECVD [126], whereas Lau *et al*. observed space-charge-limited carrier transport in films of milled Si NCs [78] that they attributed to the defects visible in high-resolution TEM images of the Si NCs. In sputtered a-SiC, extended-state conduction and Mott VRH were reported above and below 250 K [127].

Once a-Si_xC_{1-x}:H bulk films or multilayers are annealed to produce Si NC/SiC, a range of conduction mechanisms become plausible and have been proposed by different groups. The IV measurements fall broadly into two groups: lateral measurements on insulating substrates using coplanar contacts, and asymmetric, vertical transport devices. Igarashi *et al*. studied vertical transport through Si NC/SiC, prepared on p-type c-Si by patterning a Si NC nanolayer deposited by molecular beam epitaxy and covering it with SiC, using conductive atomic force microscopy and found non-Ohmic behaviour that fitted their tunnelling model [94, 128]. They also interpreted a lack of lateral contrast as evidence of strong in-plane coupling between

Si NCs. Rui *et al*. reported Fowler-Nordheim tunnelling (as well as broad electroluminescence) in Si NC/SiC sandwiched between a tin-doped indium oxide (ITO) electrode and a p-type Si wafer [129]. However, neither group discussed whether the non-Ohmic transport was due to the conduction mechanism in the film or the rectifying nature of the device itself.

In contrast, the result of lateral measurements, which are performed on symmetric devices using much lower electric fields, is typically Ohmic conduction [21, 93, 130, 131]. Kurokawa *et al*. reported room-temperature conductivities of 10^{-4} Scm^{-1} for Si NC/SiC that were largely independent of nominal NC size (2-10 nm) [131], but decreased 1-2 orders of magnitude when oxygen was incorporated into the layers by adding CO_2 during a-Si_xC_{1-x}:H deposition. Summonte *et al*. [21] reported room-temperature conductivities of 10^{-5}-10^{-4} Scm^{-1} for annealed a-SiC:H (in agreement with Ref. [132]), a-Si_xC_{1-x}:H, and a-Si_xC_{1-x}:H / a-SiC:H multilayers, as well as activation energies of 0.15-0.3 eV. This shows that the SiC matrix cannot be assumed insulating compared to the Si NCs, and that, provided Eq. 2.2 or 2.3 are applicable, even nominally intrinsic material was actually doped. It is worth noting that while the properties of SiC ought to be irrelevant if absorption and transport occur via the minibands formed by wavefunction overlap between Si NCs, in reality, due to the relatively small band offsets between Si and SiC, and due to the similarity in conductivity and conduction mechanism between nc-SiC with and without Si NCs, SiC is certainly involved in absorption, transport of carriers in Si NCs may in fact be via thermal activation to the bands of the SiC matrix, and minority carriers in Si NCs can reach recombination sites in the SiC via tunnelling. In fact, it may prove more suitable to think of the Si NC/SiC system not as Si NCs that are hosted by SiC, but as SiC whose properties are slightly modified by Si NCs.

The background dopant present in nominally intrinsic Si NC/SiC films is not identified in the aforementioned studies, but oxygen is known to dope μc-Si:H [133], a-Si:H [134], and SiC [135, 136] n-type, while nitrogen is an excellent n-type dopant in SiC [30, 137, 138] and

also dopes a-Si:H [134]. Both are easily incorporated accidentally. Gradmann found conductivities of 10^{-8}-10^{-6} Scm^{-1} in undoped Si NC/SiC and in films doped with 15-50 sccm B_2H_6 during deposition, only achieving significantly higher values with 100 sccm B_2H_6 [130]. This too suggests background n-type doping in nominally undoped films. However, as a slight increase in grain size with B_2H_6 flux was also found this may also have affected conductivity, highlighting a common problem with doping Si NC films – electrical effects of dopant incorporation are difficult to separate from nanostructural effects. This is also a factor in the study of Miyajima *et al*. on nc-SiC prepared by hot-wire CVD [139], where it was found that N, P, and Al incorporated during deposition all increased conductivity but decreased crystallinity, and the study of Eickhoff *et al*. on CVD SiC [137], where whether oxygen genuinely behaves as a dopant or simply promotes the formation of intrinsic defects with donor character remained an open question.

Information on minority carrier properties, which are crucial for solar cell applications, can be obtained from a study on the electroluminescence of a Si NC/SiC p-i-n device [140]. It found emission at ~500 nm that was maximised at an i-layer thickness of 50 nm. The wavelength is more in line with band-to-band recombination in SiC, rather than in Si NCs, but nevertheless the i-layer thickness-dependence can be taken as an indication that the diffusion or drift length is ~50 nm. This quantity needs to be maximised in solar cells and depends primarily on the product of carrier mobility and minority carrier lifetime, the $\mu\tau$ product.

Minority carrier lifetimes in 3C-SiC are typically 10^{-10}-10^{-7} s [100, 141, 142], that is, rather low compared to bulk c-Si where 0.1-5 ms is typical. The mobility in nc-SiC with a grain size of ~100 nm has been measured as ~1 $cm^2V^{-1}s^{-1}$ [137]. This suggests $\mu\tau$ products in the range of 10^{-10}-10^{-7} cm^2V^{-1} for nc-SiC of that grain size, and lower values are perhaps to be expected for Si NC/SiC as the grain size is ~5 nm. Device-grade a-Si:H, which Si NC/SiC is supposed to displace as a solar cell absorber, typically has $\mu\tau$=10^{-7} cm^2V^{-1} [143]. This suggests that mobility and lifetime will be key parameters for determining the viability of Si NC/SiC films

for photovoltaic applications. An overview of the first photovoltaic devices prepared using Si NC/SiC and Si NC/SiO_2 is given in the following section.

2.4 Si NC Solar Cells

Despite the poor electrical transport in Si NC/SiO_2 and the ambiguous electrical transport in Si NC/SiC, working solar cells have been prepared from both types of material. The structures of devices reported in the literature are shown schematically in Figure 2.7.

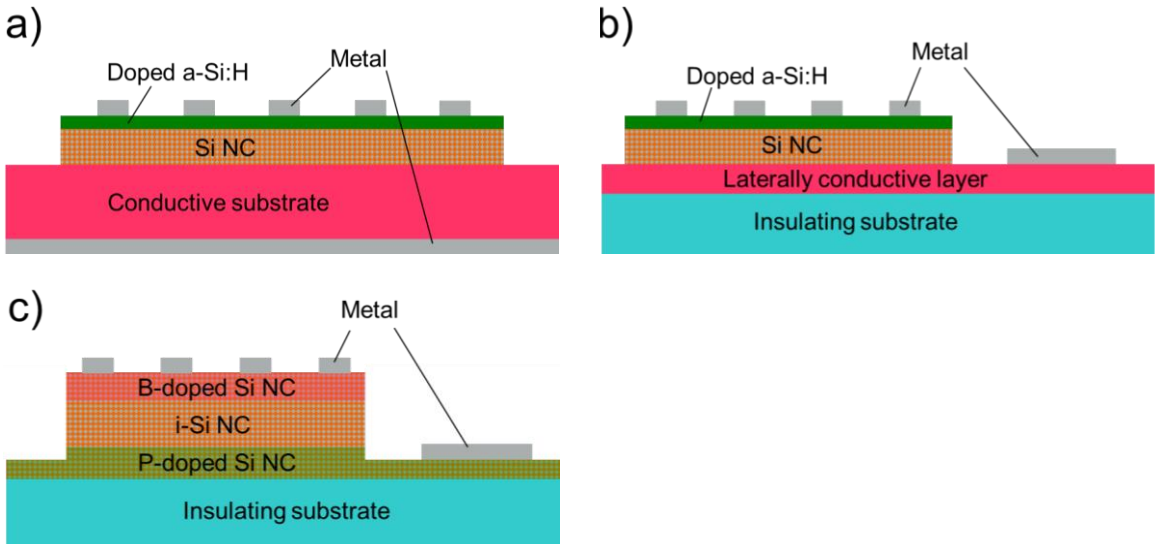

Figure 2.7. Schematic diagrams of the different Si NC solar cell architectures reported in the literature. All adapted from Refs. [34, 37].

The simplest structure is the one in Figure 2.7(a), where the p- and n-layers of the p-i-n structure are a-Si:H, and the substrate, typically a Si wafer. In some works, the a-Si:H is replaced by poly-Si, or omitted entirely and the Si NC layer doped instead. Such solar cells have been prepared from Si NC/SiO_2 [144], Si NC/SiC [93], and even Si NC/Si_3N_4 [145]. The cells using Si NC/SiO_2 and Si NC/SiC exhibited open-circuit voltages (V_{oc}) of 500-600 mV and 463 mV, respectively, as well as efficiencies of 10-13% and 5%, respectively. It should be noted that this does not typically reflect the photovoltaic performance of the Si NCs. Rather, the device is a Si wafer solar cell, with the Si NCs playing the part of the emitter or of

a series resistor in the space charge region, leading to a diminished fill factor. Nevertheless, the fact that V_{oc}>400 mV was obtained in Refs. [93, 144], even though no oppositely doped a-Si:H or poly-Si was used, indicates efficient doping of the Si NC layer in the respective works (Ref. [144] even reported built-in voltages of 0.7-1.0 V deduced from capacitance measurements).

To reduce the "parasitic" photovoltaic performance of the Si substrate, the structure in Figure 2.7(b), which is essentially the same as that in Figure 2.7(a) except the conductive substrate is shrunk to a thin laterally conductive layer, can be used. Kurokawa *et al*. have reported on the performance of such solar cells using Si NC/SiC in several studies [75, 76, 146, 147]. They used several hundred nanometres of poly-Si as the laterally conductive layer that they claim has negligible photovoltaic performance due to the high doping level (10^{19}-10^{20} cm^{-3}). They found that adding nitrogen or oxygen to the Si NC/SiC during deposition greatly improves solar cell efficiency, which they attribute to the suppression of the crystallisation of the SiC matrix in each case. They also found that after annealing the poly-Si / [Si NC/SiC] stack to form the Si NCs, phosphorus had diffused from the poly-Si to the Si NC/SiC, resulting in phosphorus concentrations of 4×10^{19} cm^{-3} in the Si NC/SiC layer [148]. This issue will be addressed in more detail in Sec. 6.2.1 of this thesis. In their work the problem was resolved by incorporating a 2 nm thick TiO_2:Nb layer between Si NC/SiC and poly-Si [148], and including this interlayer in solar cells greatly improved efficiency [147].

The best device from this group was obtained with Si NC/SiC with added oxygen, the TiO_2:Nb interlayer, p-a-Si:H, and n-type poly-Si [147, 148]. Rather strangely however, the same group reported V_{oc}=678 mV and an efficiency of 2.05% in 2011 [148], and V_{oc}=528 mV and an efficiency of 0.39% in 2013 [147], even though the Si NC/SiC film parameters were identical (except for the number of layers, which was not given in Ref. [147]). As neither reference gives the thickness of poly-Si used, it is suspected that there is indeed a residual

photovoltaic effect of the poly-Si that contributes to the overall device performance, and that upon discovering this the group reduced the poly-Si thickness, and hence the efficiency, in subsequent devices. While this is still the most efficient Si NC cell known to the author, it is in some ways not a very tidy system in which to study the photovoltaic performance of Si NCs as results are clouded by the photovoltaic performance of the poly-Si and, in absence of the TiO_2:Nb interlayer, by diffusion into the Si NC/SiC, which can affect the carrier concentration as well as the nanostructure of the film.

A somewhat tidier system that is shown in Figure 2.7(c) has been developed by Perez-Wurfl *et al*. [149, 150] and involves a p-i-n solar cell where all three layers are made of Si NC/SiO_2. This cell concept also suffers from dopant interdiffusion during annealing [149], resulting in a p-n rather than a p-i-n structure, but does not contain other semiconductors that might be responsible for the photocurrent. The V_{oc}=492 mV obtained is promising for a Si NC device, but the short-circuit current density of 20 μAcm^{-2}, and high series resistance of 28 $k\Omega cm^2$, reveal the limitations of the SiO_2 matrix on device level [150]. Furthermore, the transport and recombination mechanisms within these cells remain unclear, with several different models having been proposed by the group that developed them [149-151].

2.5 Summary

Si NC/SiO_2 and a-Si_xC_{1-x}:H are both well-understood and helpful reference systems for the Si NC/SiC system. Si NCs in SiO_2 can be synthesised with controlled size and shape and exhibit quantum confinement detectable by PL. There is also a complex interdependence of Si nanocluster size, crystallinity, and stress, all of which can affect optoelectronic properties. Si NCs in SiO_2 exhibit a quasi-direct bandgap, exciton lifetimes on the order of µs, and luminescence quantum yields exceeding 10% in the best samples. Transport is via tunnelling

in the case of isolated Si NCs, and disordered-semiconductor-like for percolating networks of Si NCs in SiO_2.

As-deposited a-Si_xC_{1-x}:H has no long-range order and thus exhibits properties that scale with carbon and hydrogen content. More carbon leads to a greater bandgap, greater defect density and band tail width, greater hydrogen content, and lower minority carrier lifetime. Hydrogen dilution of the PECVD gas mixture reduces film hydrogen content, defect density, increases the mobility-lifetime product, and can even lead to the direct deposition of µc-Si_xC_{1-x}:H. Conduction is by carriers excited from the Fermi level at which there is a finite density of states, is Ohmic in most cases, and takes place in the bands, in band tails, or at the Fermi level, depending on the density of states, the doping level, and temperature.

The properties of Si NC/SiO_2 are governed by the size and separation of the nanostructures, whereas those of a-Si_xC_{1-x}:H merely depend on composition. It is therefore to be expected that those of Si NC/SiC will be somewhere in between. The Si NC/SiC system is more difficult to synthesise in an ordered manner: the crystallisation temperatures of Si and SiC depend on a-Si_xC_{1-x}:H composition, and while the multilayer structure restrains NC growth, it itself does not seem to survive anneals above 1000°C. Absorption is stronger than in Si NC/SiO_2 as SiC also absorbs, but this also complicates the analysis of absorption data which are affected by Si NC size as well as Si crystallinity and total film composition, all of which are interrelated. Photoluminescence allows a clearer characterisation of the different bandgaps in principle, but given that only one group has reported data that is as clear as that typically obtained in Si NC/SiO_2 or a-Si_xC_{1-x}:H, all PL data on Si NC/SiC needs to be interpreted with caution. The conduction mechanism in Si NC/SiC appears to be similar to that in a-Si_xC_{1-x}:H for low electric fields, and the films exhibit significant background doping, probably due to nitrogen or oxygen. Whether a different conduction mechanism exists at high fields is unclear as the vertical devices required for such measurements are typically asymmetric and can therefore exhibit non-Ohmic IV behaviour even if transport in the Si NC/SiC layer is Ohmic.

Based on values obtained on SiC, short minority carrier lifetimes are expected for Si NC/SiC which may be the main limitation of the first Si NC/SiC solar cells that have been reported. Several different devices with encouraging results have been reported, though the difficulty in producing a cell where the measured photovoltaic effect is unambiguously from the Si NCs has also become apparent. The one device exhibiting unambiguous Si NC photovoltaic performance had an open-circuit voltage of 492 mV, with the efficiency limited by series resistance.

3. Experimental Methods

A wide range of techniques were applied to synthesise and characterise the samples studied within this thesis. In Sec. 3.1, a brief overview of the sample preparation steps is given. The two main characterisation techniques used and optimised by the author – photoluminescence (PL) and current-voltage (IV) measurements – will then be presented in detail in Sec. 3.2 and 3.3, respectively. A brief description of all other characterisation techniques used can be found in Appendix A: Other Characterisation Techniques.

3.1 Sample Preparation

All samples were prepared by plasma-enhanced chemical vapour deposition (PECVD) of a-Si_xC_{1-x}:H bulk films or a-Si_xC_{1-x}:H / a-SiC:H multilayers, followed by annealing. Samples for electrical characterisation also had contacts deposited on them, and some samples were exposed to hydrogen for defect passivation. These processes are described briefly in the following. The additional processing steps required for the diffusion studies in Sec. 6.2 or the full solar cell structure in Sec. 7.1 are described in those sections. The exact processing parameters of the samples used for any particular experiment are listed right before the results in the corresponding chapter.

3.1.1 Substrate Selection and Cleaning

Float-zone Si substrates were used for all structural measurements while both oxidised Si and fused silica were considered for electrical measurements, the silica substrates also being suitable for spectrophotometry and PL. The disadvantage of silica substrates is their low

thermal expansion coefficient, which is mismatched with that of the Si NC/SiC films and limits the thickness of crack-free films to ≤150 nm. Sapphire substrates would have resolved this problem but were too expensive. Fused silica substrates were purchased with unknown cleanliness and typically contain residual moisture. They are amorphous but are nevertheless referred to as quartz substrates henceforth to avoid confusion with silicon.

Before use, the quartz substrates were cleaned in acetone, propan-2-ol, boiling HNO_3, 1% HCl + 1% H_2O_2, and 1% HF, and annealed at 1100°C for ≥1.5 h, the rationale being that any moisture that was not driven out by this anneal would not be an issue as the rest of the process chain involves lower thermal budgets. Prior to film deposition, all substrates were cleaned in boiling HNO_3 for 10 min followed by a 20-60 s etch in 1% HF. HNO_3 oxidises organic contaminants and the top few nm of the Si substrates, and HF removes the surface oxide (or a few nm of the bulk material in the case of quartz) to leave a pristine surface. At CNR, Si and quartz substrates received a full RCA clean, which also involves HNO_3 and HF as well as some preceding steps that remove metallic contamination [152].

3.1.2 Plasma-enhanced Chemical Vapour Deposition (PECVD)

The a-Si_xC_{1-x}:H films were deposited in an AK400 PECVD chamber from Roth&Rau using the precursor gases SiH_4, CH_4, and H_2, a deposition pressure of 30 Pa, substrate temperature of 270°C, and high-frequency power of 65 W (100 $mWcm^{-2}$) at 13.56 MHz. These conditions correspond to the silane-starving plasma regime [33] where the plasma power is so low that only SiH_4 is dissociated directly; CH_4 can only be dissociated in reactions with SiH_x radicals. This permits low depositions rates but requires a high CH_4/SiH_4 flux ratio for a given stoichiometry: 7 sccm SiH_4 and 60 sccm CH_4 yields stoichiometric a-SiC:H, and carbon contents above 60% are essentially impossible [33, 34]. The compositions of all films used in this thesis had once been determined by Rutherford backscattering spectrometry (RBS) [34].

At CNR, films were deposited with the same process gases and high-frequency source but a lower power density (28 $mWcm^{-2}$), and higher substrate temperature (325-350°C) were used, and gas fluxes adjusted accordingly to obtain the desired compositions as once calibrated by RBS. Following the findings presented in Sec 6.1.2 and Refs. [153, 154] CNR deposited an a-Si:H capping layer on top of all films.

When Si-rich films were to be deposited, a 15-20 nm thick stoichiometric a-SiC:H layer was always deposited first to prevent epitaxial growth of Si from a Si substrate upon subsequent annealing, both at ISE and at CNR. To ensure reproducibility this was done for depositions on all substrates. This 15-20 nm a-SiC:H layer is omitted from the sample description at the beginning of each results chapter but is included in the total film thickness *t* when this is used in calculations. As films shrink significantly on annealing the sample descriptions specify whether film thicknesses are "before" or "after" annealing.

3.1.3 Annealing

Annealing was carried out in tube furnaces in N_2 unless otherwise stated. At ISE, the furnace tube was evacuated to $\leq 2\times10^{-5}$ mbar at ~150°C to remove surface adsorbates, and moisture and particles in the air, before flooding with N_2 and heating to the target temperature at 10°Cmin^{-1}. CNR also typically annealed in N_2 with ramps of 5°Cmin^{-1}, except for the later films with the a-Si:H capping layer (see Sec. 6.1.2) that were annealed in N_2/10% O_2. They did not evacuate the tube, but did hold samples at 600°C for 4 h before heating to the maximum temperature. In cases where films were annealed with an a-Si:H capping layer, this was removed after annealing by etching in HF to remove the oxidised portion and tetramethylammoniumhydroxide (TMAH) or KOH to remove the rest. The capping layer approach was used for all films prepared by CNR and none of the films prepared at ISE unless otherwise stated. Samples that were not annealed are referred to as "as-deposited".

3.1.4 Hydrogen Passivation

Hydrogen passivation (RPHP) was carried out using a remote hydrogen plasma at 450°C, usually for 45 min. A plasma of 55 sccm H_2, 50 sccm Ar, and 3-6 sccm O_2 was struck and the samples positioned so as not to be directly exposed to the plasma radiation. The parameters had been optimised for passivating thin-film Si [155] but a recent study [156] showed that temperatures in the range of 400-500°C are also best for passivating Si NC/SiC films. In one experiment, a forming gas anneal (FGA, N_2/5% H_2) at 425°C for 25 min was also used for comparison. Samples that did not undergo hydrogen passivation may be referred to as "as-prepared" for clarity.

3.1.5 Contact Formation

The majority of contacts to samples in this thesis were made using tin-doped indium oxide (ITO), though Al and a Ti-Pd-Ag stack were also used. ITO 70 nm thick was sputtered with a power of 200 W in 0.3 sccm O_2 with the substrate held at 100°C. This is the standard process used at ISE for heterojunction solar cells; it provides a good contact to a-Si:H and has a sheet resistance of 50 Ω/sq. Where used, Al and Ti-Pd-Ag contacts were thermally evaporated. This is preferable to electron beam evaporation or sputtering as it does not produce any radiation – it does however involve substrate temperatures of up to 200°C. Al was used for simplicity and Ti was used as it is known to form good contacts to SiC [157, 158] (Ni forms even better contacts but Ni evaporation was not possible at ISE for health and safety reasons). Ag is added to Ti to improve current flow within the contact, and Pd is a diffusion barrier; the stack is routinely used at ISE for contacting n-type c-Si [159, 160]. Contact structures were produced either with a shadow mask or by photolithography; more details are given in Sec. 3.3.1.

3.2 Photoluminescence (PL) Spectroscopy

3.2.1 Principle

Photoluminescence spectroscopy involves monitoring the radiative recombination of electron-hole pairs excited with incident light as a function of wavelength. When a sample is irradiated with photons whose energy $h\nu$ is equal to the energetic separation of an occupied state i and an unoccupied state j, it can be absorbed and excite an electron from one state to the other, creating an electron-hole pair, or exciton. Since the transition rate between i and j scales with the joint density of states (DoS) $\int N_i(E)N_j(E+h\nu)dE$ [88], where $N_i(E)$ and $N_j(E)$ are the densities of states i and j per unit energy, respectively, excitation is usually from the largely occupied valence band to the largely unoccupied conduction band (provided $h\nu > E_g$) as shown in Figure 3.1.

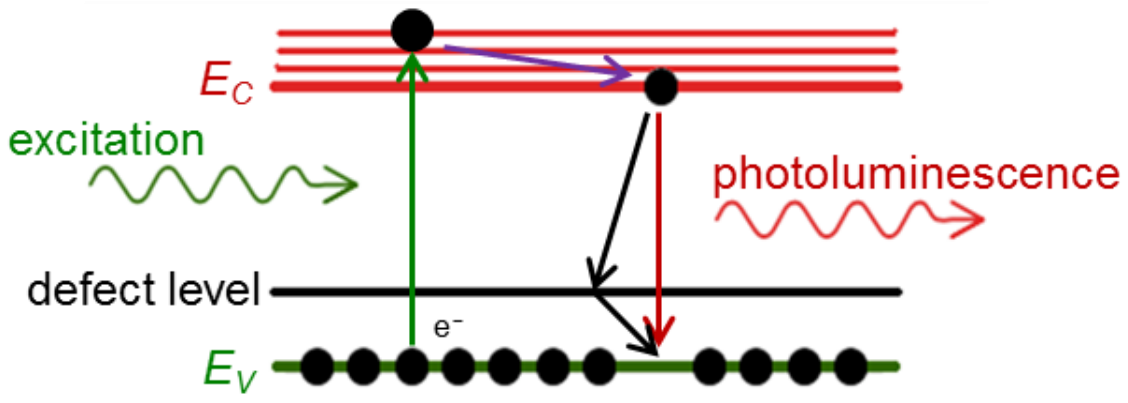

Figure 3.1. Schematic diagram of the photoluminescence process. Incident light (green) excites an electron (e^-) from the valence band to the conduction band, creating an electron-hole pair, or exciton. The electron and hole then thermalise to the band edges (purple) and recombine, either non-radiatively, via defect levels with the emission of phonons (black), or radiatively, with the emission of a photon (red). E_C and E_V denote the conduction and valence band edges, respectively.

Since the DoS within valence and conduction bands is high, the joint DoS for phonon-mediated transitions within each band, $\int N_i(E)N_j(E \pm h\Omega)dE$, where $h\Omega$ is the energy of a phonon, is high and charge carriers typically thermalise to the band edges in $\sim 10^{-13}$ s in bulk

semiconductors (purple arrow in Figure 3.1). Radiative transitions (red arrow in Figure 3.1) therefore occur almost exclusively between energetically well-defined states or band edges, which means their energetic separation can be accurately measured by PL. Charge carriers can also relax across the bandgap by phonon emission (black arrows in Figure 3.1). Since $\hbar\Omega \ll E_g$ for most semiconductors, this requires defect states in the bandgap that permit relaxation in several small steps. Non-radiative relaxation to shallow gap states followed by radiative recombination is also possible, an example being donor-acceptor pair luminescence in SiC [98]. Fully non-radiative recombination cannot be measured directly, but can be inferred from the PL intensity since all carriers that do not recombine radiatively must recombine non-radiatively (provided no excited carriers are extracted from the sample). Non-radiative recombination is detrimental to solar cell performance, which makes PL intensity a simple optimisation criterion for potential solar cell absorber materials. The only caveat is that non-radiative recombination can be reduced by low defect density *and* by low carrier mobility, and only the former is desirable in solar cells.

3.2.2 Experimental Setup

A schematic diagram of the experimental setup used for PL measurements is shown in Figure 3.2.

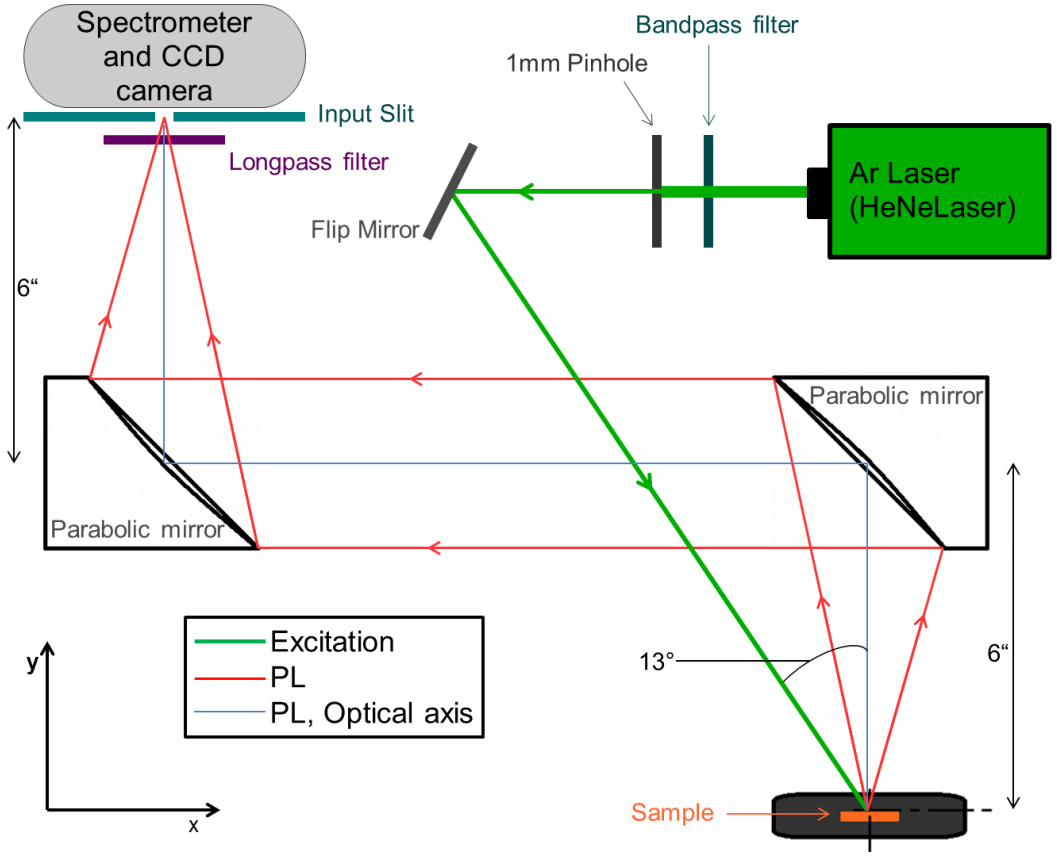

Figure 3.2. Schematic diagram of the PL setup. The sample is irradiated with light from an Ar or HeNe Laser and luminescence detected using parabolic mirrors, a spectrometer and a thermoelectrically cooled Si CCD.

The 514.5 nm line (2.41 eV) of an Ar ion laser (Coherent Innova 90), and the 632.8 nm line (1.96 eV) of a HeNe laser (Thorlabs HRR170), are used as excitation sources. A bandpass filter removes the other laser lines of each laser, and a 1 mm pinhole selects the central part of the beam, ensuring that a beam of equal diameter and relatively uniform intensity is incident on the sample regardless of which laser is used. Parabolic mirrors (Newport, 50331AL) are used to collect the PL signal and focus it onto the input slit of the spectrometer (Andor Shamrock 303i) since they do not suffer from the chromatic aberration that lenses exhibit. An

input slit width of 300 µm was found to be the best trade-off between resolution and signal-to-noise ratio. A longpass (LP) filter is positioned at the input slit to block elastically scattered light. A 550 nm LP filter is used for measurements with the 514.5 nm line, and a 650 nm LP filter for the 632.8 nm line. The spectrometer then collimates the light, disperses it with one of three gratings (300, 600, 1200 lines/mm) that are mounted on a turret, and focuses it onto a Si charge-coupled device (CCD) detector (Andor DU401A-BRDD). For most spectra the 300 lines/mm grating was used as it maximises the signal-to-noise ratio. The Si CCD is thermoelectrically cooled (with auxiliary water cooling) to -95°C to increase its signal-to-noise ratio and dynamic range. The CCD output can be vertically binned to obtain spectra, or read out as an image.

3.2.3 Measurement Procedure

The laser to be used for the measurement session is turned on, set to the required intensity, and allowed to stabilise for 20-30 min. The intensity is measured directly in front of the sample position using a powermeter that was previously calibrated for both laser wavelengths using a reference solar cell with known wavelength-dependent external quantum efficiency. All PL measurements were performed with laser intensities of 0.12-1.2 Wcm^{-2} (i.e., a 1-10 mW circular beam with a diameter of 1 mm). Where laser intensity and/or spectrum integration time were varied for samples that were to be compared this was accounted for by assuming a linear dependence of the signal on intensity and integration time. Laser intensities were sufficiently low to keep excitation levels below one exciton per NC provided the minority carrier lifetime τ is below 100 ns. This is considered to be a realistic assumption as τ=100 ns in 3C-SiC grown epitaxially on Si [8, 88, 89], and it stands to reason that the nanocrystalline samples studied in this thesis would exhibit shorter carrier lifetimes.

Most components of the setup are never moved so only the flip mirror has to be aligned before each measurement session (it is needed since there is another setup to the left of the one in Figure 3.2 which uses the same lasers). This is done by positioning a GaInP reference sample at a fixed x-y position (see Figure 3.2) using the x-y stage that the sample holder is mounted on, and checking whether the laser spot is imaged to the centre of the CCD when the grating in the spectrometer is set to the position where it acts as a mirror. If necessary, the flip mirror is rotated in one or both axes to bring the spot to that position on the CCD. This procedure also helps in identifying accidental misalignment of other components as adjusting the flip mirror only is then not sufficient to bring the spot image to the required position.

Next, a PL spectrum of the GaInP reference sample is acquired and its peak position and intensity logged. Its intensity divided by the laser power provides a value for the sensitivity of the setup during that session which allows comparison of PL intensities measured in different sessions. The error in this procedure is estimated to be ≤20% and arises mainly from the inhomogeneous PL intensity across the central 3 mm×3 mm of the GaInP sample where the measurement is made (see Figure 3.3).

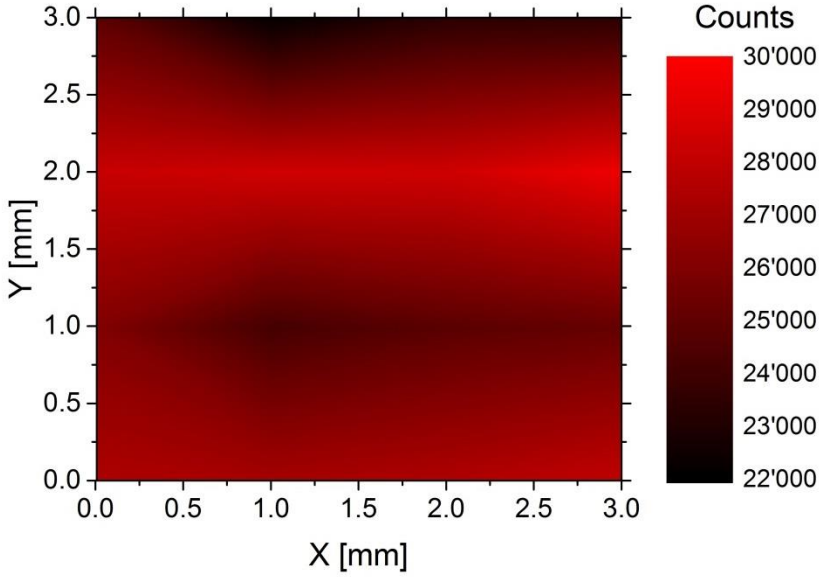

Figure 3.3. PL intensity map of the central 3 mm×3 mm of the GaInP reference sample used to compare PL intensities across measurement sessions.

After these alignment steps the samples can be measured. Each sample is mounted and a laser spot image acquired. The sample is moved left or right until the image is "clean" (Figure 3.4(a)) since measuring at a "dirty" location (Figure 3.4(b)) can severely alter the measurement.

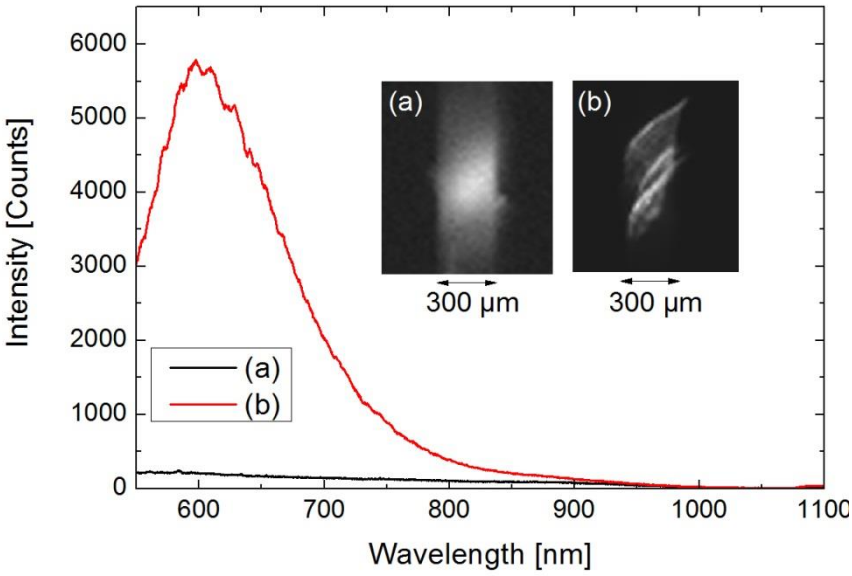

Figure 3.4. Spectra acquired on two locations on the same sample: a "clean" location (a), and a "dirty" location (b). The corresponding beam images with the 300 µm input slit width used are shown.

The "dirt" seen in the spot image (b) is macroscopic as can be seen from the scale bar. It is thought to consist of dust, contamination, scratches, or cracks. Towards the end of the work presented in this thesis samples were routinely cleaned in acetone and propan-2-ol before PL measurement which made finding "clean" spots significantly easier. Once a "clean" location is found, the sample position is optimised for maximum PL intensity in the y-direction (the reason being that differences in mounting between the GaInP reference and the sample can result in the sample not being at the focal point of the parabolic mirror), and a spectrum is acquired. Then the pinhole is blocked and a background spectrum is acquired. Background spectra and laser power are checked at regular intervals within one measurement session.

3.2.4 Data Analysis

The corresponding background spectrum is subtracted from each spectrum to eliminate stray light and dark counts of the detector from the measurement. As the alignment is never perfect, light is usually coupled into the spectrometer at an incorrect angle which leads to the photons hitting different CCD pixels than intended and results in an error in the wavelength axis. Fortunately, this error was found to be merely a shift in wavelength by a constant value. To correct for this, the spectrum is shifted in wavelength such that the laser peak is at the correct wavelength. Spectra acquired with different integration times or laser intensities are divided by the integration time and laser intensity, and spectra measured in different sessions are divided by the PL intensity of the GaInP reference in the respective session. Finally, the spectra are corrected for the spectral response of the setup by multiplying by the transfer function of the setup which is described in the next section. The data analysis procedure is shown graphically in Figure 3.5.

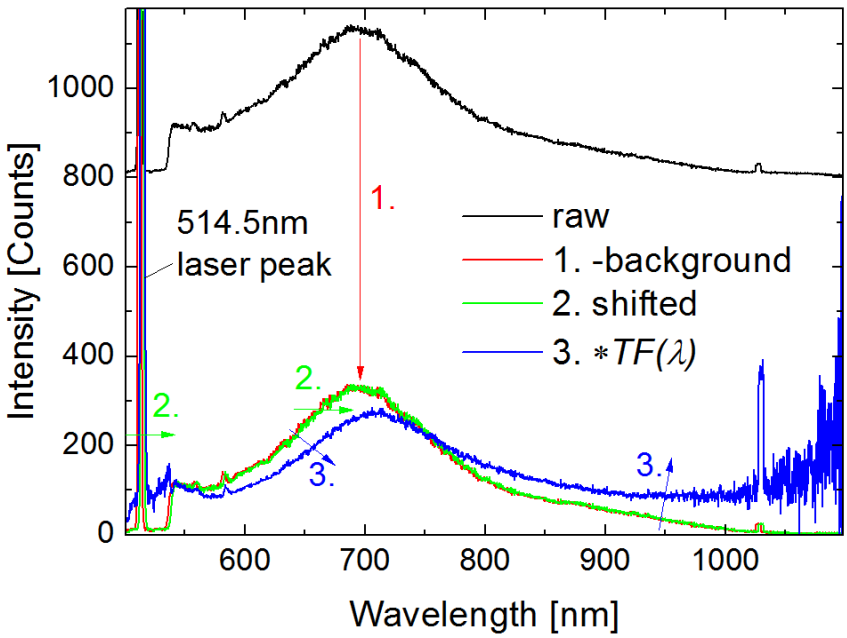

Figure 3.5. Data analysis routine for PL spectra. The background signal is subtracted from the raw spectrum (black) to yield the background-corrected spectrum (red). This is shifted in wavelength such that the laser peak is at the correct wavelength (green) and multiplied by the transfer function *TF(λ)* (blue).

3.2.5 Transfer Function

The measured PL has, *a priori*, little to do with the PL of the sample since it also depends on the reflectance of the collecting and dispersing optics, and the sensitivity of the detector, which vary considerably with wavelength (e.g. Figure 3.6(a)).

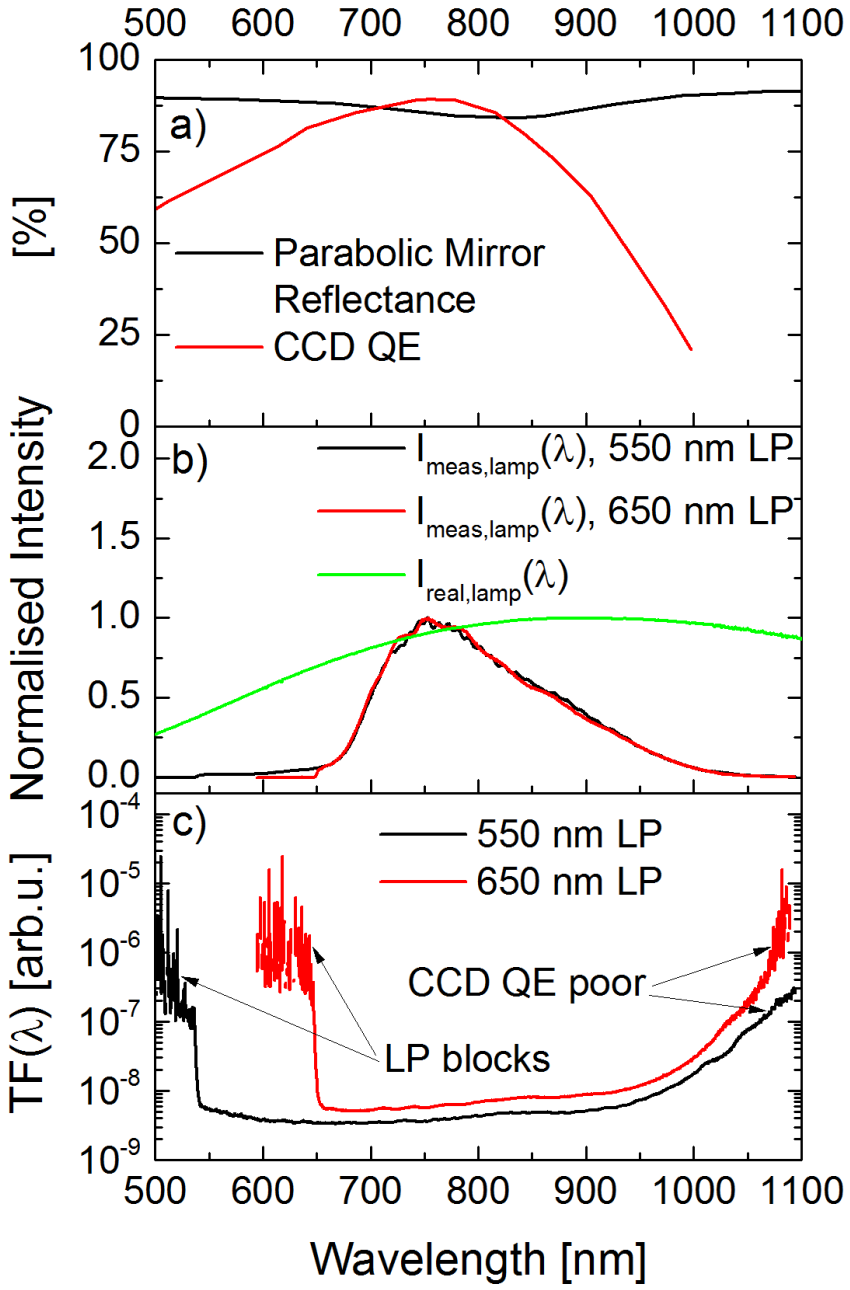

Figure 3.6. (a) Wavelength-dependence of the parabolic mirror reflectance (which enters *TF(λ)* twice) and CCD quantum efficiency (QE). (b) Real spectrum of calibration lamp and spectra measured with 550 nm and 650 nm long pass (LP) filters. (c) Transfer functions for measurements with 550 nm and 650 nm LP filters.

This was corrected by measuring the spectrum of a lamp whose real emission spectrum $I_{real,lamp}(\lambda)$ is known (USHIO FHD JC6V-10W operated at 1.4 A, calibrated at Fraunhofer ISE CalLab), and establishing the ratio of emitted light to detected light at each wavelength, henceforth termed the transfer function $TF(\lambda)$ of the setup. To avoid saturating the CCD with the bright light of the lamp, two neutral density filters (OD 3.0 and OD 1.5, with transmission $T_{OD\ 3.0}(\lambda)$ and $T_{OD\ 1.5}(\lambda)$, respectively) are used to reduce the incident light intensity. $TF(\lambda)$ is then given by

$$TF(\lambda) = \frac{I_{real,lamp}(\lambda) T_{OD\ 3.0}(\lambda) T_{OD\ 1.5}(\lambda)}{I_{meas,lamp}(\lambda)}, \tag{3.1}$$

where $I_{meas,lamp}(\lambda)$ is the measured spectrum that has been corrected for the background signal and wavelength shift as described in Sec. 3.2.4. $I_{meas,lamp}(\lambda)$ is measured separately with each LP filter so that the correct $TF(\lambda)$ is available for each. Real and measured spectra are shown in Figure 3.6(b), and transfer functions are shown in Figure 3.6(c). The most obvious features are the high values of $TF(\lambda)$ where detection is poor – at low wavelengths, because the light is blocked by the LP filter, and at high wavelengths, because the CCD has poor sensitivity. At intermediate wavelengths, $TF(\lambda)$ is a weaker function of λ and mirrors the interference fringes produced by the LP filters.

3.2.6 Substrate and Stray Light Effects

As mentioned in Sec. 3.2.4, the background signal (black curve, Figure 3.7(a)) is acquired with the 1 mm pinhole blocked. This means that it does not account for any luminescence that the beam excites in the substrate or behind the sample. Quartz substrates are transparent, and since typical Si NC/SiC films absorb <30% at 514.5 nm and <10% at 632.8 nm, a significant portion of the beam passes through the sample. If it is allowed to hit the black curtain behind

the sample, as in a measurement with no sample present ("empty channel"), PL from the curtain is detected that is much more intense than that of most samples (red curve, Figure 3.7(a)). Placing a beam dump between the sample holder and the curtain strongly reduces this PL (green curve, Figure 3.7(a)). The strongest reduction is obtained by placing a mirror between the sample holder and the curtain that sends the beam far away from the detecting optics (black curve, Figure 3.7(b) and (c), different ordinate), and this method is used for all measurements presented in Sec. 4.2.

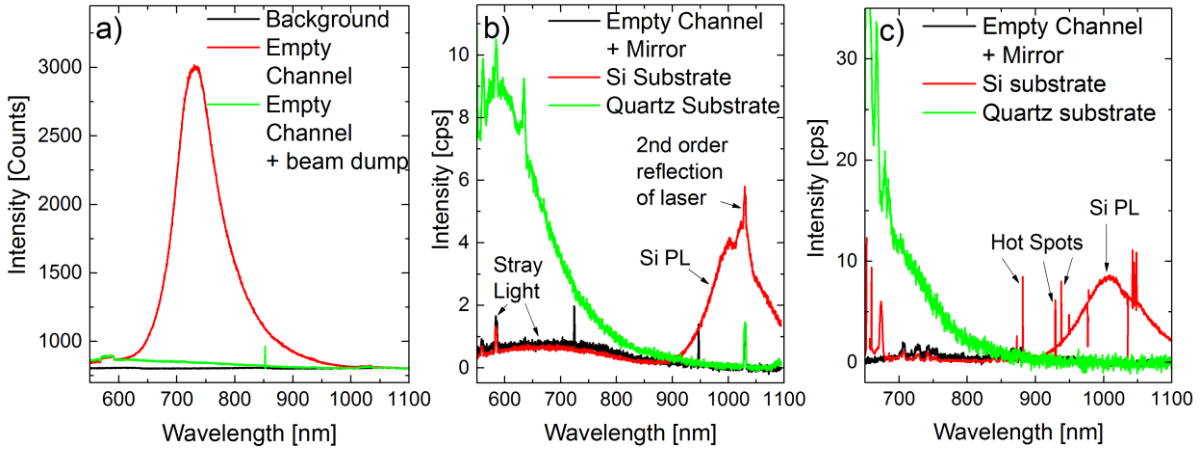

Figure 3.7. (a) PL signal detected with no sample present with (green) and without (red) a beam dump between the sample holder and the curtain. The background signal with the laser blocked is also shown (black). (b) PL signal detected with no sample and a mirror between the sample holder and the curtain (see text, black), a Si substrate (red), and a quartz substrate (green) under 514.5 nm excitation. (c) as (b), but under 632.8 nm excitation.

Due to the partial transparency of Si NC/SiC films a contribution of the substrate to the measured PL is also expected. The PL of bare Si and quartz substrates under 514.5 nm and 632.8 nm excitation is shown in Figure 3.7(b) and (c), respectively. Spectra in these figures are corrected as described in Sec. 3.2.4, but were not multiplied by $TF(\lambda)$ as it is unclear via which optics the measured signal reaches the detector. Si substrates exhibit band-to-band luminescence above 900 nm as well as a weak signal at shorter wavelengths that follows the empty channel signal and is thus attributed to stray light. The quartz substrates exhibit strong PL at short wavelengths. In an attempt to determine whether this PL arises from bulk or

surface defects a quartz substrate was ground down from an initial thickness of 1 mm to 0.3 mm and remeasured. However, the mechanical damage led to a strongly increased PL signal that does not permit any conclusions about the origin of PL in the undamaged quartz to be drawn.

None of these spectra can be subtracted from the spectra of Si NC/SiC films since it is unclear whether they should be scaled by the sample transmittance or not. Therefore, the only spectrum that is subtracted from the film spectra is the background described in Sec. 3.2.4. The substrate and empty channel spectra are nevertheless plotted alongside the sample spectra to allow a qualitative assessment of whether substrate and stray light contributions are relevant. Care is taken to ensure a substrate that underwent the same processing is measured – in the case of Si, the rear side of the actual Si NC/SiC sample is used. For this reason, substrate spectra differ across the different experiments discussed in Chapter 4.

Preliminary measurements with a cryostat as a sample holder, which would have permitted low-temperature measurements, revealed that the luminescence of the cryostat window is significantly stronger than that of typical Si NC/SiC samples. Since the window is indispensable, only room-temperature measurements using a clamp as a sample holder were performed.

3.3 Current-Voltage (IV) Measurements

IV measurements allow the electrical properties of Si NC/SiC films to be studied. Two types of measurements are possible on thin films: in-plane measurements with lateral current flow (Figure 3.8(a)), or vertical measurements through the film (Figure 3.8(b)).

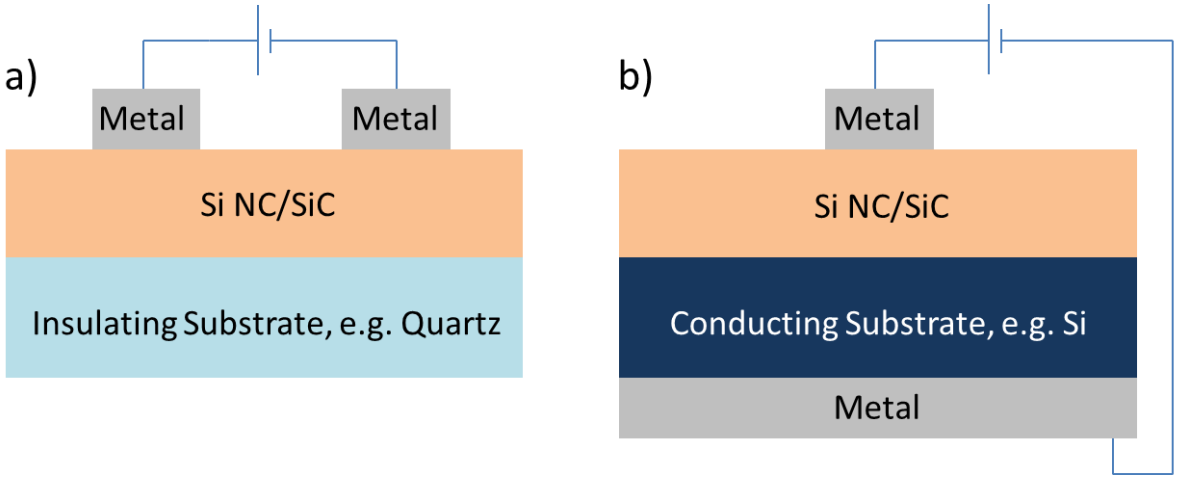

Figure 3.8. Schematic diagrams of device structures for studying electrical transport in Si NC/SiC. (a) lateral, (b) vertical.

Vertical measurements have the advantage that much higher currents flow for a given voltage which facilitates the measurement; that the part of the film through which current flows is buried underneath the contact, which reduces environmental effects; and that the device area is well-defined by the top contact. However, vertical measurements can be compromised if the film has pinholes, if insulating layers or rectifying junctions are formed at any of the interfaces, or if the high electric field created even by modest applied voltages leads to breakdown. As preliminary experiments using lock-in thermography of vertical test structures, and pinhole electroplating, showed that pinholes may be present, lateral test structures were used to characterise Si NC/SiC films, and vertical structures used only to characterise the tunnel junctions studied in Sec. 6.3 and the tandem cells in Chapter 7.

Lateral structures have the advantage that pinholes only minimally alter the cross-section through which current flows, and that relatively low electric fields are involved, which

precludes breakdown phenomena. On the other hand, currents are much lower, and the conducting part of the film is exposed to the ambient. For these reasons samples were cleaned in propan-2-ol before measurement, and measurements carried out in a cryostat evacuated to $<4\times10^{-4}$ mbar using a HP 4140B picoammeter. Samples were checked for cracks using light microscopy and samples with cracks were discarded (see Figure 3.9).

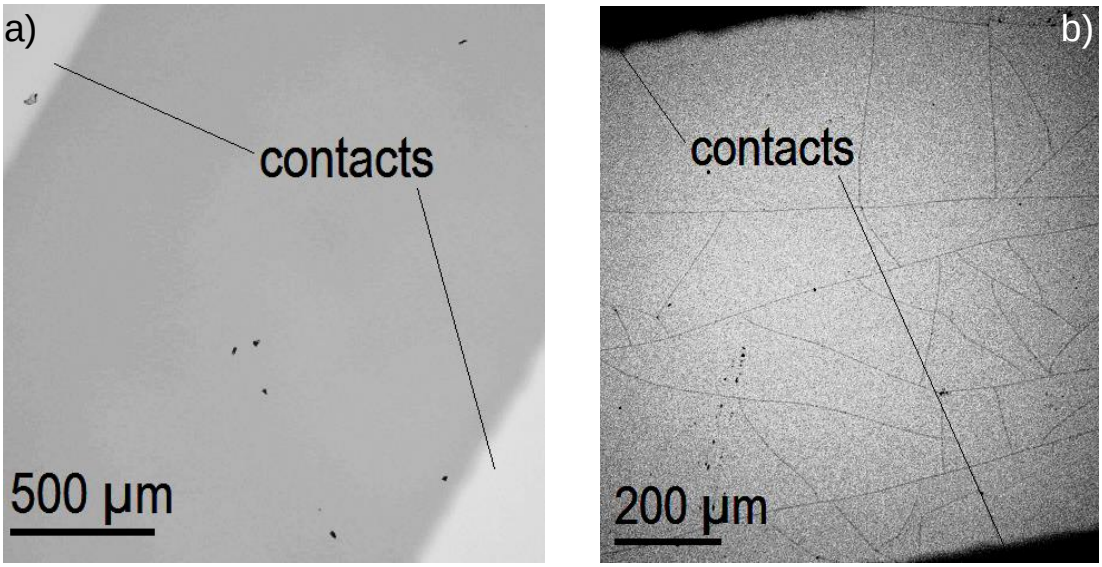

Figure 3.9. Si NC/SiC films suitable (a) or unsuitable (b) for lateral IV characterisation based on the observation of cracks (or not) by light microscopy.

3.3.1 Contact Geometry

In a lateral IV measurement the measured resistance is the sum of the setup, contact, and film resistance. The setup resistance can be eliminated with a four-point probe measurement but the effect of contact resistance R_c remains. In order to eliminate setup and contact resistance, IV curves were measured as a function of contact spacing; this is known as a transmission line measurement (TLM) [161, 162]. Contacts with an area of 3 mm×9 mm and separations of 1, 2, 3, 4, 6, and 8 mm were produced within a 24 mm×24 mm area using a shadow mask as shown in Figure 3.10(a) and (b). The contacts were arranged so as to match the probe

arrangement in the cryostat (Figure 3.10(c)), allowing all IV curves to be acquired sequentially without venting the cryostat.

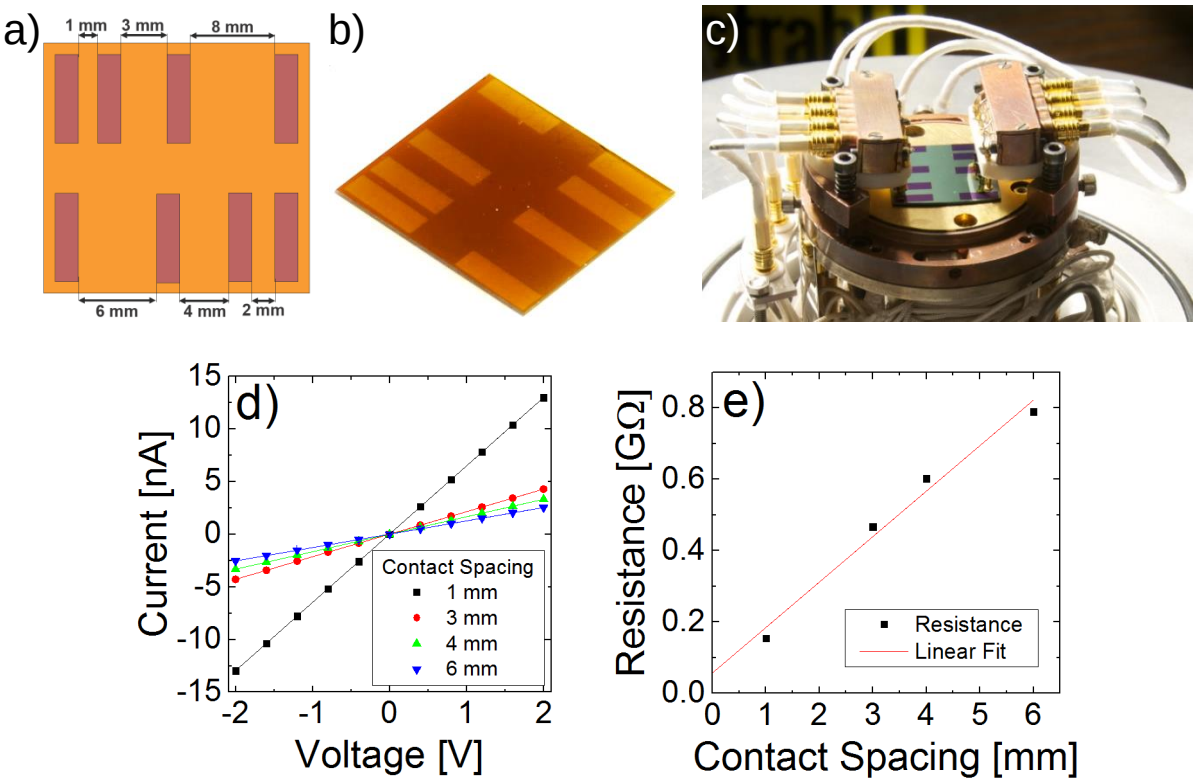

Figure 3.10. (a) Schematic diagram of the TLM structure used. (b) Si NC/SiC film on 25 mm×25 mm quartz substrate with ITO contacts. (c) Si NC/SiC film on oxidised Si with ITO contacts in the IV setup. The probe array in the setup matches the TLM contact structure so all contact spacings can be measured without moving the probes. Resulting IV curves for a typical sample are shown in (d), and the resistance for each contact spacing plotted as a function of contact spacing in (e). A linear fit to (e) yields the sheet resistance of the film. (b) and (c) © Peter Kurzok.

Figure 3.10(d) shows the IV curves obtained on a typical sample. IV curves are Ohmic and resistance increases with contact spacing. Plotting resistance R against contact spacing x yields Figure 3.10(e). The gradient of this plot $dR/dx=R_{sh}/w$, where R_{sh} is the sheet resistance and w the contact width, while the ordinate intercept is equal to $2R_c$. In the event that an insulating layer is present between the contact and the Si NC/SiC film R_c accounts for this as well. Using the contact structure in Figure 3.10(a) also means R_{sh} is a mean value averaged across the entire specimen. Poor contacts, bad contacting with the probes, or areas with cracks

that were missed by light microscopy usually appear as deviations from a good linear fit in Figure 3.10(e) and can be excluded at this stage.

3.3.2 Surfaces and Interfaces

The conductivity σ can be derived from $\sigma^{-1}=\rho=R_{sh}t$, where ρ is the resistivity and t the film thickness, provided the entire thickness of the film conducts via a bulk process. To ascertain whether this is the case, 40 and 80 nm thick SiC bulk films were prepared on two wet-oxidised Si wafers ($t_{SiO2}\approx$1 µm) and contacted with ITO. Figure 3.11 shows sheet conductance ($=R_{sh}^{-1}$) as a function of t.

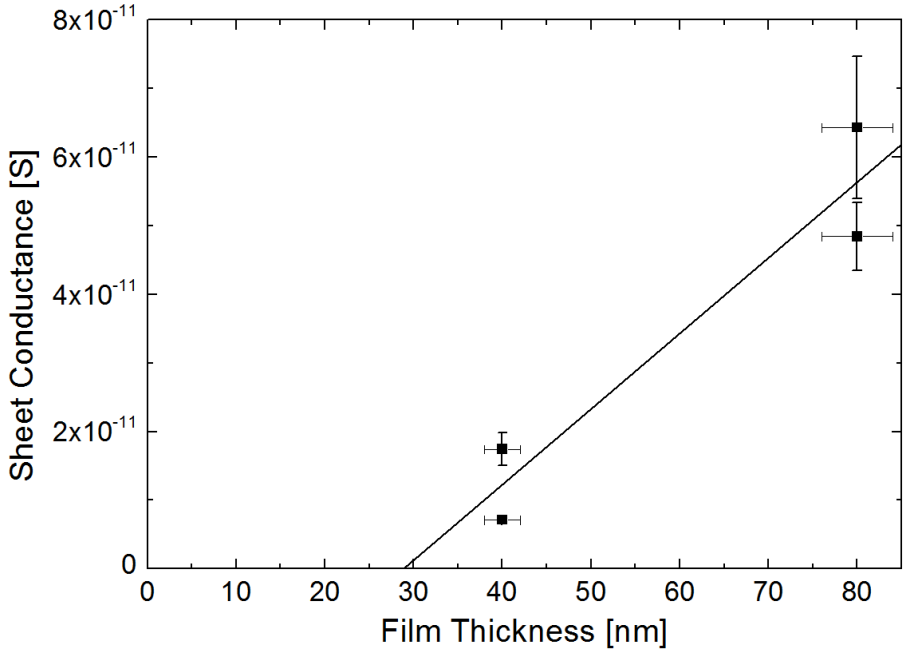

Figure 3.11. Sheet conductance as a function of SiC film thickness. The line is a linear fit to the data.

Sheet conductance increases with t, demonstrating that conduction is a bulk process and does not occur solely at the film surface or interface. A finite intercept at the abscissa indicates that ~30 nm of each film does not carry any current. This could be due to oxidation of the film surface, interface reactions with the substrate, or the formation of depletion regions. Chemical

reactions are likely to be similar for all films, while depletion regions are likely to be widest for the films in Figure 3.11 since all other films studied in this thesis were more conductive. This means that no more than 30 nm of any film studied in this thesis do not conduct, which means that a bulk conductivity can be found from $\sigma=(R_{sh}t)^{-1}$ with a ≤30 nm error in t.

3.3.3 Substrates

Lateral IV measurements on Si NC/SiC films require insulating substrates that can withstand annealing at ≤1100°C. Quartz substrates fulfil this criterion, but are not ideal since their low thermal expansion coefficient precludes the formation of thick, crack-free films, and since their poor thermal conductivity leads to bad thermal coupling in temperature-dependent measurements. It was thought that dry-oxidised Si wafers, which have ~300 nm SiO_2, would mitigate these issues while also being cheaper and more compatible with Si cleanroom processes, but a diploma thesis carried out at ISE revealed that these substrates were prone to shunting [163].

Here, two approaches to produce insulating substrates that support crack-free films were investigated: quartz substrates coated with an additional SiO_2 layer deposited by PECVD, which was thought to be softer and more accommodating of stress, and wet-oxidised Si wafers. It was found that a 1 µm SiO_2 interlayer deposited by PECVD actually made films on quartz more prone to cracking, while wet-oxidised wafers (t_{SiO_2}≈1 µm) worked very well: R scaled with contact spacing, $1/R_{sh}$ scaled with film thickness (see Figure 3.11), and the resistance measured when contacts were deposited directly on the oxidised wafer exceeded the detection limit. Unfortunately, this result was only obtained after all other samples studied in this thesis had been produced, but wet-oxidised wafers are recommended as an alternative to quartz for future measurements.

3.3.4 Measurement Settings

IV curves measured from -10 V to +10 V with 1 V steps, and a short holding time of the voltage t_H before current readout of 2 s, often appeared non-Ohmic and hysteretic as seen in Figure 3.12(a). This was not related to a poor contact, as reversing the polarity of the measurement had no effect, but to the sweep rate: increasing t_H to 30 s strongly reduced hysteresis, and t_H=3 min eliminated it completely.

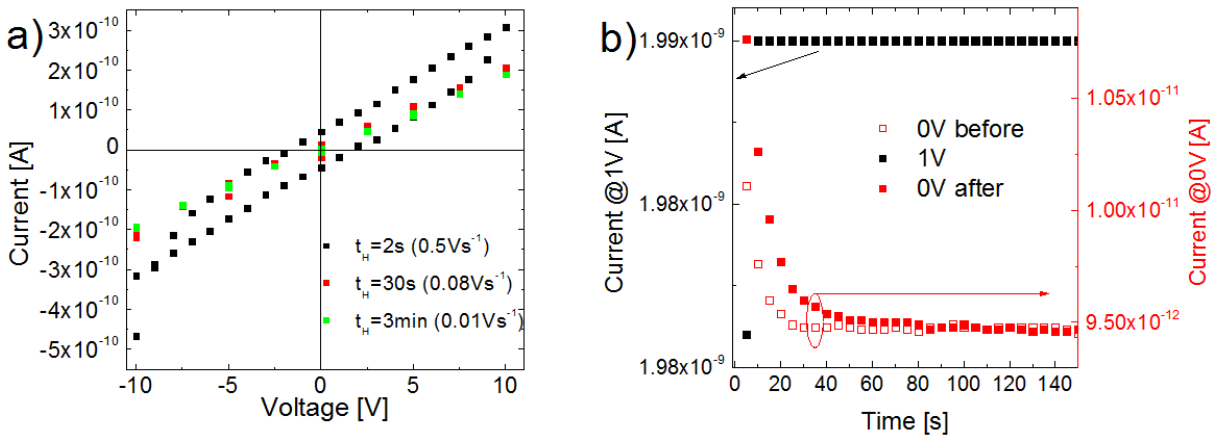

Figure 3.12. (a) IV curves obtained with different sweep rates. Sweep rates must be kept sufficiently low to avoid non-Ohmic and hysteretic IV curves. (b) Current as a function of time at 0 V, at 1 V, and at 0 V directly after 1 V had been applied.

Hysteresis in IV curves is typically due to a time-dependent charging current being superimposed on the steady-state conduction current, which for a circuit with a resistance R and a capacitance C decays exponentially with time $t=RC$ [6]. The hysteresis in Figure 3.12(a) was independent of the length of coaxial cable used in the setup, while the discharging behaviour in Figure 3.12(b) (to be described in the following) was also observed when measuring a 1 MΩ resistor. The capacitance is therefore thought to be in the fixed components of the setup, which with the high resistance of the films leads to a macroscopic discharge time. To determine the shortest t_H that can be used, current is measured as a function of time at 0 V, 1 V, and 0 V bias for each sample before IV measurement. The initial 0 V measurement permits discharging of any charge present after mounting the sample, while

the 1 V and following 0 V measurements monitor charging and discharging behaviour. The shortest time after which both are reasonably stable – 60 s for the sample monitored in Figure 3.12(b) – is used for t_H in the IV measurement. The largest contact spacing and, for temperature-dependent measurements, the lowest temperature, is used to determine t_H as that is where R is greatest. Furthermore, to avoid the particularly strong hysteresis at the beginning of the ±10 V sweep in Figure 3.12(a), a sweep of ±U V is always carried out from 0 V to +U V, then from 0 V to -U V.

3.3.5 Temperature-dependent IV

Temperature-dependent IV (IVT) measurements are carried out with the same procedure as IV measurements, except that only a single contact spacing is used and a PT100 thermocouple is mounted near it to monitor the temperature on the film surface (this deviates significantly from the nominal temperature set by the Eurotherm 902s temperature controller). The largest, and hence most resistive, reliable contact spacing on the sample is used to minimise the effect of contact resistance. The temperature is recorded at each IV data point, and the temperature variation during the acquisition of an IV curve used for the corresponding temperature error bar in an Arrhenius plot of conductivity (see Figure 5.3 and Figure 5.7).

To assess the reproducibility of the PT100 temperature measurement, the same sample was measured twice, and the PT100 temperature plotted as a function of conductivity for both measurements in Figure 3.13(a). As the real sample temperature must be the same for a given conductivity, the difference, also plotted in Figure 3.13(a), indicates the reproducibility of the PT100 temperature measurement. The error is <5 K, and <2 K for T>120 K. To avoid temperature instabilities, measurements were always carried out towards room temperature, i.e. from 77 K to 300 K, or from 400 K to 300 K. As can be seen in Figure 3.13(b), the curves measured from 200 to 400 K and from 400 to 300 K overlap well near room temperature,

demonstrating that there is no systematic difference and that data acquired under heating or cooling to room temperature can be joined to obtain a single dataset for the full temperature range (77-400 K). On the other hand, the conductivity of the sample used for the measurements in Figure 3.13(b) seems to have decreased slightly in the course of a year. Since high-temperature measurements were not available for part of this thesis, high- and low-temperature measurements of many samples in Chapter 5 were carried out a year apart. Figure 3.13(b) was taken as justification for multiplying the high-temperature measurement by a constant (1.0-1.2) such that the room-temperature conductivities match.

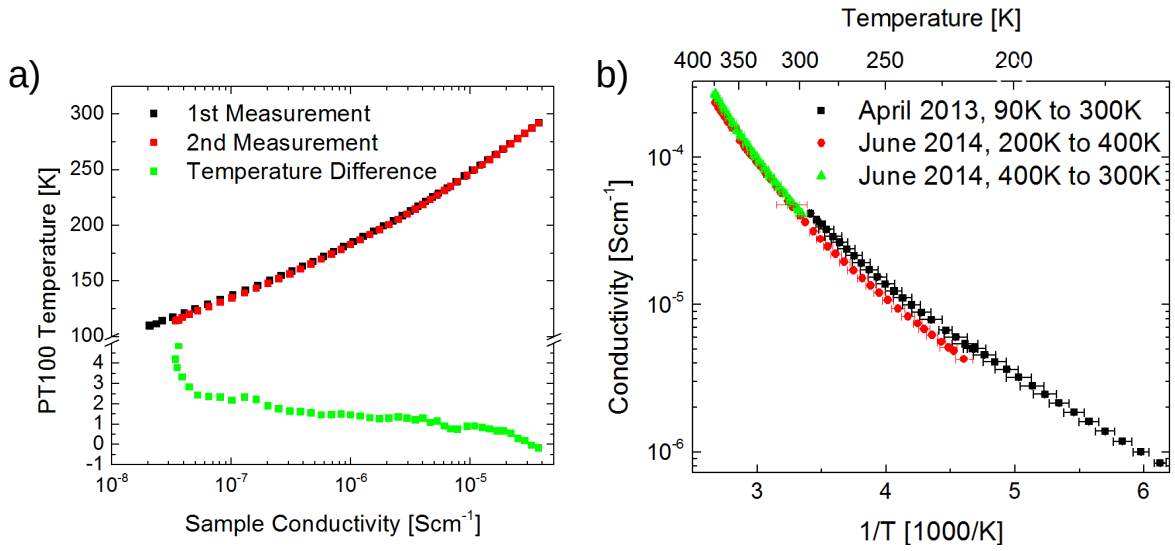

Figure 3.13. (a) PT100 temperature as a function of sample conductivity for two consecutive measurements on the same sample. The difference in measured temperature for a given conductivity is also plotted and represents the random temperature error arising from the way the PT100 thermocouple is mounted on the sample. (b) Arrhenius plot of three different IVT measurements carried out on the same sample. Whether the measurement is done under heating or cooling makes no difference; however, the conductivity decreases slightly of the course of one year.

In summary, great care has been taken to ensure that IV measurements are unaffected by parasitic resistance, shunts, charging, and random errors in electrical and thermal contacting, such that an accurate bulk conductivity averaged across a large area can be extracted for each sample.

4. Photoluminescence

This chapter reports photoluminescence results on Si NCs in SiC (Si NC/SiC) in an attempt to improve on the conflicting results reported in the literature and develop an understanding of recombination mechanisms in the material. The effects of annealing, nominal Si NC size, and substrate are studied. The results have been published in Refs. [164, 165].

4.1 Annealing

In this section, a comparison of as-deposited precursor films and films annealed at 600, 900, 1000 and 1100°C, as well as a comparison of tube furnace and rapid thermal annealing, is undertaken. All samples were prepared by CNR.

4.1.1 Annealing Temperature

The annealing temperature-dependence of PL was studied on multilayer (ML) samples listed in Table 4.1. The only parameter varied between samples was the a-Si_xC_{1-x}:H composition (x=0.6, 0.65, 0.75). The samples were prepared on quartz substrates and without the a-Si:H capping layer. The PL spectra of ML2 films as a function of annealing temperature under 2.41 eV excitation are given in Figure 4.1(a).

Table 4.1. Sample parameters for annealing temperature study.

Sample	*Deposition Parameters*[a]	*Annealing Temperatures*
ML1	30x [3 nm a-$Si_{0.75}C_{0.25}$:H / 3 nm a-SiC:H]	As-deposited, 600, 900, 1000, 1100°C
ML2	30x [3 nm a-$Si_{0.65}C_{0.35}$:H / 3 nm a-SiC:H]	
ML3	30x [3 nm a-$Si_{0.60}C_{0.40}$:H / 3 nm a-SiC:H]	

[a]thicknesses are before annealing.

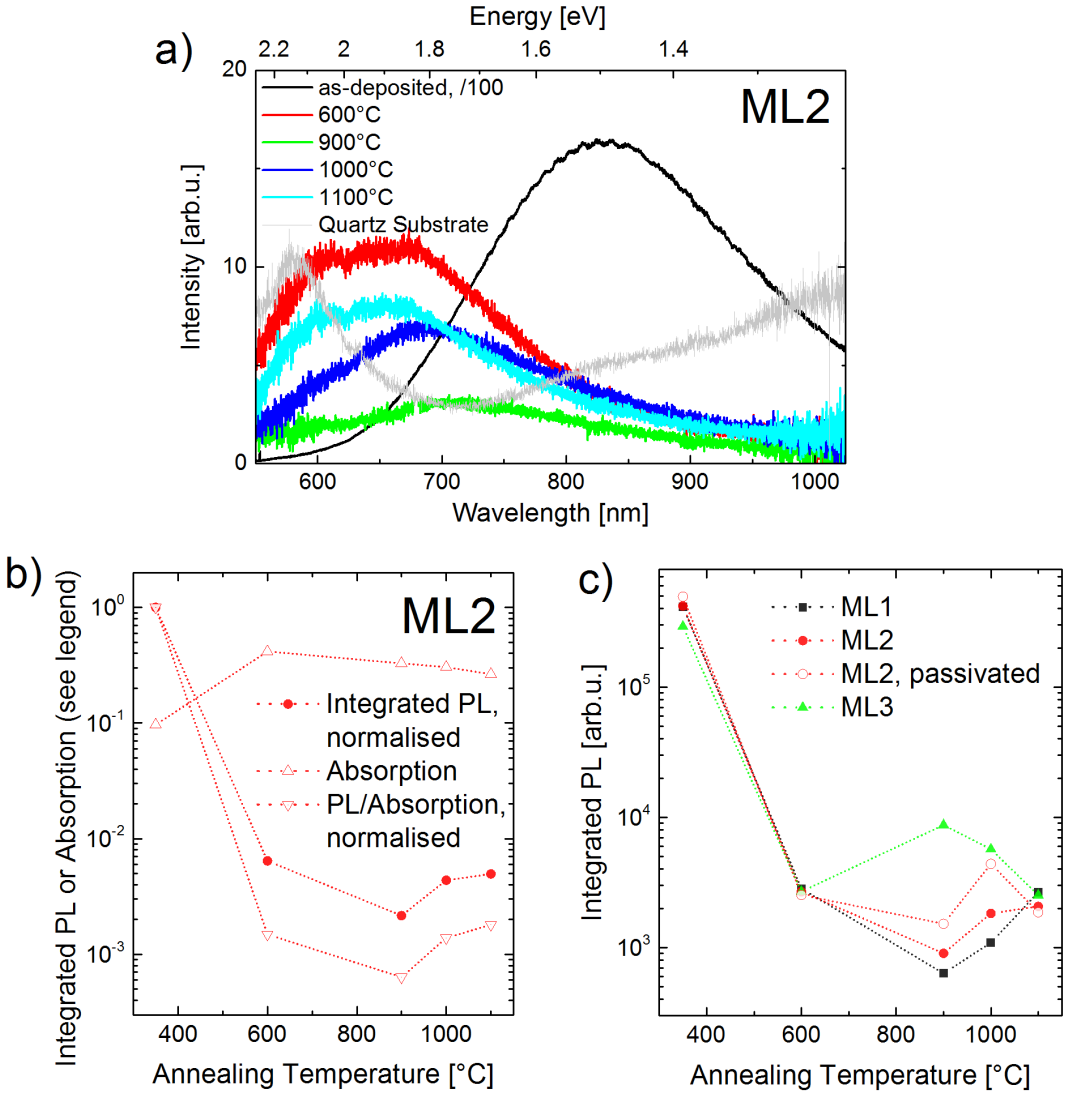

Figure 4.1. (a) PL spectra of ML2 as a function of annealing temperature. Note that the spectrum of the as-deposited sample is reduced 100× for clarity. (b) Integrated PL intensity, absorption, and quantum yield (represented by the ratio of integrated PL and absorption) of ML2 as a function of annealing temperature. Integrated PL and quantum yield are both normalised to the value for the as-deposited sample which is plotted at the deposition temperature of 350°C. (c) Integrated PL as a function of annealing temperature for ML1, ML2, and ML3. For ML2, the integrated PL of the samples passivated by RPHP is also shown. Lines in (b), (c) are guides to the eye.

The as-deposited sample exhibits a strong, Gaussian PL band as one might expect for an a-Si_xC_{1-x}:H film [62, 92]. Upon annealing at 600°C, the overall PL intensity is reduced more than 100×. This is shown most clearly in Figure 4.1(b), where the integrated PL is plotted as a function of annealing temperature. The absorption of the films actually increases upon annealing, which means that the luminescence quantum yield, represented by the ratio of integrated PL and absorption in Figure 4.1(b), decreases by almost three orders of magnitude. Figure 4.1(c) shows that this is the case for all three multilayers. Bulk films with x=0.6, 0.65, 0.75 were also prepared and exhibited similar trends upon annealing at 600°C and 1100°C. This can be understood with reference to energy-filtered transmission electron microscopy (EFTEM) images of the multilayer samples acquired by UB [166]. These showed that the multilayers studied in this experiment intermix fully on annealing, which means that no general difference between bulk films and multilayers is expected. All this is in stark contrast to Si NCs in SiO_2, where the integrated PL exceeds that of the amorphous precursor [132].

The strong decrease in PL intensity on annealing at 600°C is due to the effusion of hydrogen from the samples as that is the only change they are known to undergo at that temperature [15, 60, 63, 73]. The hydrogen leaves behind dangling bonds that act as non-radiative recombination sites, and for most samples this effect becomes even more pronounced at 900°C. Above 900°C, the PL intensity rises again for most samples. This is in agreement with the results on annealed a-Si_xC_{1-x}:H bulk films reported in Refs. [79, 80]. The trend is attributed to the crystallisation of Si and SiC that begins in this temperature range [17, 167]. However, Figure 4.1(a) shows that the 600°C and 1100°C PL spectra are rather similar, which would suggest that the luminescent centre is not related to the presence of crystals. One might think that the luminescence could originate from the quartz substrate in all cases, given that the PL of a bare quartz substrate is of similar intensity (see Figure 4.1(a)). However, it can also be seen that the PL of all samples is much weaker than that of the quartz substrate at 1000 nm. Since the PL of the substrate is most likely to be detected at long wavelengths

where absorption of the films is minimised, one can conclude that the substrate PL makes a negligible contribution to the PL measured on the films at all wavelengths.

Spectra obtained on annealed a-SiC:H bulk films (not shown in Figure 4.1) peak between 2.0 and 2.2 eV, suggesting that some of the PL emitted <2.0 eV by ML2 must be related to excess Si. Figure 4.1(c) shows that applying an RPHP treatment (see Sec. 3.1.4) only leads to a modest change in PL intensity, and does not even come close to recovering the strong PL of the as-deposited films. On the other hand, it does not reduce PL, as reported in Ref. [79], nor does it give rise to a new PL band centred at 1.2 eV, as reported in Refs. [79, 92]. Since the strong PL of as-deposited films is related to efficient hydrogen passivation of dangling bonds by hydrogen [91], the annealed films either contain new defects that cannot be passivated by hydrogen, or do not permit hydrogen diffusion to dangling bonds. These points are addressed in more detail in Sec. 4.2 and 5.1.2.

This annealing series shows that for a range of films PL is drastically reduced upon annealing, leading to a broad PL band in the 1.6-2.1 eV range that does not exhibit a clear correlation with crystallinity or hydrogen passivation and whose origin is not entirely clear.

4.1.2 Rapid Thermal Annealing

In order to determine to what extent the thermal budget of Si NC synthesis can be reduced, rapid thermal annealing (RTA) of precursor films was compared to tube furnace annealing using PL. A multilayer and a SiC bulk film were studied; relevant sample parameters are given in Table 4.2. All films were prepared on quartz substrates. Grazing incidence x-ray diffraction (GIXRD) and Raman measurements performed by CNR and UB, respectively, indicate that both tube furnace annealing and RTA yield Si NCs of the same size. However, the Si crystallinity is lower after RTA, 30% as opposed to 41%. CNR also found that the additional 900°C anneal that some RTA samples see does not change the nanostructure.

Table 4.2. Sample parameters for RTA study.

Sample	*Deposition Parameters*[a]	*Anneal*
3 nm-D		1100°C, 30 min, N_2/10% O_2
3 nm-F	30x [3 nm a-$Si_{0.85}C_{0.15}$:H / 5 nm a-SiC:H]	1150°C, 2 min, Ar
3 nm-G		1150°C, 2 min + 900°C, 1 h; Ar
B-D		1100°C, 30 min, N_2/10% O_2
B-F	174 nm a-SiC:H	1150°C, 2 min, Ar
B-G		1150°C, 2 min + 900°C, 1 h; Ar

[a]thicknesses are after annealing, for the 1100°C 30 min-annealed films. However, as most shrinkage occurs due to hydrogen effusion which is complete in all films, no large differences are expected.

The PL spectra of all six samples under 1.96 eV excitation, along with the relevant empty channel and quartz substrate spectra, are shown in Figure 4.2. With this excitation energy no PL related to band-to-band transitions in the SiC phases is expected.

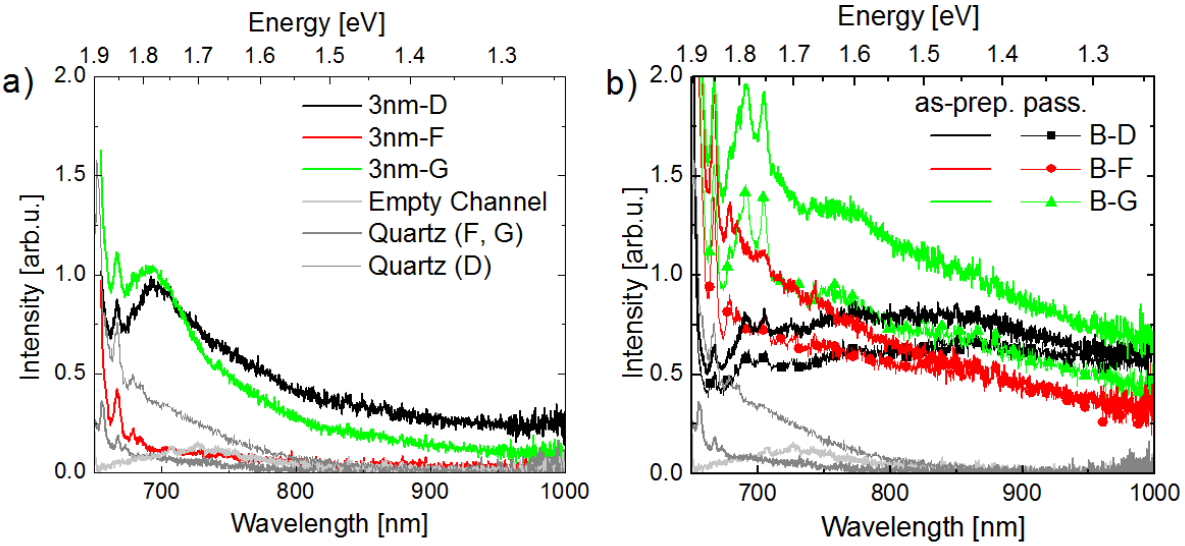

Figure 4.2. PL spectra of as-prepared 3 nm films (a) and as-prepared and hydrogen-passivated B films (b) as a function of heat treatment. Empty channel (see Sec. 3.2.6) and quartz spectra are also shown and are the same in both panels.

As the PL signal measured on bare quartz substrates varies with heat treatment, two quartz spectra are given: one comparable to RTA films (“Quartz (F, G)”), whose signal barely

exceeds the empty channel signal, and one comparable to tube furnace-annealed films ("Quartz (D)"). In both cases the quartz PL may be responsible for the peak at 1.85 eV but is negligible below 1.8 eV.

The as-prepared 3 nm-D film is characterised by a PL peak at 1.78 eV, as well as rather featureless but finite PL in the 1.2-1.6 eV range. Neither is observed for the 3 nm-F (RTA) sample, whose PL does not significantly exceed that of the substrate. If, however, the RTA film undergoes a post-anneal at 900°C for 1 h (3 nm-G), the PL is greatly increased, and now resembles that of the tube furnace-annealed film (3 nm-D). Unfortunately, the scatter in PL across any one of the 3 nm samples is so large that no clear conclusions regarding differences in PL intensity between 3 nm-D and 3 nm-G can be drawn. The same applies to measurements performed on the same samples after hydrogen passivation (RPHP, not shown in the figure); no effect exceeding the scatter across any one of the samples was found.

The findings as a function of heat treatment are in qualitative agreement with findings on Si NCs in SiO_2 [55, 56]. Here too a strong reduction in PL intensity was found for more rapidly annealed samples even though the nanostructure of the film was the same, and an improvement in PL of rapidly annealed samples under prolonged post-annealing at lower temperature was shown. In the case of Si NCs in SiO_2, it is known that PL arises from quantum-confined states in the Si NCs [23], and that the quenching and recovery of PL is therefore associated with more defects and the out-annealing of defects, respectively [55, 56]. It would stand to reason to draw the same conclusion here, in which case the material would be found to contain Si NCs with a mean bandgap of ~1.8 eV. This, however, is questionable since EFTEM has shown the mean nanocluster size in 3 nm-D to be ~5 nm [166]. The Bohr radius of the exciton in Si is ~4.5 nm [168], and SiC is not a strongly confining matrix: Jiang *et al*. predict a shift of E_C and E_V by ≤0.15 eV each for 5 nm Si NCs in 3C-SiC, leading to $E_g \leq 1.4$ eV. Since only 40% of the Si in 3 nm-D is crystalline, emission from a-Si nanoclusters is a possible explanation for the ~1.8 eV band.

The PL below 1.6 eV is likely to originate from the SiC matrix as it resembles the PL of B-D. The PL of the RTA film B (B-F) is, as that of 3 nm-F, found to improve somewhat upon post-annealing, and the PL of all B films decreases slightly upon hydrogen passivation. Otherwise, drawing clear conclusions regarding PL of this film remains difficult, particularly since the excitation energy of 1.96 eV used for these measurements is below the Tauc gap of B-D (2.12 eV [165]), and below the bandgap of 3C-SiC (2.39 eV [30]) and a-SiC:H (2.0-2.6 eV [91]). This PL is tentatively attributed to defect luminescence in the SiC matrix.

4.2 Nominal Si NC Size

In order to obtain a better understanding of photoluminescence, the key parameter in the case of quantum dot band-to-band luminescence, the nanocrystal size, ought to be varied. This was attempted via a variation of the a-Si_xC_{1-x}:H sublayer thickness in the precursor multilayer. A summary of the samples prepared for this experiment by CNR is given in Table 4.3. Two samples were prepared for each film and one exposed to an RPHP treatment which, as will be shown in Sec. 5.1.2, decreases the density of dangling bonds in Si NC/SiC films.

Table 4.3. Sample parameters for nominal Si NC size study.

Film	***Deposition Parameters***[a]	***Anneal***
2 nm	30x [**2** nm a-$Si_{0.85}C_{0.15}$:H / 5 nm a-SiC:H]	1100°C, 30 min, N_2/10% O_2
3 nm	30x [**3** nm a-$Si_{0.85}C_{0.15}$:H / 5 nm a-SiC:H]	
4 nm	30x [**4** nm a-$Si_{0.85}C_{0.15}$:H / 5 nm a-SiC:H]	
B	174 nm a-SiC:H	

[a]thicknesses are after annealing.

In order to allow for a more in-depth correlation of PL with the actual nanostructure the nanostructure of the annealed films was studied by UB using EFTEM and Raman

spectroscopy. Their results can be found in Refs. [165, 166] and are summarised in the following. EFTEM images of the 2, 3, and 4 nm samples are shown in Figure 4.3.

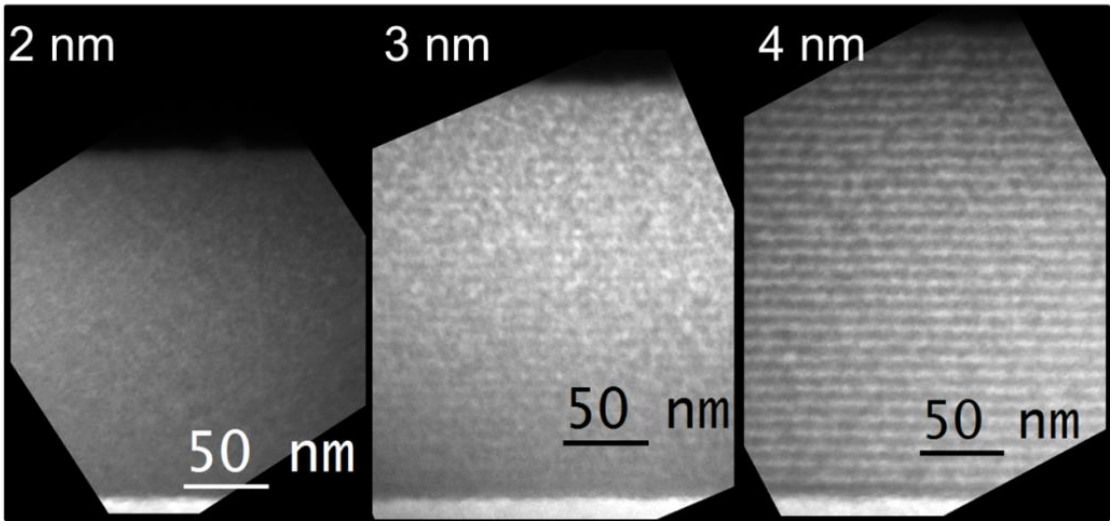

Figure 4.3. Energy-filtered transmission electron micrographs of the annealed 2, 3, and 4 nm samples. Electrons were filtered around the Si plasmon peak at 17.3 eV so bright contrast represents Si. The Si substrate can be seen at the bottom of each image, and the film surface at the top of each image. Reproduced from Ref. [165], ©2015 AIP Publishing LLC.

The micrograph of the 2 nm film shows that interdiffusion has led to a loss of the multilayer structure upon annealing, probably also leading to a loss of the intended NC size control. In contrast, the multilayer structure is still discernible in the case of the 3 nm film, and clearly visible for the 4 nm film. Mean Si NC sizes of 4.7 and 5.0 nm were found for the 3 and 4 nm sample, respectively. At CNR, it was found that when Si and quartz substrates are included in the same deposition, films on quartz are ~10% thinner [166]. The Si NC sizes in films on quartz are therefore estimated to be ~10% lower too. The volume fraction of excess Si, V_{Si}, can be calculated from the composition of the films assuming full de-mixing of the a-$Si_{0.85}C_{0.15}$:H layers into Si and SiC using the equations given in Ref. [166]. The crystallinity $X_{c,Si}$ (determined using Raman spectroscopy) of the excess Si volume fraction V_{Si} in the films increases with a-$Si_{0.85}C_{0.15}$:H thickness, from 0.09 for the 2 nm film to 0.6 for the 4 nm film. GIXRD showed that nanocrystalline SiC is present in all of the films, with Scherrer grain

sizes [169] of 3.4 ±0.5 nm in the annealed multilayers and 4.6 ±0.4 nm in film B. A summary of the nanostructure parameters is given in Table 4.4.

Table 4.4. Excess Si volume fraction V_{Si}, Si crystallinity $X_{c,Si}$, and Si NC size $d_{Si\ NC}$ in the films, as well as the derived quantities $V_{nc\text{-}Si}=V_{Si}X_{c,Si}$ (nc-Si volume fraction), and $V_{a\text{-}Si}=V_{Si}(1-X_{c,Si})$ (a-Si volume fraction). V_{Si}, $V_{nc\text{-}Si}$, and $V_{a\text{-}Si}$ are upper bounds since full de-mixing is assumed.

Film	V_{Si}	$X_{c,Si}$	$d_{Si\ NC}$ ***[nm]***	$V_{nc\text{-}Si}$	$V_{a\text{-}Si}$
2 nm	0.23	0.09	-	0.02	0.21
3 nm	0.31	0.41	4.2 ±0.3	0.13	0.18
4 nm	0.36	0.6	4.5 ±1.0	0.22	0.14
B	0	-	-	-	-

PL spectra of these samples were acquired using two excitation energies $h\nu_{exc}$, 1.96 eV and 2.41 eV, as these lie above and below the Tauc gap [8, 88, 89] of film B (2.12 eV [165]), and it is hence thought that 1.96 eV photons only excite excitons in the Si nanoclusters whereas 2.41 eV photons may also excite excitons in the SiC matrix. The resulting spectra are shown in Figure 4.4(a)-(d). Intensities in panels (a) and (b) are directly comparable as the spectra were acquired under identical conditions, as are the ones in (c) and (d). All four panels are comparable to within a factor of two. Spectra were corrected for the different photon fluxes of the 1.96 eV and 2.41 eV excitation beams but not for the differing absorption at those photon energies.

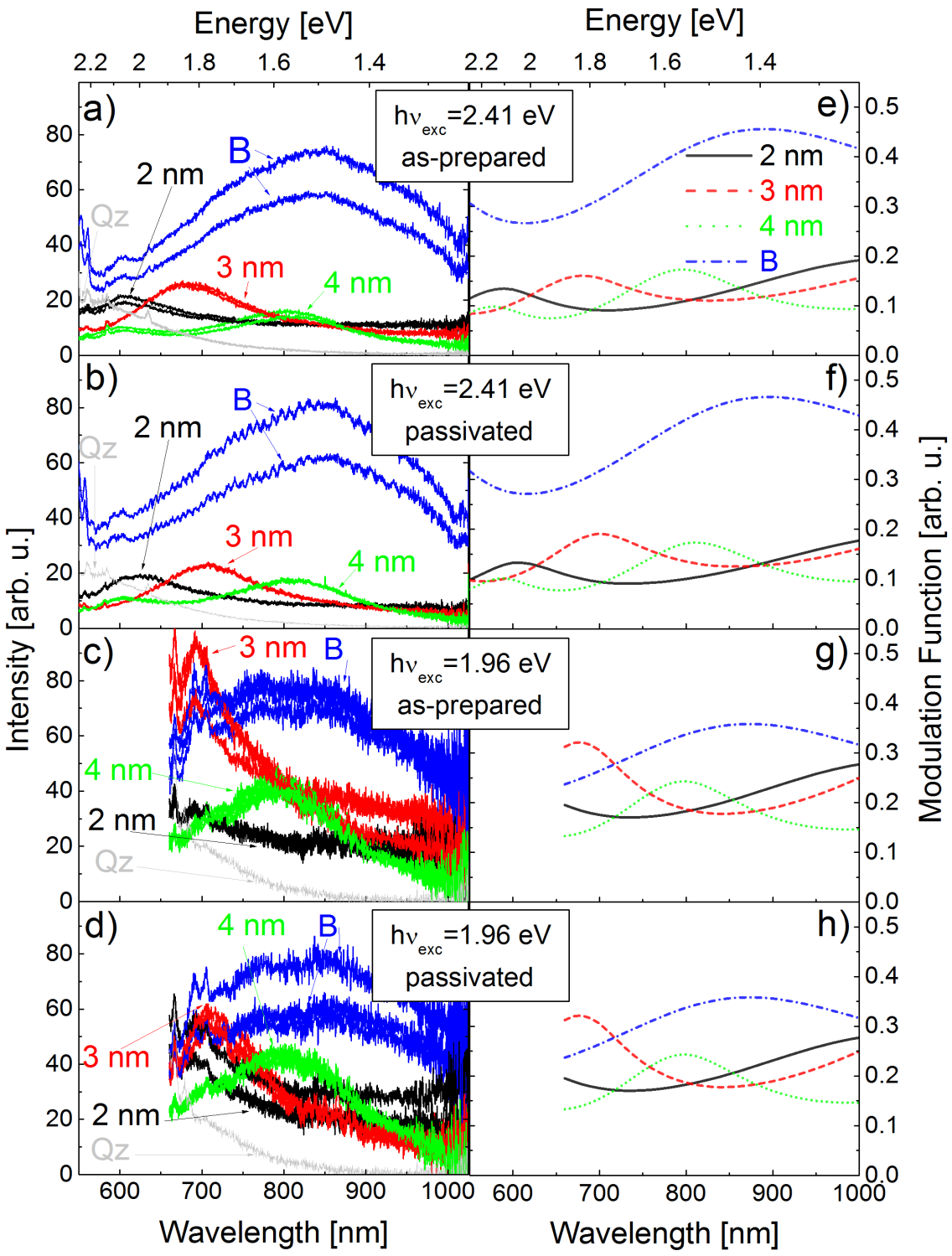

Figure 4.4. Photoluminescence spectra ((a)-(d)) and modulation functions ((e)-(h), see text for details) of 2, 3, 4 nm and B samples. (a),(e) 2.41 eV excitation, as-prepared; (b),(f) 2.41 eV excitation, passivated; (c),(g) 1.96 eV excitation, as-prepared; (d),(h) 1.96 eV excitation, passivated. "Qz" denotes the spectra of a bare quartz substrate measured under the same conditions. Passivation was by RPHP.

The PL peak position of the multilayers shifts significantly between samples: a blueshift of ~100 nm per nm of a-$Si_{0.85}C_{0.15}$:H sublayer thickness is observed in Figure 4.4(a),(b). The spectra excited with hv_{exc}=1.96 eV and 2.41 eV are very similar, suggesting that the excess Si is the source of the luminescence. Both form and intensity of PL do not vary with hydrogen passivation (RPHP), indicating that dangling bonds are neither the source of luminescence nor the dominant source of non-radiative recombination. It is tempting to conclude from these observations that PL originates from Si nanoclusters whose size is controlled by the a-$Si_{0.85}C_{0.15}$:H sublayer thickness resulting in Si quantum dots with a size-dependent bandgap [103, 170], in line with what is typically observed for Si NC/SiO_2 [11, 19].

However, several results are inconsistent with this interpretation. For one, the emission of film B, which contains no Si NCs, is much stronger than that of the films with Si NCs for hv_{exc}=2.41 eV, and is still present for hv_{exc}=1.96 eV even though that photon energy is below the Tauc gap of film B. Furthermore, it was noted previously that the a-$Si_{0.85}C_{0.15}$:H sublayer thickness did not effectively control Si nanocluster size, but rather led to three nanostructures that differed primarily in $X_{c,Si}$, and in the degree of ordering of the Si nanoclusters.

4.2.1 Correcting for Fabry-Pérot Interference

In PL studies of Si NC/SiO_2 [171-173] and Si NC/Si_3N_4 [174, 175] it had previously been found that optical interference effects within the Si NC films can have an impact on the measured PL spectrum, shifting the peak position by as much as 50 nm. In order to check whether such effects distort the spectra in Figure 4.4, Sergey Dyakov from Trinity College Dublin used input data on the refractive indices and thicknesses of the 2, 3, 4 nm and B films provided by CNR to calculate a modulation function $M(\lambda)$ for each sample. This function defines how a sample modulates its own PL, and is roughly equivalent to the product of the in-coupling efficiency for the laser wavelength and the out-coupling efficiency for the

luminescence as a function of wavelength. It is calculated by simulating the PL measurement under the assumption that the films contain randomly distributed luminescent dipoles that emit uniformly at all wavelengths. Details on the method can be found in Refs. [165, 176-179], while details on the inputs for these samples can be found in Ref. [180].

The modulation functions corresponding to the spectra in each of the panels (a)-(d) in Figure 4.4 are given in panels (e)-(h). The modulations functions are incredibly similar to the measured PL spectra even though they assume wavelength-independent emission within the samples. This means that the forms of the PL spectra in Figure 4.4(a)-(d) cannot be attributed to the actual emission processes inside the samples – in particular, not to emission from size-controlled quantum-confined nanoclusters – but are instead dominated by the Fabry-Pérot interference that the PL experiences once it has been emitted within the samples.

Fortunately, knowledge of $M(\lambda)$ permits a calculation of the spectrum actually emitted within a sample. $M(\lambda)$ was a simulation of the measured PL, $I_{meas}(\lambda)$, assuming the spectrum emitted within the sample, $I_{internal}(\lambda)$=1 at all wavelengths. Mathematically,

$$I_{meas}(\lambda) = I_{internal}(\lambda)M(\lambda), \tag{4.1}$$

so $I_{internal}(\lambda)$ can be calculated since $I_{meas}(\lambda)$ and $M(\lambda)$ are known. Since Figure 4.4 showed that the measured spectra and the modulation functions are essentially independent of hv_{exc} and passivation, this is only done for the spectra in Figure 4.4(a). The results are shown in Figure 4.5(a). In order to check that these are indeed correct $I_{internal}(\lambda)$ spectra that are not affected by errors in $M(\lambda)$, the input thicknesses for $M(\lambda)$ were varied ±3 nm and $I_{internal}(\lambda)$ recalculated in each case. Since interference depends on the product of refractive index n and film thickness, and absorption depends on the product of extinction coefficient k and film thickness, this procedure also accounts for 1-2% errors in n and k inasmuch as they affect interference and absorption. Only errors in the magnitude of reflection at a given interface,

which depends on the refractive index difference across it, are unaccounted for. The resulting distributions of $I_{internal}(\lambda)$ are shown in Figure 4.5(b). It can be seen that the calculation is relatively robust, though a few subtle features such as the peak shift between the 2 nm and 3 nm spectra in Figure 4.5(a), and the two distinct peaks of the 4 nm spectrum, should not be attributed to $I_{internal}(\lambda)$.

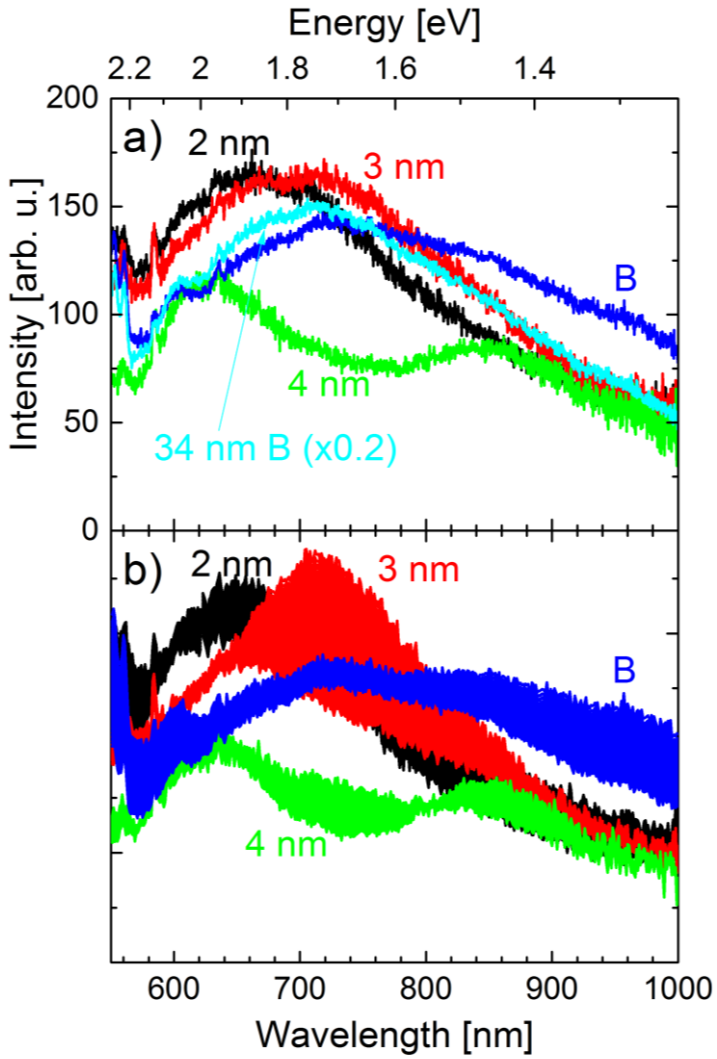

Figure 4.5. (a) Corrected PL spectra $I_{internal}(\lambda)$ of the as-prepared samples under 2.41 eV excitation extracted by dividing the measured PL by $M(\lambda)$. The resulting spectra are all quite similar. The clear peak shifts from Figure 4.4(a) are gone; these arose solely from Fabry-Pérot interference. (b) as (a), but with a variation of the film thicknesses entering the calculation of $M(\lambda)$ by ±3 nm in order to demonstrate the robustness of the calculation.

As a second control experiment, a 34 nm thick film B was prepared. Measured PL spectra $I_{meas}(\lambda)$ of both the 174 nm and 34 nm thick film B are shown in Figure 4.6(a), while

Figure 4.6(b) shows the corrected spectra $I_{internal}(\lambda)$ of both films, as well as $M(\lambda)$ in the inset. Figure 4.6(a) also shows the spectrum of an epitaxial 3C-SiC film that will be discussed later. The 34 nm film is thin enough that one would not expect significant Fabry-Pérot interference effects to occur (for this to be the case, twice the film thickness t must be at least half the wavelength, that is $t>\lambda/4n$), and indeed its $M(\lambda)$ in the inset of Figure 4.6(b) shows no oscillations, it merely rises slightly towards higher wavelengths as the reabsorption of PL decreases.

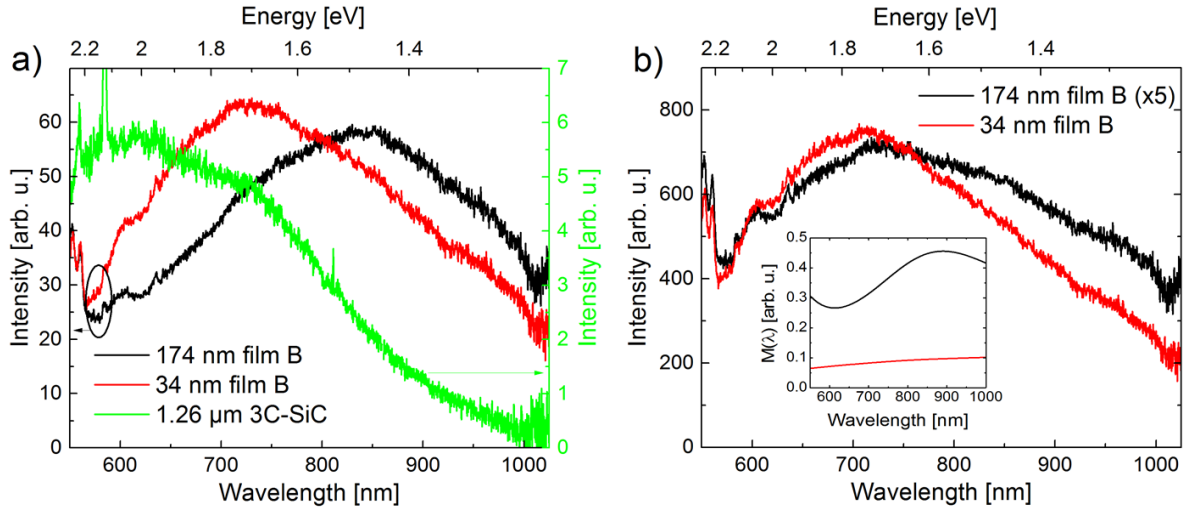

Figure 4.6. (a) Measured PL spectra of 174 nm and 34 nm thick B films (black and red, left axis), and a 1.26 µm thick 3C-SiC film grown epitaxially on Si (green, right axis). (b) Corrected spectra of 174 nm and 34 nm thick B films. The spectrum of the 174 nm film B is increased 5× for clarity. Inset: $M(\lambda)$ of the two B films.

$M(\lambda)$ of the thin B film is much lower than $M(\lambda)$ of the thick film due to the lower absorption in the thin film. Since the measured spectra in Figure 4.6(a) are of similar intensity, this leads to a difference in corrected intensities in Figure 4.6(b) of ~5×, which is roughly equivalent to the difference in film thickness. The origin of this difference in corrected PL intensity will be discussed later. Figure 4.6(a) and (b) show that the measured spectra differ significantly, while division of both spectra by $M(\lambda)$ yields corrected spectra that have very similar shapes. This further validates the method. The corrected spectrum of the 34 nm film B is also given in Figure 4.5(a), where it is reduced 5× for clarity.

4.2.2 Origin of PL

Having observed and corrected for Fabry-Pérot interference effects in the measured PL spectra in the previous section, the corrected spectra in Figure 4.5(a) can now be analysed. The luminescence cannot be related to band-to-band recombination in the SiC as 1.96 eV photons cannot excite these transitions, and neither can it be due to, or limited by, dangling bonds, as one would otherwise see an effect of hydrogen passivation (that the passivation process has any effect at all on these particular samples is confirmed in Sec. 5.2).

Emission must therefore occur either in Si nanoclusters, or at non-paramagnetic defects that are not detected by the electron spin resonance measurement described in Sec. 5.1.2, while non-radiative recombination must also proceed primarily via non-paramagnetic defects. To get an idea of the non-radiative recombination rate in these films, the passivated 3 nm film was measured together with a Si NC/SiO_2 sample borrowed from IMTEK and known to have a luminescence quantum yield (QY) of ∼0.01 (sample “5 nm-Ar” in Ref. [86]). The measured spectra of both are shown in Figure 4.7. The graph also shows substrate effects that will be discussed later. It can be seen that the PL of Si NC/SiC, as exemplified by the passivated 3 nm film on quartz, is orders of magnitude weaker than that of Si NC/SiO_2, and is in fact on the order of the PL of a bare quartz substrate. The integrated PL intensity is 2×10^4 times lower. Since Si NC/SiC is more absorptive than Si NC/SiO_2, this gives an upper limit on the QY of the passivated 3 nm film of 5×10^{-7}, and indicates that the density of non-paramagnetic defects must be substantial as it is sufficient to both effectively quench PL and make recombination via dangling bonds negligible in comparison.

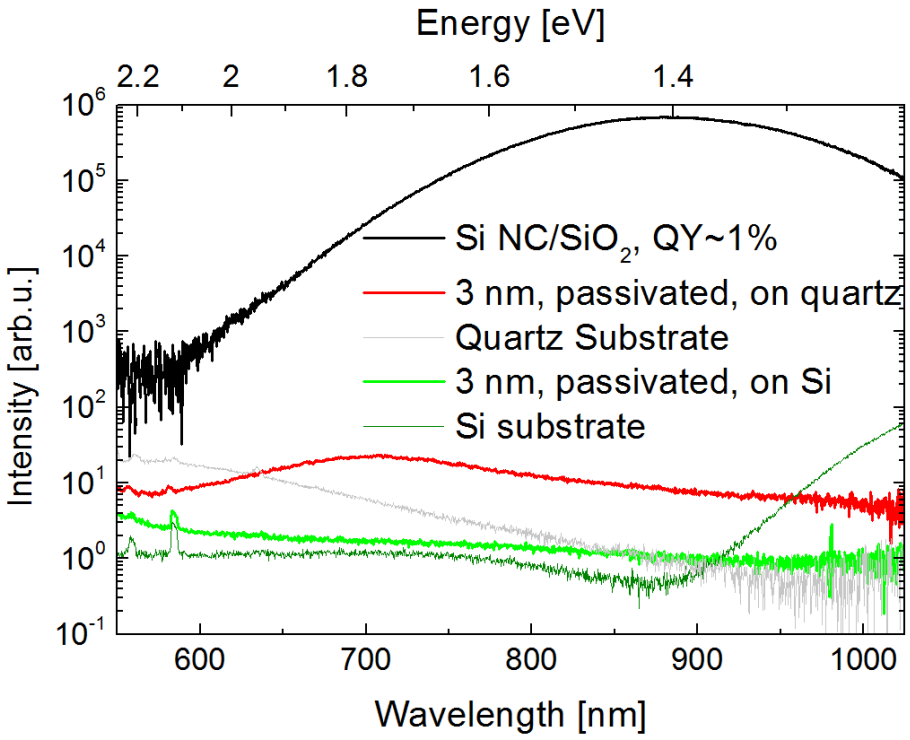

Figure 4.7. Measured PL of a Si NC/SiO_2 sample with known luminescence quantum yield (QY), and of the hydrogen-passivated 3 nm film on quartz and Si substrate as well as of the substrates themselves. The PL of Si NC/SiC is much weaker than that of Si NC/SiO_2 and is in fact on the order of the substrate PL.

Figure 4.5(a) shows that the PL that is emitted is very similar for the 2 nm, 3 nm, and B films, demonstrating the importance of having corrected for Fabry-Pérot interference. As the PL is also on the order of that measured on a bare quartz substrate, and as the PL intensity from films B was almost independent of thickness, it was initially thought that merely quartz PL might have been measured. However, a significant contribution of quartz luminescence to the measured PL of the 2, 3, and 4 nm films is unlikely since $I_{meas,quartz}(\lambda) \times T_{sample}(\lambda_{laser}) \times T_{sample}(\lambda)$, where $T(\lambda)$ is the sample transmission at wavelength λ and λ_{laser} refers to either of the excitation wavelengths used, is much lower than $I_{meas,sample}(\lambda)$ of these films. Furthermore, it was not possible to explain both the intensity and shape of the observed spectra with modulation functions that Sergey Dyakov calculated under the assumption that the emitting dipoles are located in the quartz. Empty channel spectra were negligible.

Having established that PL originates from the films and that the PL of most films resembles that of film B which consists entirely of nanocrystalline and amorphous SiC, a comparison to monocrystalline SiC was thought helpful to better understand its origin. Figure 4.6(a) shows the PL of a 1.26 µm thick 3C-SiC film epitaxially grown on a Si substrate. It is significantly weaker than that of the B films but that may be a substrate effect that will be discussed later. The reflectance of the 3C-SiC film was measured and found to oscillate weakly with a period of 60-120 nm in the 550-1000 nm spectral range. Since no similar oscillations are found in its PL spectrum the PL may be considered to be free of interference and can therefore be directly compared to the corrected spectra of the B films.

Even the monocrystalline 3C-SiC film exhibits substantial sub-bandgap emission (E_g=2.39 eV [30]), with a shoulder at 1.7 eV that corresponds to the PL peak position of the B films. 3C-SiC is known to exhibit luminescence at 1.9 eV that originates from extended defects [181], but luminescence in the 1.5-1.9 eV range is not well-understood and is attributed simply to extended or point defects [181]. It appears therefore that the most plausible explanation for the broadband luminescence of both the 34 nm and 174 nm thick B film is a wide distribution of defect states that are more abundant in these nanocrystalline films than in epitaxial 3C-SiC. Given the invariance of measured emission intensity with thickness these may be surface or interface states. These states cannot be populated solely by carriers captured from extended states since they also luminesce under sub-bandgap excitation and must hence themselves absorb light. Empirically this is conceivable as the B films do exhibit finite absorption at 1.96 eV (α(1.96 eV)≈4000 cm^{-1} [165]).

The same states are likely to contribute to the PL of the 2, 3, and 4 nm samples; in fact Figure 4.5(a) suggests that the PL of the 2 and 3 nm films is nothing other than this SiC defect PL. However, correction of the measured spectra involves a normalisation by absorption, and as only about half the absorption in the 2, 3, and 4 nm films occurs in the SiC phases (which can be inferred from the fact that these films have roughly twice the absorptivity of film B

[165]) the corrected PL of these films should, all other things being equal, only be half as intense as that of film B. Similar arguments apply if the luminescent SiC defects are surface or interface defects – again, the luminescent defects account for a smaller proportion of the absorption than in film B (which is also thinner than the 2, 3, and 4 nm films), and again, since the corrected spectra are normalised by absorption, the corrected PL of the 2, 3, and 4 nm films should be less intense than that of film B. In so arguing it was assumed that excitons remain where they were excited, and it will be argued in Chapter 5 that band offsets between Si and SiC are sufficient to confine electrons in Si nanoclusters to Si nanoclusters.

The corrected PL of the 4 nm film is about half as intense as that of film B, but that of the 2 and 3 nm films is not. The following explanations for the corrected PL intensity of these two films are possible:

- Si nanoclusters increase the concentration of luminescent defects or decrease the concentration of non-radiative recombination sites in the SiC.
- Photogenerated carriers can tunnel from Si nanoclusters to luminescent defects in the SiC. This would be in agreement with the hopping mechanism described in Chapter 5.
- Some luminescence originates from Si nanoclusters. In this case, it suggests stronger emission from a-Si nanoclusters than Si NCs as the 4 nm sample has weaker PL, and a blueshift of the bandgap as compared to c-Si (E_g=1.12 eV [6]).

To summarise, the PL of film B arises from defects similar to those in a 3C-SiC epilayer that absorb and emit light and cannot be passivated by hydrogen. The PL of the 2 and 3 nm films has the same form as that of film B, but in order to wholly attribute it to luminescent SiC defects, an increase in this defect density, a decrease in non-radiative recombination site density, or charge transfer from the nanoclusters to the defects via hopping, must be assumed. Otherwise, some PL must arise from the Si nanoclusters, primarily a-Si nanoclusters, which are then seen to exhibit a greater bandgap than bulk c-Si. The luminescence quantum yield of all films is very low and limited by non-radiative recombination at non-paramagnetic defects.

4.2.3 Lessons for PL Measurements

The previous sections showed that Fabry-Pérot interference can significantly distort the internally emitted PL spectra $I_{internal}(\lambda)$. This makes it rather difficult to interpret $I_{meas}(\lambda)$ spectra by themselves, but at the same time it is undesirable to rely on a calculation of $M(\lambda)$, which requires accurate knowledge of the complex refractive index and thickness of the film, for interpretation of every single measurement. Fortunately, it is found empirically that the forms of $M(\lambda)$ and the transmission curves $T(\lambda)$ are very similar (see Figure 4.8).

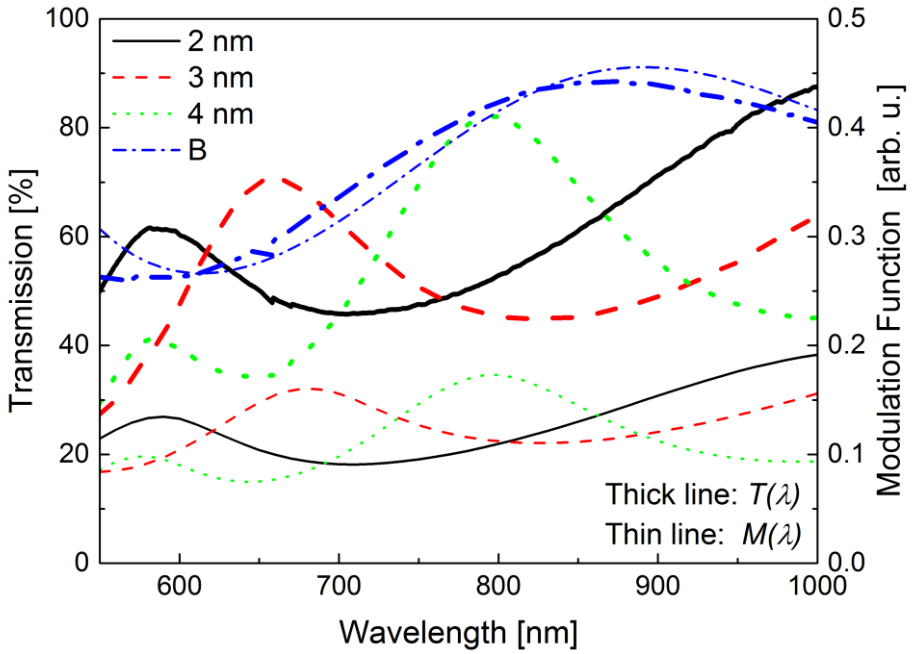

Figure 4.8. Comparison of transmission spectra (thick lines, left axis) and modulation functions (thin lines, right axis) of the 2, 3, 4 nm and B films. Both exhibit similar shapes, indicating that the shape of $T(\lambda)$ can be used as an estimate of the shape of $M(\lambda)$.

This can be understood by considering that $T(\lambda)=1-A(\lambda)-R(\lambda)$, where $A(\lambda)$ and $R(\lambda)$ are the absorption and reflection as a function of wavelength, respectively. The in-coupling of laser illumination into the film and out-coupling of luminescence both affect $M(\lambda)$, but as illumination is monochromatic, it is only out-coupling that affects the wavelength-dependence of $M(\lambda)$. Out-coupling is reduced by re-absorption of PL in the film that follows $A(\lambda)$, and by reflection back into the film which while not being equivalent to $R(\lambda)$ does exhibit the same

Fabry-Pérot interference fringes, justifying the similarity of $M(\lambda)$ and $T(\lambda)$. Since the entire beam in a transmission measurement experiences the same interference conditions while those for PL, which is emitted throughout the depth of the film, vary somewhat, fringes of lower amplitude are expected for $M(\lambda)$ than $T(\lambda)$, in agreement with what is observed in Figure 4.8. Thus, if the shapes of $T(\lambda)$ and $I_{meas}(\lambda)$ are similar, interference effects are most likely present. Since $T(\lambda)$ overestimates the contribution of $M(\lambda)$ to the shape of $I_{meas}(\lambda)$, it can be worthwhile to divide $I_{meas}(\lambda)$ by $T(\lambda)$. This is an overcorrection that may eliminate spectral features that were real, or cause new features to appear, but if $I_{meas}(\lambda)$ and $I_{meas}(\lambda)/T(\lambda)$ do not exhibit significantly different shapes interference effects in $I_{meas}(\lambda)$ are negligible.

It is also worth noting that the position of interference fringes depends on the optical thickness nt of the film. This had a particularly strong effect on this experiment because both n and t increased with a-$Si_{0.85}C_{0.15}$:H thickness. The effect on the findings in Sec. 4.1 is expected to be much weaker because it was always the PL spectra of one given film under different heat treatments that were compared, and film shrinkage upon annealing is typically complete at 900°C [15]. To illustrate this, Figure 4.9(a) shows the measured PL spectra $I_{meas}(\lambda)$ and transmission curves $T(\lambda)$ of the ML2 samples studied in Sec. 4.1.1, and Figure 4.9(b) shows $I_{meas}(\lambda)/T(\lambda)$. Shifts in interference fringes of $T(\lambda)$ for anneals at 900°C and above are much smaller than for the 2, 3, 4 nm and B films in Figure 4.8, which is reflected in Figure 4.9(b) where the shape of the spectra is not much changed by division by $T(\lambda)$ as compared to Figure 4.9(a). The transmission of the as-deposited and 600°C-annealed films does differ significantly, but the PL of these films falls off sufficiently sharply so as not to be strongly shifted by the interference (over)correction.

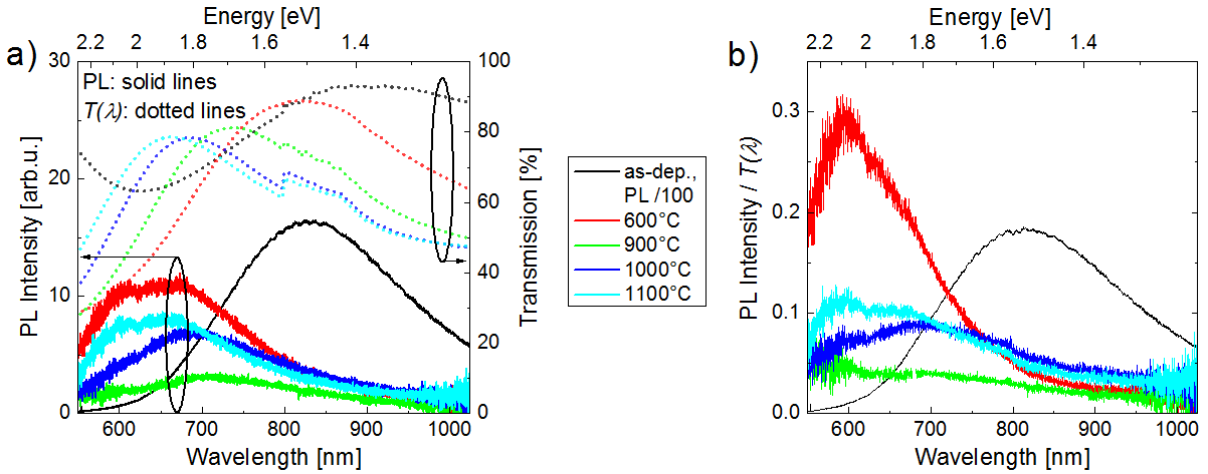

Figure 4.9. (a) Comparison of $I_{meas}(\lambda)$ and $T(\lambda)$ of the ML2 samples studied in Sec. 4.1.1. $I_{meas}(\lambda)$ of the as-deposited sample is reduced 100× for clarity. (b) $I_{meas}(\lambda)/T(\lambda)$ of the ML2 samples studied in Sec. 4.1.1. Both figures show that the differences in Fabry-Pérot interference conditions do not have as large an effect on the PL of these samples as was observed for the 2, 3, 4 nm and B films.

4.2.4 Substrate Effects

Interference effects in PL measurements can be reduced by depositing the film to be studied on a refractive index-matched substrate – if there is no reflection at the film / substrate interface, no interference takes place. This is confirmed by the modulation functions for the 2, 3, 4 nm and B films on SiO_2 and Si substrates shown in Figure 4.10 (all calculated by Sergey Dyakov).

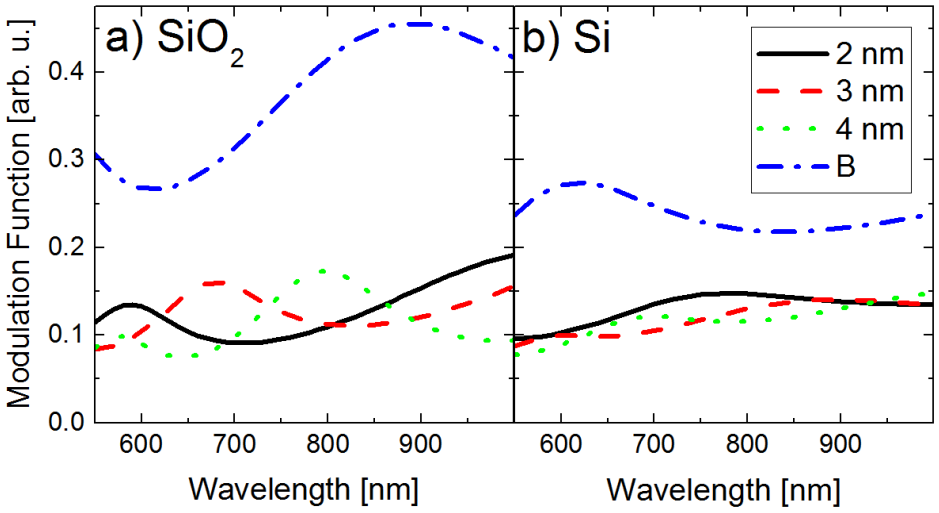

Figure 4.10. $M(\lambda)$ of 2, 3, 4 nm and B films on SiO_2 (a) and Si substrates (b).

In the case of Si substrates, whose refractive index is closer to that of the films, oscillations are reduced, as is the overall magnitude of *M(λ)* due to the fact that less of the light emitted in the direction of the substrate is reflected back towards the detector.

In order to observe this effect in practice, PL of the 2, 3, 4 nm and B films prepared on Si substrates was measured under the same conditions as the spectra in Figure 4.4. The spectra acquired on as-prepared films are shown in Figure 4.11 – as in the case of films on quartz, there was no significant change upon hydrogen passivation.

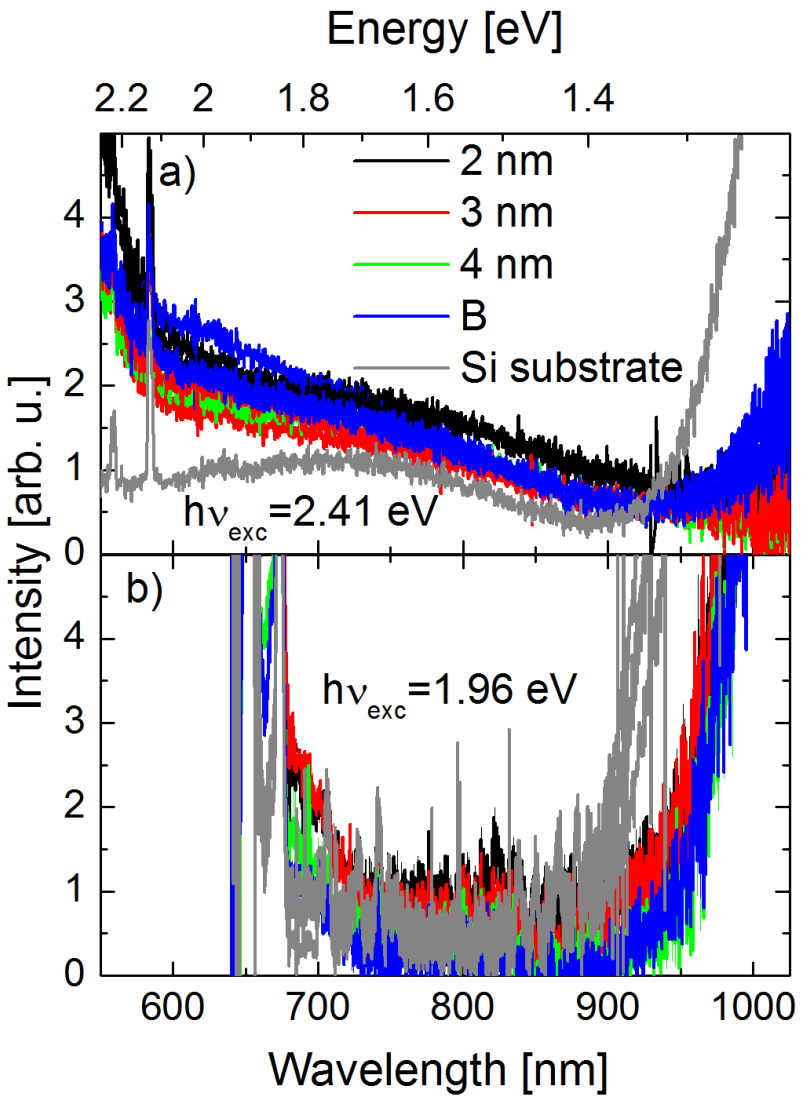

Figure 4.11. Measured PL spectra of the 2, 3, 4 nm and B films on Si substrate under excitation by 2.41 eV (a) and 1.96 eV (b) photons. The interference fringes seen in the PL of films on quartz are gone but the PL signal is also much weaker, and indiscernible from stray light in the case of 1.96 eV excitation.

No Fabry-Pérot interference fringes are present, which could indicate that the switch to a more refractive index-matched substrate worked, but at the same time the PL intensity is much weaker. The units in Figure 4.11(a),(b) are comparable to Figure 4.4(a)-(d) to within a factor of two, indicating that the PL of films on Si substrates is over an order of magnitude weaker than on quartz, and on the order of the PL signal from a Si substrate (measured on the rear side of the samples). This can also be discerned from Figure 4.7 which shows the PL of the same film on Si and quartz, as well as that of the two substrates. One might again argue that it is the scaled substrate PL $I_{meas,Si}(\lambda)\times T_{sample}(\lambda_{laser})\times T_{sample}(\lambda)$, rather than $I_{meas,Si}(\lambda)$, that ought to be compared to $I_{meas}(\lambda)$ of the samples. This would be true for the Si band-to-band PL that dominates all the spectra for λ>900 nm. The "substrate" PL at λ<900 nm however can, with reference to Figure 3.7(b) in Sec. 3.2.6, be attributed to stray light, and ought hence not to be scaled by the film transmission.

Figure 4.11(b) therefore shows that under 1.96 eV excitation, no PL clearly exceeding the stray light level is measured on any of the samples. Under 2.41 eV excitation there does seem to be weak PL from the film itself that increases towards shorter wavelengths, but it is too weak and featureless to draw conclusions about differences between samples. What is instead worth focusing on is just how weak the PL is, since it should not be so strongly decreased from purely optical considerations. In Ref. [165] it was shown that the decrease in PL expected due to weaker reflection at the film / substrate interface is <1.7×, which can be understood by considering that the main factor, lack of reflection of PL at the film / substrate interface in the direction of the detector, cannot decrease measured PL by more than a factor of two since half the PL is emitted in the other direction and never interacts with the film / substrate interface. This strong weakening of PL when films are on Si is also seen for films prepared at ISE, and there must therefore be reasons intrinsic to the films themselves as to why the PL is so weak.

It was noted initially that film thicknesses on Si and quartz differ within one deposition, suggesting differences in plasma chemistry. However, there are also differences in plasma chemistry for the 2, 3, 4 nm and B films on a given substrate, and yet the PL intensity of all four films is roughly the same on a given substrate. It is conceivable that the mismatch in thermal expansion coefficient between film and substrate causes different amounts of stress upon cooling of films on Si and quartz from the annealing temperature of 1100°C, but the expansion coefficients are such as to put films on quartz under tension, and films on Si under compression, and it is not apparent why compressive stress should lead to the formation of more non-radiative recombination sites than tensile stress. However, it may lead to the formation of fewer luminescent defects which, if these are the sole source of PL, would cause strong reduction of PL without an increase in the already high non-radiative recombination site density.

Another possible explanation is that electron-hole pairs generated in the Si NC/SiC films are able to diffuse to the Si wafer substrate and recombine there instead. In this case, the PL from electron-hole pairs generated in the films would be indiscernible from the strong substrate PL that is observed anyway. Such PL quenching due to charge transfer is well-known from organic solar cell materials, where it is used to measure the quality of charge transfer to hole or electron transport layers [182]. However, a high carrier diffusivity leading to a minority carrier diffusion length L_{diff} several times greater than the film thickness would be required. Given the low minority carrier lifetimes of ~100 ns found for epitaxial 3C-SiC films [141, 142] this means that assuming L_{diff} >1 µm, a mobility μ>1 $cm^2V^{-1}s^{-1}$ would be required even if the lifetime in the films studied here is the same. Whether this is realistic will be discussed in Chapter 5.

4.3 Summary

Overall the photoluminescence results on Si NC/SiC differ strongly from what was expected based on the Si NC/SiO_2 system, and do not permit a clear picture of quantum confinement and size- or crystallinity-dependent bandgaps and defect densities to be extracted. Nevertheless some trends have been identified:

1. The strong luminescence of as-deposited a-Si_xC_{1-x}:H bulk films or multilayers is quenched upon annealing and cannot be recovered by hydrogen passivation.
2. The PL of rapidly annealed (RTA) films is even weaker than that of standard films, but can be brought back to the same level by a 900°C post-anneal for 1 h, indicating that it is not defects that can be eliminated by the post-anneal that luminesce.
3. The PL of annealed multilayers with differing a-$Si_{0.85}C_{0.15}$:H thickness showed that measured PL can be strongly affected by Fabry-Pérot interference effects, causing peak shifts of up to 200 nm in measured spectra that are unrelated to the spectra actually emitted within the films.
4. The effect of Fabry-Pérot interference can be judged by comparing measured PL to transmission. The ratio of both can be compared to the measured PL to determine whether a correction for interference might significantly alter the spectra.
5. The PL of Si NC/SiC films is very weak. An upper limit on the luminescence quantum yield of 5×10^{-7} has been estimated, indicating rapid non-radiative recombination. The invariance with hydrogen passivation suggests non-paramagnetic defects are responsible.
6. The corrected PL spectra of annealed multilayers with differing a-$Si_{0.85}C_{0.15}$:H thickness are all very similar to that of an annealed a-SiC:H film, and independent of passivation and excitation energy (1.96 eV and 2.41 eV), suggesting that a non-paramagnetic defect in the SiC which can be populated directly by absorption, rather

than relying on carriers captured from extended states, is responsible for most of the luminescence.

7. Films prepared on quartz luminesce much more strongly than films on Si. Luminescence of the substrate or PL out-coupling effects are insufficient to account for this, indicating that the substrate directly affects recombination processes in the films.

The results as a whole are somewhat discouraging since they highlight the difficulty in obtaining reliable PL spectra and extracting from them the Si nanocluster bandgap, leaving as the best explanation for both weak, and hydrogenation-independent PL, luminescence of non-paramagnetic defects that absorb sufficient light to luminesce, and a limitation of PL by a different species of non-paramagnetic defect that quenches luminescence. The results do not bode well for photovoltaic applications since weak PL is indicative of a low minority carrier lifetime. However, lifetime is not everything – that in Si NC/SiO_2 is in the μs range [52, 84], and yet the material does not yield good solar cells because transport is poor (see Sec. 2.3, 2.4). Good transport on the other hand decreases minority carrier lifetime for a given non-radiative recombination site density since photogenerated carriers have a greater chance of reaching a non-radiative recombination site before recombining radiatively, so depending on carrier transport the much weaker PL may still be acceptable. Carrier transport is studied in the next chapter.

5. Electronic Transport

Electronic transport is expected to be one of the strengths of the host matrix SiC due to its relatively small band offsets to Si NCs [51]. This chapter discusses the results of electronic transport measurements on two batches of samples prepared at ISE and CNR, respectively. The dominant transport mechanisms are elucidated by a process of elimination and the similarities and differences between transport in the two batches of samples are highlighted and correlated with the nanostructure. The results have been published in Ref. [183].

5.1 Transport in Nanocrystalline SiC With and Without Embedded Si NCs

As the previous chapter revealed that the properties of Si NCs embedded in SiC (Si NC/SiC) can be surprisingly insensitive to the nanostructure, and that engineering of the Si NC/SiC nanostructure does not always succeed in producing the targeted nanostructure, a comparatively simple sample set was chosen to study electronic transport. It involves a stoichiometric SiC film “C”, a Si-rich film “S”, and a multilayer “M”, where the parameters are chosen such that the average composition of M and S are the same so as to be able to judge whether M intermixes fully on annealing. Films ≤150 nm thick had to be prepared to avoid cracks (see Sec. 3.1.1, 3.3.3). Samples were annealed at 1050°C under Ar or N_2 for 1 h. Unpassivated, 15 min-passivated, and 45 min-passivated films were prepared (RPHP, 450°C), and two nominally identical batches of films S and C were prepared to monitor process fluctuations. The parameters are summarised in Table 5.1.

Table 5.1. Parameters of samples used to study transport in nanocrystalline SiC with and without Si NCs. The nanostructural parameters listed are the excess Si volume fraction V_{Si}, Si crystallinity $X_{c,Si}$, and Si NC size $d_{Si\,NC}$, as well as the derived quantity $N_{Si\,NC}=V_{Si}/(\pi d_{Si\,NC}^3/6)$, the volume density of Si NCs. V_{Si} and $N_{Si\,NC}$ are upper bounds since full de-mixing is assumed; $N_{Si\,NC}$ further assumes spherical NCs.

Film	***Deposition Parameters***[a]	V_{Si}	$X_{c,Si}$	$d_{Si\,NC}$ ***[nm]***	$N_{Si\,NC}$ ***[cm^{-3}]***
M	8x [5 nm a-$Si_{0.77}C_{0.23}$:H / 5 nm a-SiC:H]	0.35 (0.69[b])	0.61	~3 nm	$\sim 2\times10^{19}$ ($\sim 3\times10^{19}$[,b])
S	82 nm a-$Si_{0.63}C_{0.37}$:H	0.4	0.67	~3 nm	$\sim 2\times10^{19}$
C	80 nm a-SiC:H	0	-	-	-

[a]film thicknesses are after annealing, and are estimated from as-deposited film thicknesses and known shrinkage rates.
[b]refers to the Si-rich sublayers only.

M, S, and C are expected to consist of nanocrystalline SiC (nc-SiC) with ordered, disordered, and no Si NCs, respectively. The presence of nc-SiC in all films is confirmed by Fourier-transform infrared (FTIR) spectroscopy and grazing incidence x-ray diffraction (GIXRD), the latter yielding a Scherrer grain size [169] of 3.5-5.0 nm for all films. Such grain sizes have been shown to be in good agreement with values from transmission electron microscopy (TEM) images [166, 184]. FTIR and spectrophotometry also show that there is no significant difference between films annealed in Ar and in N_2. Nevertheless, all measurements except for the dopant experiment in Sec. 5.1.4 were carried out on samples annealed in Ar. Raman spectra acquired at ISE and analysed at UB confirmed that there were no Si nanoclusters in film C, and fitting of the spectra of films M and S gave the values of Si crystallinity $X_{c,Si}$ and Si NC size $d_{Si\,NC}$ listed in Table 5.1. The values of $d_{Si\,NC}$ were calculated from the width of the Si NC phonon mode, and should be treated as approximate since this is also affected by instrumental resolution and stress. However, the value is in good agreement with expectations based on a prior annealing temperature study of film S. The values of $X_{c,Si}$ are lower limits on the fractions of Si nanoclusters that are crystalline since a Si NC can also have an amorphous shell which contributes to the a-Si Raman peaks even though the NC itself is crystalline [52].

The excess Si volume fraction V_{Si}, calculated using the formalism in the appendix of Ref. [166], can therefore be considered to be present primarily in the form of Si NCs. The values of V_{Si} for both films exceed the percolation threshold for spheres of 29% [185]; this will become important later. All films are contacted with tin-doped indium oxide (ITO) contacts arranged in a TLM structure (see Sec. 3.1.5).

5.1.1 Room-Temperature Conductivity

The room-temperature conductivities of both nominally identical batches of films (denoted by open and full symbols, respectively) are shown in Figure 5.1 as a function of hydrogen passivation (RPHP) time.

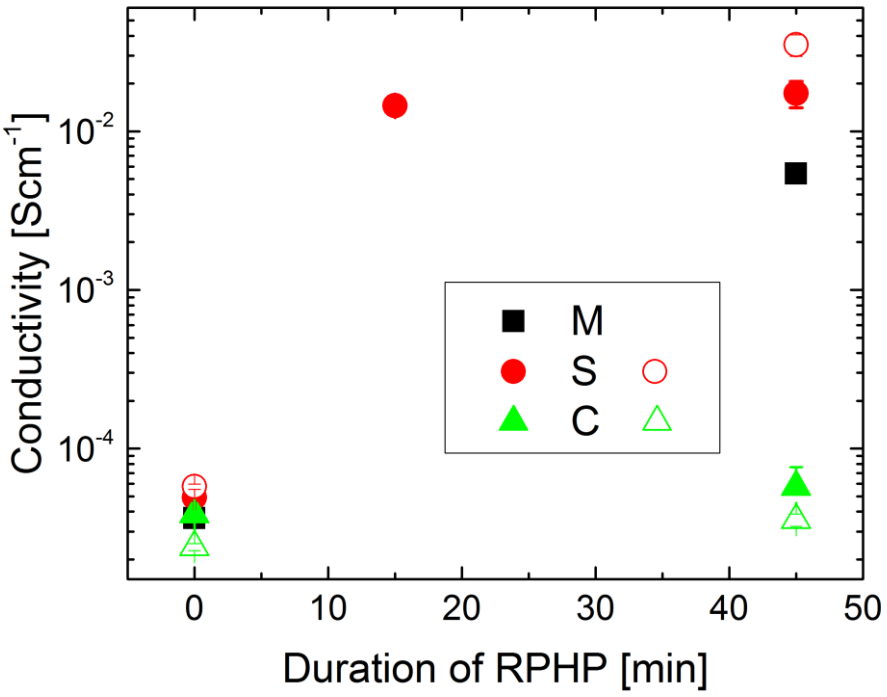

Figure 5.1. Conductivity of films M, S, and C annealed under Ar as a function of RPHP time. As-prepared films are plotted at an RPHP time of 0 min. Full and open symbols represent films from two different, nominally identical batches.

The conductivities of the as-prepared films are all similar and lie in the (2-6)×10^{-5} Scm^{-1} range. Upon passivation, the conductivities of films C increase only marginally whereas those

of films M and S increase 2-3 orders of magnitude, with the most conductive film S (annealed in N_2, not plotted) reaching a conductivity >0.1 Scm^{-1}. The increase in conductivity of film S upon passivation saturates after 15 min, implying a saturation in hydrogen uptake which in turn can be used to estimate a hydrogen diffusivity $\geq 2\times10^{-14}$ cm^2s^{-1} in film S assuming saturation requires a diffusion length exceeding twice the film thickness. That film M does not reach quite the same conductivity as S despite having similar V_{Si} and $d_{Si\,NC}$ hints at a difference in nanostructure, suggesting survival of the multilayer structure. As no evidence for saturation of the passivation process is obtained for films M and C, no conclusions on hydrogen diffusivity in these films may be drawn. Tsunoda *et al*. found that pulsed laser-crystallised Si could be made five orders of magnitude more conductive by treating with an oxygen plasma [186]; this was attributed to a reduction in dangling bond density and the same effect is suspected here.

5.1.2 Role of Hydrogen Passivation

Hydrogen can passivate dangling bonds that act as traps for free carriers, break open and passivate distorted bonds that act as shallow traps, or passivate dopant atoms, reducing the free carrier concentration [8]. In order to investigate the role of hydrogen in more detail, room-temperature electron spin resonance measurements were performed on as-prepared and 45 min-passivated films S and C in collaboration with Saskia Kühnhold (see Figure 5.2(a) and (b), respectively). Details on the method can be found in Appendix A: Other Characterisation Techniques.

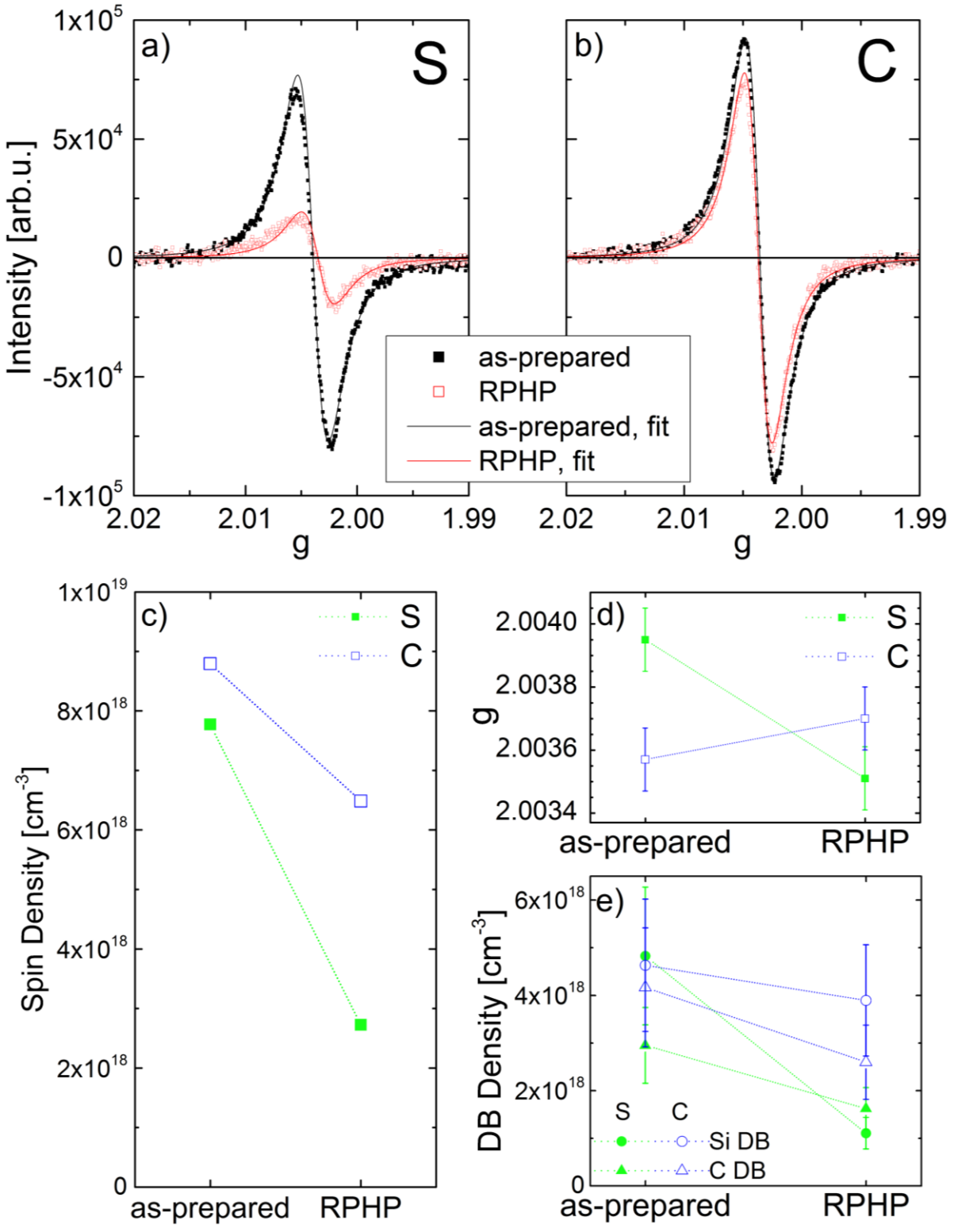

Figure 5.2. Differential ESR spectra of S (a) and C (b) films before and after 45 min passivation (RPHP). Each spectrum is fitted with a single Lorentzian band, and excellent fits are obtained. The associated spin density (c) and g-factor (d) are shown. Using the model from Ref. [187], the g-factor is used to determine the ratio of Si to C dangling bonds, from which the densities of Si and C dangling bonds for each sample are calculated (e). Lines in (c), (d), and (e) are guides to the eye.

A clear ESR resonance is observed in both films before and after passivation that must be related to a relatively deep state as shallow states are usually ionised at room temperature. The peak position, or g-factor, of the resonances is shown in Figure 5.2(d), while Figure 5.2(c) shows the absolute spin density calculated using a spin standard of comparable g-factor measured with the samples. A spin density of almost 10^{19} cm^{-3} is present in both as-prepared films. Upon passivation, the spin density in film S is reduced 3× and the g-factor also decreases, while the spin density of film C is reduced only 1.4× and the g-factor remains almost constant. The g-factor is usually a signature of the particular defect being measured but no single defect with a g-factor in the range of 2.0035-2.0040 was found in the literature on Si and SiC [188-191]. However, a study on sputtered a-Si_xC_{1-x} films where *x* was varied from 0 to 1 found that Si and C dangling bonds (DBs) do not yield separate ESR resonances, but merge into a single band [192] whose g-factor depends on composition *x*, and the ratio of the probabilities of formation of C DBs and Si DBs *r* (equal to the ratio of the concentration of C DBs to Si DBs for *x*=0.5), as

$$g(x,r) = \sum_{n=0}^{12}\left[\frac{(1-x)\bar{g}_{Si}(n)+rx\bar{g}_C(n)}{(1-x)+rx} C_n^{12} x^n (1-x)^{12-n}\right], \quad (5.1)$$

where $\bar{g}_i(n)$ is the g-factor for a DB on atom *i* that is surrounded by *n* C atoms and (12-*n*) Si atoms that can be found in Ref. [187]. At all *n*, $\bar{g}_{Si}(n) > \bar{g}_C(n)$, which means that a decrease in g generally indicates an increase in the proportion of C DBs. While films S and C were found to be largely crystalline, the g-factor, and the linewidth of 5 G, are in agreement with the mixed DB band observed in Ref. [192]. Moreover, films S and C may contain residual amorphous material, as well as a substantial proportion of grain boundary material that may be considered amorphous, and as such it is reasonable to apply the model to the data of films S and C. The values of *x* and $\bar{g}_i(n)$ are known, so Eq. 5.1 can be fitted to the experimental

g-factor to determine r provided $r \neq r(n)$. The concentrations $N_{i\text{-}DB}$ of dangling bonds on atom i can then be calculated from the total spin density N_{DB}:

$$N_{Si-DB} = \frac{(1-x)}{(1-x)+rx} N_{DB}, \tag{5.2}$$

$$N_{C-DB} = \frac{rx}{(1-x)+rx} N_{DB}. \tag{5.3}$$

Both quantities are plotted in Figure 5.2(e). In as-prepared films, $N_{C\text{-}DB}$ is higher for film C than film S, while $N_{Si\text{-}DB}$ is the same for both films. The former can be understood simply in terms of the film composition, while the latter suggests that film S contains fewer Si DBs per Si atom than film C, perhaps because Si NCs have fewer Si DBs than the SiC does. Nevertheless, a comparison of $N_{Si\text{-}DB}$ with $N_{Si\ NC}$ suggests that many NCs are likely to have a DB. $N_{Si\text{-}DB}$ of film C, and $N_{C\text{-}DB}$ of both films, all decrease by about the same factor upon passivation. $N_{Si\text{-}DB}$ of film S on the other hand decreases much more strongly. In fact, $N_{Si\text{-}DB}$ of film S is only ~0.3×, or less than (1-V_{Si})×, that of film C after passivation, which suggests that all Si DBs in and on Si NCs have been passivated and that only Si DBs in the SiC component of film S remain.

It is worth noting that ESR only detects singly occupied, i.e. neutral DBs (D^0). These act as traps for excess carriers, but unless an IV measurement injects additional carriers – which is ruled out as carrier injection typically leads to space-charge-limited current that is characterised by a non-linear dependence of current on contact spacing and/or voltage, neither of which is observed in films M, S, and C – the occupation of states will remain as it is during the ESR measurement. During IV and ESR measurements there are likely to be many DBs that are trapping carriers, but these are either doubly occupied and negatively charged if they trap an electron (D^-), or unoccupied and positively charged if they trap a hole (D^+). These

affect carrier concentration and, via Coulomb scattering, also mobility, but are not detected by ESR because ESR only measures unpaired spins. This means the absolute DB densities are likely to be significantly higher than the D^0 densities shown in Figure 5.2(c) and (e).

Whether the ratio between D^0 and total DB density remains the same after passivation depends on whether the equilibrium between the charge states is maintained. The activation energy for a change of DB charge state is the carrier de-trapping energy E_F-E_D, where E_D is the DB energy and E_F is the Fermi level. As E_D is typically at mid-gap, E_F-E_D<E_g/2. E_g can be approximated by the Tauc gap which is <2.0 eV for films M, C, and S, yielding E_F-E_D<1.0 eV. Given that the activation energy for hydrogen diffusion in Si NC/SiC was reported to be ~0.8 eV [156], it is reasonable to assume that re-equilibration of DB charge states is faster than the passivation process. Therefore, unless E_F changes significantly, the relative changes in D^0 given in Figure 5.2 reflect those in total DB population. Nevertheless, the total DB population and hence the total number of trapped carriers, or the total number of carriers released upon passivation, is unknown.

5.1.3 Conduction Mechanism

Conduction in Si NC/SiC could be controlled by a range of mechanisms. In this section, direct tunnelling, grain boundary effects, and transport via extended states, via tail states, and via bulk defects will be considered. Conduction dominated by the film surface or the film / substrate interface was already ruled out in Sec. 3.3.2.

5.1.3.1 Direct Tunnelling

Direct tunnelling of carriers between Si NCs is expected when the Si NCs are embedded in a matrix that strongly confines carriers and does not itself conduct, such as SiO_2 [106]. However, this typically leads to an exponential dependence on voltage [25, 26, 193], and no

dependence on temperature [6], whereas Ohmic but thermally activated transport is observed in films M, S, and C. Direct tunnelling between Si NCs is therefore ruled out as a transport mechanism.

5.1.3.2 Grain Boundary Effects

A material with grain sizes <5 nm necessarily has a lot of grain boundaries (GBs) that are generally more defective than the crystals themselves, leading to increased carrier trapping at GBs. Charge trapping at GBs of polycrystalline semiconductors, such as Si with a 25 µm grain size [194], or SiC with 100 nm grains [138, 195], results in band bending at GBs that impedes transport and leads to a complex non-linear dependence of current on voltage as the transport barriers are gradually lowered by the applied voltage [196]. This is at odds with the Ohmic IV curves observed here, which can be understood by considering that the grain size is much smaller than the width of any realistic depletion region. GB defects do trap carriers, but this does not cause band bending but pins E_F in the adjacent NCs. This only applies to band bending; band offsets, given by differences in electron affinity and bandgap between materials, persist even in nanostructures only 1-2 nm in size [197].

5.1.3.3 Bulk Conduction Mechanism

Having ruled out direct tunnelling, and surface-related and GB-mediated transport, some form of bulk transport mechanism must be active. Hopping transport between DBs can be ruled out as conductivity increases on passivation whereas DB population decreases, but beyond this observation Hall measurements and temperature-dependent IV (IVT) measurements are desirable to zero in on the transport mechanism.

Unfortunately, no meaningful Hall voltages were measured. Values exceeded the noise level, but the relatively high voltages measured in Hall configuration with no magnetic field, and the

variation of the detected Hall voltages with time, indicated that the measured Hall voltages arose not from a separation of electrons and holes by a magnetic field, but from a change in sheet resistance due to temperature fluctuations induced by the water-cooled electromagnet. This error could not be eliminated, even with thermally insulating sample holders. The preparation of more reliable contacts where the "Hall" voltage with no magnetic field is reduced, or Hall measurement with lock-in detection that eliminates the slow temperature-related component, could both provide solutions, but as Hall measurements were conducted towards the end of this thesis these approaches were not feasible.

Nevertheless, since the true Hall voltages cannot exceed the erroneous Hall voltages measured experimentally (they would have been detected otherwise), a lower bound on carrier concentration of 10^{16} cm^{-3} and an upper bound on majority carrier mobility of 10 $cm^2V^{-1}s^{-1}$ can be calculated for passivated S films. It had been noted in Sec. 2.3 that anomalous Hall voltages can be measured if hopping conduction is dominant, in which case this argument would be invalid. However, it will be shown later that this is not the case for passivated S films at room temperature. In addition, given that the mobility in nc-SiC with a grain size of 100 nm has been reported to be 1 $cm^2V^{-1}s^{-1}$ [137], it is probable that the mobility in films M, S, and C is lower than this value, implying $>3\times10^{17}$ cm^{-3} carriers for passivated S films. Hot probe measurements on passivated S films showed that the films are n-type, and it will be assumed that this applies to all M, S, and C films, passivated or not.

IVT measurements revealed Ohmic conduction at all temperatures. The Arrhenius plots for the M, S, and C films denoted by full symbols in Figure 5.1 are given in Figure 5.3. The shape of all curves is rather similar, indicating that the conduction mechanisms are the same; however, the high-temperature slopes decrease significantly upon passivation for films M and S and increase for film C. The plots are all curved, indicating that a single mechanism with a well-defined activation energy is insufficient to explain the data.

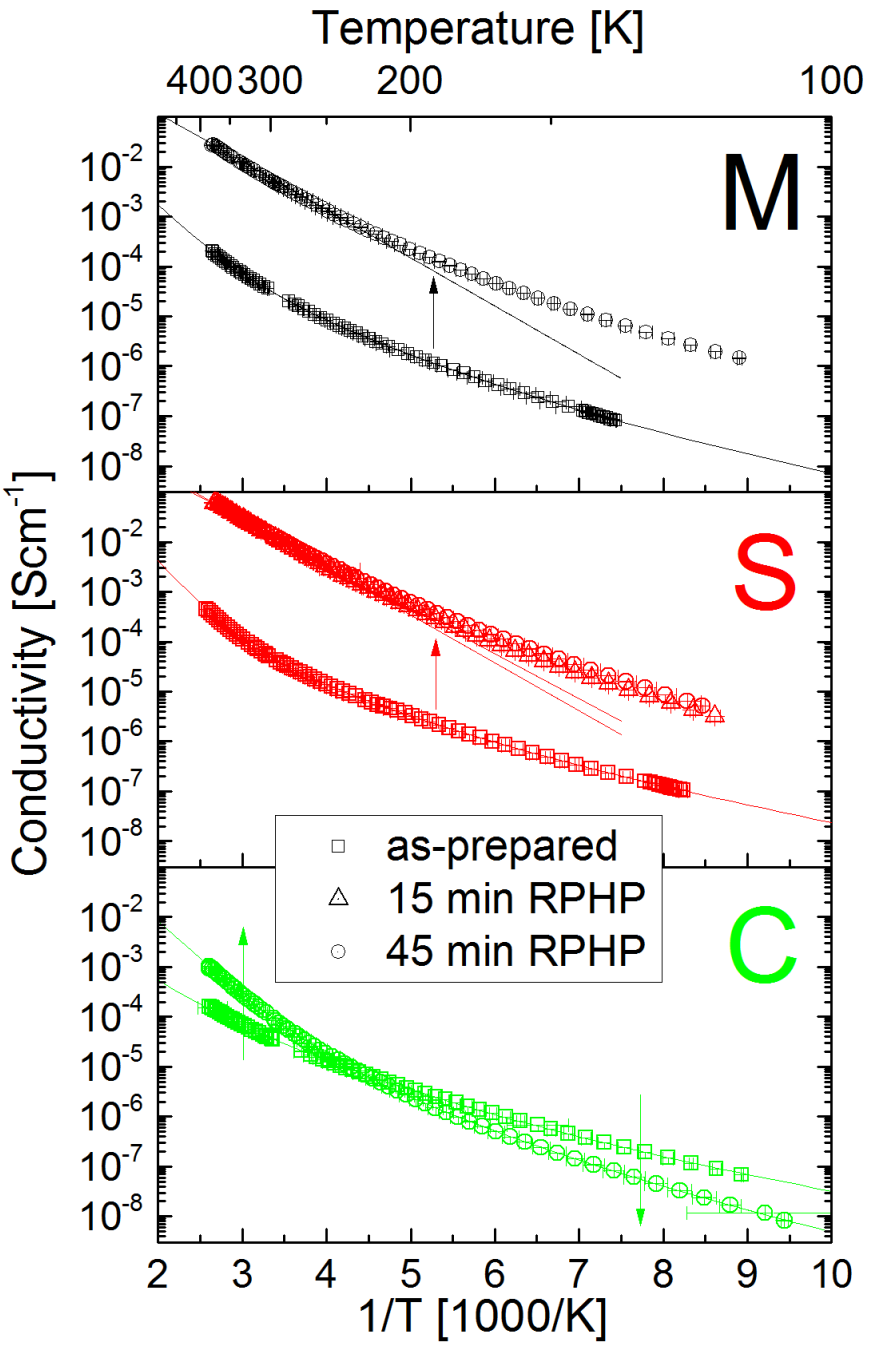

Figure 5.3. Arrhenius plots of IVT measurements of the films M, S, and C denoted by full symbols in Figure 5.1. Colours denote the different films in analogy to Figure 5.1, while the different symbols denote the passivation time and arrows indicate the trend with passivation. All plots are curved, indicating that a single conduction mechanism with a well-defined activation energy is insufficient to describe the data. Fits of the mechanisms discussed in the text are shown as lines. Except for passivated M and S films, they coincide perfectly with the data. Fit parameters are given in Table 5.2.

Since transport is thermally activated, there must be thermally surmountable transport barriers. These are unlikely to arise from the activation of carriers from well-defined dopant or trap states as the activation energy, represented by the Arrhenius slope, would not then

depend on film composition or passivation. Band bending has been excluded already, and band offsets can also be ruled out since the Arrhenius slopes for films M and S are not systematically higher than for film C, as would be expected if activation from the Si NC conduction band to the SiC conduction band occurred. It seems strange that band offsets should not play a role since they must be present in the material. Two possibilities exist: either transport in films with Si NCs is through a percolating network of Si NCs (see Figure 5.4(a)), permitting transport without the SiC conduction band, or there is no conduction band offset, only a valence band offset that does not affect majority electrons (see Figure 5.4(b)). No clear picture of band offsets between Si and SiC emerges from the literature: some studies suggest that the conduction band offset is roughly half the valence band offset [51, 129, 198], while others argue that since the electron affinities of the two phases appear to be very similar (4.05 eV for Si [6], 4.0 eV for 3C-SiC [199], 4.1 eV for a-SiC [127]), the conduction band offset ought to be very small [200-202].

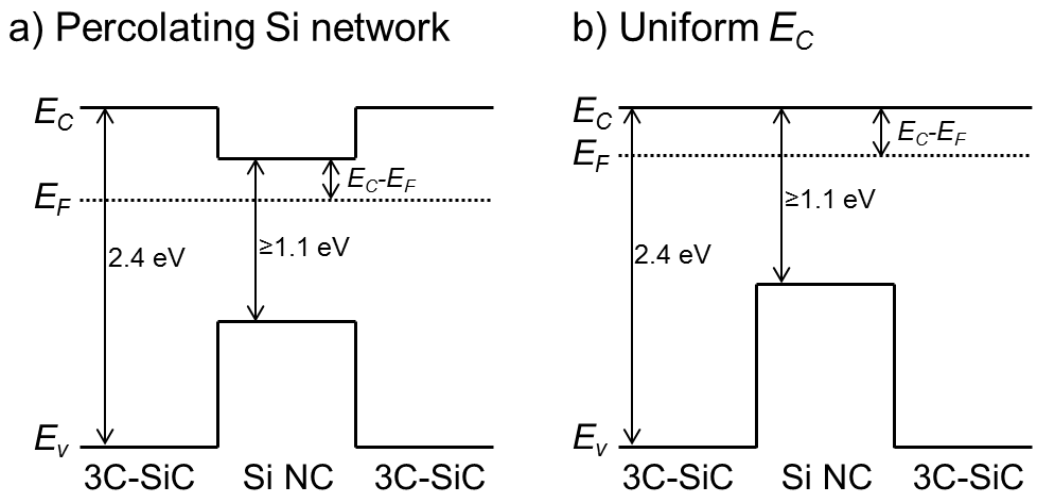

Figure 5.4. Band diagram for Si NCs embedded in SiC assuming transport through a percolating Si network (a), or in a uniform conduction band (b). The band alignment in (a) is only possible in the case of a percolating network because the data do not support thermal activation of carriers from the conduction band of Si to that of 3C-SiC. The distribution of Si levels due to the Si NC size distribution, and the positions of tail states and deep levels present in amorphous and grain boundary material, are omitted for clarity.

As the electron affinity of 3C-SiC appears only to have been calculated, not measured [199], an attempt was made to measure the band offsets between Si and the nanocrystalline SiC in these films directly by preparing Ti / p-poly-Si / nc-SiC / p-Si / Al and Ti / n-poly-Si / nc-SiC / n-Si / Ti structures and measuring the activation energy of vertical transport. Provided the nc-SiC thickness is chosen to be thick enough to avoid tunnelling through it, and thin enough to avoid carrier trapping within it, the activation energies should represent valence and conduction band offsets, respectively. The structures were formed by depositing 50 nm a-SiC:H (the same as film C) and 50 nm doped a-Si:H on Si substrates by PECVD and annealing at 1050°C for 1 h to form the desired structures. Unfortunately, the IV curves were highly non-Ohmic, and a fit with a thermionic emission model [6] gave an unrealistic value for the Richardson constant. Since the Ti / p-poly-Si / p-Si / Al and Ti / n-poly-Si / n-Si / Ti structures prepared as controls were much more resistive than expected, even when sintered at 350°C and when contacted with GaIn or GaSb pastes, it was concluded that something must have gone wrong during device preparation. The arguments for and against the band structures in Figure 5.4 are therefore limited to indirect results drawn from the behaviour of films M, S, and C.

Since both band structures involve transport through a single conduction band (either that of a percolating Si NC network or that of the entire material) the films can, due to their small grain size, be legitimately described as disordered semiconductors, albeit with slightly more delocalised states in the nanocrystals than in fully amorphous material. This is the same approach as that taken by Balberg to explain conduction in percolating networks of Si NCs in SiO_2 [106]. Disordered semiconductor theory was introduced in Sec. 2.3; to recap briefly, it involves a density of states per unit energy $N(E)$ that is finite throughout much of the bandgap and rises gradually to a critical value that defines the conduction and valence band edges E_C and E_V, rather than being zero within the bandgap and increasing rapidly at the band edges. A key consequence of this is that it is not so much the free carrier concentration that defines E_F

(as is the case in crystals, where there are not actually any states at E_F for non-degenerate doping), but that states in the bandgap are filled up to an energy E_F and this defines the carrier concentration at whatever energy transport occurs via an Arrhenius term. Extended-state transport follows

$$\sigma_{ext}(T) = \sigma_{01} \exp\left(-\left(\frac{E_C - E_F}{kT}\right)\right), \tag{5.4}$$

where $\sigma_{01}=qN(E_C)\mu_{ext}kT$, while hopping transport through states in the bandgap is typically described either by

$$\sigma_{tail}(T) = \sigma_{02} \exp\left(-\left(\frac{E_T - E_F}{kT}\right)\right), \tag{5.5}$$

or

$$\sigma_{VRH}(T) = \sigma_{00} \exp\left(-\left(\frac{T_0}{T}\right)^{\frac{s+1}{s+4}}\right), \tag{5.6}$$

depending on whether the energy required to excite carriers from E_F to the energy where transport takes place is large (5.5) or small (5.6) compared to the distribution in energies where transport can take place. These expressions were introduced as Eq. 2.2-2.4 in Sec. 2.3.

Since the Arrhenius plots in Figure 5.3 are curved, neither σ_{ext} nor σ_{tail} alone can describe the data. Variable-range hopping (σ_{VRH}) cannot describe any dataset with s=2 (Efros-Shklovskii VRH), but can fully describe the data of the as-prepared film C and the passivated films M and S with s=0. This is plausible for film C but unrealistic for passivated films M and S as these exhibit conductivities >0.1 Scm^{-1}, and hopping mobilities are typically <0.01 $cm^2V^{-1}s^{-1}$ [116, 118, 203, 204] which would imply >6×10^{19} cm^{-3} hopping electrons, an incredibly high concentration for nominally undoped material. The Arrhenius plots are well-fitted with a combination of Eq. 5.4 and Eq. 5.6 with s=0 for the high- and low-temperature data, respectively.

The following model is therefore proposed: transport in the as-prepared film C proceeds by VRH with s=0. Upon passivation, dangling bonds are eliminated, de-trapping carriers and raising E_F such that $\sigma_{ext}>\sigma_{VRH}$ at high temperature. This also applies to as-prepared films M and S, in agreement with the findings of Myong *et al.* for boron-doped nanocrystalline Si-SiC alloys deposited directly by PECVD [69, 125]. Passivation also raises E_F of films M and S, explaining the increase in conductivity and decrease of the high-temperature Arrhenius slope. The Arrhenius plots of passivated films M and S are also slightly curved, suggesting some kind of hopping mechanism is acting at low temperature, but the curvature is so weak that a reliable fit is impossible so this is not done here. The parameters of the proposed model are listed in Table 5.2, for both batches of M, S, and C films.

It is worth noting that a combination of Eq. 5.4 and 5.5, or a combination of Eq. 5.4 and 5.6 with s=2, could also fit the data. However, in these cases the as-prepared film C cannot be fitted with the hopping mechanism alone, which means that the increase in the high-temperature slope of film C upon passivation would result in an increase in E_C-E_F for film C, which appears unreasonable. It has also been reported that slightly curved Arrhenius plots can be measured on samples exhibiting a single conduction mechanism when E_F or E_C are sufficiently temperature-dependent [205]. This is unlikely to be the case for all the data here as the conductivity of film C increases upon passivation at high temperature and decreases at low temperature, indicating two conduction mechanisms, but may explain the slight curvature of passivated films M and S.

The validity of the proposed model can be evaluated further by examining the resulting fitting parameters. It is found that E_C-E_F decreases from 0.33-0.38 eV to 0.16-0.19 eV upon passivation for M and S films from both batches. The corresponding change in the Arrhenius term fully accounts for the differences in conductivity across all of these samples while the prefactor σ_{01} hardly changes. With values of 4-26 Scm^{-1} for most films it is in good agreement with the theoretical value for a-Si:H of 40 Scm^{-1} [8]. For the passivated samples where σ_{ext} is

significant in all films, E_F is systematically closer to E_C in films M and S than C, which supports the band structure in Figure 5.4(a). The band structure in Figure 5.4(b) only agrees with the room-temperature data if orders of magnitude better background doping or lower non-paramagnetic trap density in films M and S than C is assumed, which seems far-fetched (paramagnetic defect densities were shown to be similar by ESR). The similarity of room-temperature conductivities in all as-prepared films is due to the dominance of the VRH mechanism in these films at room temperature.

Table 5.2. Parameters of fits of Eq. 5.4 and Eq. 5.6 with s=0 to the IVT data of M, S, and C films.

Film	***RPHP Time***	***Batch***[a]	E_C-E_F ***[eV]***[b]	σ_{01} ***[Scm^{-1}]***	T_0 ***[K]***[c]	σ_{00} ***[Scm^{-1}]***	$N(E_F)$ ***[cm^{-3}eV^{-1}]***[d]
M	0 min	1	0.35	3.6 ±0.5	1.4×10^{8}	$(5.9\pm0.5)\times10^{6}$	2.6×10^{19}
	45 min	1	0.19	10 ±1	-	-	-
S	0 min	1	0.38	26 ±3	0.9×10^{8}	$(6.1\pm0.2)\times10^{5}$	4.0×10^{19}
		2	0.33	5 ±0.3	1.3×10^{8}	$(4.6\pm0.1)\times10^{6}$	2.8×10^{19}
	15 min	1	0.19	22 ±0.5	-	-	-
	45 min	1	0.18	14 ±0.6	-	-	-
		2	0.16	14 ±0.3	-	-	-
C	0 min	1	-	-	0.7×10^{8}	$(2\pm0.1)\times10^{5}$	4.8×10^{19}
		2	-	-	1.4×10^{8}	$(3\pm0.8)\times10^{6}$	2.6×10^{19}
	45 min	1	0.32	9.8 ±0.6	2.3×10^{8}	$(3\pm0.6)\times10^{8}$	1.6×10^{19}
		2	0.27	0.4 ±0.04	2.3×10^{8}	$(1.7\pm0.3)\times10^{8}$	1.5×10^{19}

[a]Batches 1 and 2 are nominally identical and were represented by full and open symbols, respectively, in Figure 5.1. Figure 5.3 shows Arrhenius plots of Batch 1.
[b]the fitting errors are smaller than the last significant digit. The actual error is estimated to be ±0.02 eV.
[c]the fitting errors are smaller than the last significant digit.
[d]calculated using Eq. 5.7 and assuming γ^{-1}=1 nm.

The T_0 and σ_{00} values extracted from the VRH fit are positively correlated which shows that Godet VRH through an exponential *N(E)* of tail states, rather than Mott VRH in a constant *N(E)*, is taking place [120]. Godet's equation for the *N(E)* available for VRH at E_F,

$$N(E_F)\gamma^{-3} = 310/kT_0, \tag{5.7}$$

where γ^{-1} is the decay length of the electronic wavefunction typically taken to be 0.3-3 nm [8, 88, 120], yields the values of $N(E_F)$ given in Table 5.2 assuming γ^{-1}=1 nm. These values are similar to the Si NC densities in films M and S (see Table 5.1), but since $N(E_F)$ does not differ significantly between films with and without Si NCs these can be ruled out as the origin of hopping sites at E_F. Values of $N(E_F)$ are also astoundingly similar to the dangling bond concentrations deduced from ESR measurements in Sec 5.1.2 and yet, $N(E_F)$ cannot consist of dangling bond states since these are located near the middle of the bandgap, and E_C-$E_F \ll E_g/2$. For the same reason the decrease in $N(E_F)$ upon passivation that is found is rather unexpected; $N(E_F)$ ought to increase with increasing E_F, provided *N(E)* in the conduction band tail rises monotonically with energy. As a consequence a non-monotonically increasing *N(E)* may be postulated, but a direct measurement of *N(E)*, for example by modulated photocurrent spectroscopy, would be required to state this with any degree of certainty. An independently determined *N(E)* could also be fed into Eq. 2.1 to gain further insight into the conduction process. The location of the states through which hopping occurs is uncertain, but given the similarities in $N(E_F)$ between films M and S, and C, hopping cannot be via Si NCs.

In summary, the data show thermally activated, Ohmic conduction at all temperatures that is related to a bulk process: hopping, most probably tail-state VRH, at low temperatures, and extended-state transport at high temperatures. The transition between the mechanisms occurs at lower temperature if Si NCs are present or if the film was passivated. E_C-E_F is <0.4 eV in

all films where extended-state conduction was observed, and decreases on passivation. All other fitting parameters are in good agreement with literature values.

5.1.4 Background Doping

The high conductivities observed in passivated S films, coupled with the limited mobilities that are to be expected in nanocrystalline films [137] and the observation that films are n-type, indicate that mobile electron concentrations in excess of 10^{17} cm^{-3} must be present in the passivated S films. Since the films are nominally intrinsic, background doping via intrinsic point defects or accidentally incorporated dopants must have occurred. Oxygen and nitrogen are often incorporated during growth of μc-Si [133] and SiC [30], respectively, and both are n-type dopants in Si and SiC [30, 133-137, 195].

The conductivity of passivated S films annealed in Ar and N_2 was not significantly different, suggesting negligible nitrogen doping. However, SIMS profiles acquired by RTG Microanalysis indicate that this conclusion is invalid since 10^{19}-10^{20} cm^{-3} N was already present in the as-deposited film, which did not change significantly on annealing. The only nitrous gases used in the PECVD chamber were NF_3 and N_2O, which are used periodically to etch back the SiC deposited on the chamber walls before flakes form. As can be seen in Figure 5.5, the nitrogen content of C films, and the conductivity of passivated S films, is correlated with the total thickness of SiC deposited since the last etchback step. The two batches of S films deposited at different intervals from the last etchback step are the same two batches of nominally identical samples discussed throughout this chapter. This demonstrates that the etchback gases NF_3 and N_2O are the source of N and of increased conductivity in the films.

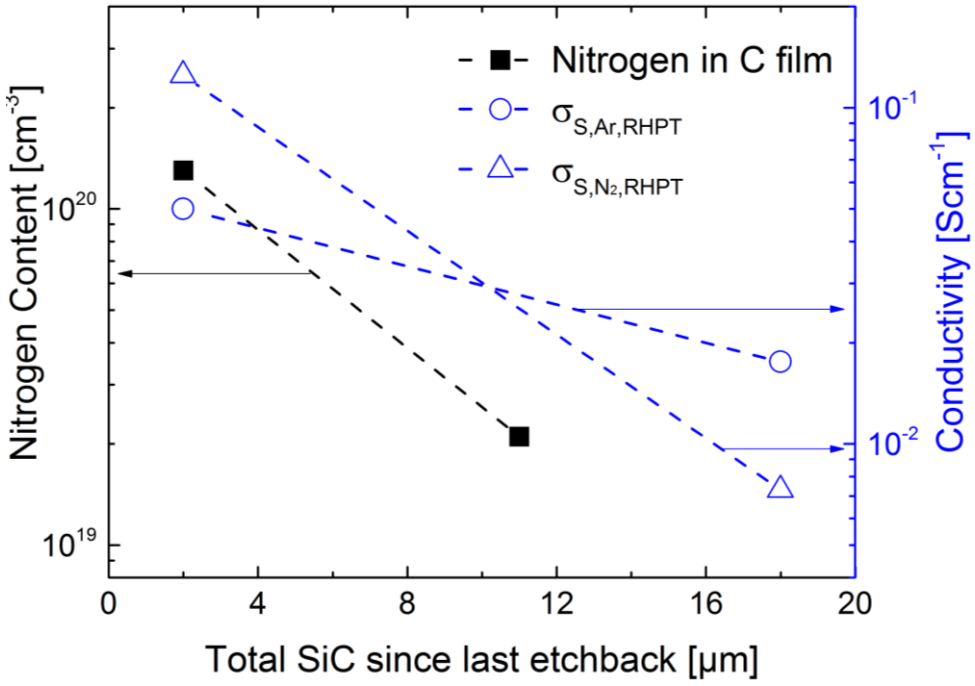

Figure 5.5. Nitrogen content of a C film (left axis) and conductivity of passivated S films annealed in Ar or N_2 (right axis) as a function of the total SiC thickness deposited in the PECVD reactor since the last etchback step (see text). Lines are guides to the eye.

This permits the exclusion of intrinsic point defects as a dominant source of background doping but does not permit the identification of N as the dominant dopant since O and F contents may likewise be correlated with conductivity. F is not an effective dopant in Si [206] or SiC [30]. It can in principle passivate defects [206] and/or act as an etchant during the PECVD step [30], but if this were the case, conductivities of as-prepared S films, and deposition rates of all films, would vary between the two batches, neither of which was observed. Oxygen however can act as a donor and was in one C film found to be present at the same mean concentration as N (although it should be noted that for lack of a SiC standard, oxygen concentrations were quantified with a Si standard so actual concentrations may differ).

The overall picture is that nanocrystalline SiC with and without Si NCs behaves as a disordered n-type semiconductor with a doping level of 10^{17} cm^{-3}-10^{20} cm^{-3} from background doping by nitrogen and/or oxygen.

5.2 Conduction in Different Si Nanocluster Arrays

Having developed a profound understanding of electronic transport in Si NC/SiC based on films prepared at ISE, it is of interest to see if the model is sufficiently robust to also explain transport in samples prepared at CNR. The 2, 3, 4 nm and B films on quartz substrates whose preparation, nanostructure, and in particular photoluminescence was already presented in detail in Section 4.2 will be used. To recap: the 2, 3, and 4 nm films are so-named after the a-$Si_{0.85}C_{0.15}$:H thicknesses in the precursor multilayers, but the nanostructure is defined less by the differently sized Si NCs that were intended than by the effect the a-$Si_{0.85}C_{0.15}$:H thickness had on Si crystallinity $X_{c,Si}$, and on the ordering of Si nanoclusters. The crystallinity varies over a wide range, which means that the Si excess in these samples cannot be considered to be present mainly as Si NCs; a significant proportion of a-Si nanoclusters is also present. The nanostructure parameters are recapped in Table 5.3.

Table 5.3. Excess Si volume fraction V_{Si}, Si crystallinity $X_{c,Si}$, and Si NC size $d_{Si\ NC}$ in the 2, 3, 4 nm and B films, as well as the derived quantity $V_{nc\text{-}Si}=V_{Si}X_{c,Si}$ (nc-Si volume fraction). V_{Si} and $V_{nc\text{-}Si}$ are upper bounds since full de-mixing is assumed.

Film	V_{Si}	$X_{c,Si}$	$d_{Si\ NC}$ ***[nm]***	$V_{nc\text{-}Si}$
2 nm	0.23	0.09	-	0.02
3 nm	0.31 (0.82[a])	0.41	4.2 ±0.3	0.13 (0.34[a])
4 nm	0.36 (0.82[a])	0.60	4.5 ±1.0	0.22 (0.49[a])
B	0	-	-	-

[a]refers to the Si-rich sublayers only.

Samples were contacted using a TLM structure of thermally evaporated Ti-Pd-Ag (see Sec. 3.1.5) and were measured at ISE, CNR, and UB. Measurements agreed with each other to within experimental error. All samples exhibited Ohmic behaviour; the results acquired by the author at room temperature are shown in Figure 5.6.

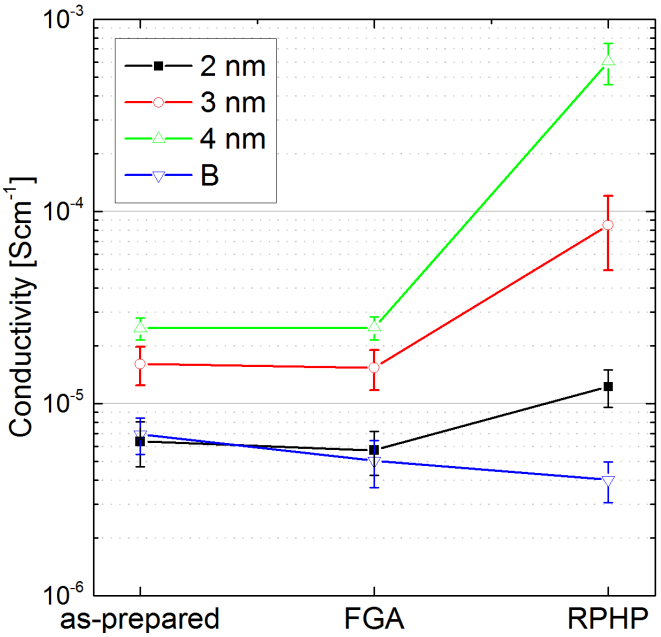

Figure 5.6. Conductivity of the 2, 3, 4 nm and B films as a function of post-metallisation hydrogen treatment. A forming gas anneal (FGA) has little effect, while a remote plasma hydrogen passivation (RPHP) step significantly increases the conductivity of multilayers. Lines are guides to the eye.

The room-temperature conductivities of as-prepared samples are on the order of 10^{-5} Scm^{-1}. The magnitude of the conductivities is in good agreement with films M, S, and C, but the variation is significantly greater across this batch, a factor 4 between the 4 nm and the B film as opposed to a factor 1.2 across films M, S, and C. Two different hydrogenation treatments were applied: a forming gas anneal (FGA) in N_2/5% H_2 at 425°C for 25 min, and a RPHP step as described in Sec. 3.1.4. FGA had no effect on conductivity whereas RPHP greatly increased the conductivity of the films with excess Si. This shows that diluted molecular hydrogen is insufficient to passivate Si NC/SiC; atomic hydrogen is required. Such an effect has previously been reported for stoichiometric SiC in Ref. [132], where it was proposed that this is due to the dense crystal structure of 3C-SiC which does not exhibit any large interstices through which H_2 could migrate. It is in contrast to Si NCs in SiO_2 which are well-passivated by molecular H_2 [207].

The magnitude of as-prepared conductivity and trend with RPHP is similar to films M, S, and C, but the increase in conductivity with RPHP is more moderate, while the effect of

nanostructure appears more pronounced. The latter is attributable to the fact that the nanostructure varies more in this batch of samples, but whether V_{Si} or $X_{c,Si}$ is the key parameter is difficult to determine since they are correlated. To determine what impact this has on the conduction mechanism, temperature-dependent conductivity measurements were performed on the 2, 3, and 4 nm films and are shown in Figure 5.7.

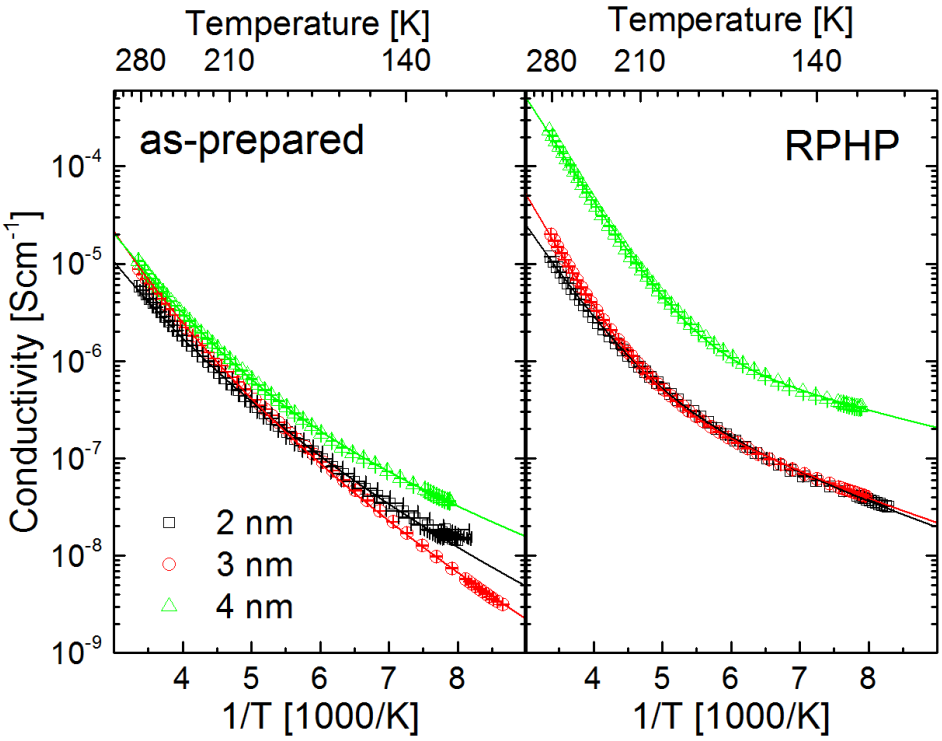

Figure 5.7. Arrhenius plots of IVT measurements of as-prepared (left) and passivated (right) 2, 3, and 4 nm films. All plots are curved, indicating that a single conduction mechanism with a well-defined activation energy is insufficient to describe the data. Fits of the mechanisms discussed in the text are shown as lines and coincide perfectly with the data. Fit parameters are given in Table 5.4.

As for films M and S, Ohmic conduction is observed at all temperatures, conductivity increases with hydrogen passivation at all temperatures, and curved Arrhenius plots are obtained that can be fitted with any combination of Eq. 5.4 with Eq. 5.5 or Eq. 5.6. However, the results are considered sufficiently similar to those of films M and S to justify applying the same model: Eq. 5.4 and Eq. 5.6 with s=0. The fit parameters are given in Table 5.4. Before examining the fit parameters, some differences as compared to films M, S, and C are worth

noting: the high-temperature Arrhenius slope increases upon passivation for all samples, and the low-temperature slope decreases significantly, while it hardly changed at all for films M, S, and C.

Table 5.4. Parameters of fits of Eq. 5.4 and Eq. 5.6 with s=0 to the data in Figure 5.7.

Film	***RPHP Time***	E_C-E_F ***[eV]***[a]	σ_{01} ***[Scm^{-1}]***	T_0 ***[K]***[b]	σ_{00} ***[Scm^{-1}]***	$N(E_F)$ ***[cm^{-3}eV^{-1}]***[c]
2 nm	0 min	-	-	1.2×10^{8}	$(4\pm1)\times10^{5}$	0.31×10^{20}
	45 min	0.21	0.04 ± 0.005	$(2.3\pm0.2)\times10^{7}$	37 ± 13	$(1.6\pm0.2)\times10^{20}$
3 nm	0 min	-	-	2.8×10^{8}	$(2.5\pm0.5)\times10^{8}$	0.13×10^{20}
	45 min	0.25	0.28 ± 0.03	1.8×10^{7}	11 ± 2	2.0×10^{20}
4 nm	0 min	0.19	0.01 ± 0.001	$(4.1\pm0.3)\times10^{7}$	$(8\pm4)\times10^{2}$	$(0.87\pm0.06)\times10^{20}$
	45 min	0.22	1 ± 0.1	$(4.4\pm0.6)\times10^{6}$	0.3 ± 0.1	$(8\pm1)\times10^{20}$

[a]the fitting errors are smaller than the last significant digit. The actual error is estimated to be ±0.02 eV.
[b]where no error is given the fitting error is smaller than the last significant digit.
[c]calculated using Eq. 5.7 and assuming γ^{-1}=1 nm.

For the 2 and 3 nm samples, the increase in high-temperature slope upon passivation is, as for film C, due to the change from VRH to extended-state transport at high temperatures as a consequence of an increased E_F. The 4 nm sample is the only one to exhibit extended-state transport before passivation, and is also the only one of these samples where V_{Si} exceeds the percolation threshold, indicating that this may promote extended-state transport. This supports the band structure in Figure 5.4(a) since that in Figure 5.4(b) is unlikely to be sensitive to the percolation of V_{Si}. However, in other ways the behaviour of the 4 nm film upon passivation is markedly different to M and S: it is the prefactor σ_{01} that is responsible for the increase in conductivity, while E_C-E_F actually increases. It is possible to concoct an explanation based on hydrogen increasing the bandgap via the hydrogen alloying effect known from a-Si:H [8, 65, 91], and hence raising E_C more than it raises E_F, while also increasing the extended-state

mobility by passivating charged impurities or DBs that scatter electrons. However, it is thought prudent not to overanalyse this one result, particularly since samples in this batch were only measured to 300 K, not 400 K as films M, S, and C were, and extending the measurement to higher temperature increases the fitted value of E_C-E_F for films which, like the as-prepared 4 nm film, transition from VRH to extended-state transport at a temperature quite close to the highest measurement temperature.

The low-temperature data, or the entire dataset in the case of as-prepared 2 and 3 nm films, are well-fitted by Eq. 5.6 with s=0 and exhibit the same positive correlation of σ_{00} and T_0 as films M, S, and C did (in fact, in a plot of σ_{00} versus T_0 for all films from both batches all points lie on the same line). Again $N(E_F)$ is calculated using Eq. 5.7 and given in Table 5.4. The values reflect the strong decrease in low-temperature slope on passivation: $N(E_F)$ increases by an order of magnitude as a consequence. This is in agreement with an increase of E_F in a $N(E)$ that increases monotonically with E. Values of $N(E_F)$ for passivated 2, 3, and 4 nm films are much higher than those for as-prepared films M and S, which correlates well with the lower E_C-E_F of the former. It is worth noting that as E_C-E_F decreases, the states at E_F become less localised and γ^{-1} also increases, decreasing $N(E_F)$. This means that the true values of $N(E_F)$ differ less than the tabulated values.

Overall, transport in the 2, 3, and 4 nm films can be described by the same model as transport in film M, S, and C, indicating that the model is not just specific to one laboratory but seems to be generally suitable for Si nanoclusters in SiC. However, hopping occurs through a larger density of states in the 2, 3, and 4 nm films and they also exhibit a stronger dependence of conductivity on nanostructure than films M and S did. In Sec. 5.1.3.3, the transport mechanisms were found to be most readily reconciled with the band diagram in Figure 5.4(a), which was ascribed to the presence of V_{Si} values above the percolation threshold. For films M and S, V_{Si} and $V_{nc\text{-}Si}$ were similar but for the 2, 3, and 4 nm films they are not, which raises the question whether extended-state conduction occurs in a percolating network of Si, or Si NCs.

Two studies have found that the conduction band offset between a-Si:H and Si NCs is negligible [208, 209], so conduction though a percolating network that includes a-Si nanoclusters and Si NCs is conceivable. For 3 and 4 nm films, both V_{Si} and $V_{nc\text{-}Si}$ exceed the percolation threshold in the Si-rich sublayers, which are the relevant values since the energy-filtered TEM (EFTEM) images in Figure 4.3 indicated some survival of the multilayer structure in both. The EFTEM images also showed that the 2 nm film intermixes fully, so for this film the values averaged over the whole film, V_{Si}=0.23 and $V_{nc\text{-}Si}$=0.02, are relevant. It seems improbable that the conductivity of a film in which only 2% of the material conducts well would exceed that of film B by a factor of 3 after passivation, so it is considered more probable that a percolating network of Si NCs *and* a-Si nanoclusters is responsible for extended-state transport.

Another difference lies in the background doping in these samples. To determine whether nitrogen contamination was present in the 2, 3, 4 nm and B samples a different film B was investigated by SIMS; the depth profile is given in Figure 5.8.

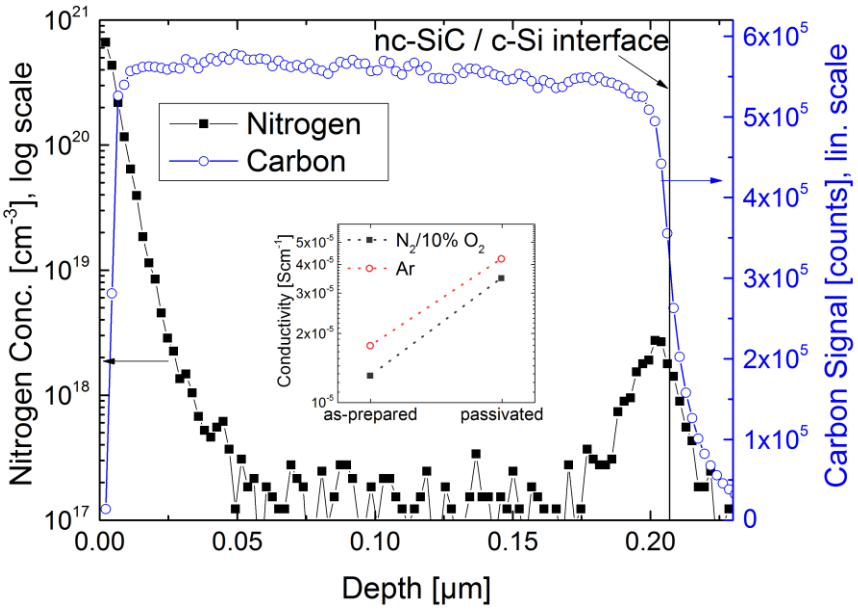

Figure 5.8. Nitrogen profile in a B film. The nitrogen concentration is not constant but decays to the detection limit within 50 nm of the film surface. The unquantified carbon signal is also plotted, as a reference for the nc-SiC / c-Si interface. Inset: Conductivity of new 3 nm films annealed under N_2/10% O_2 and Ar. Lines are guides to the eye.

There is not a homogeneous nitrogen concentration, as was the case for the C films discussed in Sec. 5.1.4, but a near-surface profile that decays over four orders of magnitude to below the detection limit within 50 nm of the film surface. It is rather improbable that this sort of profile arises during deposition, but instead is most likely to arise from nitrogen in-diffusion during annealing. In this case therefore a comparison of films annealed under N_2/10% O_2 and Ar will provide information on nitrogen doping. The results for freshly prepared 3 nm films are shown in the inset of Figure 5.8. There is no significant difference in conductivity before or after passivation, demonstrating that nitrogen is not the key background dopant. Oxygen incorporation on the other hand is known to occur in the CNR reactor from earlier experiments on µc-Si:H. It is therefore concluded that oxygen is the dominant dopant in the 2, 3, 4 nm and B films.

5.3 Photocurrent

The results presented in this chapter thus far have painted a detailed picture of majority carrier (electron) transport in Si NC/SiC. Majority carrier transport is certainly necessary for solar cells; in the Si NC/SiO_2 system, it is a key limitation on photovoltaic performance. In many other materials, however, the key limitation is the transport of photogenerated *excess* carriers, which is affected by the excess carrier lifetime as well as majority and minority carrier mobilities. To investigate this type of transport, photocurrent measurements were carried out on all samples described in this chapter. Samples were illuminated with a Xe lamp. The light was filtered with a 395 nm longpass filter so as not to expose the films to ultraviolet radiation that might create additional defects, and the illumination level was ~3 suns. Rather low photoconductivities <1.5× of the dark conductivity were found.

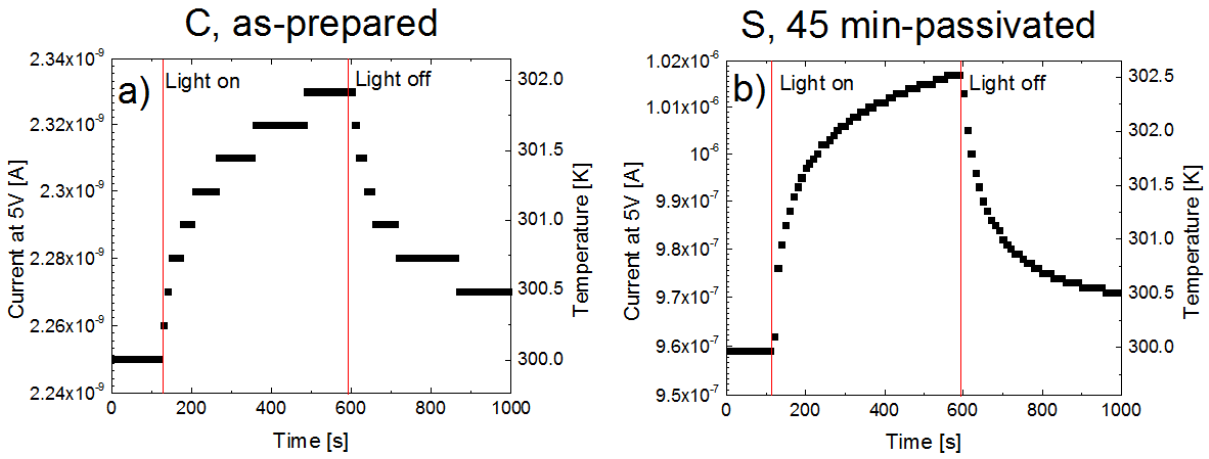

Figure 5.9. Time-dependence of the photocurrent of an as-prepared film C (a) and a 45 min-passivated film S (b). The slow increase and decrease of current as illumination is switched on and off indicates that the photocurrent measured does not arise from optical electron-hole pair generation but from optical heating of the sample. The implied sample temperature assuming an initial temperature of 300 K is plotted on the right-hand axes.

More importantly, as can be seen in Figure 5.9 for an as-prepared film C and a 45 min-passivated film S, the onset and decay of photoconductivity was very slow. It was hence thought that the change in conductivity may not actually arise from optical electron-hole pair generation, but from optical heating. Since the activation energies were found previously, the current can be converted to temperature assuming the initial temperature is 300 K; this is plotted on the right hand axes in Figure 5.9. The "photocurrents" are in agreement with heating by 2-3 K which is entirely plausible.

5.4 Summary

Electrical transport in nanocrystalline SiC films with and without embedded Si nanoclusters prepared in two different laboratories has been studied. All samples exhibited thermally activated Ohmic conduction at all temperatures. Treatment with atomic, rather than molecular, hydrogen lead to a strong increase in conductivity in all samples with Si nanoclusters and reduced the dangling bond density, particularly in and on Si NCs.

Direct tunnelling and grain boundary-mediated transport are ruled out and conduction is instead found to be through extended states at high temperature and via hopping, most likely through tail states, at low temperature. Trends in E_C-E_F support the band structure in Figure 5.4(a), indicating that transport in films with Si nanoclusters occurs through a percolating network of Si nanoclusters, analogous to transport in annealed SiO_x films with sufficiently low x for Si NC percolation [106]. Both crystalline and amorphous Si nanoclusters are involved in the percolating network. The location of the states through which hopping occurs is uncertain, but Si NCs are unlikely as $N(E_F)$ was insensitive to the presence of Si NCs.

The films are n-type, and while a direct measurement of carrier concentration was unsuccessful, it is estimated to be $>10^{17}$ cm^{-3} in passivated S films based on the highest mobility that can be expected in such materials. The high doping level is related to background doping by nitrogen and/or oxygen for films prepared at ISE, and oxygen only for films prepared at CNR. The total concentration of nitrogen and oxygen as measured by SIMS provides an upper limit on donor concentration of $\sim 10^{20}$ cm^{-3} for films prepared at ISE. However, a realistic upper limit on the *free* carrier concentration will be at least a factor $\exp(-(E_C-E_F)/kT)$ lower since the carriers donated by the donor atoms will occupy states below and at E_F and require thermal activation to E_C, not to mention the limited efficiency with which the atoms will be incorporated as donors.

Despite the high conductivities, no photocurrent related to photogenerated excess carriers was measured. This means that the photogenerated excess carrier density is negligible compared to the carrier density in dark conditions, which reinforces the idea of a relatively high background doping level coupled with a low minority carrier lifetime as inferred from photoluminescence measurements in Chapter 4.

5.5 Discussion of Optoelectronic Properties of Si NC/SiC

It has been proposed that a high dark conductivity is detrimental for solar cell absorbers as it increases the reverse saturation current density j_0, and it is the factor $\ln(j_{sc}/j_0)$, where j_{sc} is the short-circuit current of the cell, that determines the open-circuit voltage V_{oc} [75, 76, 131]. In these works, Si NC/SiC layers modified to have lower dark conductivity did indeed exhibit greatly improved solar cell performance. A promising route for future work on Si NC/SiC films is therefore to attempt to reduce both carrier concentration and defect density. Both will improve minority carrier lifetime, and hence j_{sc} and V_{oc}, by reducing Auger and Shockley-Read-Hall recombination, respectively. On the other hand, a high mobility is always desirable for solar cells as it increases the probability of carriers reaching the contacts before they recombine.

It is not entirely obvious how a decrease in carrier concentration and defect density is to be achieved. Background doping was a big problem for PECVD-deposited µc-Si:H in the 1990s, and was solved either by purifying the precursor gases [133], or compensating with low-level boron doping [210]; either might yield a substantial improvement for Si NC/SiC. Defect passivation is more problematic: even in S films, where a decrease in dangling bond density has been directly measured by ESR, and a 1000× improvement in conductivity was found, PL is weak and unaffected by hydrogen passivation. The invariance of the PL of a range of films with passivation makes it unlikely that any post-annealing treatment will eliminate PL-limiting defects in Si NC/SiC, so improvements must be made at the precursor deposition stage. Furthermore, since a range of Si nanocluster crystallinities and arrangements exhibited weak PL, it seems unlikely that there is one special nanostructure that will have vastly lower defect density, but rather that defects particular to the Si/SiC system as a whole are present. It has been pointed out in the literature that the 3C-SiC / c-Si interface has a high energy due to the large lattice mismatch of ∼19% [166].

Such interfaces seem unavoidable: Refs. [19, 52] found that Si nanoclusters must be crystalline for efficient PL and minority carrier lifetimes in the µs range, and as described in Sec. 2.1, Si never crystallises before SiC unless the carbon content is too low for isolated Si NCs. At the same time, 3C-SiC is much stiffer than Si, and since Si crystallises simultaneously or later, Si crystallisation is likely to be associated with defect formation. In the Si NC/SiO_2 system this is evidently not an issue, probably because c-Si / a-SiO_2 interfaces generally have low defect concentration [211] and because Si-O bonds are quite flexible [212], allowing them to compensate strain without defect formation. It therefore appears that the best way to improve the Si NC/SiC system is to add another atomic species during deposition that segregates to interfaces that are formed within the material on annealing and has a different valence to Si and C that permits it to eliminate interface defects or compensate strain. Given the strong PL and high lifetime in Si NC/SiO_2 [52, 84, 86, 87] one may infer that oxygen is a suitable species with which to attempt such an experiment, although care would have to be taken to ensure that the desired passivation effect dominates over any background doping effect. Annealing of a-SiC_xO_y:H bulk films should be sufficient for such an experiment since Chapter 4 showed that ordering of Si NCs has no substantial effect on recombination. This may yield a material that offers an acceptable compromise between lifetime and mobility to yield an optimised mobility-lifetime product that is needed for an efficient solar cell.

6. Process Development for Tandem Cells

Chapters 4 and 5 have dealt with the optoelectronic properties of Si NCs embedded in SiC (Si NC/SiC). In order to now incorporate these into tandem cells, additional building blocks are required. As can be seen in Figure 6.1, which shows a schematic diagram of an all-crystalline Si tandem solar cell, both the c-Si and Si NC cell require an emitter, and a tunnel diode is needed to connect the two cells. To this end, results on diffusion in Si NC/SiC films and tunnel junction formation will be presented in this chapter.

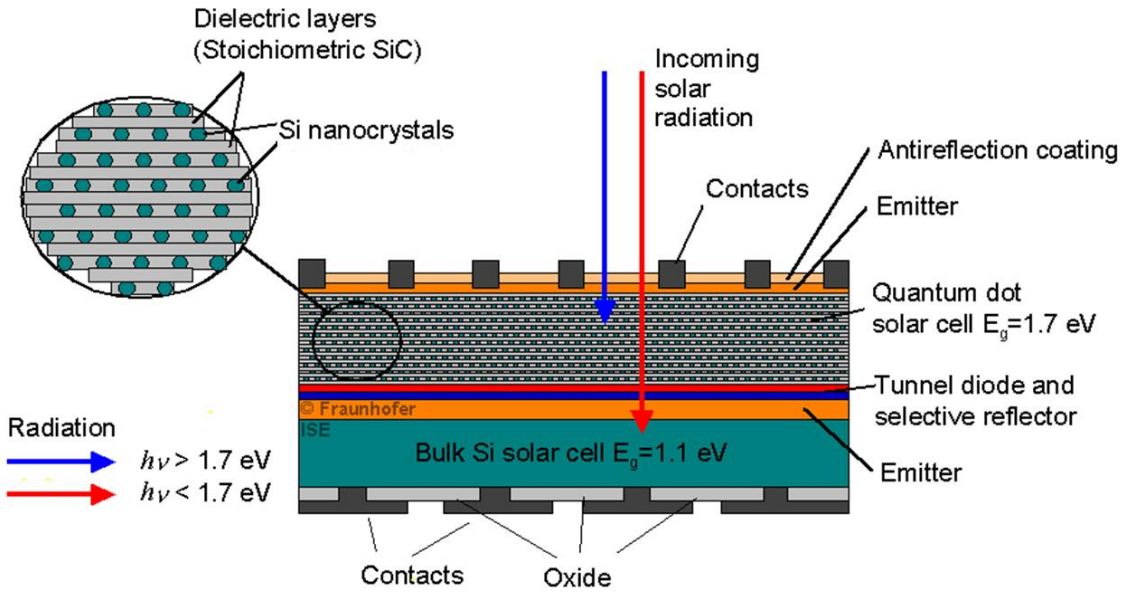

Figure 6.1. Schematic diagram of an all-crystalline Si tandem solar cell with a bandgap of the Si NC/SiC layer of 1.7 eV.

The first section, however, will cover the oxidation of the a-Si_xC_{1-x}:H films or multilayers during annealing as this needs to be avoided, or at least managed, if Si NC/SiC films are to be prepared reproducibly and reliably. The results presented in this chapter have been published in Refs. [154, 213-215].

6.1 Oxidation

6.1.1 Monitoring Oxidation

In principle, oxidation of a-Si_xC_{1-x}:H films or multilayers on annealing should not occur when annealing is carried out in pure N_2 (or Ar). In practice, some oxidation is observed, as will be presented in the following. Both multilayers (M) and stoichiometric a-SiC:H films (C) were deposited and annealed at 1050°C for 1 h. Oxidation on annealing is studied in three furnaces: A, B, and C. A and B are both tube furnaces with quartz components where annealing is performed under N_2. Key differences are the entry temperature, and that furnace A is evacuated before filling with N_2 and heating. Furnace C is completely different: it heats optically rather than resistively, in an Ar atmosphere with graphitic carriers. The sample parameters are summarised in Table 6.1.

Table 6.1. Sample parameters for oxidation study.

Sample	***Deposition Parameters***[a]	***Furnace***	***Entry Temperature***	***Carrier***
M-A	20x [4 nm a-$Si_{0.77}C_{0.23}$:H / 4 nm a-SiC:H]	A	25°C	Quartz
C-A	300 nm a-SiC:H			
M-B	20x [4 nm a-$Si_{0.77}C_{0.23}$:H / 4 nm a-SiC:H]	B	850°C	Quartz
C-B	300 nm a-SiC:H			
M-C	20x [4 nm a-$Si_{0.77}C_{0.23}$:H / 4 nm a-SiC:H]	C	25°C	Graphite
C-C	300 nm a-SiC:H			

[a]thicknesses are before annealing.

A scanning electron micrograph (SEM image) of M-B and Fourier-transform infrared (FTIR) spectra of M-A, M-B, and M-C are shown in Figure 6.2(a) and (b), respectively. The SEM image shows a 14 ±5 nm thick layer (SiO_2) on top of the multilayer (Si-C), which is rather

thick considering the film was annealed in a nominally inert atmosphere. FTIR spectra exhibit Si-O-Si stretching mode peaks at 1065-1080 cm^{-1} [216], which are enlarged in the inset of Figure 6.2(b). Film M-B exhibits the largest Si-O-Si peak showing that oxidation was strongest in furnace B, so much so that the quantity of the M film consumed is significant as shown by the decreased Si-C peak at ~800 cm^{-1} [217]. This is attributed to the entry temperature of 850°C since this means that the samples are briefly exposed to air at that temperature.

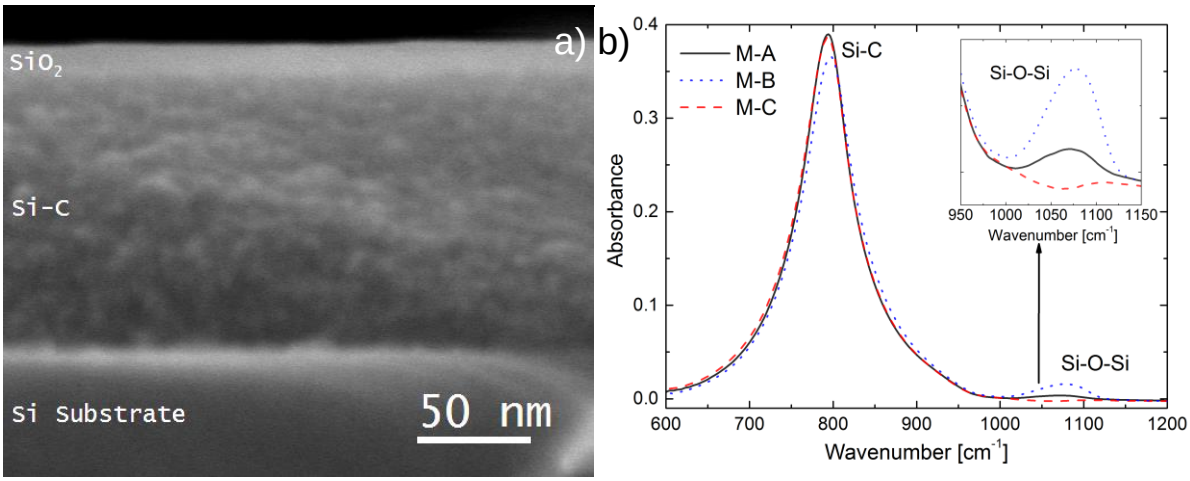

Figure 6.2. SEM image of M-B (a) and FTIR spectra of M-A, M-B, and M-C (b). The Si-O-Si peaks are enlarged in the inset of (b).

Film M-C actually exhibits a dip at the Si-O-Si peak position. This occurs because the spectra in Figure 6.2(b) have been corrected by subtracting the spectrum of a bare Si substrate that has a thicker native oxide than film M-C (the uncorrected spectrum exhibits a small peak). Oxidation in furnace C is very slow, which given that there is nothing about the furnace to suggest that it is cleaner or sealed better than furnaces A and B is attributed to oxygen reacting preferentially with the graphitic carriers.

Both SiO_2 and SiO_xC_y compounds have been reported on SiC films [218], and the latter cannot necessarily be removed in HF [153]. To determine which is formed here, the oxides formed in the three furnaces were studied by x-ray photoelectron spectroscopy (XPS). C films

were used to simplify the analysis, and IMTEK performed the XPS measurements. C-A and C-B exhibit Si2p and O1s peaks consistent with SiO_2, and no peaks related to SiC, indicating that SiO_2 films thicker than the 5 nm penetration depth of the measurement were formed. In contrast, the Si-O-related peaks of C-C are shifted to lower energy and consistent with SiO_xC_y [218]. The ratio of the Si-C and Si-O peak areas suggests a SiO_xC_y thickness of ~1 nm.

Oxide thicknesses can also be calculated from FTIR data by integrating the Si-O-Si absorbance peaks. The peak from a bare Si substrate, whose front and rear side SiO_2 thicknesses were accurately determined by spectral ellipsometry, was also integrated, and used as a standard to convert integrated absorbance into oxide thickness. The oxide thicknesses on the rear sides of the Si substrates the films are on are also measured by spectral ellipsometry to isolate the thicknesses of the oxides on the films. These are listed in Table 6.2. The method assumes all oxides are identical to the native oxide on a Si wafer. The oxide on C-C in particular is likely to have a lower Si-O bond density, in which case the oxide thickness from FTIR is an underestimation and should be seen as a lower limit.

Table 6.2. Oxide thicknesses on M-A, M-B, and M-C derived from three different techniques.

Sample	***FTIR***	***XPS***[a]	***SEM***
M-A	6 ±1 nm	≥5 nm	11 ±5 nm
M-B	16 ±1 nm	≥5 nm	14 ±5 nm
M-C	1.5 ±1 nm	1 ±1 nm	-

[a]XPS refers to C-A, C-B, C-C, respectively

Table 6.2 also lists oxide thicknesses derived from XPS and SEM, and the values of all three techniques are in astoundingly good agreement. This validates the FTIR analysis and demonstrates that FTIR is a powerful, non-destructive, and fast technique to measure oxide thicknesses on materials where this is not possible by spectral ellipsometry. The films are

prone to significant oxidation when annealed in a furnace with quartz components under N_2, even when the furnace is evacuated before filling with N_2 and heating. Graphitic carriers limit oxide thicknesses to those of native oxides, but also appear to promote SiO_xC_y formation which can be difficult to remove.

6.1.2 Preventing Oxidation

Since oxidation is strongly dependent on furnace parameters (and, in the case of furnace A, also on sample position within the furnace), and since complex oxides that may be resistant to HF may be formed, a method whereby the a-Si_xC_{1-x}:H films or multilayers are shielded from oxidation entirely is desirable. To this end, films M-A, M-B, and M-C were prepared a second time, but with a 40 nm a-Si:H capping layer on top that was deposited at the same time as the films themselves using a process with lower plasma power density and 30 sccm SiH_4, 100 sccm H_2 and 30 sccm Ar [154]. Figure 6.3(a) shows an SEM image of the capped film M-B after annealing. The thermal SiO_2, residual Si, and M-B ("Si-C") film can be clearly distinguished, indicating that the process is successful in shielding the M-B film from oxidation. Unfortunately, the process window for the a-Si:H thickness is very narrow: 20 nm a-Si:H oxidise completely, whereas 100 nm a-Si:H capping layers blister upon annealing.

After annealing, the SiO_2 was removed using HF, and residual Si was removed using CP33 or KOH (CP33 is a mixture of HF, HNO_3, and CH_3COOH). Figure 6.3(c) and (d) show SEM images of M-B after removal of residual Si in CP33 and KOH, respectively. The similarity of the nanostructure on the surface and in cross-section indicates that the M-B film has been fully uncovered, but not damaged, by both etching treatments.

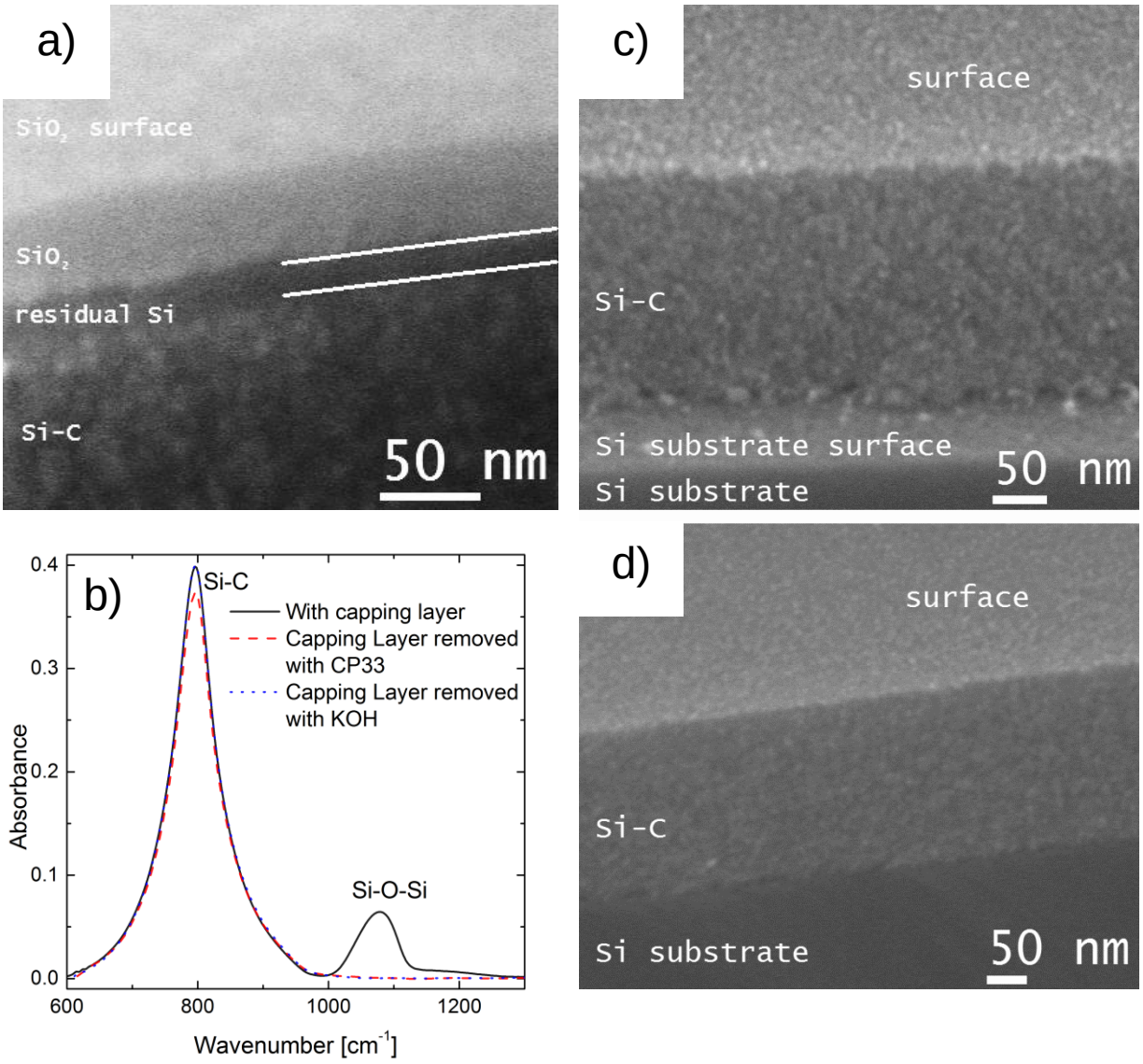

Figure 6.3. SEM image of M-B capped with 40 nm a-Si:H, after annealing (a), FTIR spectra of the film in (a) after annealing, and after removing SiO_2 in HF and residual Si in CP33 or KOH (see text) (b), and SEM images of the M-B film after removal of residual Si in CP33 (c) or KOH (d). 40 nm a-Si:H is sufficient to completely shield the M-B film from oxidation, and the oxide and residual Si are fully removed by the etching procedure to leave the annealed, unoxidised M-B film. Lines in (a) are a guide to the eye.

The FTIR spectra of the annealed film M-B before and after capping layer removal, shown in Figure 6.3(b), show that the SiO_2 is fully removed and no oxidation of the M-B film occurred. CP33 also appears to have etched the M-B film slightly, leading to a decreased Si-C peak. Atomic force microscopy was used to measure the root-mean-square surface roughness of the films. Values of 0.50-0.52 nm were obtained for a CP33-etched film M-B, 0.52-0.55 nm for KOH etching, and 0.26-0.29 nm for an uncapped M-B reference that was annealed and etched

in HF to remove the thermal oxide. Both CP33 and KOH therefore slightly roughen the film. However, both are rapid Si etches, and the residual Si was in fact overetched 40× by KOH and 200× by CP33. That the roughness only increases marginally, and that the Si-C FTIR peak only decreases for CP33, shows that film M-B is remarkably resistant to Si etchants and that the process is therefore quite robust with respect to the etching parameters. A gentler etching process may well eliminate even the modest roughening that was observed.

The capping layer approach is a promising method to completely eliminate oxidation of the Si NC/SiC films upon annealing, permitting the fabrication of reproducible films even in non-ideal furnaces. It was not used further at ISE as a new furnace in which samples did not oxidise at all became available, but CNR adapted the process to their equipment [153] and applied it to most of their samples that were studied in this thesis in order to prevent the SiO_xC_y formation that they had observed previously [153].

6.2 Diffusion

In order for the Si NC/SiC films to function as a solar cell, a p-n junction is required. A p-n junction can be formed by diffusing in dopant, but diffusion can also modify or destroy an existing p-n junction if its formation is followed by a high-temperature step. These two processes are studied using the model system a-SiC:H in Sec. 6.2.2 and 6.2.1, respectively. Amorphous SiC is a suitable model system because if the Si NCs in SiC are isolated as desired, diffusion in Si NC/SiC is limited by diffusion through nanocrystalline SiC (nc-SiC). Diffusion of boron and phosphorus is investigated as these dope c-Si [206] and a-Si:H [8, 116] very well. Phosphorus is an n-type dopant in 3C-SiC, and while boron is a deep acceptor in 3C-SiC [30], boron doping of Si NC/SiC has been shown [21, 93].

6.2.1 Diffusion During Annealing

The simplest way to form a p-n junction involving Si NC/SiC is to dope the a-Si_xC_{1-x}:H bulk film or multilayer precursor opposite to the Si substrate. During the anneal required to form the Si NC/SiC, dopant can diffuse from the substrate to the film (see Figure 6.4(a)) or from the film to the substrate (see Figure 6.4(b)). These two processes are studied using a-SiC:H films in Sec. 6.2.1.1 and 6.2.1.2, respectively.

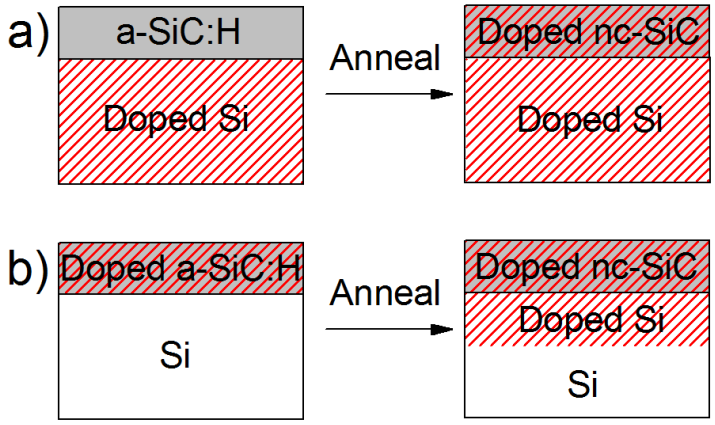

Figure 6.4. Schematic diagrams showing (a) diffusion from the Si substrate into the a-SiC:H film during annealing (Sec. 6.2.1.1), (b) diffusion from the a-SiC:H film into the Si substrate during annealing (Sec. 6.2.1.2). The anneal also crystallises the a-SiC:H.

6.2.1.1 Diffusion from Si Substrate to a-SiC:H

Boron diffusion from a Si wafer into a-SiC:H is studied by annealing a-SiC:H deposited on a p+ c-Si surface (p+ Si) and on a 1 Ωcm Si wafer (henceforth "undoped Si"). The p+ Si is prepared via a BBr_3 diffusion into a Si wafer followed by a drive-in step. The resulting doping profile exceeds 10^{19} cm^{-3} in the top 2.2 µm of the wafer. The diffusion length L of boron in Si during the 1100°C 30 min anneal that will be applied to crystallise the a-SiC:H can be estimated using

$$(L/2)^2 = \int D(T(t))dt, \quad (6.1)$$

where *D(T)* is the temperature-dependent and concentration-independent diffusivity of boron in Si from Ref. [206], and *T(t)* is the temperature profile during the anneal. This yields *L*=0.43 µm which means the p+ Si surface approximates to a p+ Si wafer for the purposes of studying diffusion. The p+ Si was prepared at ISE, and a-SiC:H deposited and annealed at 1100°C for 30 min under N_2/10% O_2 by CNR. CNR also implanted part of the film prepared on undoped Si with 2×10^{15} cm^{-2} boron at 50 keV to serve as a SIMS standard; this generates a boron profile entirely in the nc-SiC.

SIMS profiling of the nc-SiC film on p+ Si was performed by RTG Microanalysis; the result is shown in Figure 6.5. The depth axis is rescaled such that the depth where the carbon signal decreases to half its value in the nc-SiC equals the film thickness measured by SEM. Concentrations in the nc-SiC are quantified using the aforementioned standard, and concentrations in the c-Si using a Si standard (the detection sensitivity in Si is 25% lower).

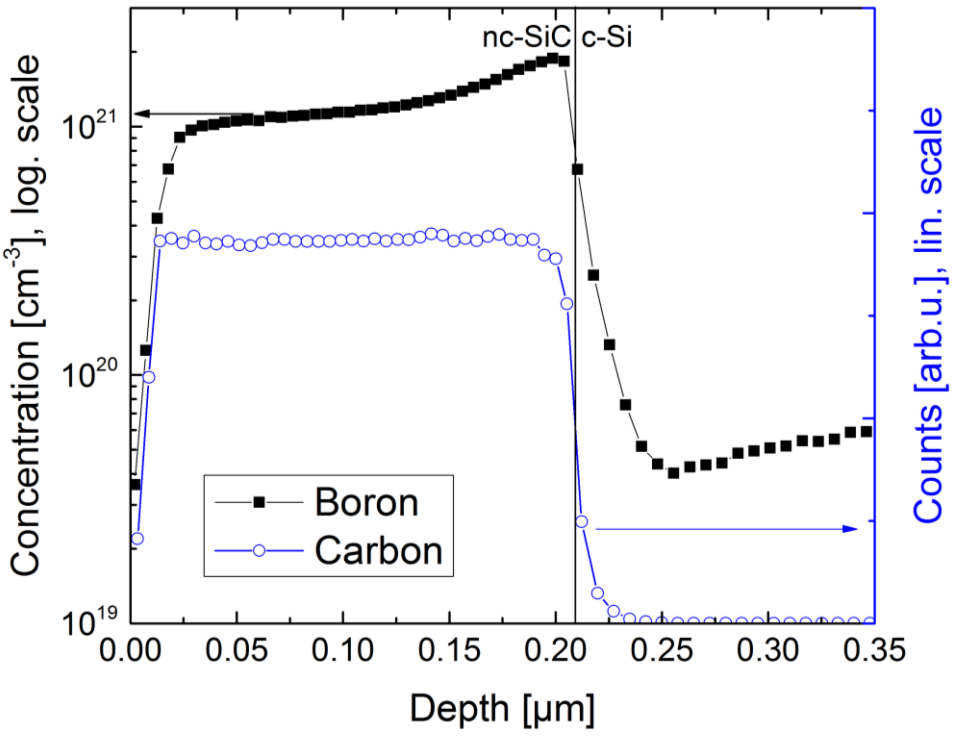

Figure 6.5. SIMS profile of the boron content of the nc-SiC film annealed on a p+ Si substrate. The unquantified carbon signal is plotted as a reference for the nc-SiC / c-Si interface.

The figure shows that annealing at 1100°C for 30 min is sufficient for boron to diffuse throughout the thickness of the nc-SiC film. However, the incredibly high concentrations of $\sim 10^{21}$ cm^{-3} measured by SIMS cannot be correct because the total boron dose in the nc-SiC then exceeds the total dose that was diffused into the Si wafer initially (never mind the fact that only a small part of that can diffuse out of the wafer during the 1100°C 30 min anneal). As quantification with a second nc-SiC standard implanted at ISE yielded the same result, it is concluded that the boron that diffused into the nc-SiC is probably present in a different, more readily detected form than the implanted boron, i.e. in the form of precipitates or clusters [219-221].

The real boron concentration in the nc-SiC was estimated by extrapolating the part of the boron profile in the p+ Si (c-Si, Figure 6.5) to a depth where it intersects the initial boron profile in the p+ Si, integrating the difference to obtain the dose that left the p+ Si, and setting the dose in the nc-SiC equal to this. The result is a boron concentration of 5×10^{19} cm^{-3} in the nc-SiC. Since this is still a very substantial doping level, grazing incidence x-ray diffraction (GIXRD) measurements were performed on the nc-SiC films on p+ and undoped Si to examine the nanostructural effects of boron in-diffusion. Scherrer analysis [169, 222] of the SiC reflections yielded the same grain size for both films, but the peak height was decreased 1.4× for the nc-SiC on p+ Si, indicating fewer crystals. This is a much more subtle effect than the 2.5× decrease in peak height observed for nc-SiC when doping the a-SiC:H precursor with boron during deposition [223], which is attributed to the fact that since the diffusion length of B in Si during the part of the anneal preceding the onset of SiC crystallisation at 900-1000°C [15, 17] is very low, in-diffusion from the substrate must occur after crystallisation has begun. Boron therefore has a much weaker effect on nc-SiC grain growth than on nucleation.

Annealing a-SiC:H on p+ Si has only a minor effect on the resulting nc-SiC nanostructure but nevertheless floods the nc-SiC film with a boron concentration of $\sim 5\times10^{19}$ cm^{-3}. SIMS

quantification can be anomalous, and should be compared to the quantity of dopant supplied. The consequences for a p-n junction depend on the role boron in Si NC/SiC plays electrically. This is not yet fully understood, but if it is an active p-type dopant then what was a n-a-SiC:H / p-c-Si junction before annealing could be a n-nc-SiC / p-nc-SiC / p-c-Si junction, or even a p-nc-SiC / p-c-Si isotype heterojunction, after annealing.

6.2.1.2 Diffusion from a-SiC:H to Si Substrate

If a n-a-SiC:H / p-c-Si junction is prepared, diffusion of n-type dopant from the n-a-SiC:H to the p-c-Si could also occur on annealing. To study this effect for n- and p-type doping, 50 nm thick a-SiC:H films doped with boron and phosphorus were prepared on Si substrates. The same films were prepared with 50 nm undoped a-SiC:H between the doped a-SiC:H and the substrate, and all samples annealed at 1100°C for 30 min. Each sample was prepared in duplicate, and the FTIR spectra of all samples are shown in Figure 6.6. The spectra exhibit a Lorentzian Si-C peak at 800 cm^{-1} that is indicative of nc-SiC, but more importantly, there is a background that increases strongly towards low wavenumbers that arises from free carrier absorption (FCA). FCA can arise from active doping of the nc-SiC or the Si. However, if it arises from active doping of the nc-SiC, the 50 nm thick undoped a-SiC:H interlayer should have no effect on FCA, whereas Figure 6.6 shows that it strongly decreases FCA. This shows that FCA instead arises primarily from boron and phosphorus that have diffused from the a-SiC:H precursor into the Si substrate on annealing.

Assuming all FCA arises in the Si substrate, the diffusion of dopant from the a-SiC:H to the Si wafer can be quantified. The absorptivity due to FCA, α_{FCA}, is given by

$$\alpha_{FCA}(\lambda, n) = \frac{q^3 \lambda^2 n}{4\pi^2 \varepsilon_0 c^3 n_{Si} m_*^2 \mu}, \tag{6.2}$$

where q is the elementary charge, λ is the wavelength, n is the free carrier concentration, ε_0 is the permittivity of free space, c is the speed of light, n_{Si} is the refractive index of Si, m_* is the effective mass, and μ is the mobility [224, 225].

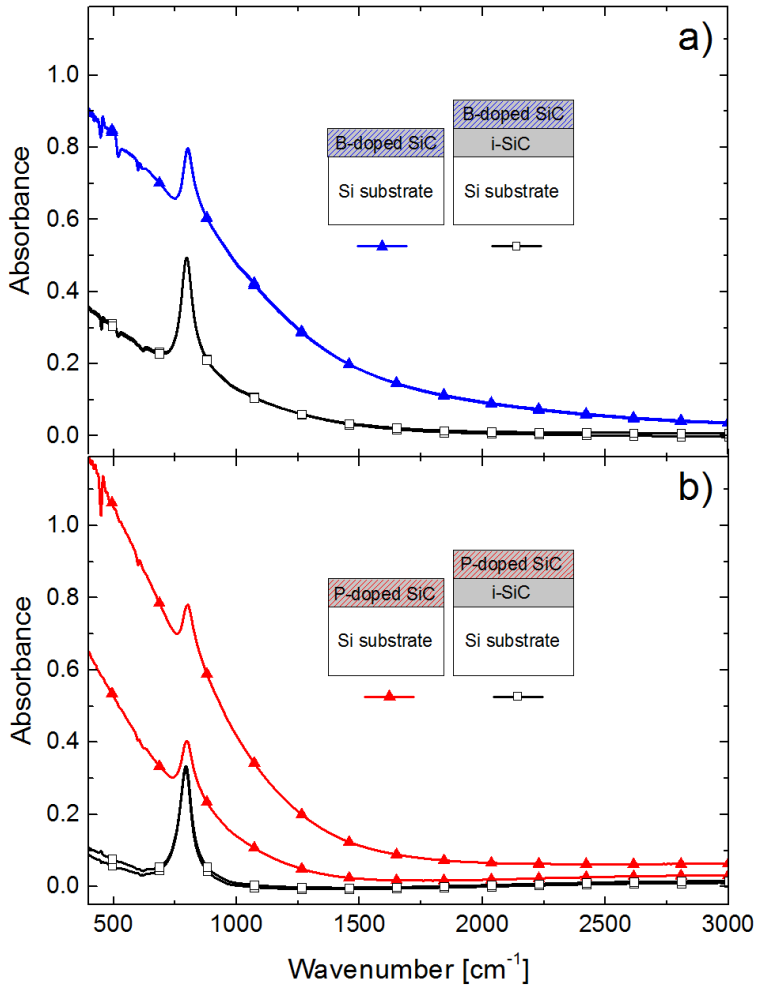

Figure 6.6. FTIR spectra of doped a-SiC:H annealed on Si substrates at 1100°C. (a) boron-doped a-SiC:H deposited directly on Si (full triangles), and with a 50 nm undoped a-SiC:H (i-SiC) interlayer (open squares). (b) as (a), but for phosphorus doping. Each sample was prepared twice and both curves are plotted in each case (in (a) these lie perfectly on top of each other).

The FCA absorbance A_{FCA} which is measured experimentally is obtained by integrating over the thickness of the wafer *w*:

$$A_{FCA}(\lambda, n) = \int_o^w \frac{q^3\lambda^2 n}{4\pi^2\varepsilon_0 c^3 n_{Si} m_*^2 \mu} dx. \quad (6.3)$$

Unfortunately, solving the integral is not straightforward because *n* will vary with *x*, and n_{Si} [226] and μ [6] vary with *n* and hence *x*. The variation is strongest for μ, for which a correction factor *M(n)* to account for *μ(n)* has been derived in Ref. [227]. This factor is applied, and variations in n_{Si} (and m_*) will be accounted for by fitting an upper and lower limit on *n* so as to envelop the experimental data. Thus,

$$A_{FCA}(\lambda, n) = \frac{q^3\lambda^2}{4\pi^2\varepsilon_0 c^3 n_{Si} m_*^2 \mu_i} \int_o^w n(x) \times M\big(n(x)\big) dx, \quad (6.4)$$

where μ_i is the value of the mobility for $n \leq 10^{17}$ cm^{-3}, and the value of the prefactor $\frac{q^3}{4\pi^2\varepsilon_0 c^3 n_{Si} m_*^2 \mu_i}$ is 10^{-10} for n-Si and 2.7×10^{-10} for p-Si [224]. It is assumed that $n(x)$ is of the form

$$n(x) = n_0 erfc(^{-x}/_L), \quad (6.5)$$

where n_0 is the concentration at the nc-SiC / c-Si interface on the Si side, and *L* is the diffusion length of B or P in Si estimated using Eq. 6.1 and data from Ref. [206]. A justification of this approach can be found in Ref. [215]. As *L* is found independently, n_0 is the only fitting parameter, allowing a straightforward fit of Eq. 6.4 to the experimental data. Fits of upper and lower bounds to the FTIR spectra of the doped films without an interlayer

are shown in Figure 6.7(top). The corresponding input profiles *n(x)* are shown in Figure 6.7(bottom).

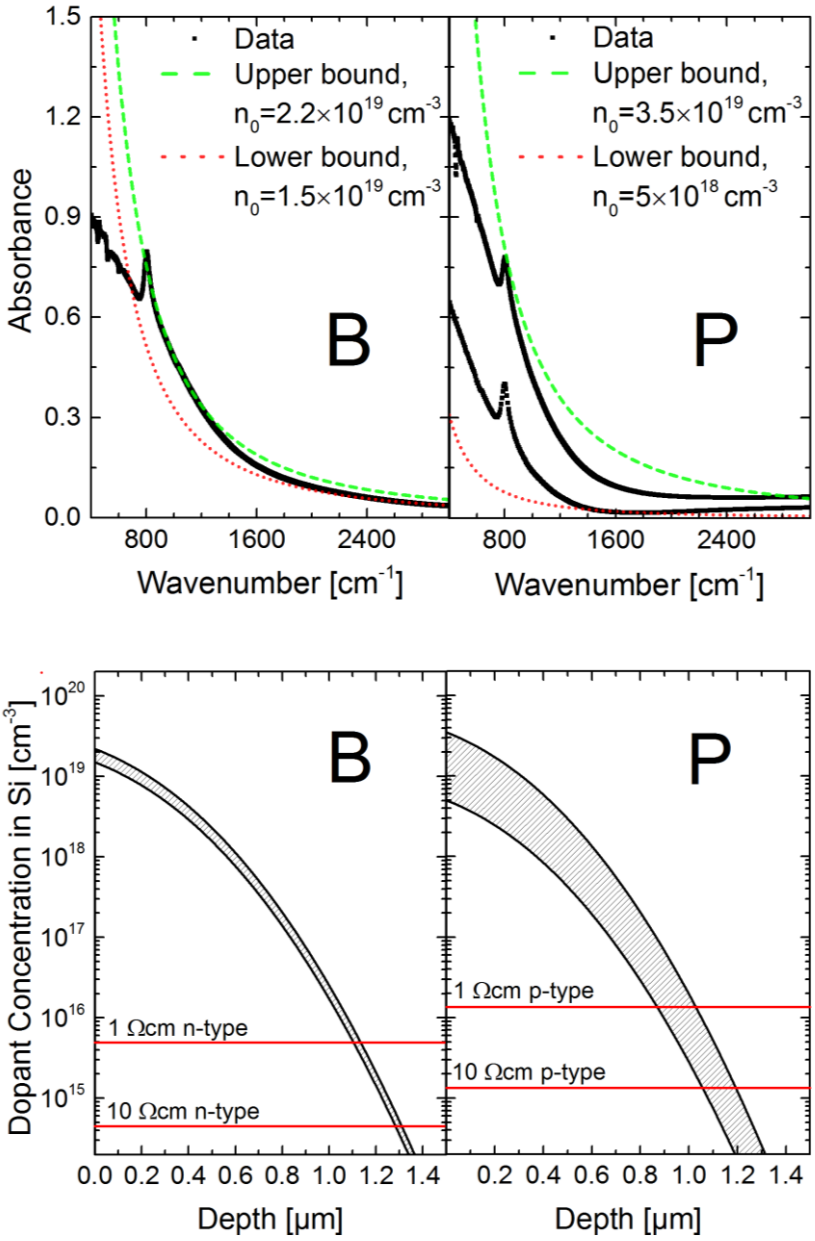

Figure 6.7. Top: Fits of Eq. 6.4 to the FTIR spectra with full triangles of Figure 6.6. Spectra from two nominally identical samples are shown for both B and P doping, and lower and upper bounds fitted so as to envelope both curves. Bottom: Doping profiles *n(x)* corresponding to the fits in the top figure, calculated from Eq. 6.5 with *L* derived using Eq. 6.1. The doping levels of oppositely doped 1 and 10 Ωcm Si wafers are also shown.

Good fits, particularly for boron, are obtained, and the doping concentration on the Si side of the nc-SiC / c-Si interface, n_0, is on the order of 10^{19} cm^{-3} for both dopants. Also shown in

Figure 6.7(bottom) are the doping levels of oppositely doped 1 and 10 Ωcm Si wafers. The intersection with *n(x)* at a depth of ~1 µm for either dopant indicates that a correspondingly deep p-n junction would be formed in a Si wafer if oppositely doped a-SiC:H is annealed on it at 1100°C for 30 min. This means that an anisotype heterojunction may well be converted into a homojunction in the Si wafer by annealing. This has been found to be beneficial for 3C-SiC / Si transistors [228, 229], diodes [230], and solar cells [231], but is clearly detrimental when charge carrier extraction from the nc-SiC is desired. It also means that in the solar cells consisting of doped Si NC/SiO_2 [144] and Si NC/SiC [93] prepared on oppositely doped wafers that were presented in Sec. 2.4, the Si NC layer may not be the emitter but a series resistor. Interdiffusion can be reduced by using an undoped SiC interlayer (see Figure 6.6), by using a nm-thin, conductive and transparent TiO_2:Nb layer (see Sec. 2.4) [147, 148], or by annealing at 1000°C instead of 1100°C.

Overall, the results indicate that doping profiles in a-Si_xC_{1-x}:H / c-Si junctions cannot be expected to survive the anneal required for Si NC formation. Rather, interdiffusion is so rapid that a p-n junction can be moved from the interface to a depth of ~1 µm within the Si wafer, or that the nc-SiC can be flooded with dopant. Some methods to mitigate this exist, but generally better control over doping profiles is expected if they are formed *after* Si NC crystallisation.

6.2.2 Diffusion After Annealing

In order to determine under what conditions doping profiles in Si NC/SiC can be formed by post-crystallisation diffusion, the diffusion of boron and phosphorus into as-crystallised nc-SiC was studied. The nc-SiC films were prepared by CNR by depositing a-SiC:H and annealing at 1100°C for 30 min under N_2/10% O_2. The GIXRD diffractogram in Figure 6.8(a) shows that the resulting films are nanocrystalline and Scherrer analysis [222, 232] yields a

grain size of 4.0 ±0.4 nm. B-doped or P-doped poly-Si was then deposited on the nc-SiC films by atmospheric-pressure CVD at 950°C for 3.5 min to give ~4 µm thick poly-Si films with doping levels of 3×10^{19} cm^{-3} and 1.3×10^{20} cm^{-3}, respectively. For each dopant, separate samples then underwent drive-in anneals at 900°C for 30 min, 1000°C for 3 min, and 1100°C for 30 s and 30 min using an optically heated furnace with 150°Cmin^{-1} heating and cooling ramps. The temperatures listed are as measured by a thermocouple within the furnace used. A prior measurement using a thermocouple bonded to a Si wafer had indicated that the *sample* temperature is 100°C higher. Sample temperatures are taken to be 100°C higher henceforth, with the error of this procedure estimated at ±30°C.

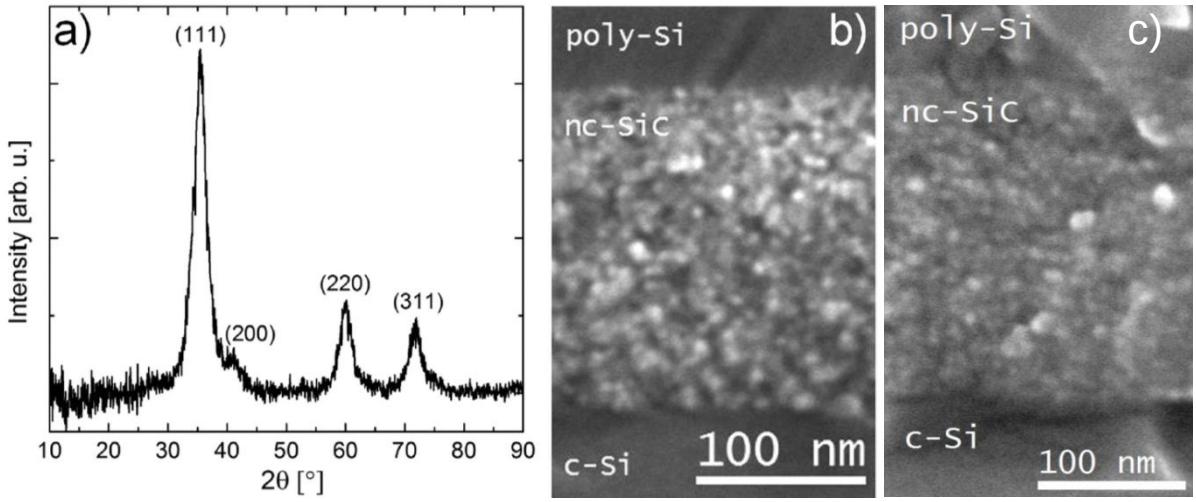

Figure 6.8. GIXRD diffractogram of the as-prepared nc-SiC (a), SEM cross-section of nc-SiC with B-doped poly-Si after 1200°C 30 min annealing (b) and with P-doped poly-Si after 1200°C 30 s annealing (c).

SEM images of the samples exposed to the highest drive-in temperatures (Figure 6.8(b) for boron, (c) for phosphorus doping) show that the layers are neatly stacked with flat interfaces, indicating that processing has not damaged the nc-SiC in any way. The poly-Si dopant source was removed using KOH, and SIMS profiles were acquired by RTG Microanalysis (see Figure 6.9). Again the depth axes were rescaled such that the half-height of the carbon signal corresponds to the film thickness measured by SEM, and concentrations in the nc-SiC

quantified with an implanted standard produced from the same material while concentrations in the Si wafer were quantified with a Si standard.

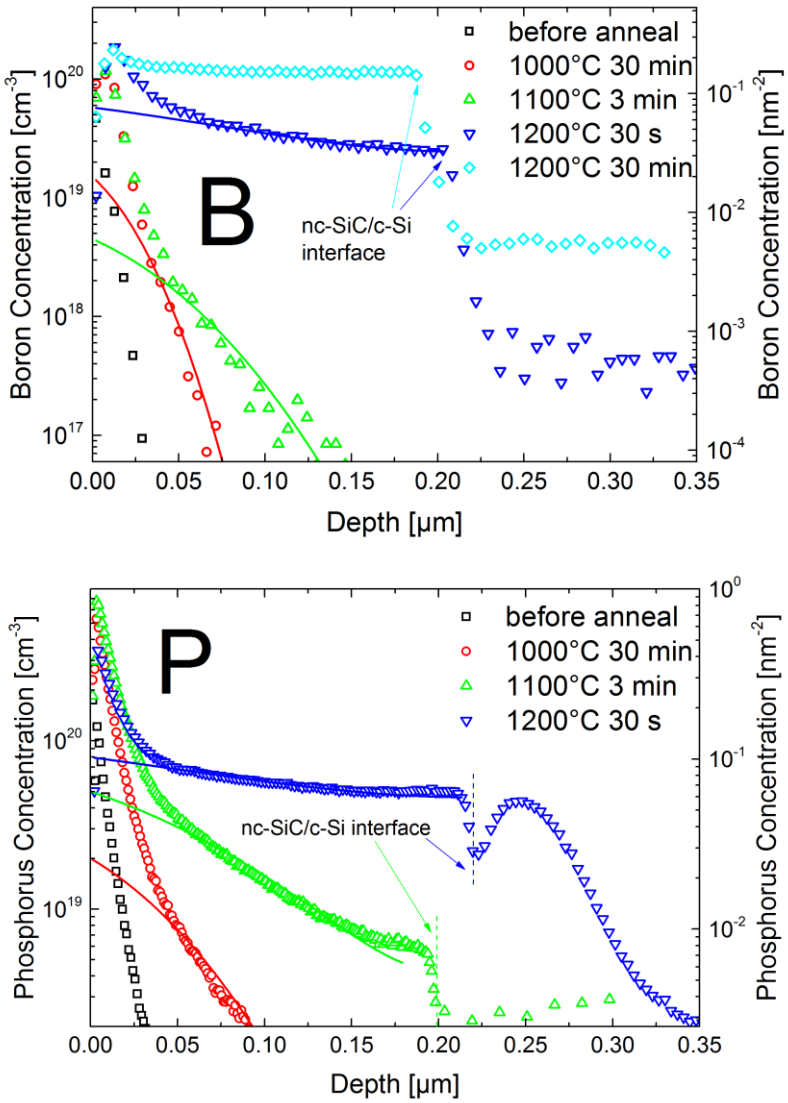

Figure 6.9. Boron (top) and phosphorus (bottom) profiles in nc-SiC after poly-Si deposition ("before anneal") and after different drive-in anneals. Lines are fits of Eq. 6.6 to the data from the bulk of the films. Concentrations are given per cm^3 (left axis) and per nm^2 of grain boundary assuming a grain size of 4.0 nm (right axis, calculated using Eq. 6.9, not applicable to concentrations in the Si substrate).

For both B and P the poly-Si deposition step alone is sufficient to create a shallow doping profile in the nc-SiC ("before anneal"). The profiles become successively deeper for higher drive-in temperatures and 1200°C, even for 30 s, is sufficient to drive either dopant through the entire film. This is unexpected since in monocrystalline SiC (mono-SiC) temperatures of

1700°C and above are required for B diffusion [233], and P diffusion only occurs at 2400°C where SiC begins to evaporate [234]. The observed diffusion must therefore be grain boundary (GB) diffusion. The described diffusion processes are shown schematically in Figure 6.10.

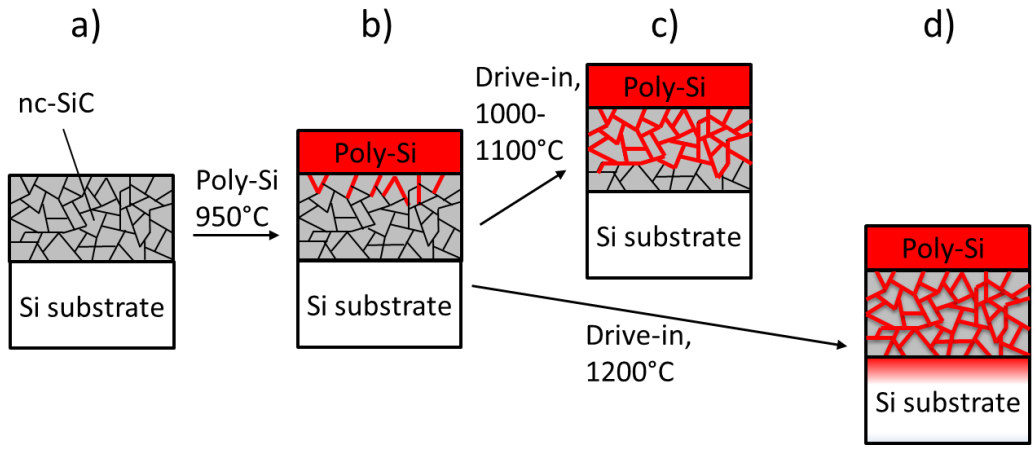

Figure 6.10. Schematic illustrations of the diffusion processes described in this section. Nanocrystalline SiC is formed first (a). Upon poly-Si deposition on the nc-SiC film (b), a shallow diffusion profile forms in the nc-SiC GBs. Annealing at 1000-1100°C causes the GB diffusion profile to extend deeper and deeper into the nc-SiC (c), and annealing at 1200°C leads to diffusion through the entire film and into the substrate (d).

Since intragranular diffusion is utterly negligible, complex models developed for interacting bulk and GB diffusion mechanisms [235, 236] are unnecessary. Instead, Fickian diffusion is assumed and later corrected for the limited cross-section of the GBs. Fickian diffusion [237] into a thick film of thickness *w* follows

$$C(x) = C_0 \left[\mathrm{erfc}\left(\frac{x}{L}\right) + \mathrm{erfc}\left(\frac{2w-x}{L}\right)\right], \tag{6.6}$$

where *C(x)* is the dopant concentration at depth *x*, *L* is the diffusion length, and C_0 is the concentration on the nc-SiC side of the poly-Si / nc-SiC interface. The equation assumes a negligible flux across the nc-SiC / c-Si interface, which is valid for all but the 1200°C 30 min boron and the 1200°C 30 s phosphorus profiles. In the latter case, this is tackled by not fitting

the near-interface points. C_0 is allowed to vary freely because the segregation coefficient as a function of temperature between poly-Si and nc-SiC is unknown. The resulting fits to the "bulk" of the profiles are shown as lines in Figure 6.9. Excellent fits are obtained for all but the top 50 nm of each film.

At 1000°C and 1100°C the effective diffusivity D_{eff} was found from L via $L = 2\sqrt{D_{eff}t}$, where t is the duration of the drive-in anneal, but for the 1200°C 30 s profiles, this was not reasonable since the heating ramps are not negligible. Instead, an iterative process was used. For each dopant, an Arrhenius fit to the effective diffusivities at 1000°C and 1100°C was performed to evaluate a trial form of $D_{eff}(T)$, $D_{eff,trial}(T)$. Then, L_{trial}(1200°C), the diffusion length resulting from the 1200°C 30 s anneal under the assumption that $D_{eff,trial}(T)$ is correct, was calculated using the temperature profile $T(t)$ recorded by a thermocouple inside the furnace tube and the following equation:

$$L_{trial}(1200°C) = 2\left[\int D_{eff,trial}(T(t) + 100°C)\, dt\right]^{1/2}, \tag{6.7}$$

where 100°C was added to $T(t)$ to account for the difference between tube and sample temperature. A difference between L_{trial}(1200°C), and L(1200°C), the value extracted from the 1200°C 30 s profile by fitting Eq. 6.6, indicates that $D_{eff,trial}(T)$ is inaccurate. To remedy this, $D_{eff,trial}$(1200°C) is multiplied by $[L(1200°C)/L_{trial}(1200°C)]^2$ to give a probable value for D_{eff}(1200°C). Next, another Arrhenius fit using this new value for 1200°C and the existing values for 1000°C and 1100°C was performed to find a new $D_{eff,trial}(T)$, and the entire process iterated until convergence. The final values of D_{eff}(1200°C) thus obtained are ~4× lower than would have been obtained by $L = 2\sqrt{D_{eff}t}$. Differently put, the "effective" duration of the 1200°C 30 s anneal when ramps are included is ~120 s, and this value will be used in Eq. 6.11 later.

The values of D_{eff} extracted from L at each temperature for both dopants are shown in Figure 6.11. Since diffusion is solely via GBs which make up a small part of the material cross-section, the real values of flux, and hence of D, are higher. The GB diffusivity D_{GB}, and the dopant concentration per unit area of GB N_{GB}, are given by

$$D_{GB} = \frac{5}{9} D_{eff} \frac{d}{\delta}, \tag{6.8}$$

and

$$N_{GB}(x) = \frac{C(x)d}{3}, \tag{6.9}$$

where d is the grain size, and δ is the GB width [214]. Values of $D_{GB}\delta$ found assuming d=4.0 nm are given on the right-hand axis of Figure 6.11.

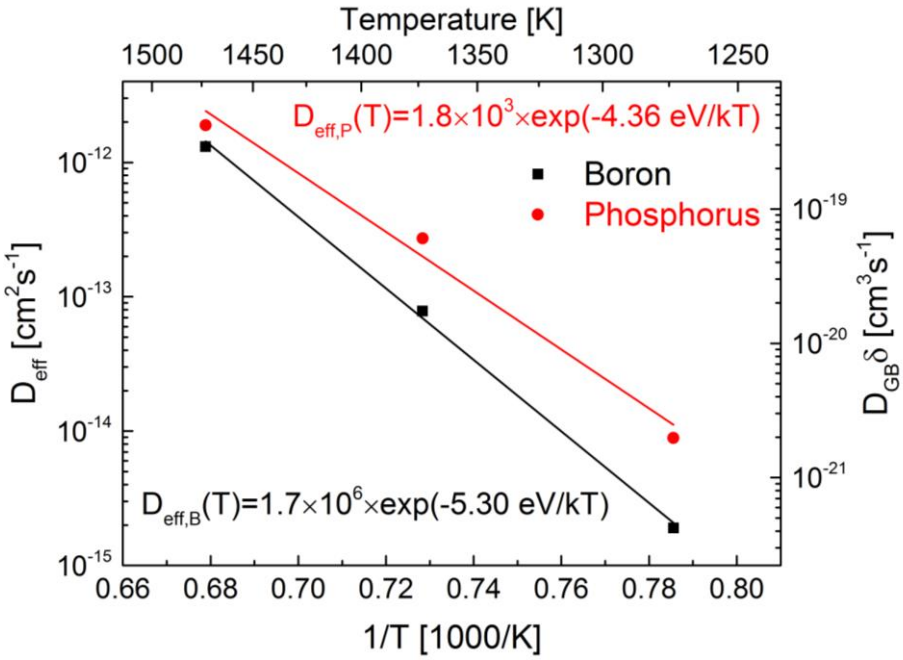

Figure 6.11. Effective diffusivity D_{eff} (left axis) and grain boundary diffusivity-width product $D_{GB}\delta$ (right axis) for boron and phosphorus diffusion in nc-SiC. Arrhenius fits and expressions are shown.

The data follow Arrhenius behaviour very well and the best Arrhenius fits to the data are given in the figure. These are equivalent to the converged $D_{eff,trial}(T)$. Consideration of both the fitting error, and the ±30°C error arising from the conversion to sample temperature, yields activation energies of 5.3 ±0.4 eV for boron and 4.4 ±0.7 eV for phosphorus, with commensurately large variation in the prefactor.

In the case of phosphorus, this activation energy is less than half the value of 11.6 eV measured in mono-SiC [234]. This can be explained in terms of the larger gaps between atoms and more smeared-out energetic landscape in GBs arising from the absence of well-defined lattice sites, and is in agreement with the findings of Hon and Davis for carbon self-diffusion in polycrystalline SiC with d=10 µm [238]. The activation energy of 5.3 ±0.4 eV for boron diffusion is more puzzling as an activation energy of 4.7 eV was reported for B diffusion in mono-SiC [239], particularly since that energy is dominated by kick-out and kick-in barriers that will certainly be much lower, if not absent, at GBs [220]. The value of 5.3 ±0.4 eV thus points to the trapping of boron at point defects at GBs. Dangling bonds known to be present in nc-SiC (see Sec. 5.1.2) are probable trapping sites, and as B prefers C sites in SiC [220, 240, 241] it is proposed that Si dangling bonds trap boron. The implication for Si NC/SiC is that boron diffusion will likely be *slower* in films with Si NCs as more Si dangling bonds are expected, making the values here an upper limit for B diffusivity in Si NC/SiC.

For both boron and phosphorus diffusion the top 50 nm of the films, where concentrations are highest, were not well-fitted by Eq. 6.6. SEM, and modelling of optical reflectance data, did not reveal significant differences in nanostructure [214]. In the case of boron, the scarcity of data points in this region precludes a deeper analysis, but precipitation [221], or the formation of complex immobile point defects [220], are both plausible explanations for a decreased diffusivity that leads to a steeper concentration gradient in that region. In the case of phosphorus, the greater data point density, coupled with the fact that even where Eq. 6.6 fits

the data it has opposite curvature to the data, warrants further analysis via Boltzmann-Matano analysis. In this approach, Fick's Second Law of Diffusion is rearranged to give

$$-2\eta\frac{dC}{d\eta} = \frac{d}{d\eta}\left[D_{eff}(C)\frac{dC}{d\eta}\right], \tag{6.10}$$

$$\eta = \frac{x}{2\sqrt{t}}, \tag{6.11}$$

which is solved numerically for the concentration-dependent effective diffusivity $D_{eff}(C)$. The solutions obtained are shown in Figure 6.12(top).

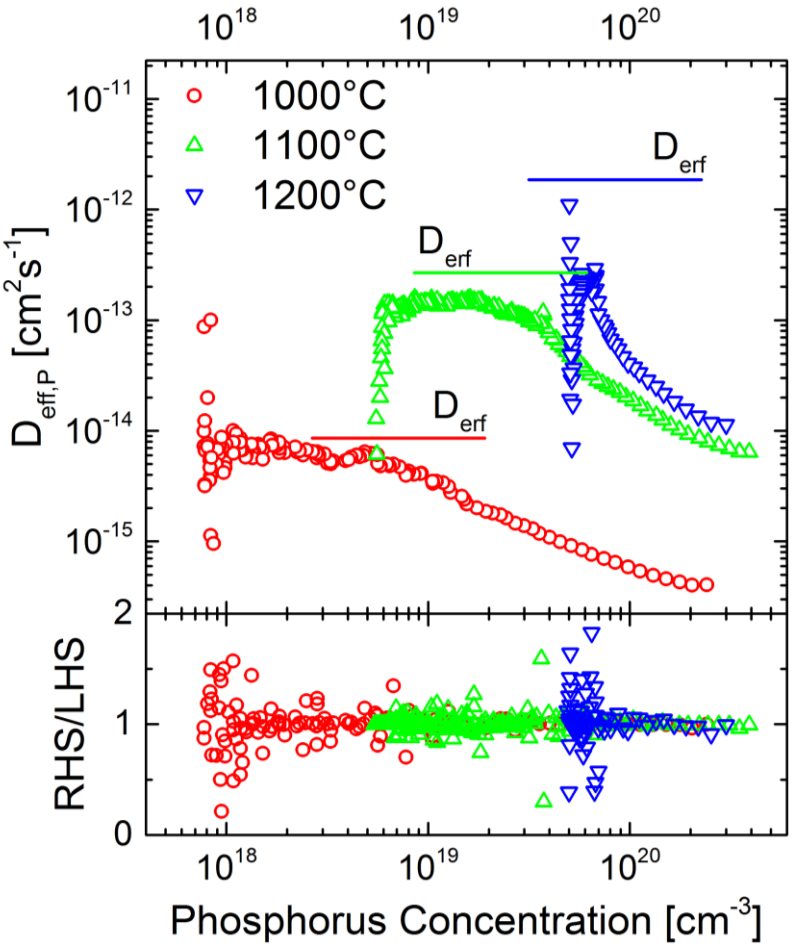

Figure 6.12. Concentration-dependent effective phosphorus diffusivity $D_{eff,P}(C)$ derived from the profiles in Figure 6.9(bottom) using Eq. 6.10 (top), RHS/LHS ratio of Eq. 6.10 for $D_{eff,P}(C)$ (bottom). $D_{eff,P}$ values from Figure 6.11 are reproduced as lines labelled D_{erf}.

The bottom panel gives the ratio of the right- and left-hand side (RHS, LHS) of Eq. 6.10 for the solutions in the top panel and shows that consistent solutions are obtained for most of the examined concentration range. Relatively constant diffusivities are obtained in the lower concentration ranges that are in good agreement with the diffusivities previously derived by fitting Eq. 6.6 (see Figure 6.9, Figure 6.11). An exception is the 1200°C dataset where Eq. 6.10 and 6.11 were applied with t=120 s as discussed previously. Boltzmann-Matano analysis hence validates the previous fits to 1000°C and 1100°C data but also reveals a decrease in diffusivity with concentration at higher concentrations at all temperatures. The onset of the decrease increases with temperature. This is in agreement with the onset of Fermi level-dependent diffusion as well as precipitation since the intrinsic carrier concentration and solubility limit both typically increase with temperature. Rudimentary IV measurements performed with silver paint contacts indicate that phosphorus is electrically active in the nc-SiC, so both are plausible explanations.

In summary, it is found that diffusion precludes the survival of a-Si_xC_{1-x}:H / c-Si p-n junctions formed before the anneal required for Si NC formation, but permits the formation of doping profiles in as-crystallised nc-SiC films. Shallow doping profiles can be formed at 950-1000°C. Boron and phosphorus diffusion proceed exclusively along grain boundaries, with activation energies of 5.3 ±0.4 and 4.4 ±0.7 eV, respectively. At high concentrations, profiles deviate from a constant diffusivity fit, indicating a reduced diffusivity either due to a Fermi level dependence, or a reduction of mobile diffusant due to precipitation.

6.3 Tunnel Junctions

A functioning two-terminal tandem cell requires a series connection between the top and the bottom cell (see Figure 6.1). This is perhaps the most difficult component to design because unless the Si NC/SiC film is transferred onto the Si cell from a different substrate, the series

connection must withstand the anneal needed for Si NC formation. From an electrical viewpoint a metallic material would suffice, but metals do not exhibit the necessary transparency, and the highest temperature to which transparent conducting oxides have been reported to be stable is 900°C [37]. In the following, the viability of tunnel diodes, which are the standard series interconnect for III-V multijunction solar cells [242, 243], is examined. In tunnel diodes, both the p- and the n-type region are doped degenerately, giving rise to the band diagram and current-voltage (IV) curve in Figure 6.13. In order for them to work well as tandem cell interconnects, the short-circuit current density j_{sc} must be transmitted at negligible applied voltage.

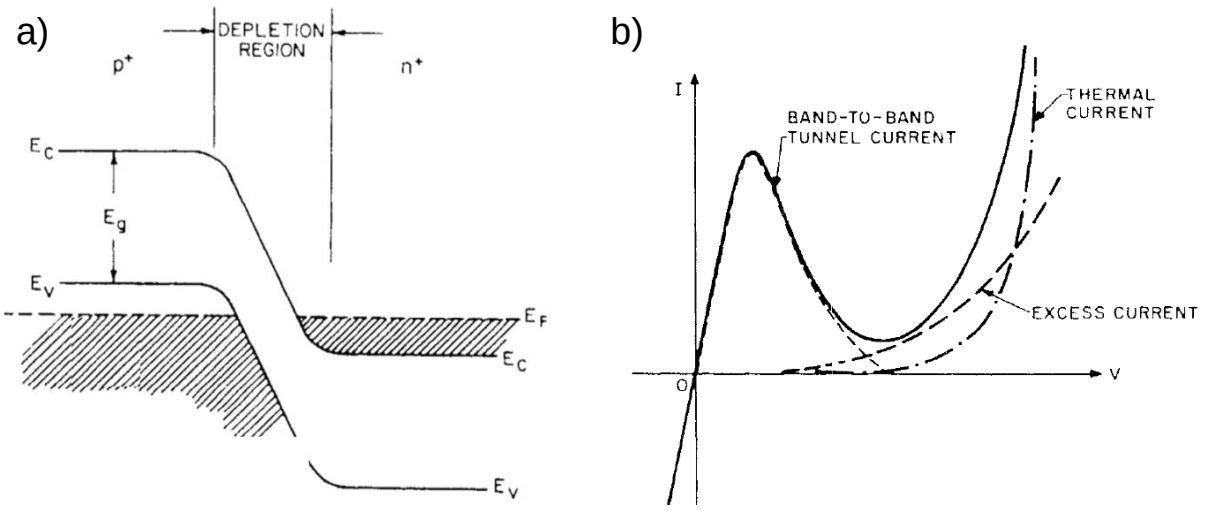

Figure 6.13. (a) Band diagram and (b) IV curve of a tunnel diode, both reproduced from Ref. [6]. The thermal current is the regular diode current $I=I_0(\exp(qV/kT)-1)$, where I_0 is the reverse saturation current; the band-to-band tunnelling current flows between the conduction band of the n+ semiconductor and the valence band of the p+ semiconductor, and is reduced once $V_{bi}-V<E_g/q$, where V_{bi} is the built-in voltage; and the excess current is an additional current that arises from tunnelling via defects in the depletion region.

6.3.1 Si / Si Diodes

Si / Si tunnel diodes have been around since the 1960s [244] and would be the most straightforward to integrate as no new materials would be needed. The question is whether they can withstand the NC anneal. To examine this, abrupt epitaxial n+ Si / p+ Si diodes were

prepared using atmospheric-pressure (AP)CVD. The highest available doping concentrations of 1.0×10^{20} cm^{-3} phosphorus and 6×10^{19} cm^{-3} boron were used, and the process time at 1075°C limited to 3 min. Nevertheless, the resulting devices exhibited regular diode behaviour, indicating that the interdiffusion that occured during the 1.5 min where n+ Si is deposited at 1075°C widened the depletion region sufficiently to stop band-to-band tunnelling. Since lower deposition temperatures would have yielded poly-Si, and since 1075°C for 3 min is still short of the thermal budget used for Si NC crystallisation (1100°C for 30 min or 1050°C for 60 min), Si / Si tunnel diodes were determined to be unlikely to work in a tandem cell and therefore not investigated further.

6.3.2 Si / SiC Junctions

Since Si and SiC are the two main materials in a [Si NC/SiC] / c-Si tandem cell it is reasonable to stick to these for developing a suitable tunnel junction. SiC / SiC tunnel diodes are impossible as no sufficiently soluble and shallow p-type dopant exists for degenerate doping [30]. However, p+ Si / n+ SiC tunnel diodes could be possible. Degenerate p+ Si and n+ SiC can be prepared using boron and nitrogen doping, respectively. Nitrogen has very low solubility in Si, so compensation of p+ Si by in-diffusing nitrogen should not occur. Boron diffusion from p+ Si into n+ SiC may occur via SiC grain boundaries if the SiC is polycrystalline (see Sec. 6.2.2), compensating the n-type SiC doping [30]. As seen in Sec. 6.2.2 and Ref. [245], boron also segregates to SiC, leading to the risk of boron depletion on the p+ Si side of a p+ Si / n+ SiC junction. Nevertheless, previous work conducted at ISE showed that a junction involving p-Si molten and recrystallised on an n-SiC surface exhibited an Ohmic IV curve provided the nitrogen doping of the SiC was strong enough [246]. No region of negative differential resistance that one expects for direct tunnelling was found, but no rectifying behaviour occurred either.

To investigate this point further, two types of n+ SiC / p+ Si test devices were prepared that are shown in Figure 6.14(a),(b). The first type of device (henceforth "SiC / Si junction") was prepared on RCA-cleaned p+ Si wafers by p+ Si epitaxy (APCVD, 1000°C, doped with 3×10^{19} cm^{-3} boron), with cooling under B_2H_6 to ≤600°C. Samples were then cleaned in HNO_3 and HF, and polycrystalline n+ SiC (grain size of ~0.1 µm, resistivity $\rho\approx100$ Ωcm [246]) deposited by APCVD at 1100°C. Samples were heated to 1100°C under a slight B_2H_6 flux, followed by a 2 min deposition of n+ SiC resulting in n+ SiC thicknesses of 0.4-1.2 µm. All APCVD depositions of Si needed for work within this thesis were carried out by Thomas Rachow, and all APCVD n+ SiC depositions by Kai Schillinger, both at ISE. In the second type of device (henceforth "Si / SiC junction"), SiC and Si are reversed. 6-10 µm n+ SiC was deposited on mechanically polished graphite substrates, followed by 1.4-1.8 µm p+ poly-Si (3×10^{18} cm^{-3} boron), also by APCVD. For both types of junctions substrates were chosen so as to have minimal impact on the measured IV curves. For all samples, APCVD of Si and SiC occurred in different reactors, and thicknesses were determined from weight differences. All samples were metallised with 5 µm electron beam-evaporated Al, full-area on the rear side and dots produced with a shadow mask on the front side. Sample edges were removed by laser cutting to eliminate edge leakage currents.

The corresponding IV curves in Figure 6.14(c) and (d) show that all devices exhibit essentially Ohmic conduction. Conductances for Si / SiC junctions are uniform, whereas those of SiC / Si junctions vary considerably across wafers, seemingly as a function of n+ SiC thickness t_{SiC}. It is improbable that this is a genuine series resistance (R_s) effect since R_s of the n+ SiC - assuming current is limited to the dot area and ρ=100 Ωcm - is only ~1 Ω. If it were an R_s effect, it would imply that ρ is in fact 3×10^4 Ωcm, which given that these are the sorts of resistivities obtained on C films in Chapter 5, which have a smaller grain size and are nominally undoped, is rather unrealistic. Furthermore, the Si / SiC junction wafers 1, 2, and 3 have t_{SiC}=6.3, 6.3, 8.4 µm, respectively, and yet junctions on wafer 1 are the most resistive.

The performance of SiC / Si junctions must therefore be strongly affected by a different parameter that varies with t_{SiC} (although not the local temperature, which is known to be uniform throughout the reactor [247]).

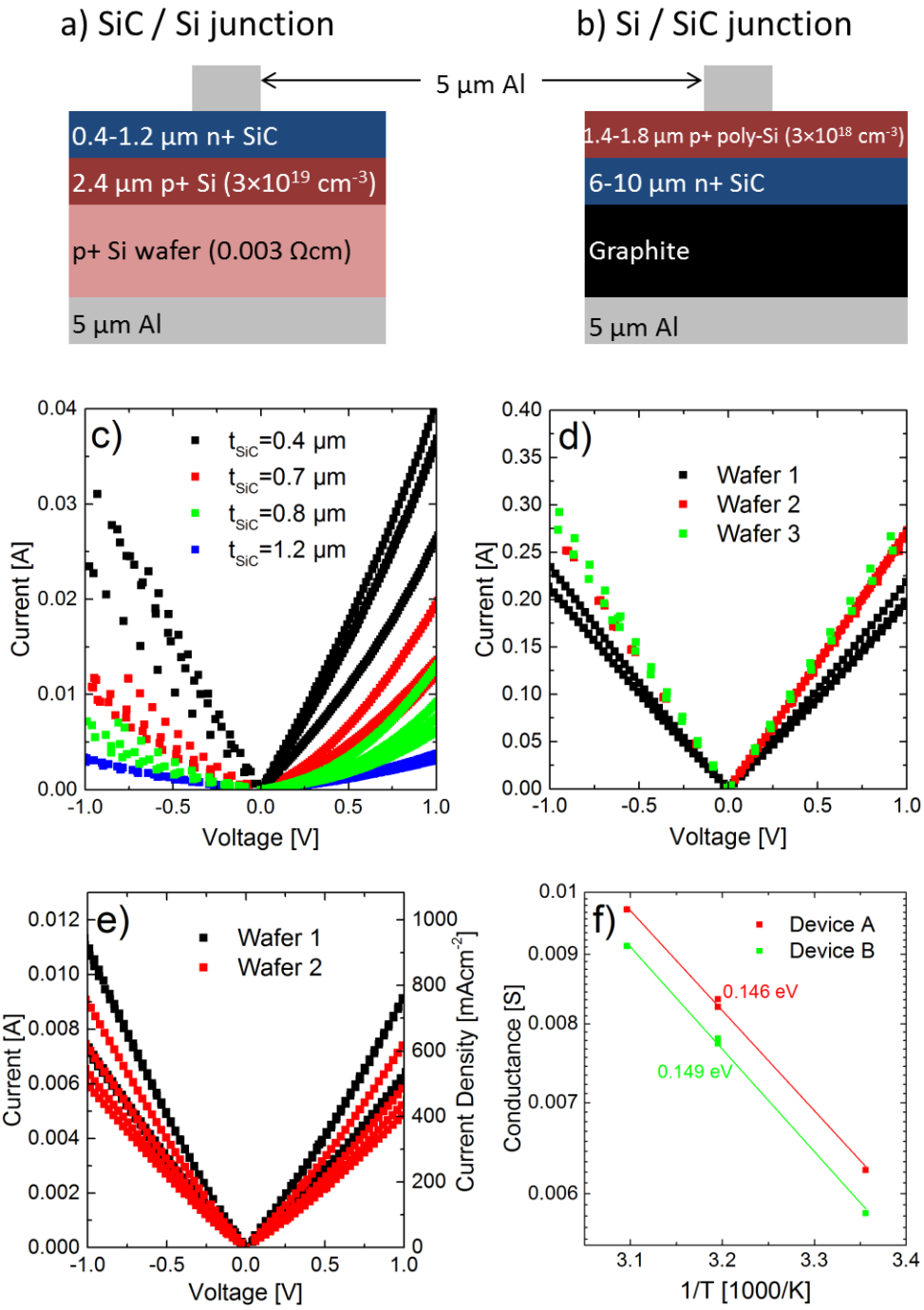

Figure 6.14. Schematic diagrams of (a) n+ SiC / p+ Si and (b) p+ Si / n+ SiC test devices (SiC / Si, Si / SiC junctions, respectively). Device preparation is described in the text. (c), (d): IV curves of devices in (a), (b), respectively. (e) IV curves of mesa-etched Si / SiC junctions. (f) Arrhenius plots of conductance of two mesa-etched Si / SiC junctions. In (c),(d),(e) multiple IV curves are shown for each sample.

Si / SiC junctions exhibit ~10× greater conductance than SiC / Si junctions (see Figure 6.14(c),(d)). To check whether this is due to current spreading in the poly-Si, a mesa etch was performed on some Si / SiC junctions by reactive ion etching. The Al dots are not etched and act as a mask for the etch. IV curves of mesa-etched Si / SiC junctions are shown in Figure 6.14(e); the resulting currents are an order of magnitude lower. SiC / Si junctions could not be mesa-etched so the effective device area is not certain. However, for current spreading outwards from a disc of radius r by Δr, the resistance R follows

$$R = \int_r^{r+\Delta r} \frac{\rho}{2\pi r t_{SiC}} dr = \frac{\rho}{2\pi t_{SiC}} \ln\left(\frac{r+\Delta r}{r}\right), \tag{6.12}$$

which for $\Delta r = 0.01r$, ρ=100 Ωcm, t_{SiC}=1 µm gives R≈1500 Ω. This suggests current spreading in SiC / Si junctions is negligible, and indicates that they are comparable to the mesa-etched Si / SiC junctions, which both exhibit very similar conductances. Since the p+ Si part of the junction consists of epitaxial Si in the case of SiC / Si junctions, and of poly-Si with a 10× lower doping concentration in the case of Si / SiC junctions, the similarity in conductance is unexpected. It is attributed to the fact that the epitaxial Si in SiC / Si junctions is exposed to the n+ SiC deposition at 1100°C, and that during this process boron diffuses from the p+ Si to the n+ SiC such that the effective p+ doping level at the p-n junction is similar for both types of devices.

This raises the question how these junctions, in which p+ Si doping is insufficient for degeneracy, can exhibit Ohmic conduction. A band-to-band tunnelling current is not possible and the normal diode current ("thermal current" in Figure 6.13(b)) is highly non-Ohmic, leaving the excess current as an explanation. It arises from carriers tunnelling from the conduction band of the n+ semiconductor to the valence band of the p+ semiconductor via defect states in the depletion region. This is the key mechanism in a-Si / µc-Si tandem cells [248, 249], where the junction connecting the two cells is often termed a "tunnel

recombination junction" (TRJ) [250]. It is illustrated schematically in Figure 6.15(a). This must be so because a-Si:H / µc-Si:H tandem cell efficiencies would be much lower than observed in practice if only a thermal current flowed in the TRJ [249].

These junctions also exhibit Ohmic IV curves [251] and the conductances of the junctions as well as the efficiencies of the tandem cells are enhanced by deliberately increasing the defect density in the space charge region of the TRJs [249, 251, 252]. That an increased defect density improves any part of a semiconductor device appears counterintuitive, but the sole purpose of the interconnect between cells is to allow holes from one cell and electrons from the other cell to recombine with minimum loss of energy [253], whether it be by direct tunnelling from the conduction to the valence band, by flowing into a metallic interconnect (metals are taken to exhibit infinite recombination velocity), or by defect-assisted tunnelling.

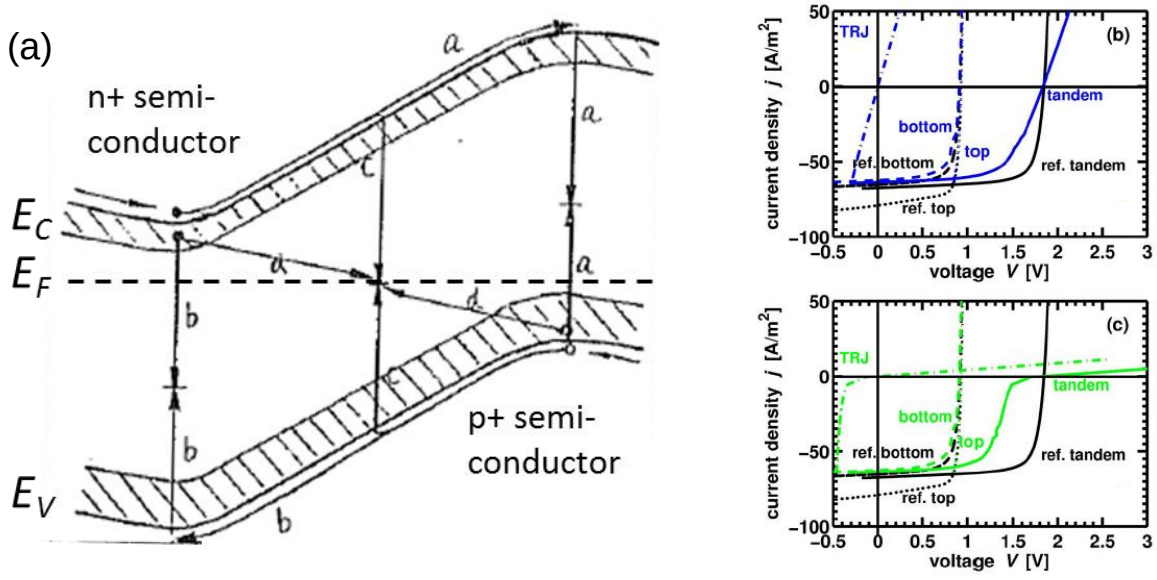

Figure 6.15. (a) Band diagram of a tunnel recombination junction (TRJ). The finite widths of E_C and E_V represent tail states that may, but need not be present. Electrons in the n+ and holes in the p+ semiconductor must recombine, but direct tunnelling is not possible. Excitation of either electrons (process a) or holes (process b) or both (process c) over the barrier requires an energy qV_{bi} where V_{bi} is the TRJ built-in voltage; this is undesirable. Recombination via defects in the space charge region (process d) can proceed without an energy barrier. Figure adapted from Ref. [249], reproduced with permission. (b),(c) IV curves of the TRJ, bottom cell, top cell, and tandem cell as compared to a reference with a perfect TRJ for an Ohmic TRJ (b) and a diode-like TRJ (c). Both reproduced from Ref. [250] with permission from WIP.

It is worth noting that even though defect-assisted tunnelling appears from Figure 6.15(a) to involve a loss of energy (process d), this does not lower the open-circuit voltage (V_{oc}) of the tandem cell because V_{oc} derives from the sum of the quasi-Fermi level separations in the two cells which is not lowered as long as the quasi-Fermi levels for electrons in the n+ and holes in the p+ semiconductor of the TRJ are the same. This requires negligible Fermi level splitting within the TRJ, which can be achieved with high doping and thin layers, and sufficiently rapid recombination in the TRJ to avoid pile-up of carriers from the two cells, as this would result in a voltage across the TRJ that opposes the V_{oc} of the two cells it connects.

The key issue is what voltage is needed to drive a current density j through the TRJ as $V(j)$ of the tandem cell will be reduced by this amount. This has little effect on V_{oc} as no current needs to be driven through the TRJ at open-circuit for a current-matched tandem cell [250], and little effect on j_{sc} as dj/dV at j_{sc} is low in a standard solar cell, but leads to a reduction of $V(j)$ at and above the maximum power point where j and dj/dV are significant [250, 254], much like any other series resistance in the cell [255] (see Figure 6.15(b)). A diode-like TRJ leads to an S-shaped jV curve (see Figure 6.15(c)). For SiC / Si and Si / SiC junctions, $V(j$=20 mAcm^{-2}) is 9-130 mV and 25-60 mV, respectively, which represents a reasonable upper bound on voltage loss since $j_{sc}\leq$20 mAcm^{-2} is a good estimate for two-junction tandem cells under one sun illumination.

Tunnelling is generally independent of temperature, which was confirmed for defect-assisted tunnelling in TRJs made of a-Si:H and µc-Si:H by Hegedus [248]. The Si / SiC junctions, however, exhibit thermally activated conduction with an activation energy E_a=0.15 eV (see Figure 6.14(f)). This agrees with the values of 0.13-0.25 eV reported by Kwak *et al*. for n-µc-Si:H / p-a-SiC:H TRJs [256], who, however, did not identify the origin of this thermally surmountable barrier, and did not see a strong effect of E_a on tandem cell performance. It is thus unclear what this value represents, but even the sum of E_a/q and $V(j$=20 mAcm^{-2}), which is an upper limit on the voltage that *might* be dropped across the TRJ if E_a is in fact an

additional barrier, is <0.3 V, which is substantial but still acceptable for a tandem cell test device. Such TRJs will therefore be used to fabricate tandem cells, and this and other results from this chapter drawn upon to develop a suitable tandem cell processing route which is detailed in the next chapter.

7. Tandem Cells

Based on the results in previous chapters tandem cells with a c-Si bottom cell and a top cell with an absorber of Si NCs embedded in SiC (Si NC/SiC) were prepared and characterised. The process chain followed for the preparation of the cells and the results obtained from them are described in this chapter. The results have also been published in Ref. [257].

7.1 Processing

Broadly speaking the tandem cell requires a Si cell with a p-n junction, a Si NC/SiC cell with a p-n junction, a tunnel junction connecting the two, and contacts on top and bottom of the tandem cell. It is therefore a complex device, and since the Si NC/SiC material itself is also not perfectly understood, the simplest or most practical, rather than the optimum, solution is sought for the different device components. For this reason, a float-zone (FZ) Si wafer bottom cell is used, even though due to the limited photocurrent expected for the Si NC/SiC cell based on the poor photoluminescence (see Chapter 4), undetectable photoconductivity (see Sec. 5.3), and poor short-circuit current density j_{sc} of Si NC/SiC membrane cells [258], a thin film Si bottom cell would likely suffice for current matching. The tandem cell current will therefore be limited by the Si NC/SiC cell. The overall device structure is shown in Figure 7.1; the reasons for this particular structure are described in the following and the complete process chain is given in Appendix B: Full Tandem Cell Process Chain.

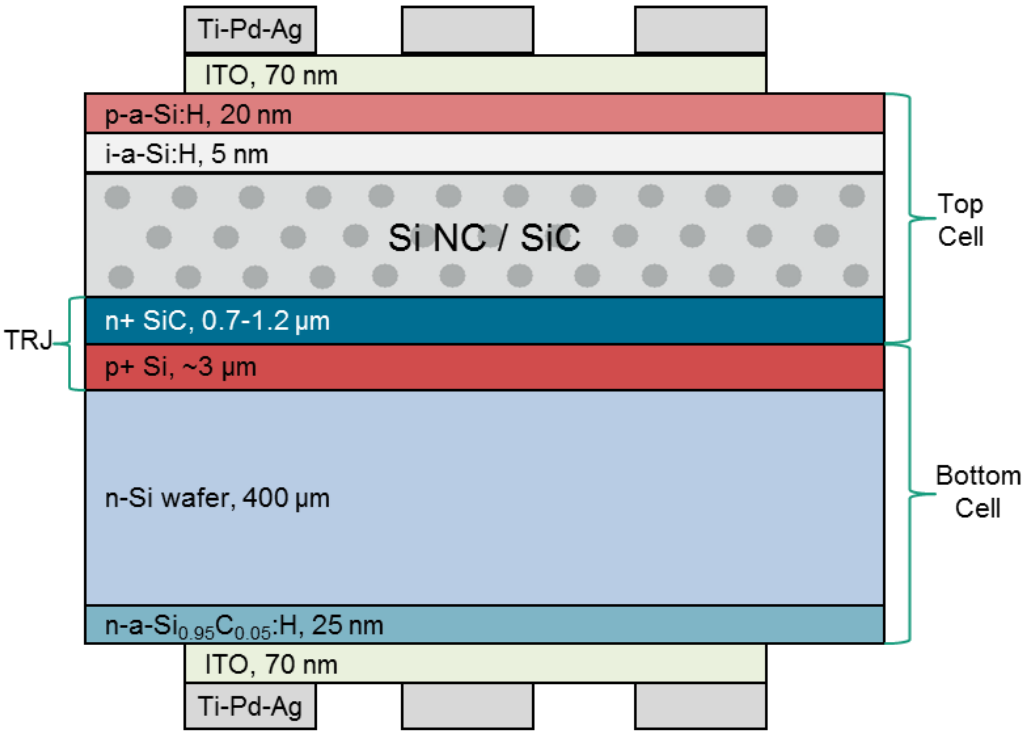

Figure 7.1. Schematic diagram of the [Si NC/SiC] / c-Si tandem cells prepared within this thesis. The layers comprising the two subcells, and the tunnel recombination junction (TRJ) serving as the series connection, are labelled with brackets.

The only tunnel junction within the Si-SiC system that was found to work in Sec. 6.3 was a n+ SiC / p+ Si tunnel recombination junction (TRJ). Since the n+ SiC has never been used as an emitter or back surface field for a Si solar cell before, the TRJ will be deposited such that the p+ Si is connected to the Si wafer. The p+ Si can be an emitter on a n-Si wafer, or a front surface field on a p-Si wafer. Due to foreseeable problems in preparing a clean rear-side junction, the former option was chosen. Thus far, the structure is n+ SiC / p+ Si / n-Si wafer.

The n+ SiC is known to cause bowing of Si wafers when it is only deposited on one side of the wafer. To check for this, 1 µm and 4 µm n+ SiC was deposited on Si wafers of different thickness. 4 µm n+ SiC caused bowing visible to the naked eye, while 1 µm n+ SiC led to a bow of 22-25 µm for 250 µm wafers, but <3 µm for 400 µm wafers. Therefore 400 µm, 5 Ωcm n-Si wafers were used, and a n+ SiC thickness of 1 µm targeted. Actual thicknesses as determined by weighing varied from 0.7-1.2 µm. Depositing thinner n+ SiC was not feasible as the deposition tool is set up for $\mu m \cdot min^{-1}$ growth rates.

Since the n+ SiC is deposited at 1100°C, and the Si NC/SiC annealed at 1100°C for 30 min, the p+ Si emitter must be able to withstand these thermal budgets. To improve reproducibility, a BBr_3 diffusion was used instead of the APCVD Si epitaxy processes from Sec. 6.3, and to ensure that the p+ Si emitter survives the aforementioned high-temperature steps, the established diffusion process with the highest dose was selected. A PECVD SiO_2 layer was deposited on the rear side of the n-Si wafers to achieve a single-sided diffusion. The successful shielding from diffusion by this layer was confirmed on reference samples using sheet resistance measurements before and after diffusion. The boron profile obtained before and after a 1100°C 30 min anneal under N_2/10% O_2, as measured by electrochemical capacitance-voltage spectroscopy, is given in Figure 7.2.

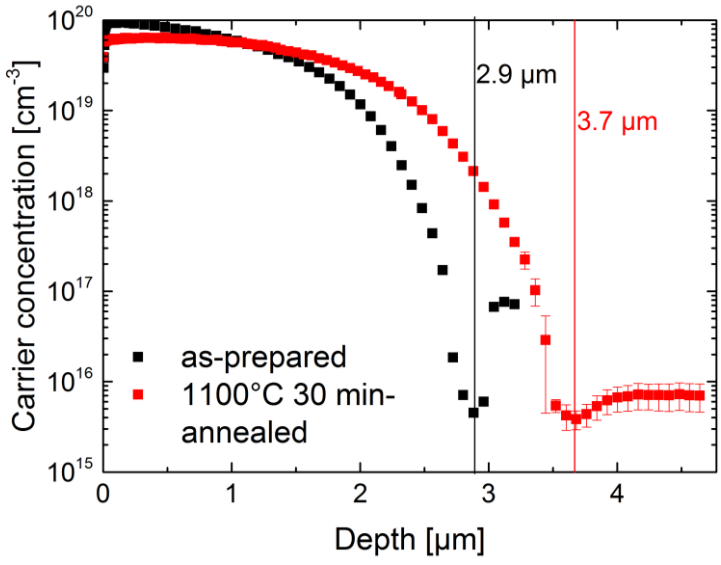

Figure 7.2. Doping profile of the diffused boron emitter used for the Si bottom cell before and after a 1100°C 30 min anneal, as measured by electrochemical capacitance-voltage spectroscopy (ECV). As ECV measures carrier concentration, the minimum represents the p-n junction whose depth is labelled in the figure.

The profile is deepened somewhat by the anneal but a high surface concentration is maintained. Unfortunately, these profiles had to be measured on reference samples as a measurement through the n+ SiC is not possible, and do not therefore take into account boron diffusion from Si to n+ SiC. Jonas Schön simulated diffusion of boron from Si to n+ SiC

using as inputs the highest boron diffusivity reported for SiC in the literature [259] as well as a segregation coefficient of 20 in favour of the SiC taken from Ref. [245]. He found that the interfacial boron concentration on the Si side never dropped below 10^{18} cm^{-3}. Since a boron concentration of 3×10^{18} cm^{-3} was sufficient for TRJ performance in the Si / SiC junctions in Sec. 6.3.2, TRJ performance is not expected to be compromised by annealing.

To check this, TRJ devices were prepared with this particular TRJ by carrying out the BBr_3 diffusion and n+ SiC deposition on p+ Si wafers, followed by electron beam evaporation of Al on the front and rear side. Front-side metallisation was in the form of dots structured by a lift-off process. Squares twice the size of the dots were laser scribed around some dots, but no systematic change in resistance was observed, indicating that the effective device area is at most two times larger than the dot. In the following it is assumed that no current spreading occurs.

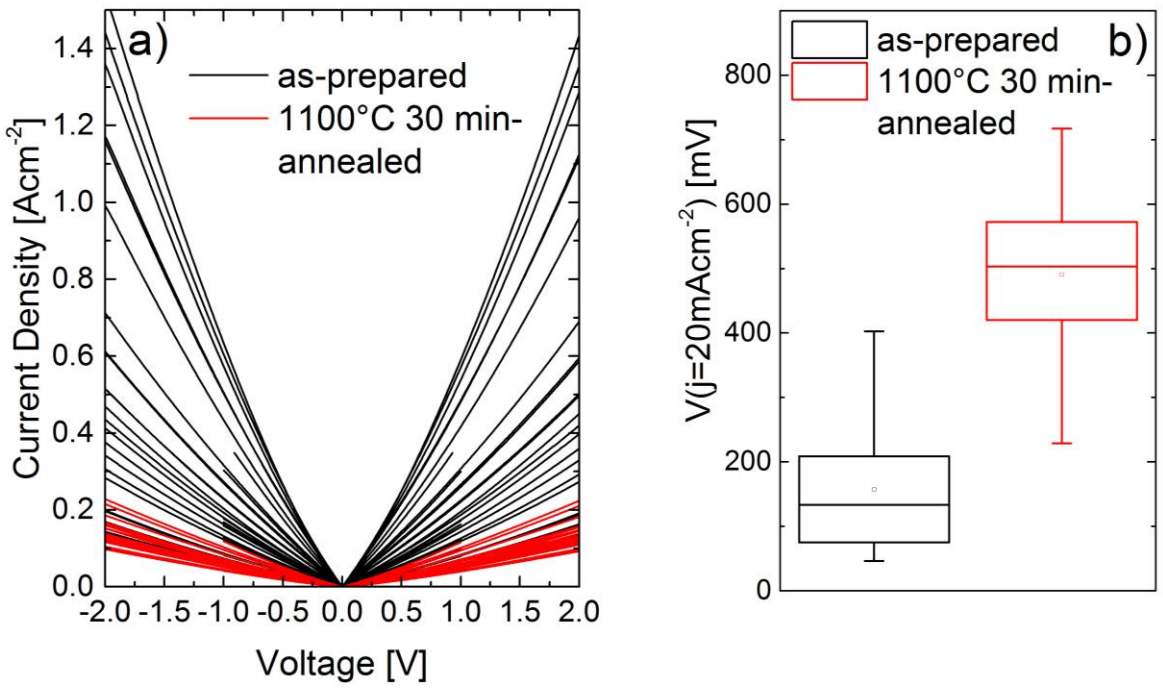

Figure 7.3. (a) Current density-voltage (*jV*) curves of TRJs resembling those used for the tandem cells, as-prepared and after a 1100°C 30 min anneal. 32 curves are shown for each type of TRJ. All devices exhibit Ohmic conductance which is reduced by annealing. The voltages required for a current density of 20 $mAcm^{-2}$ are shown in (b). Features of the box diagram are as in Figure 7.7(b)-(e).

Figure 7.3(a) shows that these TRJs are also Ohmic, both as-prepared and after a 1100°C 30 min anneal under N_2/10% O_2. As-prepared TRJs exhibit quite a large scatter in conductance. The anneal lowers the conductance ~3×, leading to the requirement of higher voltage to transmit a current density j=20 mAcm^{-2} ($V(j$=20 mAcm^{-2})). In both cases, mean $V(j$=20 mAcm^{-2}) is much higher than in the test devices described in Sec. 6.3.2; ~160 mV for as-prepared junctions and ~490 mV for annealed junctions (see Figure 7.3(b)). This kind of voltage loss would cripple the performance of the tandem cell, but the real short-circuit current density of the tandem cells may be lower than the best-case estimate of 20 mAcm^{-2}, in which case the voltage loss at the TRJ would be lower too. The activation energy for conduction is 0.19-0.21 eV for both as-prepared and annealed TRJs. At any rate, an impairment of device performance due to the TRJ would be evident from a tandem cell current density-voltage (jV) curve resembling Figure 6.15(b),(c).

The n+ SiC for all tandem cells was deposited in a tool developed for double-sided coating of substrates. To ensure one-sided deposition, wafers were placed back-to-back. This approach failed in some cases, and miscellaneous parasitic deposition occurred on the rear side of the wafers. The parasitically deposited films were successfully removed by reactive-ion etching (RIE); however, RIE led to significant roughening of the rear side of the wafers. This roughness was never fully eliminated, but it had little effect on minority carrier lifetime (see Figure 7.4(b)), and devices with and without this roughness yielded similar results. It is the reason why no rear-side emitter was used.

Once the n+ SiC / p+ Si / n-Si structures had been prepared they were sent to CNR for Si NC/SiC precursor deposition and 1100°C 30 min annealing under N_2/10% O_2. The capping layer was employed to avoid Si NC/SiC oxidation. The TMAH etch that is performed to remove residual capping Si also reduces the rear-side roughness arising from RIE on the wafers where this was applied. Then wafers were sent back to ISE for completion of the cell process, which began with a hydrogen passivation (RPHP) treatment of all but two reference

wafers. The sample parameters of the different cell types produced are summarised in Table 7.1. The Si NC/SiC layers in the 3 nm, 4 nm, and B cells are nominally identical to the films of the same name studied in Sec. 4.2 and 5.2. For each cell type listed two wafers with seven cells each were prepared.

Table 7.1. Sample parameters for tandem cells.

Cell Type	***Si NC/SiC Precursor Deposition Parameters***[a]	***1100°C 30 min Anneal***	***RPHP***
3 nm	30x [**3** nm a-$Si_{0.85}C_{0.15}$:H / 5 nm a-SiC:H]	X	X
3 nm, no RPHP	30x [**3** nm a-$Si_{0.85}C_{0.15}$:H / 5 nm a-SiC:H]	X	-
4 nm	30x [**4** nm a-$Si_{0.85}C_{0.15}$:H / 5 nm a-SiC:H]	X	X
5 nm	30x [**5** nm a-$Si_{0.85}C_{0.15}$:H / 5 nm a-SiC:H]	X	X
B	174 nm a-SiC:H[b]	X	X
No NC	-	X	X
No NC, No Anneal	-	-	X

[a]thicknesses are target thicknesses after annealing.
[b]this film does not contain Si NCs, but in this chapter only, "Si NC/SiC" designates the layer in Figure 7.1, rather than the material it is made of.

It is worth noting at this stage that the high-temperature steps may have reduced the electronic quality of the Si wafers. The n+ SiC deposition tool is not entirely free from metallic contamination [247], and the minority carrier lifetime of Si wafers can generally degrade during thermal treatments [260, 261]. In order to determine to what extent processing has degraded the 400 µm n-Si wafers, reference samples were produced of the same material, and lifetimes measured by quasi-steady-state photoconductance (QSSPC, see Sec. 9.1.12). Both sides of each wafer were passivated using a-$Si_{0.95}C_{0.05}$:H layers unless that side already had n+ SiC deposited on it. Results evaluated at an injection level of (3-5)×10^{14} cm^{-3} are summarised in Figure 7.4.

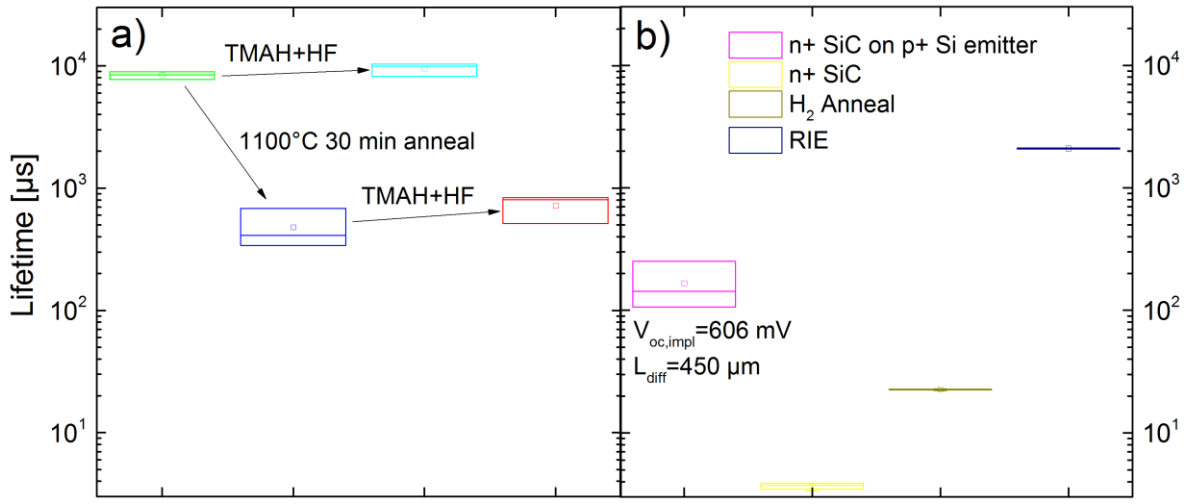

Figure 7.4. Minority carrier lifetimes of n-Si wafers as a function of (a) 1100°C 30 min annealing and etching in TMAH and HF, and (b) n+ SiC deposition with and without an underlying emitter as well as reactive-ion etching (RIE). The effect of an anneal under H_2 in the n+ SiC deposition chamber is also examined. The n+ SiC was only deposited on one side of the wafers; the other side, and both sides for samples without n+ SiC, were passivated with a-$Si_{0.95}C_{0.05}$:H layers. Lifetimes were evaluated at injection levels of 5×10^{14} cm^{-3} (a) and 3×10^{14} cm^{-3} (b). Features of the box diagrams are as in Figure 7.7(b)-(e).

Panel (a) shows that the initial lifetime of 8 ms (green) is decreased to ~500 µs by the 1100°C 30 min anneal. In contrast, the TMAH etch used at CNR to remove the capping layer has a slight positive effect. The lifetimes in (b) can also be compared to the 8 ms reference in (a), and indicate that depositing n+ SiC on one side of the wafer decreases the lifetime to a few µs (yellow), more so than simply annealing wafers in the n+ SiC chamber under H_2 (dark yellow). This suggests metallic contamination of the n+ SiC precursor gases or poor Si surface passivation by n+ SiC as compared to a-$Si_{0.95}C_{0.05}$:H, perhaps due to stress-related defects at the n+ SiC / Si interface [166]. Fortunately, the p+ Si emitter that is present between the n-Si wafer and the n+ SiC in the tandem cells repels electrons from the p+ Si / n+ SiC interface, which reduces recombination and increases the lifetime to ~150 µs (pink). This implies a diffusion length L_{diff} for minority carriers of 450 µm, and a maximum open-circuit voltage $V_{oc,impl}$ of 606 mV under 1 sun illumination. While the bottom cell will therefore not perform quite as well as one might expect when using FZ-Si, it will still yield an acceptable voltage, collect most of the current, and not limit tandem cell performance.

Following Si NC formation, the next step was to produce a p-type emitter for the Si NC/SiC layer. Based on the findings of Sec. 6.2.2 a controlled boron diffusion is possible, but as it is not certain if it will yield sufficient p-type doping to give the required built-in voltage for the Si NC cell, a 20 nm p-a-Si:H / 5 nm i-a-Si:H bilayer (henceforth simply "p-a-Si:H layer") was used instead. Then sputtered ITO was deposited on the p-a-Si:H for lateral transport, followed by deposition of a metal grid for current collection. A n-a-$Si_{0.95}C_{0.05}$:H / ITO stack was deposited on the rear side of the wafers as it forms a good contact to n-Si and also permits the fabrication of bifacial tandem cells which allows more detailed characterisation. A thickness of 70 nm was chosen for both ITO layers as that thickness minimises reflection.

Grids consisted of 50 nm Ti, 50 nm Pd and 2 µm Ag and were prepared on the front and rear side of the wafers using thermal evaporation and a lift-off process. Ti adheres well to ITO while Ag provides the necessary conductivity. The 2 cm×2 cm devices were then isolated from each other by patterning a photoresist onto the front and rear side of the cells and removing the ITO between them with HCl (see Figure 7.6(a)). A deeper mesa-etch was not thought viable because of the remaining layers, the n+ SiC and p+ Si provide the most lateral conductivity, and these cannot be etched. A few cells were isolated using a dicing saw but these could not be measured reliably. All other cells were therefore left on the 4" wafers they were processed from and the non-perfect shunt (parallel) resistance R_p accepted as given. Nevertheless, *jV* curves of cells measured before and after the ITO mesa etch under AM1.5G [262] illumination (henceforth "light *jV* curves", see Figure 7.5 for two devices) indicate that this step already greatly improves R_p of the cells.

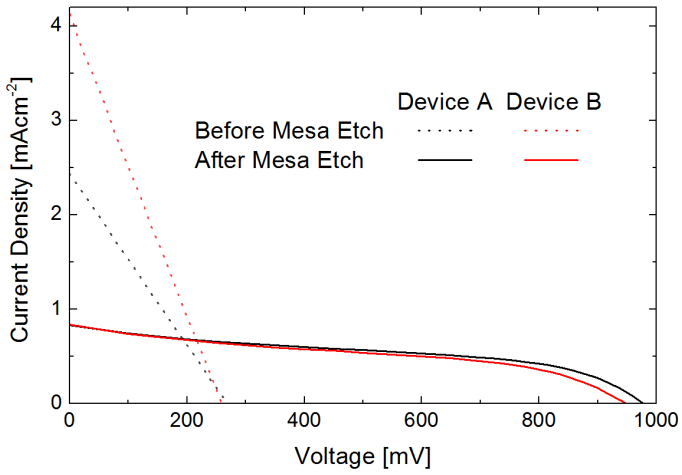

Figure 7.5. Light *jV* curves of two nominally identical devices before and after the ITO mesa etch. Without the mesa etch, performance varies more strongly, and a shunt path exists that is able to extract more current but reduces the open-circuit voltage more than threefold.

Further measurements taken to examine the quality and reproducibility of the processed tandem cells are shown in Figure 7.6. Figure 7.6(a) shows a photograph of a wafer with 4 nm tandem cells. Even though some damage is visible at the bottom-left edge, the seven 2 cm×2 cm cells are perfectly intact and the ITO (blue-purple) is removed between cells. Some wafers were less perfectly processed, with grid delamination or ITO removal on the active cell area. Nevertheless, for each cell type (3 nm, 4 nm, …) at least 6 of the 14 cells prepared appeared intact to the naked eye. Light *jV* curves of all unpassivated 3 nm cells which were not visibly damaged are shown in Figure 7.6(b). Very good uniformity across all cells of that type is observed. This confirms the robustness and reproducibility of the entire process chain and allows some statistics on cell performance to be presented. A median cell was selected for each cell type for more detailed analysis and comparison between cell types.

To ensure that the device structure of any given cell type is as intended, cross-section SEM images were acquired. Figure 7.6(c) shows a low-magnification image which reveals the flat interfaces between the n-Si wafer, the p+ Si emitter, and the n+ SiC. The n+ SiC is significantly thicker than previously determined by weighing, ~2 µm as opposed to 0.7-1.2 µm, as weighing averages over the whole wafer area. As the other layers are much

thinner, the area marked orange is enlarged in Figure 7.6(d) for a 5 nm cell and in Figure 7.6(e) for a B cell.

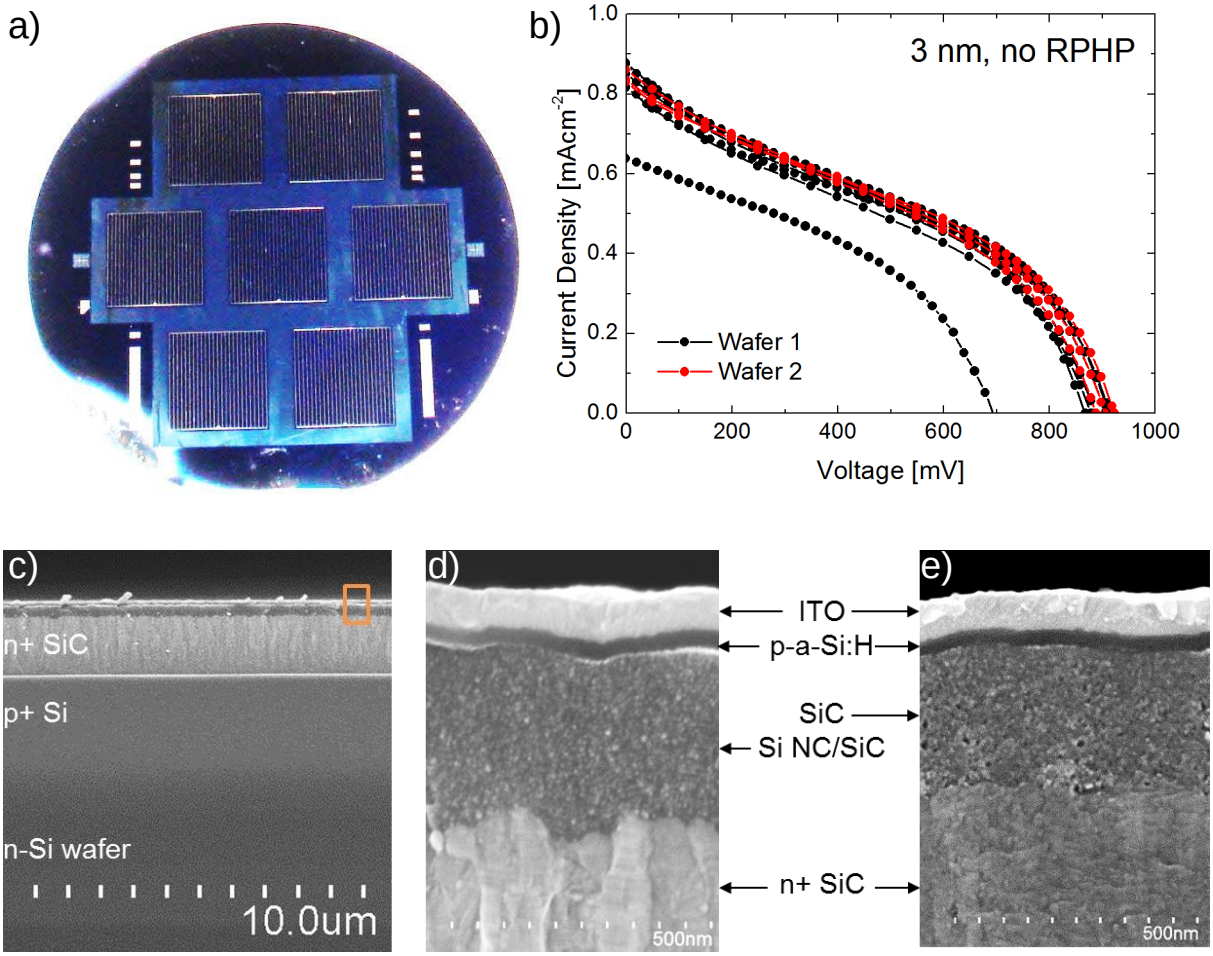

Figure 7.6. (a) Photograph of a 4" wafer containing seven intact 2 cm×2 cm tandem cells. The ITO (blue-purple) is removed between the cells to isolate them. (b) Light *jV* curves of all 12 cells of one type (3 nm, no RPHP) that were not visibly damaged, e.g. due to ITO removal on the cell or grid delamination. (c) SEM cross-section of a tandem cell showing the p+ Si via dopant contrast and the n+ SiC layer on top. The area marked by an orange box is enlarged in (d) and (e) for a 5 nm and a B tandem cell, respectively.

Even though the n+ SiC exhibits some surface roughness, the subsequent films are evenly deposited on top, and cross-sections appear as in Figure 7.6(d) and (e) over much larger fields of view than are shown here. Since the Si NC/SiC layer in a B cell is simply nc-SiC, there is almost no contrast at the interface with the n+ SiC. The nc-SiC appears porous, but since all SEM images are acquired on cleaved cross-sections this may be due to the cleavage process.

On the other hand, there is strong contrast between Si NC/SiC and n+ SiC in Figure 7.6(d), and the Si NCs are clearly visible as white dots. Close inspection of the Si NC/SiC layer reveals that the multilayer structure is still intact to some extent, despite deposition on such a rough n+ SiC surface.

Due to the low-risk process chain that was selected, reliable and reproducible devices whose intended structure is clearly confirmed by SEM were produced. Emitter diffusion and wafer lifetime were found to be sufficient for the bottom cell not to limit tandem cell performance.

7.2 Results

This section presents and discusses the *jV* behaviour of the tandem cells produced. Due to the complexity of any one tandem cell, the general behaviour of the tandem cells is discussed first, before examination of the differences between cell types (see Table 7.1) in Sec. 7.2.4.

Median light *jV* curves of all tandem cell types are shown in Figure 7.7(a). Box diagrams of open-circuit voltage V_{oc}, short-circuit current density j_{sc}, fill factor *FF*, and efficiency η of all visibly intact cells are shown in Figure 7.7(b)-(e). The fill factor is defined as the ratio of the maximum output power and the $V_{oc}j_{sc}$ product. Typical values for a high-efficiency Si cell are V_{oc}=700 mV, j_{sc}=41 mAcm^{-2}, *FF*=0.83, and η=24% [263]. For an ideal tandem cell, j_{sc} would be halved, and V_{oc} more than doubled.

As can be seen from Figure 7.7, the tandem cells fall short of reaching these ideals, for a range of reasons to be discussed in the following. Nevertheless, it should be stressed that the V_{oc} of virtually all cells exceeds 800 mV, and the mean V_{oc} of all annealed and hydrogen-passivated cell types is ~900 mV. This exceeds the V_{oc} that is attainable with the Si bottom cell alone and proves that the devices work as tandem cells.

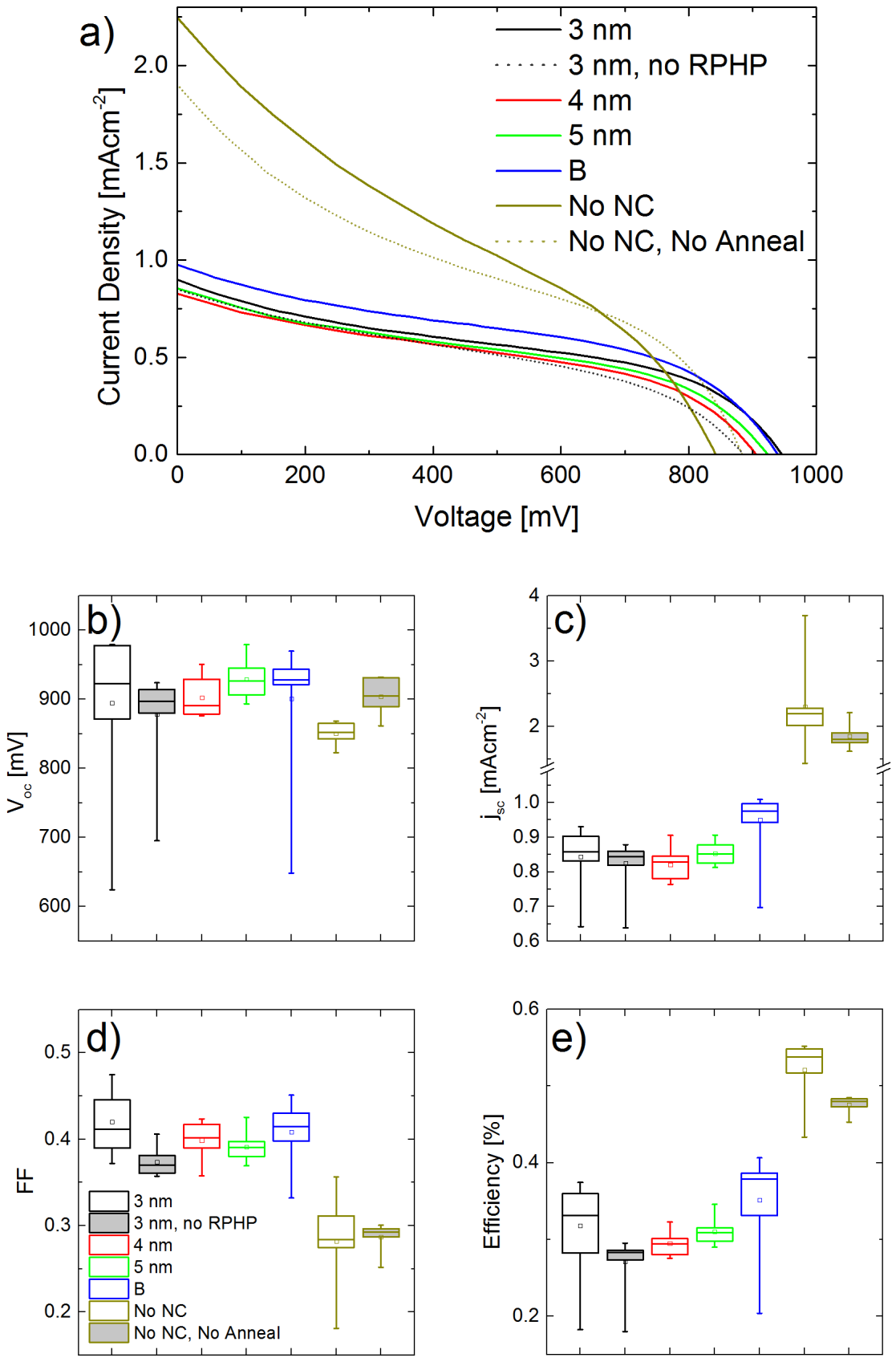

Figure 7.7. Light *jV* curves of median cells for each cell type (a), box diagrams of V_{oc} (b), j_{sc} (c, split axis), *FF* (d), and efficiency (e). The legend of (d) applies to all box diagrams. Squares denote the mean, boxes the interquartile range, the line within the box the median, and the lines extend to the maximum and minimum values.

7.2.1 Open-Circuit Voltage

The proportion of the V_{oc} that arises from the Si bottom cell is likely to be less than the 700 mV cited above for a high-efficiency cell due to the lifetime reductions shown in Figure 7.4, the non-ideal TRJ, etc. Two methods are available to estimate the bottom cell V_{oc}. One is simply the upper limit on V_{oc} given for the n+ SiC / p+ Si / n-Si structure in Figure 7.4(b), although that value is under 1 sun illumination and a more appropriate value would be that corresponding to the illumination level that reaches the bottom cell. Based on optical simulations by CNR (see Table 7.2, discussed in more detail later), and neglecting the fact that the light that reaches the bottom cell is largely infrared whereas lifetime measurements were done with a standard Xe lamp, the upper limit on V_{oc} at the correct illumination level can be evaluated as 550-580 mV. The second approach is to measure the tandem cells under rear-side (RS) illumination. RS and FS (front-side) measurements on median 3 nm cells are shown in Figure 7.8(a), and statistics on open-circuit voltages presented in Figure 7.8(b).

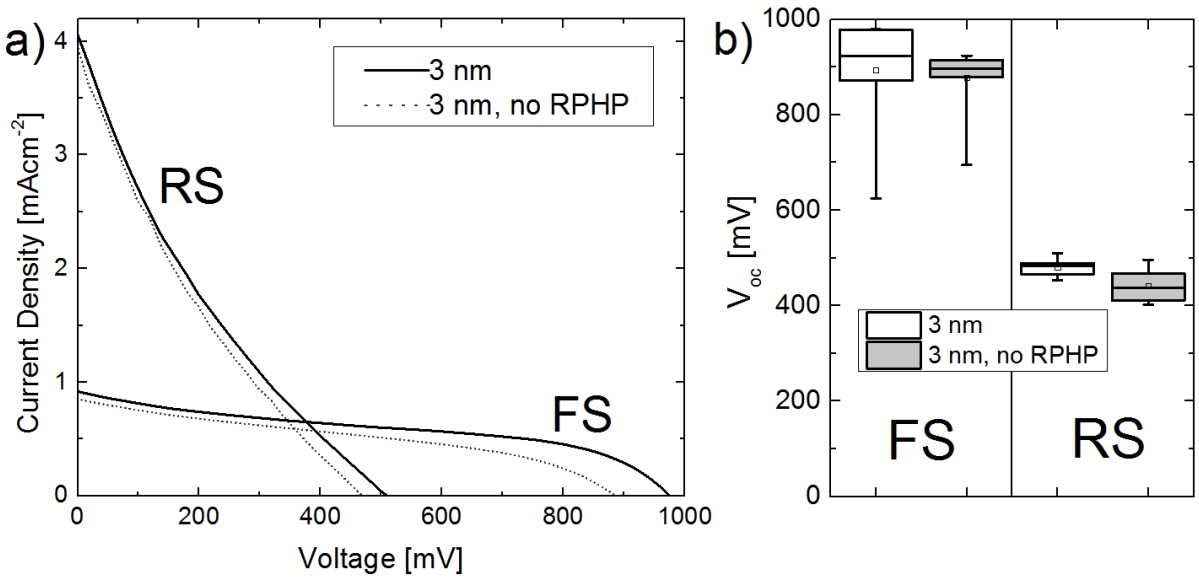

Figure 7.8. (a) Light *jV* curves of median passivated and unpassivated 3 nm cells under front-side (FS) and rear-side (RS) illumination. (b) Box diagram of open-circuit voltages of passivated and unpassivated 3 nm cells under FS and RS illumination. Features of the box diagram as in Figure 7.7(b)-(e).

Measurements under RS illumination yield significantly lower V_{oc} and *FF*, but higher j_{sc}. Under RS illumination, the "bottom" Si wafer cell absorbs all the light and generates all the output power while no excess carriers are generated in the Si NC cell which therefore simply behaves as a series resistor. This also explains the low *FF* of ~0.25, which arises when series resistance is very high and/or shunt resistance is particularly low. The V_{oc} under RS illumination therefore arises solely from the Si wafer cell, and from Figure 7.8(b) it can be seen that it rarely exceeds 500 mV. The V_{oc} of the bottom cell under FS illumination will differ slightly as the bottom cell receives less light, and the Si NC cell may be less resistive if photocarriers are generated within it, but the RS measurement is nevertheless a reasonable estimate. Based on this, it can be estimated that for a typical tandem cell with V_{oc}=900 mV (see Figure 7.7(b)), 450-550 mV are due to the Si wafer cell, which means 350-450 mV arise from the Si NC/SiC cell. This is in agreement with a previous measurement of V_{oc}=370 mV made on a Si NC/SiC membrane cell [35]. The voltage dropped across the TRJ is neglected in this estimation; why this is reasonable is discussed later.

To put the V_{oc} values of ~900 mV into context one can look to tandem cells made from µc-Si:H and a-Si:H: here, the parameters of the most efficient two-junction cell reported are V_{oc}=1342 mV, j_{sc}=13.45 mAcm^{-2}, *FF*=0.702, and η=12.7% [4]. Comparison of the data in Figure 7.7(b)-(e) to these values indicates that while there is room for improvement for the V_{oc} and *FF* of the tandem cells presented here, they are not the key factor in limiting the efficiency of tandem cells with Si NCs to 0.25-0.4% (see Figure 7.7(e)).

7.2.2 Short-Circuit Current

The short-circuit current j_{sc} of tandem cells with Si NCs is, at 0.8-0.9 mAcm^{-2}, over an order of magnitude lower than that of the most efficient a-Si:H / µc-Si:H tandem cell and therefore the main limitation on cell efficiency. Moreover, it appears that any variable that one would

expect to reduce cell performance – measuring with RS illumination (see Figure 7.8), omitting the Si NC layer (see Figure 7.7(c)), or not isolating the cells (see Figure 7.5) – greatly improves j_{sc}. While this occurs at the expense of V_{oc} and *FF*, an overall improvement in efficiency to ~0.5% is observed when omitting the Si NC layer (see Figure 7.7(e)). This was wholly unexpected as the purpose of developing Si NC/SiC layers in the first place was to be able to construct efficient tandem cells with them. The short-circuit current therefore merits a more detailed examination.

A key variable affecting j_{sc} is where light is absorbed. Optical simulations performed by CNR yielded the absorption of FS AM1.5G illumination in different device layers. This is tabulated in Table 7.2 in the form of a photogenerated current density j_{gen}, which represents the j_{sc} that would be extracted from that layer if it were the absorber in a perfect solar cell.

Table 7.2. Photogenerated current densities j_{gen} in the p-a-Si:H, Si NC/SiC, n+ SiC, and Si wafer layers in units of mAcm^{-2} under AM1.5G illumination from the front side.

	Top Cell			***Bottom Cell***
Cell Type	***p-a-Si:H***	***Si NC/SiC***	***n+ SiC***	***Si wafer***
3 nm	3.3	7.2	14	11
4 nm	3.3	8.2	14	10
5 nm	3.3	8.8	13	10
B	3.2	3.0	16	12

Regardless of whether absorption in the p-a-Si:H, Si NC/SiC, and n+ SiC, or only absorption in the Si NC/SiC, contributes to the top cell j_{sc}, j_{gen}>7.2 mAcm^{-2} in all bottom and all top cells with Si NCs. Since the measured j_{sc} is significantly lower, and since it was noted previously that the minority carrier lifetime in the Si wafer is still sufficient for extraction of most photogenerated current, j_{sc} must be limited by charge carrier collection in the top cell. In a previous study on Si NC/SiC membrane cells, a j_{sc}/j_{gen} ratio of 6.8% was reported [258],

which is in good agreement with j_{sc}=0.8-0.9 mAcm^{-2} and j_{gen}=7.2-25 mAcm^{-2} for the top cells with Si NCs. The large spread in j_{gen} arises from the lack of clarity as to whether light absorbed in the n+ SiC and p-a-Si:H contributes to j_{sc}. Ideally, one would expect these to merely act as electron and hole contacts, respectively, but as cells without a Si NC/SiC layer have higher j_{sc}, this is improbable. Instead, trends in j_{sc} indicate that the p-a-Si:H / n+ SiC top cell delivers the current. This is not unreasonable as the n+ SiC is much thicker than the Si NC/SiC layers and absorbs more light.

That the Si NC/SiC layer lowers j_{sc} despite increasing j_{gen} suggests that the electron-hole pairs generated in the Si NC/SiC layer are not collected, but lost due to rapid recombination. The decrease in j_{sc} could then be a shading effect, as the Si NC/SiC layer reduces absorption in the n+ SiC, or due to the Si NC/SiC layer behaving as a transport barrier. Table 7.2 shows that the absorption of the Si NC/SiC layer is more strongly reduced by removing the Si NCs from the layer (Cell Type B) than it would be by removing layer B completely. Since B cells have only marginally higher j_{sc} than 3, 4, and 5 nm cells, the shading effect is not dominant. Rather, the Si NC/SiC layer appears to act as a transport barrier for j_{gen} from the p-a-Si:H and the n+ SiC. This is analogous to role of the Si NC layers in some of the Si NC / Si wafer single-junction cells discussed in Sec. 2.4.

7.2.3 Resistances

The idea that the Si NC/SiC layer is merely a transport barrier is suitable for explaining trends in j_{sc} but cannot account for the fact that it also leads to an increase in V_{oc} and FF. A transport barrier can, to a first approximation, be viewed as an additional series resistance (R_s), and the dark jV curves of the cells shown in Figure 7.9 do appear to be limited by R_s above 0.7 V forward bias. However, they also show that the current under reverse and low forward bias is much higher when no Si NC/SiC layer is present. This can be explained in terms of a

decreased shunt resistance R_p or an increased reverse saturation current density j_0 of the top cell [255].

This explanation is difficult to verify since it is not possible to measure a dark IV curve of the top cell alone. However, the increased R_s is certainly feasible since the Si NC/SiC material forms an additional layer in which the hole transport that is required here may be much poorer than the electron transport studied in Chapter 5. An improvement in R_p can be explained by considering that while the 170-300 nm thick Si NC/SiC layers were successfully grown on fairly rough n+ SiC, and created a smoother surface on which the p-a-Si:H was then deposited (see Figure 7.6(d),(e)), deposition of p-a-Si:H directly on the rough n+ SiC may not have been as successful. Pinholes in the p-a-Si:H would lead to a direct ITO / n+ SiC contact, leading to decreased R_p and increased j_0.

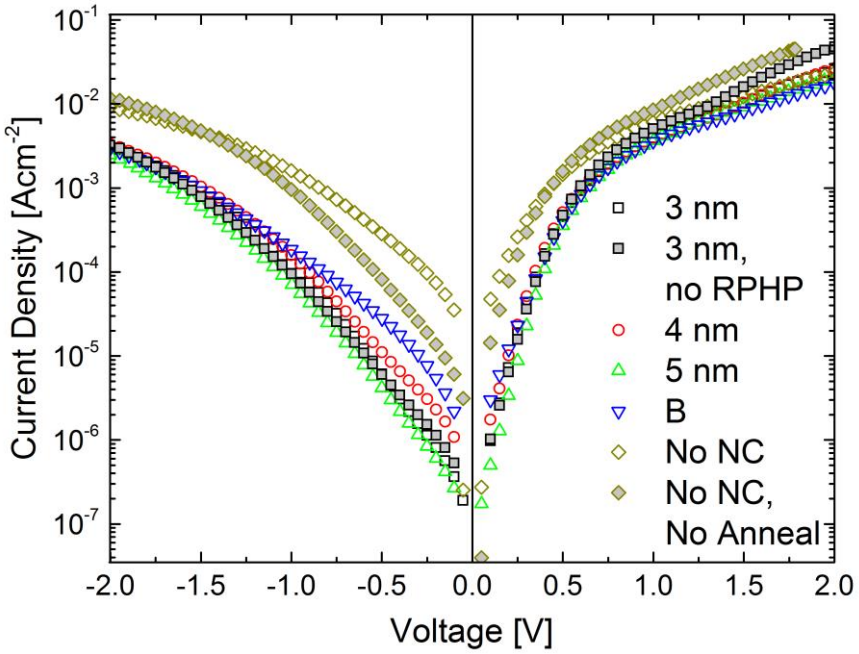

Figure 7.9. Dark *jV* curves of median tandem cells. The reverse and low-bias forward currents of cells without a Si NC/SiC layer are significantly higher. Above 0.7 V forward bias all cells begin to be R_s-limited.

As mentioned previously, greatly enhanced j_{sc} is also observed under RS illumination and when devices are not properly isolated via a mesa etch. In the former case, photocurrent is

generated solely in the bottom cell, and relies on the poor R_p of the top cell to be collected efficiently. In the latter case, the same is possible since the full-area ITO on the front and rear side of the wafers permits current flow over the wafer edges. Sufficient shunts appear to exist for j_{sc} collected from the Si wafer cell via shunts in the Si NC cell (or via the wafer edges, for non-isolated cells) under 1 sun illumination to exceed the j_{sc} of normally operating tandem cells where the Si wafer cell receives only ~0.3 suns illumination. The increased j_{sc} measured under FS illumination with no Si NC/SiC layer may therefore arise not so much from the R_s of Si NC/SiC as from the fact that without it a n+ SiC / ITO contact may exist, allowing a net current from the bottom cell to flow across the TRJ and straight to the ITO contact. In this case the top cell can be thought of as a cell and a resistor connected in parallel, where the Si NC/SiC film increases the resistance of the resistor.

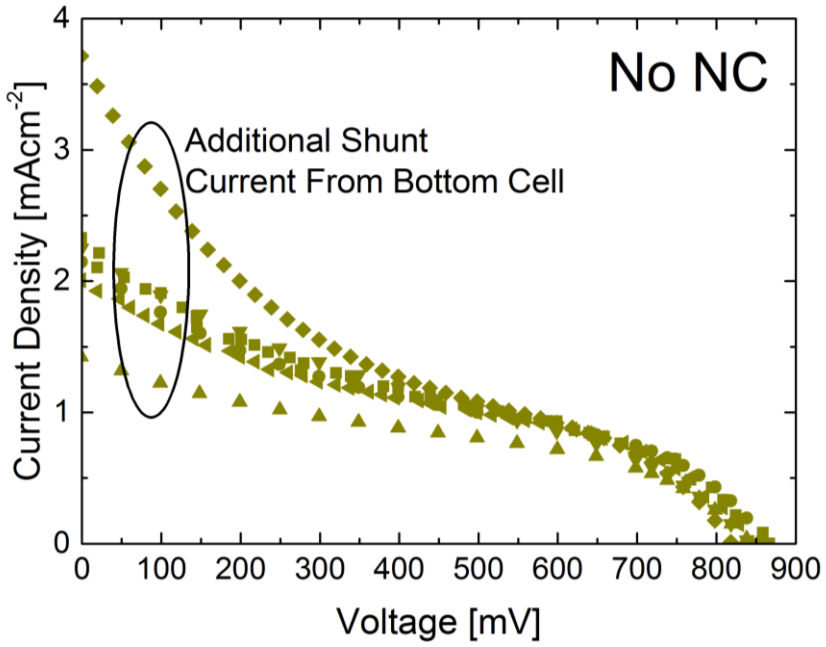

Figure 7.10. Light *jV* curves of "No NC" tandem cells under FS illumination. Performance is reproducible at high bias but varies strongly at low bias. It is proposed that at low bias an additional current from the bottom cell flows through the top cell via random shunts.

This is supported by light *jV* curves of tandem cells without Si NC/SiC layers acquired under FS illumination (see Figure 7.10). The behaviour at biases >500 mV is largely reproducible

across devices but j_{sc} is not. This supports the idea of an additional shunt current that is somewhat random (as shunts are), provides additional current at low bias, and leads to $FF \approx 0.25$ as is expected for high R_s and poor R_p.

Given the limitation of tandem cell performance by the top cell, there is no evidence that the TRJ limits performance. With $j_{sc} \approx 1$ mAcm^{-2}, the voltage dropped across the TRJ is expected to be 20× lower than depicted in Figure 7.3(b), and moreover, while the light *jV* curves have unusual shapes, they do not exhibit the S-shape that is characteristic of tandem cells with diode-like TRJs (see Figure 6.15(c)).

7.2.4 Effect of Processing Parameters

Having established an overall understanding of the cells, the effect of annealing, passivation, and nominal NC size can be examined in more detail. Figure 7.11 shows the dark and light *jV* curves of median tandem cells without Si NC/SiC layers before and after 1100°C 30 min annealing.

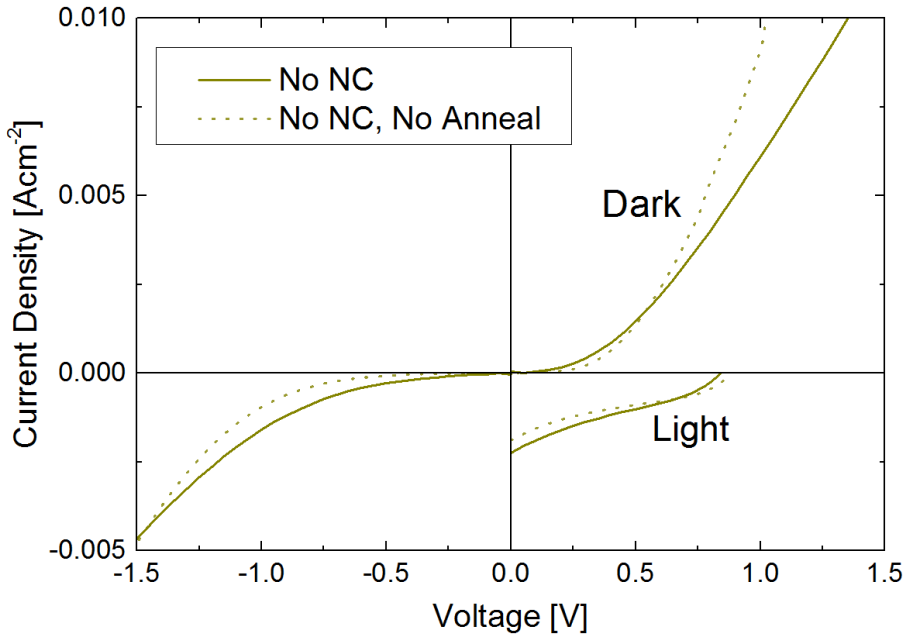

Figure 7.11. Dark and light *jV* curves of median tandem cells without Si NC/SiC layers before and after 1100°C 30 min annealing.

Annealing leads to an increased dark current at reverse and low forward bias, greater $j_{sc,}$ and lower V_{oc}. In analogy to the analysis of Figure 7.9, this indicates that annealing decreases R_p and/or increases j_0. The cross-over of the dark IV curves at high forward bias suggests annealing also increases R_s [255].

The same diagram as a function of hydrogen passivation for median 3 nm tandem cells is shown in Figure 7.12. From Figure 7.7(b)-(e) it is known that passivation improves every cell parameter – V_{oc}, j_{sc}, and *FF*. Since these are cells with Si NC/SiC layers, the additional bottom cell shunt current postulated previously does not play a large role and effects are as expected – passivation decreases recombination, improving current collection and open-circuit voltage. The effect on *FF* is less clear since the decreased dark current at high forward bias actually suggests increased R_s, which ought to decrease *FF*.

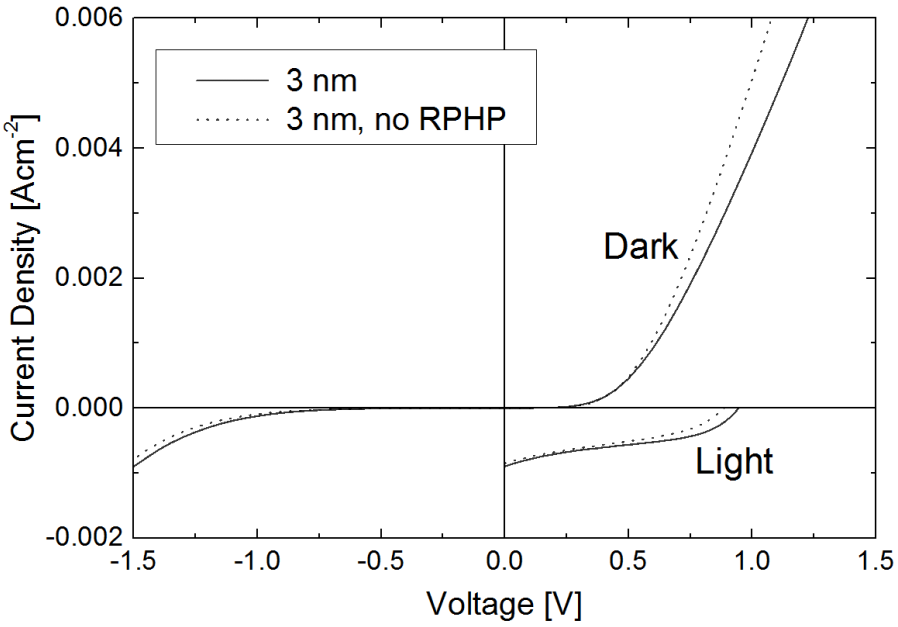

Figure 7.12. Dark and light *jV* curves of median 3 nm tandem cells before and after hydrogen passivation (RPHP).

It is worth noting at this stage, as is also evident from Figure 7.13 which shows dark and light *jV* curves of median tandem cells with different Si NC/SiC layers, that the light *jV* curves are not equivalent to the dark *jV* curves shifted downwards by j_{sc}, as is the case for standard Si

solar cells [264]. Instead, the light *jV* curves exhibit a finite gradient R_{sc}^{-1} at 0 V, where R_{sc} is the short-circuit resistance, and lower curvature (d^2j/dV^2). The former suggests a decrease in R_p upon illumination [265], and was also observed in Si NC/SiC membrane cells [258] where it was found to be a consequence of a voltage-dependent photocurrent.

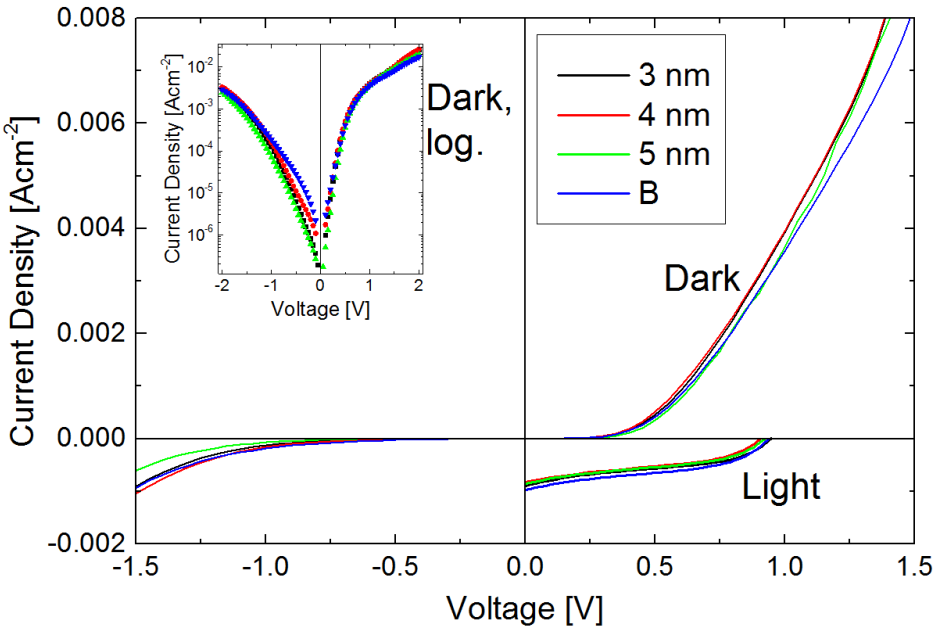

Figure 7.13. Dark and light *jV* curves of median tandem cells with different Si NC/SiC layers (see Table 7.1). Inset: dark *jV* curves on a logarithmic scale.

Photocurrent can be voltage-dependent if carrier collection is by drift, rather than diffusion. In this case, carrier collection depends on the electric field across the depletion region, which is maximum at j_{sc} and is decreased by the applied (forward) voltage. The decrease in photocurrent is, to a first approximation, linear with applied voltage for sufficiently low $\mu\tau$, and since constant dj/dV implies $d^2j/dV^2=0$, this could explain the overall decrease of curvature. However, voltage-dependent photocurrent also implies a crossover of light and dark *jV* curves when the applied voltage completely balances the built-in voltage (flatband voltage), and while this was observed for membrane cells [34], it does not appear as if the dark and light *jV* curves of any tandem cells are likely to intersect at higher voltages.

Figure 7.13 also shows that both light and dark *jV* curves are remarkably unaffected by the nature of the Si NC/SiC layer. Given the differences in electrical conductivity found in Sec. 5.2, particularly between hydrogen-passivated B films and films with Si NCs, this is quite surprising. As Sec. 5.2 dealt with lateral majority carrier (electron) transport, the insensitivity of tandem cell *jV* curves to Si NC/SiC film composition suggests either anisotropic conductivity, or a limitation by hole transport. Figure 7.7 indicates that there are some subtle differences; for example, the 5 nm cells exhibit the highest V_{oc} and lowest *FF*, as well as the lowest dark current at low bias (see Figure 7.13). This reinforces the interpretation that a low dark current at low bias indicates high R_p and low j_0 which increases V_{oc}, whereas the fact that the 5 nm Si NC/SiC film is simply thicker than all the others may be responsible for a higher R_s, decreasing *FF*. Overall, however, the nature of the Si NC/SiC film plays only a minor role in determining tandem cell performance.

7.3 Summary

Tandem cells consisting of a Si NC/SiC top cell and a Si wafer bottom cell have been prepared and studied. The process chain was designed using as many existing processes as possible, and control experiments carried out at every step to minimise errors. As a result, reproducible tandem cells were produced, Si wafer bowing was avoided, Si wafer lifetime degradation and bottom cell emitter shunting were ruled out as limiting factors for device performance, and lifetime measurements were used to estimate the bottom cell V_{oc} before the first tandem cell was measured. SEM images confirmed that the device structure was realised as desired, and revealed that Si NC multilayers can be prepared on rough surfaces. These are the first ever tandem cells produced using Si NCs (in any host matrix).

The resulting devices functioned as tandem cells, with V_{oc} exceeding that attainable from a single c-Si [263] or Si NC/SiC cell [35]. Surprisingly, however, Si NC/SiC seemed to have a

detrimental effect on j_{sc}: cells without Si NC/SiC layers, or cells measured under RS illumination where the Si NC/SiC cell does not contribute any current, exhibited much higher j_{sc}, albeit with reduced V_{oc} and FF. Furthermore, the j_{sc} of cells with Si NC/SiC layers was much lower than expected from optical considerations. The most suitable model to explain these observations was found to be that of a tandem cell with low j_{sc}, limited by poor extraction of j_{gen} from the Si NC/SiC cell, where some additional photocurrent is collected from the Si wafer cell via shunts in the Si NC/SiC cell at low bias. Shunts are more prominent in cells without Si NC/SiC layers and become more common upon 1100°C 30 min annealing. In cells where shunts do not play a large role, hydrogen passivation improves all device parameters and should always be used when preparing such tandem cells. The presence or nominal size of Si NCs in the Si NC/SiC layer has little effect on device performance.

8. Conclusion and Outlook

The goal of this thesis has been to investigate the optoelectronic properties of Si nanocrystals embedded in SiC (Si NC/SiC) using PL and IV measurements, and to investigate and develop processing steps for [Si NC/SiC] / c-Si tandem cells, culminating in the preparation and characterisation of such devices. Chapter 1 showed that tandem cells are the most promising route to achieve substantial advances in solar cell efficiency. It was further argued that tandem cells ought to become cheaper than the ones based on III-V semiconductors that are currently available, and that quantum-confined Si offers a cheaper alternative for bandgap engineering. SiC provides a suitable host matrix for Si quantum dots as it improves absorption and makes the device fairly insensitive to slight variations in Si NC size and separation.

With this application in mind the recombination of photogenerated carriers was studied by PL in Chapter 4. It was found that the strong PL of as-deposited a-Si_xC_{1-x}:H bulk films or multilayers is strongly reduced upon annealing due to the out-diffusion of hydrogen that had previously passivated dangling bonds, and that this effect cannot be reversed by hydrogen passivation. The resulting PL is very weak, and an upper limit on the luminescence quantum yield of 5×10^{-7} has been estimated. The invariance of the weak PL with dangling bond density and Si nanostructure indicates that PL is both limited by, and mainly due to, non-paramagnetic defects. The only case in which the luminescence of a sample was improved after annealing was that of a rapidly annealed film whose PL improved upon prolonged annealing at 900°C. It was also found that care had to be taken not to misinterpret PL spectra since Fabry-Pérot interference of PL emitted within the films led to artificial peak shifts of up to 200 nm. Simulations of Fabry-Pérot interference within the films were used to correct for this, and a comparison of transmission and PL spectra was proposed as a simple method to

evaluate whether interference plays a role in measured PL. Furthermore, the PL of films prepared on Si was found to be even weaker than that of films on quartz substrates.

The PL was much weaker than expected based on the Si NC/SiO_2 system. This is thought to be at least in part due to the improved carrier transport, which makes it easier for photogenerated carriers to reach nonradiative recombination sites. Carrier transport was studied in Chapter 5 and found to be Ohmic at all temperatures for a wide range of samples prepared in two different laboratories. Conductivity increased up to 1000 times, and dangling bond density decreased, upon passivation with atomic hydrogen, while molecular hydrogen has no effect. With atomic hydrogen, conductivities up to 0.1 Scm^{-1} can be reached. By systematically excluding other transport mechanisms, majority carrier transport was found to be via extended states at high temperature, and via hopping, most likely within tail states, at low temperature, which is reminiscent of transport in amorphous semiconductors. Fitting parameters suggest a type I band offset between Si nanoclusters and SiC, with extended-state transport in samples with Si nanoclusters occurring in a percolating Si network, while hopping may take place throughout the films. The percolating network consists of amorphous and nanocrystalline Si domains. Films are n-type, with estimated carrier concentrations of over 10^{17} cm^{-3} due to background doping by nitrogen and/or oxygen. No photocurrent related to photogenerated carriers was detected, implying a combination of high carrier concentration and low minority carrier lifetime and mobility.

In order to permit further characterisation of Si NC/SiC on a tandem cell device level several processing options were examined in Chapter 6. An examination of film oxidation on annealing revealed that oxides up to 16 nm thick can form even in nominally inert atmospheres, with thinner oxides formed when inserting samples into the furnace at lower temperature or working with a reducing sample holder. As the latter can lead to the formation of complex oxides, a more universal solution to oxidation, an a-Si:H capping layer, was developed. It is deposited with the Si NC/SiC precursor film, and while its thickness must be

well-controlled, its removal by wet-chemical etching is a robust process, yielding pristine and only slightly roughened Si NC/SiC surfaces.

Diffusion experiments carried out on nc-SiC films to assess different methods of forming p-n junctions with Si NC/SiC materials revealed that boron and phosphorus diffuse rapidly from a-SiC:H to a Si wafer, or vice versa, upon annealing at 1100°C for 30 min. This can move a p-n junction from the a-SiC:H / c-Si interface to a location fully within the nc-SiC that is formed on annealing, or fully within the c-Si. Free carrier absorption as measured by FTIR was found to be a quick, non-destructive method for monitoring dopant diffusion into Si substrates. Doping concentrations in nc-SiC as measured by SIMS were found to be anomalous, and a comparison to the amount of dopant supplied is recommended for accurate quantification. Due to the difficulty in controlling diffusion during the anneal required to form Si NCs, diffusion into crystallised nc-SiC was also studied. Both boron and phosphorus diffuse exclusively within the grain boundary (GB) network, and do so rather rapidly, penetrating 200 nm nc-SiC films within 30 s at 1200°C. Diffusion is thermally activated, with an activation energy of 5.3 ±0.4 eV for boron and 4.4 ±0.7 eV for phosphorus. The activation energy for phosphorus is much lower than in the case of intragranular diffusion, while for boron diffusion it is the same or greater. Trapping of boron at Si dangling bonds is proposed as a mechanism to explain the unexpectedly high activation energy, which implies that the boron diffusivities in Si NC/SiC are likely to be lower than those measured in nc-SiC. Near-surface concentrations are higher than predicted by these diffusivities for both dopants. This is attributed to partial immobilisation of dopants in the case of boron. In the case of phosphorus, active doping was detected, suggesting that both Fermi level-dependent diffusion and partial dopant immobilisation may play a role.

Si / Si and Si / SiC junctions were considered as series interconnects for [Si NC/SiC] / c-Si tandem cells. Si / Si diodes cannot withstand the thermal budget needed to synthesise Si NC/SiC whereas p+ Si / n+ SiC junctions produced at similar temperatures are sufficiently

conductive. They do not exhibit classical tunnel diode behaviour, but work by permitting rapid defect-assisted recombination in the depletion region (and are hence termed tunnel recombination junctions or TRJs). They are used in the preparation of tandem cells in Chapter 7, whereas the use of diffused junctions for the Si NC/SiC cell was foregone and p-a-Si:H used instead to form the emitter of the Si NC/SiC cell. A process chain was developed that focused on using established processes combined with a range of control experiments to minimise errors and uncertainties. As a result, tandem cells with reproducible performance whose intended structure is clearly confirmed by SEM were produced. Control experiments showed that the bottom cell would not limit device performance, and identified when the TRJ might be limiting.

Almost all the cells produced exhibited open-circuit voltages V_{oc} greater than 850 mV, thereby exceeding what could be expected from a single c-Si [263], or Si NC/SiC cell [35], and proving tandem cell functionality. However, multiple factors that would be expected to degrade device performance, such as omitting the Si NC/SiC layer, illuminating tandem cells from the rear side, or not isolating the cells, led to greatly enhanced short-circuit current j_{sc} at the expense of V_{oc} and fill factor. It is proposed that this is due to the large current mismatch between the top and the bottom cell, which arises not from optical factors – similar amounts of light are absorbed in the top and the bottom cell – but from poor current collection in the top cell. Since the bottom cell can potentially deliver much more current, it does deliver some additional current via shunts in the top cell in cases where these are present. In the absence of a Si NC/SiC layer these shunts are more common, and are promoted by the 1100°C 30 min anneal. In cells with a “3 nm” Si NC/SiC layer, the additional shunt current from the bottom cell plays only a small role, and passivation is found to improve all device parameters. That tandem cell performance is largely insensitive to the presence or nature of Si NCs in the Si NC/SiC layer (provided the layer is present), even though lateral electron transport studied

in Chapter 5 varied much more strongly, suggests that the layers either exhibit anisotropic conductivity, or that hole transport is the key factor limiting device performance.

It is a recurring theme within this thesis that many properties are surprisingly insensitive to the nature of the Si nanoclusters embedded in SiC. Photoluminescence and tandem cell performance are both largely independent of the Si nanostructure, while lateral electron transport depends mainly on the quantity of excess Si (and of course on hydrogen passivation). As many experiments were designed with prior results from the Si NC/SiO_2 system in mind these results were rather unexpected. The reasons can be found in the poor luminescence quantum yield, the absence of detectable photocurrent, and poor current extraction from the Si NC/SiC top cell in tandem cells. All suggest poor minority carrier lifetime, and the photocurrent and tandem cell results additionally point to a low mobility-lifetime ($\mu\tau$) product. Lateral electron transport measurements appear to contradict the idea of low mobility, but a combination of high electron and poor hole mobility is plausible since the similarity between Si and 3C-SiC electron affinities suggests that the valence band offset exceeds the conduction band offset, and since the hole mobility is much lower than electron mobility in both Si [6] and 3C-SiC [30].

At any rate, the origin of this effect must lie in a high defect density which cannot be significantly reduced by hydrogen passivation. It strongly limits minority carrier properties as well as trapping majority carriers and providing states for hopping transport at low temperature, and overshadows any effect that the size, crystallinity, or arrangement of Si nanoclusters may have. The impact of the Si nanostructure is likely to be more limited than for Si NC/SiO_2 even in perfect Si NC/SiC material because the dependence of transport on NC separation is weaker (see Figure 1.5), and because the weaker confinement of the electronic states of Si NCs by SiC might yield broader PL peaks. However, as it is, the key parameter is a rather tenacious defect population, which must be reduced if the potential of Si NC/SiC for photovoltaic applications is to be harnessed.

The positive side is twofold: first, even with this poorly understood and severely limiting defect concentration, functioning tandem cells were produced whose j_{sc} (as well as the j_{sc} of Si NC/SiC membrane cells [258]) exceeds that of cells made from the better understood and less defective Si NC/SiO_2 material [150]. Second, it is the *only* problem that needs to be tackled at this stage. Absorption is sufficient for tandem cell performance (see Table 7.2), and as discussed in Chapter 7, the tandem cells are not limited by the bottom cell or the TRJ. Once the $\mu\tau$ product has been improved, the Si nanostructure-dependence that had been expected might surface, at which point Si nanocluster size and arrangement ought to be optimised. Within the tandem cell architecture, the n+ SiC thickness and roughness should at some stage be reduced in order to produce better cells and eliminate ambiguity regarding where precisely the top cell photocurrent is generated.

Alternatively, if the Si nanostructure never becomes a key factor, homogeneous, rather than multilayer precursor films can be deposited, which removes the requirement of precise control over deposition rate, enabling faster and hence more cost-efficient preparation of Si NC/SiC films. A reduction in background doping would also be viable as the carrier concentration may soar to levels where Auger recombination becomes relevant once the trap density is reduced, while eliminating donor ions will also improve mobility. For the time being, however, the key objective going forward ought to be the reduction of the defect density in any single Si NC/SiC layer. As hydrogen passivation makes little difference it may, as argued in Sec. 5.5, be more prudent to introduce an atomic species that is to occupy defect sites during deposition of the Si NC/SiC precursor, thus preventing the formation of defects upon annealing. It is not clear if, or how exactly, this reduction in defect density is to be achieved, but what is clear is that it is the key issue which, if resolved, could enable the production of cost-efficient [Si NC/SiC] / c-Si tandem cells.

9. Appendices

9.1 Appendix A: Other Characterisation Techniques

9.1.1 Spectroscopic Ellipsometry (SE)

SE is a technique whereby the ratio Ψ and the phase shift Δ between s-polarised and p-polarised reflection from a sample can be measured as a function of wavelength and angle of incidence, and fitted with a model in order to extract the thicknesses and/or refractive indices of the films on the sample [266]. Some prior knowledge of both is required, particularly for samples consisting of multiple films, to ensure a physically sensible fit. In this work, a Woollam M-2000 instrument was used to measure SE from 300-1000 nm at an angle of incidence of 70°. Tabulated refractive index values were used to fit SiO_2 data [267], while data of as-deposited a-Si_xC_{1-x}:H films was well-fitted by a Cody-Lorentz oscillator model [268]. The fitted refractive index of a-Si_xC_{1-x}:H films at 633 nm was recorded to monitor variations in film composition across depositions.

9.1.2 Scanning Electron Microscopy (SEM)

In SEM, images are acquired by scanning an electron beam across the sample and mapping the signal [269]. Most images in this work are acquired with the secondary electron signal only. The instrument used was a Hitachi SU70 with a cold trap, operated at 5-6 kV accelerating voltage and a working distance of 2.5-16 mm. A working distance of 10 mm was used for most images and adjusted when particularly high resolution or a particularly large field of view was required. SEM was mainly used to measure thicknesses of annealed films

which cannot be well-fitted with SE models [268] and to confirm correct processing of the sample structure.

9.1.3 Fourier-transform Infrared Spectroscopy (FTIR)

Infrared spectroscopy is used to detect the type and quantity of polar bonds which absorb infrared radiation at their resonant frequency. A broadband infrared source is used for excitation, and the excitation light passed through a Michelson interferometer to permit the measurement of infrared transmittance as a function of optical path length difference between the interferometer arms. The obtained interferogram is then Fourier-transformed to yield transmittance as a function of wavenumber (in units of cm^{-1}) [270]. In this thesis, a Bruker IFS 113v instrument was used to acquire spectra in the range of 400-4000 cm^{-1} with 6 cm^{-1} resolution. The transmittance T is converted to absorbance A by $A=-\log_{10}(T)$, and the absorbance of a reference substrate with the same doping level and thickness as the sample is subtracted to yield that of the Si NC/SiC film only. Except where free carrier absorption is studied, a baseline subtraction is also performed. The baseline is fitted to the parts of the spectrum where no peaks are present. Si substrates are used as Si-Si bonds are non-polar and therefore transparent to infrared radiation.

9.1.4 Grazing Incidence X-ray Diffraction (GIXRD)

GIXRD permits the study of diffraction in thin polycrystalline films by measuring with a shallow angle of incidence of the x-ray beam in order to maximise the volume of material that the x-rays can diffract in. A Philips X'Pert MRD system equipped with a CuKα (λ=0.154 nm) x-ray source was used, and the angle of incidence fixed at 0.3°. Only the detection angle is scanned; it, with respect to the incident beam, is equal to 2θ and the positions of peaks from *hkl* planes are, as for regular XRD, given by the Bragg condition $\lambda=2d_{hkl}\cos\theta$, where d_{hkl} is the

hkl interplanar spacing. The limitation of GIXRD with respect to regular XRD is that for all reflections to be observed, the grains must be randomly oriented with respect to the incident beam. GIXRD can confirm the presence of crystalline Si and SiC in the films, and provide an estimate of the grain size *d* from the full width at half maximum (FWHM) using the Scherrer formula

$$d = \frac{K\lambda}{\beta_d \cos(\theta)}, \tag{9.1}$$

where β_d is the contribution of grain size to the measured FWHM β, and K is a shape factor [169] usually taken to be 0.9 for spherical grains of cubic symmetry [271], which prior TEM studies have shown is valid for Si NC/SiC [15, 272]. Other reasons for peak broadening include instrumental broadening β_i, which is measured with coarse-grained Si and SiC powder and subtracted, and strain-related broadening, which can be neglected since it usually leads to a particular dependence of β on θ that is not observed for the Si NC/SiC films studied in this thesis [273, 274].

9.1.5 Raman Spectroscopy

Under optical excitation, electrons can be excited to virtual states from which they can radiatively recombine directly or after absorption or emission of one or more phonons. In Raman spectroscopy, emission is measured as a function of energy difference (Stokes shift) between excitation and emission, i.e., as a function of the sum of the energies of the phonons that interacted with the excited carrier. This is particularly useful for studying Si nanoclusters since a-Si and c-Si have different optical phonon energies (490 cm^{-1} [275, 276] and 520 cm^{-1}, respectively), and since Si NCs have slightly lower optical phonon energies of 500-520 cm^{-1} [277]. The crystallinity $X_{c,Si}$ of Si in a film can be calculated from the integrals

of the a-Si and Si NC optical phonon peaks and the amorphous-to-crystalline cross-section [278]**.** Both the position [276] and FWHM [279] of the Si NC peak can be used to estimate the Si NC size.

9.1.6 Spectrophotometry

Optical reflection and transmission (R&T) measurements can be used to empirically quantify absorption, to find the absorption coefficient α using the Beer-Lambert law

$$\alpha t = \ln(\frac{1-R}{T}) , \tag{9.2}$$

where *t* is the film thickness, or, in analogy to SE, to determine thicknesses and refractive indices of a multilayer system by fitting a model, given some prior knowledge of the parameters [180]. At ISE, spectra were acquired from 250-2000 nm using a Varian Cary 500i spectrophotometer with an integrating sphere, and only absorption or absorption coefficients were quantified. At CNR, a HP8542A diode array spectrophotometer was used, and data simulated using the computer programme OPTICAL that they wrote. This permitted the determination of film thicknesses and proportions of a-Si, Si NCs, and SiC in the films, under the assumption that Si NCs have the dielectric function of μc-Si [180].

9.1.7 Light Microscopy

An Olympus MX61 light microscope was used to check films for inhomogeneity, pits, blisters, and cracks. Cracks are particularly detrimental for lateral IV measurements as they severely restrict current flow, so all films for lateral IV measurements were checked and films with cracks were discarded. Light microscopy was also used to check to what extent the

contacts overlapped with the film in the one batch where the overlap was not perfect (presented in Sec. 5.2), and conductivities corrected accordingly.

9.1.8 Secondary Ion Mass Spectrometry (SIMS)

In SIMS, a sample is sputtered with primary ions and ejected secondary ions are detected with a mass spectrometer. Only secondary *ions* are detected, and the proportion of atoms that are ionised upon sputtering depends strongly on the material studied. Implanted standards of the analyte in the material of interest are therefore necessary for quantification. SIMS yield can be monitored over time to obtain depth profiles of the analyte species in the sample. Depth resolution deteriorates with sputtering time due to increased roughening of the surface and knock-on of the analyte atoms deeper into the sample. SIMS was carried out by the company RTG Microanalysis using a Cameca ims-4f instrument with either 8 keV O^{2+} primary ions (boron and nitrogen profiles) or 14.5 keV Cs^{+} primary ions (phosphorus profiles). To quantify boron and phosphorus contents, nc-SiC films identical to those to be studied were ion-implanted with boron (2×10^{15} cm^{-2}, 50 keV) and phosphorus (2.5×10^{15} cm^{-2}, 120 keV). Nitrogen contents were quantified with RTG's own monocrystalline N/SiC standard. As SIMS amorphises the sample surface before removing material, SIMS yield is mainly dependent on the immediate atomic environment of the analyte, not the crystal structure or grain size [280].

9.1.9 X-ray Photoelectron Spectroscopy (XPS)

In XPS, x-rays incident on a sample eject core-level electrons which are detected as a function of energy. The binding energy of core-level electrons is specific to the orbital they were in but can be shifted by the Fermi level or by local bonding. This allows composition, and bonding environment of the species present, to be determined. XPS is a surface technique as electrons

can only be ejected from the top ~5 nm of a sample. Surface cleanliness is crucial, and since organic contamination is almost impossible to avoid carbon is rarely analysed (but is often used to calibrate the energy axis).

9.1.10 Hall Effect

By applying a magnetic field B orthogonal to an electric field that induces a current I in a sample of thickness t, the electron and hole currents can be spatially separated by the Lorentz force, which is reflected in a Hall voltage V_H that is orthogonal to both fields. Its sign indicates the carrier type, and its magnitude the carrier mobility μ as faster carriers are more strongly displaced by a magnetic field. Mathematically,

$$V_H = -\frac{IB}{nqt} = (\pm)\frac{\mu B}{t}. \tag{9.3}$$

The setup used consisted of a Keithley 6220 current source, a Keithley 2700 multimeter, and a Bruker B-E10 electromagnet, all run by LabVIEW software.

9.1.11 Electron Spin Resonance (ESR)

The energy level of an unpaired spin can be split by an applied magnetic field B such that the spin-up and spin-down state are separated by an energy $\Delta E = g\mu_B B$, where μ_B is the Bohr magneton and g is the so-called g-factor which is equal to 2.0023 for free electrons [281]. Under these conditions, the spins absorb microwaves whose angular frequency ω satisfies $\Delta E = \hbar\omega$, where $\hbar$ is the reduced Planck's constant. In practice, microwave absorption at fixed ω is measured as a function of B. The g-factor at an absorption peak is characteristic of the spin-active site, e.g. a dangling bond, a vacancy, or an unionised dopant. The density of such sites can be found from the peak area provided a reference sample with known spin density is

also measured. The reference should ideally contain the same spin-active sites as the same absorption cross-section for microwaves is assumed. Within this thesis, X-band ESR (ω=9.8 GHz) was performed at room temperature using an EMX instrument and the Super High Q resonator 4122 from Bruker Biospin. Lock-in detection with a modulation amplitude of 3 G was used, and the magnetic field and spin density were calibrated using DPPH and a 0205 W112 standard (g=2.0033) from Bruker Biospin, respectively. The signal of each sample was scaled by the sample's quality factor.

9.1.12 Quasi-Steady-State Photoconductance (QSSPC)

QSSPC is a standard technique for measuring the minority carrier lifetime τ in Si wafers which involves generating an excess carrier concentration Δn in the sample using a flash lamp and monitoring the decay in excess conductance with an induction coil that the sample is placed on. From the temporal decay of both the flash intensity and the excess conductance, τ as a function of Δn can be determined at all Δn accessible with the flash lamp. Details on the method can be found in Refs. [282-284]. In this thesis, a Sinton WCT-120 lifetime tester was used to investigate the lifetime of Si wafers at different stages of the process chain in Sec. 7.1. FZ Si wafers (1 Ωcm, n-type) passivated with 30 nm a-$Si_{0.95}C_{0.05}$:H from the AK400 PECVD chamber were also prepared routinely to monitor the quality of films deposited in the chamber. In the case of τ <0.5 ms, the chamber was coated with SiC until higher values were obtained.

9.2 Appendix B: Full Tandem Cell Process Chain

Given below is the full process chain for [Si NC/SiC] / c-Si tandem cells, including all cleaning and structuring steps. Processes are merely listed; where thought necessary they are explained in detail in Sec. 7.1. Figure 7.1 shows the resulting tandem cell structure. Only the process chain for the full tandem cells is given. Rear side and front side are abbreviated as RS and FS, respectively.

1. RCA clean of n-Si wafers.
2. RS deposition of 500 nm SiO_2 by PECVD.
3. Clean in hot HNO_3 followed by dilute HF.
4. BBr_3 diffusion and drive-in.
5. Removal of borosilicate glass in HF.
6. FS APCVD 1 µm n+ SiC at 1100°C.
7. (where needed) RS RIE to remove parasitic APCVD deposition.
8. Transfer to CNR.
9. RCA clean.
10. FS PECVD of Si NC/SiC precursor layer followed by a-Si:H capping layer.
11. Anneal at 1100°C for 30 min in N_2/10% O_2.
12. Removal of oxide and residual capping layer by etching in HF, TMAH, HF.
13. Transfer to ISE.
14. Remote Plasma Hydrogen Passivation at 450°C for 45 min (all but 2 references).
15. Clean in hot HNO_3 followed by dilute HF.
16. RS PECVD 25 nm n-a-$Si_{0.95}C_{0.05}$:H.
17. RCA clean.

18. FS PECVD 5 nm i-a-Si:H, 20 nm p-a-Si:H.
19. Clean in dilute HF.
20. FS + RS 70 nm sputtered ITO.
21. FS + RS application of photoresist, exposure and development of grid mask on FS.
22. FS evaporation 50 nm Ti, 50 nm Pd, 2 µm Ag.
23. Stripping of resist.
24. FS + RS application of photoresist, exposure and development of grid mask on RS.
25. RS evaporation 50 nm Ti, 50 nm Pd, 2 µm Ag.
26. Stripping of resist.
27. FS + RS application of photoresist, exposure and development of mesa etch mask on FS.
28. HCl etching of exposed ITO.
29. Stripping of resist.
30. FS + RS application of photoresist, exposure and development of mesa etch mask on RS.
31. HCl etching of exposed ITO.
32. Stripping of resist.

The author is indebted to the clean room staff at ISE for performing most of the processing steps.

9.3 Appendix C: Abbreviations

The table below lists all abbreviations used in the thesis. It does not include standard chemical formulae of elements and compounds.

Acronym	*Meaning*
3C, 6H	SiC polytypes
a-	amorphous
AM1.5G	Air mass 1.5 global solar spectrum; standardised spectrum used for solar cell testing that approximates solar illumination at European latitudes
APCVD	Atmospheric-pressure CVD
c-	crystalline
CCD	Charge-coupled device
CNR	Consiglio Nazionale delle Ricerche - Istituto per la Microelettronica e i Microsistemi in Bologna, Italy
CP33	A mixture of HF, HNO_3, and CH_3COOH that etches Si
CVD	Chemical vapour deposition
DB	Dangling bond
DFTEM	Dark-field transmission electron microscopy
DoS	Density of States
EFTEM	Energy-filtered transmission electron microscopy
ESR	Electron spin resonance
FCA	Free carrier absorption
FGA	Forming gas anneal
FS	Front side
FTIR	Fourier-transform infrared (spectroscopy)

Acronym	*Meaning*
FWHM	Full width at half maximum
FZ	Float-zone
GB	Grain boundary
GIXRD	Grazing incidence X-ray diffraction
:H	containing hydrogen
HRTEM	High-resolution transmission electron microscopy
IMTEK	Institute of Microsystems Technology in Freiburg, Germany
ISE	Fraunhofer-Institute for Solar Energy Systems in Freiburg, Germany
ITO	Tin-doped indium oxide
IV	Current-voltage
IVT	Temperature-dependent IV
LP	Longpass (filter)
µc-	microcrystalline
mono-	monocrystalline
MS	Magnetron sputtering
NC	Nanocrystal
nc-	nanocrystalline
OD	Optical density. Logarithmic unit of transmission, $OD=-\log_{10}(T)$
PECVD	Plasma enhanced CVD
PL	Photoluminescence (spectroscopy)
PLE	Photoluminescence excitation (spectroscopy)
poly-	polycrystalline
PV	Photovoltaics, photovoltaic
QD	Quantum dot

Acronym	*Meaning*
QE	Quantum efficiency
QSSPC	Quasi-steady-state photoconductance
QY	Quantum yield
RBS	Rutherford backscattering spectrometry
RCA	Radio Corporation of America (standard cleaning sequence)
RIE	Reactive ion etching
RPHP	Remote plasma hydrogen passivation (see Sec 3.1.4 for details).
RS	Rear side
R&T	Reflection and transmission, typically as a function of wavelength resulting from spectrophotometry measurements
RTA	Rapid thermal annealing
SE	Spectroscopic ellipsometry
SEM	Scanning electron microscopy
SIMS	Secondary ion mass spectrometry
SiO_x	Non-stoichiometric (usually Si-rich) silicon oxide
Si_xC_{1-x}	Non-stoichiometric (usually Si-rich) silicon carbide
TEM	Transmission electron microscopy
TLM	Transmission line measurement
TMAH	Tetramethylammoniumhydroxide
TRJ	Tunnel recombination junction
UB	Universitat de Barcelona
VRH	Variable-Range Hopping
XPS	X-ray photoelectron spectroscopy
/	Separator for several phases in one layer, or for several layers in a stack

9.4 Appendix D: Symbols

The table below lists all symbols used in this thesis. The "dimension" column only indicates dimension, it is not equivalent to the units used for that quantity. For example, units of cm^{-3} and $mAcm^{-2}$ are typically used for concentrations and current densities, respectively. When a symbol is not listed with the same subscript as in the text the meaning of the subscript can be inferred from the text.

Symbol	***Dimension***	***Meaning***
A		Absorbance,
		Absorptance/Absorption
α	m^{-1}	Absorption coefficient
B	T	Magnetic flux density
β	varies	Full width at half maximum
C	m^{-3}	Atomic concentration,
	F	Capacitance
c	ms^{-1}	Speed of light in vacuum, 2.99792×10^{8} ms^{-1} [6]
D	m^2s^{-1}	Diffusivity
d	m	Nanocrystal size
d_{hkl}	m	Distance between (hkl) lattice planes
Δ	°	Phase shift,
	varies	Difference in a quantity
δ	m	Grain boundary width
E	eV	Energy
E_a	eV	Activation energy

Symbol	*Dimension*	*Meaning*
E_C	eV	Conduction band edge
E_F	eV	Fermi level
E_g	eV	Bandgap
E_{Tauc}	eV	Tauc gap, E_g derived using the approach in Ref. [89]
E_V	eV	Valence band edge
ε_0	Fm^{-1}	Permittivity of free space, 8.85418×10^{-14} Fcm^{-1} [6]
η		Efficiency
FF		Fill factor; maximum power output of a solar cell divided by $V_{oc}j_{sc}$
g		g-factor, dimensionless magnetic moment
γ	m^{-1}	Inverse decay length of the electronic wavefunction
h	Js	Planck's constant, 6.62612×10^{-34} Js [6]
hkl		Miller indices
$h\nu$	eV	Photon energy
$h\Omega$	eV	Phonon energy
$\hbar$	Js	Reduced Planck's constant ($h/2\pi$), 1.05458×10^{-34} Js [6]
I	A	Current,
	arb.u.	Light intensity, typically as a function of λ
I_0	A	Reverse saturation current
j	Am^{-2}	Current density
j_0	Am^{-2}	Reverse saturation current density
j_{sc}	Am^{-2}	Short-circuit current density
j_{gen}	Am^{-2}	Optically generated current density

Symbol	*Dimension*	*Meaning*
k	m^{-1}	Extinction coefficient,
	JK^{-1}	Boltzmann's constant, 1.38066×10^{-23} JK^{-1} [6]
L	m	Diffusion length of atoms
L_{diff}	m	Diffusion length of charge carriers
λ	m	Wavelength
$M(\lambda)$		Modulation function, relates PL emitted *by* a film to the PL emitted *within* a film
m_*	kg	Effective mass of an electron
μ	$m^2V^{-1}s^{-1}$	Charge carrier mobility
μ_B	JT^{-1}	Bohr magneton, 9.27400968×10^{-24} JT^{-1} [285]
μ_{ext}	$m^2V^{-1}s^{-1}$	Extended-state charge carrier mobility
$\mu\tau$	m^2V^{-1}	Mobility-lifetime product
$N(E)$	$m^{-3}eV^{-1}$	Density of states per unit energy
N_{GB}	m^{-2}	Areal density at GBs
$N_{Si\ NC}$	m^{-3}	Volume density of Si NCs
$N_{Si\text{-}DB}$	m^{-3}	Si DB density
$N_{C\text{-}DB}$	m^{-3}	C DB density
n	m^{-3}	Charge carrier density,
		Refractive index,
		Integer
Δn	m^{-3}	Excess charge carrier density
ν	Hz	frequency
π		Number Pi
ψ		Wavefunction

Symbol	*Dimension*	*Meaning*
q	C	Elementary charge, 1.60218×10^{-19} C [6]
R		Reflectance/Reflection,
	Ω	Resistance
R_c	Ω	Contact resistance
R_p	Ωm^2	Parallel (Shunt) resistance
R_s	Ωm^2	Series resistance
R_{sh}	Ω/sq	Sheet resistance
r	m	Spatial variable
ρ	Ωm	Resistivity
s		VRH fitting parameter
σ	Sm^{-1}	Conductivity
σ_{ext}	Sm^{-1}	Conductivity through extended states
σ_{tail}	Sm^{-1}	Conductivity through tail states
σ_{VRH}	Sm^{-1}	Variable-range hopping conductivity
σ_{00}	Sm^{-1}	Prefactor for σ_{VRH}
σ_{01}	Sm^{-1}	Prefactor for σ_{ext}
σ_{02}	Sm^{-1}	Prefactor for σ_{tail}
θ	°	Angle
T	K	Absolute temperature,
	°C	Temperature,
		Transmittance/Transmission
T_0	K	VRH fitting parameter
$TF(\lambda)$		Transfer function, relates the PL detected by the setup to the PL emitted by the sample

Symbol	*Dimension*	*Meaning*
t	s	Time,
	m	Thickness
t_H	s	Hold time, time between applying voltage and measuring current in an IV measurement
τ	s	Minority carrier lifetime
V	V	Potential, Voltage
V_0	eV	Confinement potential
$V_{a\text{-}Si}$		Volume fraction of a-Si
V_{bi}	V	Built-in voltage
$V_{nc\text{-}Si}$		Volume fraction of nc-Si
V_{oc}	V	Open-circuit voltage
V_{Si}		Volume fraction of excess Si
w	m	Thickness,
	m	Contact width
Ω	Hz	Phonon frequency
ω	Hz	Angular frequency, $\omega=2\pi v$
$X_{c,Si}$		Crystallinity of V_{Si}
x		Compositional parameter,
	m	Spatial variable
y	m	Spatial variable

10. References

1. EPIA. *Global Market Outlook for Photovoltaics 2014-2018*. 2014.
2. Fraunhofer ISE. *Photovoltaics Report*. 2014.
3. Fraunhofer ISE. *Energy Charts*. 2014 [accessed 06.08.2014]; available from: https://www.energy-charts.de/power.htm.
4. M.A. Green, et al. *Solar cell efficiency tables (Version 45).* Progress in Photovoltaics: Research and Applications **23** (1), 1-9 (2015).
5. A. Richter, M. Hermle, and S.W. Glunz. *Reassessment of the limiting efficiency for crystalline silicon solar cells.* IEEE Journal of Photovoltaics **3** (4), 1184-91 (2013).
6. S.M. Sze, *Physics of semiconductor devices*. 2nd ed. 1981, New York: John Wiley & Sons.
7. M.A. Green, *Third generation photovoltaics - advanced solar energy conversion*. Springer Series in Photonics, ed. T. Kamiya et al. Vol. 12. 2003, Berlin/Heidelberg/ New York: Springer.
8. R.A. Street, *Hydrogenated amorphous silicon*. 2005: Cambridge University Press.
9. M.L. Mastronardi, et al. *Size-dependent absolute quantum yields for size-separated colloidally-stable silicon nanocrystals.* Nano Letters **12** (1), 337-42 (2011).
10. R. Müller, *Elektrische und photovoltaische Eigenschaften von Silicium-Nanokristallen in einer dielektrischen Matrix*. Diploma Thesis, Technische Fakultät, Universität Freiburg, Freiburg, Germany, 2011.
11. M. Zacharias, et al. *Size-controlled highly luminescent silicon nanocrystals: A SiO/SiO_2 superlattice approach.* Applied Physics Letters **80** (4), 661-3 (2002).

12. K. Surana, et al. *Enhanced conduction in Si quantum dot superlattice in SiO_2 matrix*, in *Proceedings of the 25th EU PVSEC* (Valencia, Spain, 2010)

13. G. Fu, et al. *The evolution of photoluminescence from Si cluster to nanocrystal in Si-rich oxide/SiO_2 multilayer films.* Journal of Alloys and Compounds **579**, 284-9 (2013).

14. V. Vinciguerra, et al. *Quantum confinement and recombination dynamics in silicon nanocrystals embedded in Si/SiO_2 superlattices.* Journal of Applied Physics **87** (11), 8165-73 (2000).

15. M. Künle, et al. *Annealing of nm-thin $Si_{1-x}C_x$/SiC multilayers.* Solar Energy Materials and Solar Cells **115**, 11-20 (2013).

16. Y. Kurokawa, et al. *Preparation of nanocrystalline silicon in amorphous silicon carbide matrix.* Japanese Journal of Applied Physics **45** (40), L1064 (2006).

17. D. Song, et al. *Structural characterization of annealed $Si_{1-x}C_x$/SiC multilayers targeting formation of Si nanocrystals in a SiC matrix.* Journal of Applied Physics **103**, 083544 (2008).

18. E.-C. Cho, et al. *Silicon quantum dots in a dielectric matrix for all-silicon tandem solar cells.* Advances in OptoElectronics **2007**, 1-11 (2007).

19. A.M. Hartel, et al. *Formation of size-controlled silicon nanocrystals in plasma enhanced chemical vapor deposition grown SiO_xN_y/SiO_2 superlattices.* Thin Solid Films **520** (1), 121-5 (2011).

20. M. Künle, et al. *Si-rich a-SiC:H thin films: structural and optical transformations during thermal annealing.* Thin Solid Films **519** (1), 151-7 (2010).

21. C. Summonte, et al. *Boron doping of silicon rich carbides: electrical properties.* Materials Science and Engineering B **178** (9), 551-558 (2013).

22. C. Summonte, et al. *Growth and characterization of Si nanodot multilayers in SiC matrix*, in *Proceedings of the 23rd EU PVSEC* (Valencia, Spain, 2008).

23. S. Godefroo, et al. *Classification and control of the origin of photoluminescence from Si nanocrystals.* Nature Nanotechnology **3**, 174-8 (2008).

24. G. Seguini, et al. *The energy band alignment of Si nanocrystals in SiO_2.* Applied Physics Letters **99** (8), 082107 (2011).

25. R.A. Puglisi, et al. *Charge transport in ultrathin silicon rich oxide/SiO_2 multilayers under solar light illumination and in dark conditions.* Journal of Applied Physics **108**, 023701 (2010).

26. S. Gutsch, et al. *Charge transport in Si nanocrystal/SiO_2 superlattices.* Journal of Applied Physics **113** (13), 133703 (2013).

27. C.-W. Jiang and M.A. Green. *Silicon quantum dot superlattices: Modeling of energy bands, densities of states, and mobilities for silicon tandem solar cell applications.* Journal of Applied Physics **99**, 114902 (2006).

28. P. Löper, et al. *Quasi-Fermi-level splitting in ideal silicon nanocrystal superlattices.* Physical Review B **84**, 195317 (2011).

29. W. Hu, et al. *Realistic quantum design of silicon quantum dot intermediate band solar cells.* Nanotechnology **24**, 265401 (2013).

30. G.L. Harris, *Properties of silicon carbide*. 1995, London, UK: INSPEC, the Institution of Electrical Engineers.

31. C. Summonte, et al. *Systematic characterisation of Silicon Nanodot Absorption in Silicon Carbide*, in *Proceedings of the 26th EU PVSEC* (Hamburg, Germany, 2011).

32. F. Meillaud, et al. *Efficiency limits for single-junction and tandem solar cells.* Solar Energy Materials and Solar Cells **90** (18-19), 2952-9 (2006).

33. M.T. Künle, *Silicon carbide single and multilayer thin films for photovoltaic applications*. Ph.D. Thesis, Mathematisch-Naturwissenschaftliche Fakultät, Universität Tübingen, Tübingen, Germany, 2011.

34. P. Löper, *Silicon Nanostructures for Photovoltaics*. Ph.D. Thesis, Technische Fakultät, Universität Freiburg, Freiburg, Germany, 2013.

35. P. Löper, et al. *A membrane device for substrate-free photovoltaic characterization of quantum dot based p-i-n solar cells.* Advanced Materials **24**, 3124-9 (2012).

36. S. Janz, P. Löper, and M. Schnabel. *Silicon nanocrystals produced by solid phase crystallisation of superlattices for photovoltaic applications.* Materials Science and Engineering B **178** (9), 542-50 (2013).

37. S. Janz, P. Löper, and M. Schnabel. *Prototype PV cells with Si nanoclusters*, in *Nanotechnology and Photovoltaic Devices: Light Energy Harvesting with Group IV Nanostructures*, ed. J. Valenta and S. Mirabella. 2014: Pan Stanford Publishing. p. 381-415.

38. M. Schnabel, et al. *Self-assembled silicon nanocrystal arrays for photovoltaics.* physica status solidi (a) (accepted).

39. S. Furukawa and T. Miyasato. *Three-Dimensional Quantum Well Effects in Ultrafine Silicon Particles.* Japanese Journal of Applied Physics **27** (11A), L2207 (1988).

40. L.T. Canham, *Silicon quantum wire array fabrication by electrochemical and chemical dissolution of wafers.* Applied Physics Letters **57** (10), 1046-8 (1990).

41. H. Takagi, et al. *Quantum size effects on photoluminescence in ultrafine Si particles.* Applied Physics Letters **56** (24), 2379-2380 (1990).

42. L. Tsybeskov, et al. *Stable and efficient electroluminescence from a porous silicon-based bipolar device.* Applied Physics Letters **68** (15), 2058-2060 (1996).

43. L.A. Nesbit, *Annealing characteristics of Si-rich SiO_2 films.* Applied Physics Letters **46** (1), 38-40 (1985).

44. Y. Kanzawa, et al. *Size-dependent near-infrared photoluminescence spectra of Si nanocrystals embedded in SiO_2 matrices.* Solid State Communications **102** (7), 533-7 (1997).

45. M. Dovrat, et al. *Radiative versus nonradiative decay processes in silicon nanocrystals probed by time-resolved photoluminescence spectroscopy.* Physical Review B **69**, 155311 (2004).

46. J. Heitmann, et al. *Silicon nanocrystals: size matters.* Advanced Materials **17** (7), 795-803 (2005).

47. D.J. Lockwood, Z.H. Lu, and J.-M. Baribeau. *Quantum confined luminescence in Si/SiO_2 superlattices.* Physical Review Letters **76** (3), 539-41 (1996).

48. G.F. Grom, et al. *Ordering and self-organization in nanocrystalline silicon.* Nature **407**, 358-61 (2000).

49. L. Tsybeskov, et al. *Nanocrystalline-silicon superlattice produced by controlled recrystallization.* Applied Physics Letters **72** (1), 43-5 (1998).

50. E.-C. Cho, et al. *Silicon quantum dot/crystalline silicon solar cells.* Nanotechnology **19**, 245201 (2008).

51. G. Conibeer, et al. *Silicon nanostructures for third generation photovoltaic solar cells.* Thin Solid Films **511-2**, 654-62 (2006).

52. F. Iacona, et al. *Formation and evolution of luminescent Si nanoclusters produced by thermal annealing of SiO_x films.* Journal of Applied Physics **95** (7), 3723-32 (2004).

53. L. Zhang, et al. *The dependence of the interface and shape on the constrained growth of nc-Si in a-SiN_x/a-Si:H/a-SiN_x structures.* Journal of Physics: Condensed Matter **14**, 10083-91 (2002).

54. S. Mirabella, et al. *Light absorption in silicon quantum dots embedded in silica.* Journal of Applied Physics **106**, 103505 (2009).

55. D. Hiller, S. Goetze, and M. Zacharias. *Rapid thermal annealing of size-controlled Si nanocrystals: Dependence of interface defect density on thermal budget.* Journal of Applied Physics **109** (5), 054308 (2011).

56. D. Hiller, et al. *A low thermal impact annealing process for SiO_2-embedded Si nanocrystals with optimized interface quality.* Journal of Applied Physics **115** (13), 134311 (2014).

57. J. Heitmann, et al. *Size controlled nc-Si synthesis by SiO/SiO_2 superlattices.* Journal of Non-Crystalline Solids **299-302**, 1075-8 (2002).

58. F. Ehrhardt, et al. *Control of silicon nanoparticle size embedded in silicon oxynitride dielectric matrix.* Journal of Applied Physics **114** (3), 033528 (2013).

59. S. Hernández, et al. *Tailoring the surface density of silicon nanocrystals embedded in SiO_x single layers.* Journal of Applied Physics **114** (23), 233101 (2013).

60. J. Barbé, et al. *Silicon nanocrystals on amorphous silicon carbide alloy thin films: Control of film properties and nanocrystals growth.* Thin Solid Films **522**, 136-144 (2012).

61. S. Kageyama, N. Matsuki, and H. Fujiwara. *Local network structure of a-SiC:H and its correlation with dielectric function.* Journal of Applied Physics **114** (23), 233513 (2013).

62. W. Siebert, et al. *Photoluminescence in a-$Si_{1-x}C_x$:H films.* Physica Status Solidi B **140** (1), 311-21 (1987).

63. M. Künle, et al. *Thermal annealing of SiC thin films with varying stoichiometry.* Materials Science and Engineering B **159-160**, 355-60 (2009).

64. A. Desalvo, et al. *Optoelectronic properties, structure and composition of a-SiC:H films grown in undiluted and H_2 diluted silane-methane plasma.* Journal of Applied Physics **81** (12), 7973-80 (1997).

65. H. Fritzsche, *Amorphous Silicon and Related Materials*. 1989: World Scientific.

66. A. Matsuda, *Growth mechanism of microcrystalline silicon obtained from reactive plasmas.* Thin Solid Films **337** (1–2), 1-6 (1999).

67. M. Fathallah, et al. *Light-soaking in a-SiC:H films grown by PECVD in undiluted and hydrogen diluted SiH_4+CH_4 gas mixtures.* Journal of Non-Crystalline Solids **200**, 490-4 (1996).

68. S. Gaiaschi, et al. *Structural properties of hydrogenated microcrystalline silicon–carbon alloys deposited by Radio Frequency Plasma Enhanced Chemical Vapor Deposition: Effect of microcrystalline silicon seed layer and methane flow rate.* Thin Solid Films **550**, 312-318 (2014).

69. S.Y. Myong, K.S. Lim, and M. Konagai. *Effect of hydrogen dilution on carrier transport in hydrogenated boron-doped nanocrystalline silicon-silicon carbide alloys.* Applied Physics Letters **88**, 103120 (2006).

70. F. Demichelis, C.F. Pirri, and E. Tresso. *Influence of doping on the structural and optoelectronic properties of amorphous and microcrystalline silicon carbide.* Journal of Applied Physics **72** (4), 1327-33 (1992).

71. D.A. Anderson and W.E. Spear. *Electrical and optical properties of amorphous silicon carbide, silicon nitride and germanium carbide prepared by the glow discharge technique.* Philosophical Magazine **35** (1), 1-16 (1977).

72. P. Löper, et al. *Silicon quantum dot absorber layers for all-silicon tandem solar cells: optical and electrical characterisation*, in *Proceedings of the 24th EU PVSEC* (Hamburg, Germany, 2009).

73. M. Künle, A. Hartel, and S. Janz. *Analysis of microstructural transformations during annealing of a-Si_xC_{1-x}:H/a-SiC:H layer stacks for the preparation of silicon quantum dot superlattices*, in *Proceedings of the 23rd EU PVSEC* (Valencia, Spain, 2008).

74. Y. Wang, et al. *High temperature annealing of hydrogenated amorphous silicon carbide thin film.* Thin Solid Films **384**, 173-6 (2001).

75. Y. Kurokawa, et al. *Effects of nitrogen on the electrical properties of Si quantum dots superlattice using a-SiC Matrix*, in *Proceedings of the 24th EU PVSEC* (Hamburg, Germany, 2009).

76. S. Yamada, et al. *High open-circuit voltage oxygen-containing silicon quantum dots superlattice solar cells*, in *Proceedings of the 35th IEEE PVSC* (Honolulu, HI USA, 2010).

77. D. Song, et al. *Fabrication and characterization of Si nanocrystals in SiC matrix produced by magnetron cosputtering.* Journal of Vacuum Science Technology B **25** (4), 1327-35 (2007).

78. H.W. Lau, O.K. Tan, and D.A. Trigg. *Charge injection and tunneling mechanism of solid state reaction silicon nanocrystal film.* Applied Physics Letters **89** (11), 113119 (2006).

79. M. Künle, et al. *Nanostructure and phase formation in annealed a-$Si_{1-x}C_x$:H thin films for advanced silicon solar cells*, in *Proceedings of the 21st Workshop on Quantum Solar Energy Conversion* (Rauris, Salzburg, Austria, 2009).

80. P. Löper, et al. *Silicon quantum dot superstructures for all-silicon tandem solar cells*, in *Proceedings of the 21st Workshop on Quantum Solar Energy Conversion* (Rauris, Salzburg, Austria, 2009).

81. C. Summonte, et al. *Optical properties of silicon nanodots in SiC matrix*, in *Proceedings of the 25th EU PVSEC* (Valencia, Spain, 2010).

82. D. Kovalev, et al. *Breakdown of the k-conservation rule in Si nanocrystals.* Physical Review Letters **81** (13), 2803-6 (1998).

83. L.V. Dao, et al. *Time-resolved and time-integrated photoluminescence and analysis of state filling and quantum confinement of silicon quantum dots.* Journal of Applied Physics **97**, 013501 (2005).

84. A.M. Hartel, et al. *Intrinsic nonradiative recombination in ensembles of silicon nanocrystals.* Physical Review B **87** (3), 035428 (2013).

85. A.M. Hartel, et al. *Fundamental temperature-dependent properties of the Si nanocrystal band gap.* Physical Review B **85** (16), 165306 (2012).

86. B.G. Lee, et al. *Strained interface defects in silicon nanocrystals.* Advanced Functional Materials **22** (15), 3223-32 (2012).

87. R.J. Walters, et al. *Photoluminescence quantum efficiency of dense silicon nanocrystal ensembles in SiO_2.* Physical Review B **73** (13), 132302 (2006).

88. N.F. Mott and E.A. Davis. *Electronic processes in non-crystalline materials*. 2nd ed. International series of monographs on physics. 1979, Oxford, UK: Clarendon Press.

89. J. Tauc, R. Grigorovici, and A. Vancu. *Optical properties and electronic structure of amorphous germanium.* Physica Status Solidi B **15** (2), 627-37 (1966).

90. J. Bullot, et al. *Electronic and optical properties of glow-discharge amorphous silicon-carbon alloys.* Philosophical Magazine B **49** (5), 489-501 (1984).

91. J. Bullot and M.P. Schmidt. *Physics of amorphous silicon-carbon alloys.* Physica Status Solidi B **143** (2), 345-418 (1987).

92. A. Hartel, et al. *Amorphous Si_xC_{1-x}:H single layers before and after thermal annealing: correlating optical and structural properties,* in *Proceedings of the EMRS Spring Meeting* (Strasbourg, France, 2009).

93. D. Song, et al. *Structural, electrical and photovoltaic characterization of Si nanocrystals embedded SiC matrix and Si nanocrystals/c-Si heterojunction devices.* Solar Energy Materials and Solar Cells **92**, 474-81 (2008).

94. M. Igarashi, et al. *Effects of formation of mini-bands in two-dimensional array of silicon nanodisks with SiC interlayer for quantum dot solar cells.* Nanotechnology **24** (1), 015301 (2013).

95. C. Summonte, et al. *Systematic characterization of silicon nanodot absorption for third generation photovoltaics*, in *Proceedings of the 26th EU PVSEC* (Hamburg, Germany, 2011).

96. C. Summonte, et al. *Optical properties of silicon rich oxides.* Physica Status Solidi C **8** (3), 996-1001 (2011).

97. C. Summonte, et al. *Optical properties of silicon nanoparticles for photovoltaic applications*, in *Proceedings of the 24th EU PVSEC* (Hamburg, Germany, 2009).

98. A. Suzuki, H. Matsunami, and T. Tanaka. *Photoluminescence due to Al, Ga, and B acceptors in 4H-, 6H-, and 3C-SiC grown from a Si melt.* Journal of The Electrochemical Society **124** (2), 241-6 (1977).

99. R. Reitano, et al. *Room temperature blue light emission from ECR-CVD deposited nano-crystalline SiC.* Materials Science and Engineering C **15** (1-2), 299-302 (2001).

100. W. Yu, et al. *Decay processes of photoluminescence in a nanocrystalline SiC thin film.* Applied Surface Science **258** (5), 1733-7 (2011).

101. G.-R. Chang, et al. *Multi-band silicon quantum dots embedded in an amorphous matrix of silicon carbide.* Nanotechnology **21** (46), 465605/1-8 (2010).

102. G. Wen, et al. *Photoluminescence properties and crystallization of silicon quantum dots in hydrogenated amorphous Si-rich silicon carbide films.* Journal of Applied Physics **115** (16), 164303 (2014).

103. Y. Kurokawa, et al. *Effects of rehydrogenation on silicon quantum dots superlattice*, in *Proceedings of the 22nd EU PVSEC* (Milan, Italy, 2007).

104. R. Rölver, et al. *Si/SiO_2 multiple quantum wells for all silicon tandem cells: Conductivity and photocurrent measurements.* Thin Solid Films **516** (20), 6763-6 (2008).

105. I.V. Antonova, et al. *Charge storage, photoluminescence, and cluster statistics in ensembles of Si quantum dots.* Physical Review B **77** (12), 125318 (2008).

106. I. Balberg, *Electrical transport mechanisms in three dimensional ensembles of silicon quantum dots.* Journal of Applied Physics **110**, 061301 (2011).

107. X.J. Hao, et al. *Synthesis and characterization of boron-doped Si quantum dots for all-Si quantum dot tandem solar cells.* Solar Energy Materials and Solar Cells **93**, 273-9 (2009).

108. M. Xie, et al. *The location and doping effect of boron in Si nanocrystals embedded silicon oxide film.* Applied Physics Letters **102** (12), 123108 (2013).

109. H. Gnaser, et al. *Phosphorus doping of Si nanocrystals embedded in silicon oxynitride determined by atom probe tomography.* Journal of Applied Physics **115** (3), 034304 (2014).

110. S. Gutsch, et al. *Doping efficiency of phosphorus doped silicon nanocrystals embedded in a SiO_2 matrix.* Applied Physics Letters **100** (23), 233115 (2012).

111. X.J. Hao, et al. *Phosphorus-doped silicon quantum dots for all-silicon quantum dot tandem solar cells.* Solar Energy Materials and Solar Cells **93** (9), 1524-30 (2009).

112. S. Gutsch, *Electronic transport in ordered silicon nanocrystal networks*. Ph.D. Thesis, Technische Fakultät, Universität Freiburg, Freiburg, Germany, 2014.

113. H. Overhof, et al. *The transport mechanism in micro-crystalline silicon.* Journal of Non-Crystalline Solids **227–230 (Part 2)**, 992-5 (1998).

114. R. Lechner, et al. *Electronic properties of doped silicon nanocrystal films.* Journal of Applied Physics **104**, 053701 (2008).

115. W.E. Spear and P.G. Le Comber. *Electronic properties of substitutionally doped amorphous Si and Ge.* Philosophical Magazine **33** (6), 935-49 (1976).

116. P.G. Le Comber and W.E. Spear. *Electronic transport in amorphous silicon films.* Physical Review Letters **25** (8), 509-11 (1970).

117. B.I. Shklovskii and A.L. Efros. *Electronic Properties of Doped Semiconductors*. 1984: Springer-Verlag Berlin Heidelberg.

118. C. Godet, *Hopping model for charge transport in amorphous carbon.* Philosophical Magazine Part B **81** (2), 205-222 (2001).

119. M. Pollak, *A percolation treatment of dc hopping conduction.* Journal of Non-Crystalline Solids **11** (1), 1-24 (1972).

120. C. Godet, *Variable range hopping revisited: the case of an exponential distribution of localized states.* Journal of Non-Crystalline Solids **299–302 (Part 1)**, 333-8 (2002).

121. A.L. Efros and B.I. Shklovskii. *Coulomb gap and low temperature conductivity of disordered systems.* Journal of Physics C: Solid State Physics **8** (4), L49-51 (1975).

122. B. Skinner, T. Chen, and B.I. Shklovskii. *Theory of hopping conduction in arrays of doped semiconductor nanocrystals.* Physical Review B **85** (20), 205316 (2012).

123. I. Solomon, T. Dietl, and D. Kaplan. *Influence of interface charges on transport measurements in amorphous silicon films.* Journal de Physique **39** (11), 1241-6 (1978).

124. H.K. Lee, et al. *Electrical properties of photo-CVD boron-doped hydrogenated nanocrystalline silicon-carbide (p-nc-SiC:H) films for uncooled IR bolometer applications.* Journal of Non-Crystalline Solids **316** (2-3), 297-301 (2003).

125. S.Y. Myong, et al. *Charge transport in hydrogenated boron-doped nanocrystalline silicon-silicon carbide alloys.* Journal of Applied Physics **98**, 054311 (2005).

126. S.B. Concari and R.H. Buitrago. *Hopping mechanism of electric transport in intrinsic and p-doped nanocrystalline silicon thin films.* Journal of Non-Crystalline Solids **338-40**, 331-5 (2004).

127. L. Magafas, N. Georgoulas, and A. Thanailakis. *Electrical properties of a-SiC/c-Si(p) heterojunctions.* Semiconductor Science and Technology **7**, 1363-8 (1992).

128. M. Igarashi, et al. *Generation of high photocurrent in three-dimensional silicon quantum dot superlattice fabricated by combining bio-template and neutral beam etching for quantum dot solar cells.* Nanoscale Research Letters **8** (228), 1-7 (2013).

129. Y. Rui, et al. *Size-dependent electroluminescence from Si quantum dots embedded in amorphous SiC matrix.* Journal of Applied Physics **110**, 064322 (2011).

130. R. Gradmann, *Charakterisierung von Silizium-Nanokristallen in einer Siliziumkarbid-Matrix*. Diploma Thesis, Institut für Kristallographie, Universität zu Köln, Köln, Germany, 2010.

131. Y. Kurokawa, et al. *Effects of oxygen addition on electrical properties of silicon quantum dots/amorphous silicon carbide superlattice.* Current Applied Physics **10** (3), S435-8 (2010).

132. K. Ding, et al. *Defect passivation by hydrogen reincorporation for silicon quantum dots in SiC/SiO_x hetero-superlattice.* Journal of Non-Crystalline Solids **358** (17), 2145-2149 (2012).

133. P. Torres, et al. *Device grade microcrystalline silicon owing to reduced oxygen contamination.* Applied Physics Letters **69** (10), 1373-5 (1996).

134. A. Morimoto, et al. *Doping effect of oxygen or nitrogen impurity in hydrogenated amorphous silicon films.* Applied Physics Letters **59** (17), 2130-2132 (1991).

135. T. Dalibor, et al. *Oxygen in silicon carbide: shallow donors and deep accepters.* Materials Science and Engineering B **61-62**, 454-9 (1999).

136. A. Gali, et al. *Isolated oxygen defects in 3C- and 4H-SiC: A theoretical study.* Physical Review B **66** (12), 125208 (2002).

137. M. Eickhoff, et al. *Influence of crystal quality on the electronic properties of n-type 3C-SiC grown by low temperature low pressure chemical vapor deposition.* Journal of Applied Physics **95** (12), 7908-17 (2004).

138. W. Hellmich, et al. *Electronic transport in thermally crystallized SiC films on sapphire.* Materials Science and Engineering B **29** (1–3), 147-150 (1995).

139. S. Miyajima, A. Yamada, and M. Konagai. *Characterization of undoped, n- and p-type hydrogenated nanocrystalline silicon carbide films deposited by hot-wire*

chemical vapor deposition at low temperatures. Japanese Journal of Applied Physics **46** (4A), 1415-26 (2007).

140. H.-Y. Tai, C.-H. Cheng, and G.-R. Lin. *Blue-green light emission from Si and SiC quantum dots co-doped Si-rich SiC p-i-n junction diode.* IEEE Journal of Selected Topics in Quantum Electronics **20** (4), 1-7 (2014).

141. V. Grivickas, et al. *Excess carrier recombination lifetime of bulk n-type 3C-SiC.* Applied Physics Letters **95** (24), 242110 (2009).

142. G. Manolis, et al. *Optical Investigation of Electronic Properties in Bulk and Surface Region of Sublimation-grown 3C-SiC Crystals.* Materials Science Forum **615-17**, 303-306 (2009).

143. R.E.I. Schropp and M. Zeman. *Amorphous and microcrystalline silicon solar cells: modeling, materials and device technology*. 1998, Boston/Dordrecht/London: Kluwer Academic Publishers.

144. S. Park, et al. *Study of the electrical properties of Si QD heteroface and p-i-n junction devices on crystalline silicon substrate*, in *Proceedings of the 23rd EU PVSEC* (Valencia, Spain, 2008).

145. A.K. Panchal, et al. *Photovoltaic devices with silicon quantum wells and dots structures in silicon nitride dielectric*, in *Proceedings of the 26th EU PVSEC* (Hamburg, Germany, 2011).

146. Y. Kurokawa, et al. *Observation of the photovoltaics effect from the solar cells using silicon quantum dots superlattice as a light absorption layer*, in *Proceedings of the 33rd IEEE PVSC* (San Diego, CA, USA, 2008).

147. S. Yamada, et al. *Improvement of electrical properties of silicon quantum dot superlattice solar cells with diffusion barrier layers.* Japanese Journal of Applied Physics **52** (4S), 04CR02 (2013).

148. S. Yamada, Y. Kurokawa, and M. Konagai. *High thermostable and conductive niobium doped titanium oxide for the application to a diffusion barrier layer of silicon quantum dot superlattice solar cell structure*, in *Proceedings of the 37th IEEE PVSC* (Seattle, WA, USA, 2011).

149. I. Perez-Wurfl, et al. *Si nanocrystal p-i-n diodes fabricated on quartz substrates for third generation solar cell applications.* Applied Physics Letters **95**, 153506 (2009).

150. I. Perez-Wurfl, et al. *Silicon nanocrystals in an oxide matrix for thin film solar cells with 492 mV open circuit voltage.* Solar Energy Materials and Solar Cells **100**, 65-8 (2012).

151. L. Wu, et al. *Silicon nanocrystal photovoltaic device fabricated via photolithography and its current–voltage temperature dependence.* Solar Energy Materials and Solar Cells **128**, 435-440 (2014).

152. W. Kern and D. Puotinen. *Cleaning solutions based on hydrogen peroxide for use in silicon semiconductor technology.* RCA Review **31**, 187-205 (1970).

153. M. Canino, et al. *Identification and tackling of a parasitic surface compound in SiC and Si-rich carbide films.* Materials Science and Engineering B **178** (9), 623– 629 (2013).

154. M. Schnabel, et al. *Thermal oxidation and encapsulation of silicon–carbon nanolayers.* Thin Solid Films **527**, 193-9 (2013).

155. S. Lindekugel, et al. *Plasma hydrogen passivation for crystalline silicon thin-films*, in *Proceedings of the 23rd EU PVSEC* (Valencia, Spain, 2008).

156. S. Yamada, et al. *Investigation of hydrogen plasma treatment for reducing defects in silicon quantum dot superlattice structure with amorphous silicon carbide matrix.* Nanoscale Research Letters **9** (72), 1-8 (2014).

157. J. Crofton, L.M. Porter, and J.R. Williams. *The physics of ohmic contacts to SiC.* Physica Status Solidi B **202** (1), 581-603 (1997).

158. L.M. Porter and R.F. Davis. *A critical review of ohmic and rectifying contacts for silicon carbide.* Materials Science and Engineering B **34** (2–3), 83-105 (1995).

159. U. Jäger, et al. *A laser based process for the formation of a local back surface field for n-type silicon solar cells.* Thin Solid Films **519** (11), 3827-30 (2011).

160. C. Schmiga, M. Hermle, and S.W. Glunz. *Towards 20% efficient n-type silicon solar cells with screen-printed aluminium-alloyed rear emitter,* in *Proceedings of the 23rd EU PVSEC* (Valencia, Spain, 2008).

161. H.H. Berger, *Contact resistance and contact resistivity.* Journal of the Electrochemical Society **119** (4), 507-14 (1972).

162. G.K. Reeves and H.B. Harrison. *Obtaining the specific contact resistance from transmission line model measurements.* IEEE Electron Device Letters **3** (5), 111-3 (1982).

163. A. Witzky, *Elektrische und optische Charakterisierung von Silicium-Carbid-Schichten mit eingebetteten Silicium-Nanokristallen für Silicium-basierte Solarzellen mit hoher Bandlücke*. Diploma Thesis, Fakultät für Mathematik und Physik, Universität Freiburg, Freiburg, Germany, 2012.

164. M. Schnabel, et al. *Electrical and optical characterisation of silicon nanocrystals embedded in SiC.* Solid State Phenomena **205-6**, 480-5 (2014).

165. M. Schnabel, et al. *Absorption and Emission of Silicon Nanocrystals Embedded in SiC: Eliminating Fabry-Pérot Interference.* Journal of Applied Physics (in press).

166. C. Summonte, et al. *Silicon nanocrystals in carbide matrix.* Solar Energy Materials and Solar Cells **128**, 138-49 (2014).

167. V.P. Kunets, et al. *Electron transport in quantum dot chains: Dimensionality effects and hopping conductance.* Journal of Applied Physics **113** (18), 183709 (2013).

168. J. Singh, *Radiative lifetime and spontaneous emission in amorphous semiconductors.* Journal of Optoelectronics and Advanced Materials **7** (1), 129-36 (2005).

169. P. Scherrer, *Bestimmung der Größe und der inneren Struktur von Kolloidteilchen mittels Röntgenstrahlen.* Nachrichten von der Gesellschaft der Wissenschaften zu Göttingen, Mathematisch-Physikalische Klasse **1918**, 98-100 (1918).

170. U. Coscia, G. Ambrosone, and D.K. Basa. *Room temperature visible photoluminescence of silicon nanocrystallites embedded in amorphous silicon carbide matrix.* Journal of Applied Physics **103**, 063507 (2008).

171. J. Barreto, et al. *Photoluminescence characterization of silicon nanostructures embedded in silicon oxide.* Superlattices and Microstructures **43**, 588-93 (2008).

172. R. Ferre, et al. *Optical-geometrical effects on the photoluminescence spectra of Si nanocrystals embedded in SiO_2.* Journal of Applied Physics **98**, 084319 (2005).

173. S.M. Orbons, M.G. Spooner, and R.G. Elliman. *Effect of material structure on photoluminescence spectra from silicon nanocrystals.* Journal of Applied Physics **96** (8), 4650-4652 (2004).

174. A. Zelenina, et al. *Structural and optical properties of size controlled Si nanocrystals in Si_3N_4 matrix: The nature of photoluminescence peak shift.* Journal of Applied Physics **114** (18), 184311 (2013).

175. A. Rodriguez-Gómez, et al. *Effect of thickness on the photoluminescence of silicon quantum dots embedded in silicon nitride films.* Journal of Applied Physics **113** (23), 233102 (2013).

176. S.A. Dyakov, et al. *Thermal radiation dynamics in two parallel plates: The role of near field.* Physical Review B **90** (4), 045414 (2014).

177. S.A. Dyakov, et al. *Influence of the buffer layer properties on the intensity of Raman scattering of graphene.* Journal of Raman Spectroscopy **44** (6), 803-9 (2013).

178. S.A. Dyakov, et al. *Enhancement of photoluminescence signal from ultrathin layers with silicon nanocrystals.* Applied Physics Letters **100** (6), 061908 (2012).

179. K.A. Neyts, *Simulation of light emission from thin-film microcavities.* Journal of the Optical Society of America A: Optics, Image Science & Vision **15** (4), 962-71 (1998).

180. C. Summonte, *Dielectric function and spectrophotometry: from bulk to nanostructures*, in *Nanotechnology and Photovoltaic Devices: Light Energy Harvesting with Group IV Nanostructures*, ed. J. Valenta and S. Mirabella. 2014: Pan Stanford Publishing. p.27-64.

181. W.J. Choyke, Z.C. Feng, and J.A. Powell. *Low-temperature photoluminescence studies of chemical-vapor-deposition-grown 3C-SiC on Si.* Journal of Applied Physics **64** (6), 3163-3175 (1988).

182. P. Docampo, et al. *Efficient organometal trihalide perovskite planar-heterojunction solar cells on flexible polymer substrates.* Nature Communications **4**, 2761 (2013).

183. M. Schnabel, et al. *Charge Transport in Nanocrystalline SiC with and without embedded Si Nanocrystals.* submitted to Physical Review B.

184. F. Lau, et al. *A model for phosphorus segregation at the silicon-silicon dioxide interface.* Applied Physics A **49** (6), 671-5 (1989).

185. C.D. Lorenz and R.M. Ziff. *Precise determination of the critical percolation threshold for the three-dimensional "Swiss cheese" model using a growth algorithm.* The Journal of Chemical Physics **114** (8), 3659-3661 (2001).

186. Y. Tsunoda, T. Sameshima, and S. Higashi. *Improvement of electrical properties of pulsed laser crystallized silicon films by oxygen plasma treatment.* Japanese Journal of Applied Physics **39** (4R), 1656 (2000).

187. N. Ishii, M. Kumeda, and T. Shimizu. *A simple molecular orbital calculation of ESR g-values for amorphous $Si_{1-x}C_x$, $Si_{1-x}Ge_x$ and $Ge_{1-x}C_x$.* Solid State Communications **41** (2), 143-6 (1982).

188. V.V. Afanas´ev, et al. *Elimination of SiC/SiO_2 interface states by preoxidation ultraviolet-ozone cleaning.* Applied Physics Letters **68** (15), 2141-3 (1996).

189. M.H. Brodsky and R.S. Title. *Electron spin resonance in amorphous silicon, germanium, and silicon carbide.* Physical Review Letters **23** (11), 581-5 (1969).

190. O. Chevaleevski, et al. *ESR studies of hydrogenated nanocrystalline silicon carbide*, in *Proceedings of the 3rd World Conference on Photovoltaic Energy Conversion* (Osaka, Japan, 2003).

191. H. Itoh, et al. *Intrinsic defects in cubic silicon carbide.* Physica Status Solidi A **162** (1), 173-98 (1997).

192. T. Shimizu, M. Kumeda, and Y. Kiriyama. *ESR studies on sputtered amorphous Si-C, Si-Ge and Ge-C films.* Solid State Communications **37** (9), 699-703 (1981).

193. J. López-Vidrier, et al. *Charge transport and electroluminescence of silicon nanocrystals/SiO_2 superlattices.* Journal of Applied Physics **114** (16), 163701 (2013).

194. C.H. Seager and T.G. Castner. *Zero-bias resistance of grain boundaries in neutron-transmutation-doped polycrystalline silicon.* Journal of Applied Physics **49** (7), 3879-89 (1978).

195. W. Hellmich, et al. *Optical absorption and electronic transport in ion-implantation-doped polycrystalline SiC films.* Applied Physics A **61** (2), 193-201 (1995).

196. G. Blatter and F. Greuter. *Carrier transport through grain boundaries in semiconductors.* Physical Review B **33** (6), 3952-66 (1986).

197. Y.-M. Niquet and C. Delerue. *Band offsets, wells, and barriers at nanoscale semiconductor heterojunctions.* Physical Review B **84** (7), 075478 (2011).

198. J.D. Hwang, et al. *A novel β-SiC/Si heterojunction backward diode.* IEEE Electron Device Letters **16** (5), 193-195 (1995).

199. M.J. Bozack, *Surface studies on SiC as related to contacts.* Physica Status Solidi B **202** (1), 549-80 (1997).

200. M.I. Chaudhry, *Electrical transport properties of crystalline silicon carbide/silicon heterojunctions.* IEEE Electron Device Letters **12** (12), 670-2 (1991).

201. L.F. Marsal, et al. *Annealing effects on the conduction mechanism of p^+-amorphous-$Si_{0.8}C_{0.2}$:H/ n-crystalline-Si diodes.* Journal of Applied Physics **94** (4), 2622-6 (2003).

202. J. Pelletier, D. Gervais, and C. Pomot. *Application of wide-gap semiconductors to surface ionization: Work functions of AlN and SiC single crystals.* Journal of Applied Physics **55** (4), 994-1002 (1984).

203. D.J. Gibbons and W.E. Spear. *Electron hopping transport and trapping phenomena in orthorhombic sulphur crystals.* Journal of Physics and Chemistry of Solids **27** (11-12), 1917-25 (1966).

204. J. Hirsch, *Hopping transport in disordered aromatic solids: a re-interpretation of mobility measurements on PKV and TNF*. Journal of Physics C: Solid State Physics **12** (2), 321-35 (1979).

205. W. Beyer and H. Overhof. *Transport properties of doped amorphous silicon.* Solid State Communications **31** (1), 1-4 (1979).

206. P. Pichler, *Intrinsic Point Defects, Impurities, and Their Diffusion in Silicon*. Computational Microelectronics, ed. S. Selberherr. 2004: Springer Verlag.

207. D. Hiller, et al. *$P_{b(0)}$ centers at the Si-nanocrystal/SiO_2 interface as the dominant photoluminescence quenching defect.* Journal of Applied Physics **107**, 084309 (2010).

208. L. Bagolini, et al. *Quantum confinement by an order-disorder boundary in nanocrystalline silicon.* Physical Review Letters **104**, 176803 (2010).

209. M.T. Lusk, et al. *Quantum confinement of nanocrystals within amorphous matrices.* Physical Review B **89** (7), 075433 (2014).

210. R. Flückiger, et al. *Electrical properties and degradation kinetics of compensated hydrogenated microcrystalline silicon deposited by very high-frequency-glow discharge.* Journal of Applied Physics **77** (2), 712-716 (1995).

211. H. Nagel, C. Berge, and A.G. Aberle. *Generalized analysis of quasi-steady-state and quasi-transient measurements of carrier lifetimes in semiconductors.* Journal of Applied Physics **86** (11), 6218- 21 (1999).

212. D. Hiller, et al. *Absence of quantum confinement effects in the photoluminescence of Si_3N_4–embedded Si nanocrystals.* Journal of Applied Physics **115** (20), 204301 (2014).

213. M. Schnabel, et al. *Phosphorus Diffusion in Nanocrystalline 3C-SiC.* submitted to Applied Physics Letters.

214. M. Schnabel, et al. *Boron diffusion in nanocrystalline 3C-SiC.* Applied Physics Letters **104** (21), 213108 (2014).

215. M. Schnabel, et al. *Nanocrystalline SiC formed by annealing of a-SiC:H on Si substrates: A study of dopant interdiffusion.* Journal of Applied Physics **116**, 024315 (2014).

216. G. Lucovsky, et al. *Oxygen-bonding environments in glow-discharge-deposited amorphous silicon-hydrogen alloy films.* Physical Review B **28** (6), 3225-33 (1983).

217. P.I. Rovira and F. Alvarez. *Chemical (dis)order in a-$Si_{1-x}C_x$:H for $x<0.6$.* Physical Review B **55** (7), 4426-34 (1997).

218. A. Avila, et al. *Behavior of oxygen doped SiC thin films: an x-ray photoelectron spectroscopy study.* Journal of Applied Physics **89** (1), 212-6 (2001).

219. A. Agarwal, H.-J. Gossmann, and D.J. Eaglesham. *Boron-enhanced diffusion of boron: Physical mechanisms.* Applied Physics Letters **74** (16), 2331-3 (1999).

220. M. Bockstedte, A. Mattausch, and O. Pankratov. *Different roles of carbon and silicon interstitials in the interstitial-mediated boron diffusion in SiC.* Physical Review B **70** (11), 115203 (2004).

221. H. Gu, Y. Shinoda, and F. Wakai. *Detection of boron segregation to grain boundaries in silicon carbide by spatially resolved electron energy-loss spectroscopy.* Journal of the American Ceramic Society **82** (2), 469-72 (1999).

222. L. Pavesi and R. Turan. *Silicon nanocrystals: fundamentals, synthesis and applications*. 2010: John Wiley & Sons.

223. M. Schnabel, et al. *Electrical properties of recrystallised SiC films from PECVD precursors for silicon quantum dot solar cell applications*, in *Proceedings of the 26th EU PVSEC* (Hamburg, Germany, 2011).

224. D.K. Schroder, R.N. Thomas, and J.C. Swartz. *Free carrier absorption in silicon.* IEEE Journal of Solid-State Circuits **13** (1), 180-7 (1978).

225. R.A. Smith, *Semiconductors*. 2nd ed. 1978, New York, USA: Cambridge University Press.

226. P.A. Schumann, Jr., et al. *Silicon optical constants in the infrared.* Journal of the Electrochemical Society **118** (1), 145-8 (1971).

227. J. Isenberg, *Neue Infrarotmesstechniken der Photovoltaik*. Ph.D. Thesis, Fakultät für Physik, Universität Konstanz, Konstanz, Germany, 2003.

228. A. Orpella, et al. *In situ-doped amorphous $Si_{0.8}C_{0.2}$ emitter bipolar transistors.* IEEE Electron Device Letters **20** (11), 592-4 (1999).

229. M.J.J. Theunissen, et al. *Experimental Study of Diffusion and Interface Segregation of P in an LPCVD Si-Carbon Emitter Structure.* Journal of the Electrochemical Society **142** (1), 226-231 (1995).

230. L.F. Marsal, et al. *Analysis of conduction mechanisms in annealed n-$Si_{1-x}C_x$:H/ p-crystalline Si heterojunction diodes for different doping concentrations.* Journal of Applied Physics **85** (2), 1216-21 (1999).

231. F.A. Rubinelli, L.F. Marsal, and J. Pallares. *Performance of annealed hybrid silicon heterojunctions: A numerical computer study.* Journal of Applied Physics **97** (3), 034904 (2005).

232. P. Scherrer, *Bestimmung der inneren Struktur und der Größe von Kolloidteilchen mittels Röntgenstrahlen*, in *Kolloidchemie Ein Lehrbuch*. 1912: Springer Berlin Heidelberg. p. 387-409.

233. H. Bracht, et al. *Diffusion of boron in silicon carbide: evidence for the kick-out mechanism.* Applied Physics Letters **77** (20), 3188-90 (2000).

234. E.N. Mokhov, et al. *Diffusion of phosphorus in silicon carbide.* Soviet Physics Solid State **34** (6), 1043-5 (1992).

235. J.C. Fisher, *Calculation of diffusion penetration curves for surface and grain boundary diffusion.* Journal of Applied Physics **22** (1), 74-7 (1951).

236. T. Suzuoka, *Lattice and grain boundary diffusion in polycrystals.* Transactions of the Japan Institute of Metals **2** (1), 25-33 (1961).

237. J. Crank, *The mathematics of diffusion*. 1979: Oxford University Press.

238. M.H. Hon and R.F. Davis. *Self-diffusion of ^{14}C in polycrystalline β-SiC.* Journal of Materials Science **14** (10), 2411-21 (1979).

239. M. Laube, G. Pensl, and H. Itoh. *Suppressed diffusion of implanted boron in 4H–SiC.* Applied Physics Letters **74** (16), 2292-4 (1999).

240. J. Bernholc, et al. *Theory of native defects, doping and diffusion in diamond and silicon carbide.* Materials Science and Engineering B **11** (1–4), 265-72 (1992).

241. M. Bockstedte, A. Mattausch, and O. Pankratov. *Ab initio study of the migration of intrinsic defects in 3C-SiC.* Physical Review B **68** (20), 205201 (2003).

242. W. Guter, *Tunneldioden und deren Bandstruktur in III-V Mehrfachsolarzellen*. Diploma Thesis, Fakultät für Mathematik und Physik, Universität Freiburg, Freiburg, Germany, 2005.

243. W. Guter, et al. *Current-matched triple-junction solar cell reaching 41.1% conversion efficiency under concentrated sunlight.* Applied Physics Letters **94** (22), 223504 (2009).

244. L. Esaki and Y. Miyahara. *A new device using the tunneling process in narrow p-n junctions.* Solid-State Electronics **1** (1), 13-21 (1960).

245. D. Suwito, *Dünnschichtsolarzellen aus zonengeschmolzenen Siliziumschichten mit in-situ Back Surface Field*. Diploma Thesis, Fakultät für Mathematik und Physik, Universität Freiburg, Freiburg, Germany, 2006.

246. K. Schillinger, S. Janz, and S. Reber. *Atmospheric pressure chemical vapour deposition of 3C-SiC for silicon thin-film solar cells on various substrates.* Journal of Nanoscience and Nanotechnology **11**, 8108-13 (2011).

247. Personal Communication with K. Schillinger, 27.10.2014.

248. S.S. Hegedus, F. Kampas, and J. Xi. *Current transport in amorphous silicon n/p junctions and their application as "tunnel" junctions in tandem solar cells.* Applied Physics Letters **67** (6), 813-5 (1995).

249. J.Y. Hou, J.P. Xi, and F. Kampas. *Non-local recombination in "tunnel junctions" of multijunction amorphous Si alloy solar cells*, in *MRS Symposium Proceedings* (San Francisco, CA, USA, 1994).

250. J.P. Ostertag, O. Schmidt, and R. Brüggemann. *Semi-empirical model to describe the tunnel junction in tandem solar cells*, in *Proceedings of the 27th EU PVSEC* (Frankfurt, Germany, 2012).

251. D.S. Shen, et al. *Improving tunneling junction in amorphous silicon tandem solar cells.* Applied Physics Letters **56** (19), 1871-3 (1990).

252. J.Y. Hou, et al. *An examination of the tunnel-junctions in triple junction a-Si-H based solar cells: modeling and effects on performance*, in *Proceedings of the 22nd IEEE PVSC* (Las Vegas, USA, 1991).

253. F.A. Rubinelli, J.K. Rath, and R.E.I. Schropp. *Microcrystalline n-i-p tunnel junction in a-Si:H/a-Si:H tandem cells.* Journal of Applied Physics **89** (7), 4010-8 (2001).

254. Y.S. Lee, et al. *Nitrogen-doped cuprous oxide as a p-type hole-transporting layer in thin-film solar cells.* Journal of Materials Chemistry A **1** (48), 15416-15422 (2013).

255. S.W. Glunz, *Ladungsträgerrekombination in Silicium und Siliciumsolarzellen*. Ph.D. Thesis, Fakultät für Physik, Universität Freiburg, Freiburg, Germany, 1995.

256. J. Kwak, S.W. Kwon, and K.S. Lim. *Fabrication of a n–p–p tunnel junction for a protocrystalline silicon multilayer/amorphous silicon tandem solar cell.* Journal of Non-Crystalline Solids **352** (9–20), 1847-50 (2006).

257. S. Janz, et al. *Processing and characterisation of tandem solar cells from crystalline silicon materials,* in *Proceedings of the 28th EU PVSEC* (Paris, France, 2013).

258. P. Löper, et al. *Silicon nanocrystals embedded in silicon carbide: investigation of charge carrier transport and recombination.* Applied Physics Letters **102** (3), 033507 (2013).

259. I.G. Atabaev, et al. *Diffusion and electroluminescence studies of low temperature diffusion of boron in 3C-SiC.* Materials Science Forum **600-603**, 457-60 (2009).

260. A. Poggi, et al. *Rapid thermal annealing of p-type silicon. Correlation between deep-level transient spectroscopy and lifetime measurements.* Journal of the Electrochemical Society **141** (3), 754-8 (1994).

261. C.T. Sah and C.T. Wang. *Experiments on the origin of process−induced recombination centers in silicon.* Journal of Applied Physics **46** (4), 1767-1776 (1975).

262. NREL. *Reference Solar Spectral Irradiance: Air Mass 1.5*. 2014 [accessed 31.10.2014]; available from: http://rredc.nrel.gov/solar/spectra/am1.5/#refs.

263. F. Feldmann, et al. *Tunnel oxide passivated contacts as an alternative to partial rear contacts.* Solar Energy Materials and Solar Cells **131**, 46-50 (2014).

264. P. Würfel, *Physics of Solar Cells - From principles to new concepts*. 2005, Weinheim: Wiley-Vch Verlag GmbH & Co KgaA.

265. J. Merten, et al. *Improved equivalent circuit and analytical model for amorphous silicon solar cells and modules.* IEEE Transactions on Electron Devices **45** (2), 423-9 (1998).

266. J.A. Woollam, P.G. Snyder, and M.C. Rost. *Variable angle spectroscopic ellipsometry: A non-destructive characterization technique for ultrathin and multilayer materials.* Thin Solid Films **166**, 317-23 (1988).

267. E.D. Palik, *Handbook of Optical Constants of Solids*. Vol. 3. 1998: Academic Press.

268. M. Rothfelder, *Spektrale Ellipsometrie zur optischen und strukturellen Charakterisierung von amorphen Siliciumkarbid-Schichtsystemen*. Diploma Thesis, Fakultät für Mathematik und Physik, Universität Freiburg, Freiburg, Germany, 2010.

269. J. Goldstein, *Scanning Electron Microscopy and X-ray Microanalysis: Third Edition*. 2003: Springer US.

270. H. Günzler and H.U. Gremlich. *IR-Spektroskopie*. 2012, Weinheim: Wiley-Vch Verlag GmbH & Co KgaA.

271. H.P. Klug, *X-Ray Diffraction Procedure for Polycrystalline and Amorphous Materials*. 1974, New York: John Wiley & Sons.

272. J. López-Vidrier, et al. *Structural, optical and electrical properties of silicon nanocrystals embedded in Si_xC_{1-x}/SiC multilayer systems for photovoltaic applications.* Materials Science and Engineering B **178**, 639-44 (2013).

273. A.R. Stokes and A.J.C. Wilson. *The diffraction of X rays by distorted crystal aggregates - I.* Proceedings of the Physical Society **56** (3), 174-81 (1944).

274. G.K. Williamson and W.H. Hall. *X-ray line broadening from filed aluminium and wolfram.* Acta Metallurgica **1** (1), 22-31 (1953).

275. S. Hernández, et al. *Silicon nanocluster crystallization in SiO_x films studied by Raman scattering.* Journal of Applied Physics **104** (4), 044304 (2008).

276. V. Paillard, et al. *Improved one-phonon confinement model for an accurate size determination of silicon nanocrystals.* Journal of Applied Physics **86** (4), 1921-4 (1999).

277. Z. Iqbal and S. Veprek. *Raman scattering from hydrogenated microcrystalline and amorphous silicon.* Journal of Physics C: Solid State Physics **15** (2), 377 (1982).

278. E. Bustarret, M.A. Hachicha, and M. Brunel. *Experimental determination of the nanocrystalline volume fraction in silicon thin films from Raman spectroscopy.* Applied Physics Letters **52** (20), 1675-7 (1988).

279. C. Ossadnik, S. Vepřek, and I. Gregora. *Applicability of Raman scattering for the characterization of nanocrystalline silicon.* Thin Solid Films **337**, 148-51 (1999).

280. Personal Communication with RTG Microanalysis, 21.08.2012.

281. B. Odom, et al. *New Measurement of the Electron Magnetic Moment Using a One-Electron Quantum Cyclotron.* Physical Review Letters **97** (3), 030801 (2006).

282. P. Rosenits, *Electrical characterisation of crystalline silicon thin-film material*. Ph.D. Thesis, Fachbereich Physik, Universität Konstanz, Konstanz, Germany, 2010.

283. C. Reichel, *Decoupling charge carrier collection and metallization geometry of back-contacted back-junction silicon solar cells*. Ph.D. Thesis, Technische Fakultät, Universität Freiburg, Freiburg, Germany, 2012.

284. R.A. Sinton, A. Cuevas, and M. Stuckings. *Quasi-steady-state photoconductance, a new method for solar cell material and device characterization*, in *Proceedings of the 25th IEEE PVSC* (Washington DC, USA, 1996).

285. N.W. Ashcroft and N.D. Mermin. *Solid state physics*. 1976, Tokyo/Philadelphia: Holt-Saunders.